Semi-analytic Methods for Modelling Photonic Woodpiles

Dougal J. Kan

Thesis submitted for the degree of Doctor of Philosophy

2011

Declaration of Originality

I certify that the work in this thesis has not previously been submitted for a degree nor has it been submitted as part of requirements for a degree. I also certify that the thesis has been written by me. Any help that I have received in my research work and the preparation of the thesis itself has been acknowledged. In addition, I certify that all information sources and literature used are indicated in the thesis.

Signature of Author .....

Acknowledgements

I was very fortunate to have such capable supervisors in Dr. Chris Poulton, Dr. Ara Asatryan, and Prof. Lindsay Botten, who were patient, generous with their ideas, and who set high standards. Also, I thank Dr. Kokou Dossou for the helpful discussions and for carefully reviewing various manuscripts. These people taught me more than just the intricacies of the multipole method; they also gave me an appreciation of how optical physics abounds with opportunities for mathematical ingenuity, and for this I thank them.

Although it sounds terribly clichéd, I thank my family, who by now, I am sure, would much rather tell people that I have a job than tell people that I am still a PhD student.

I wish to acknowledge the financial support that was given to me in the form of a Doctoral Scholarship from the University of Technology, Sydney. Financial support for my PhD was also provided by the Centre for Ultrahigh-bandwidth Devices for Optical Systems (CUDOS) and Department of Mathematical Sciences, University of Technology, Sydney.

This thesis was perpared under the guidance of my supervisors, and contains many of their suggestions. Also, chapters 3, 4 and 5 are based on the following papers, which were authored jointly by my supervisors, Dr. Kokou Dossou and me over the course of my PhD:

D. J. Kan, A. A. Asatryan, C. G. Poulton, and L. C. Botten, "Multipole method for modeling linear defects in photonic woodpiles," J. Opt. Soc. Am. B ***27****, 246-258 (2010).*

D. J. Kan, A. A. Asatryan, C. G. Poulton, K. B. Dossou, and L. C. Botten, "Modelling waveguides in photonic woodpiles using the fictitious source superposition method," J. Opt. Soc. Am. B ***28****, 746-755 (2011).*

*D. J. Kan, L. C. Botten, C. G. Poulton, A. A. Asatryan, and K. B. Dossou, "Semianalytical formulations for the surface modes of photonic woodpiles," Phys. Rev. A **84**, 043805 (2011).*

In addition, the work in the above papers was presented at the following international conferences:

D. J. Kan, C. G. Poulton, L. C. Botten, and A. A. Asatryan, "Waveguide defect modes in woodpile photonic crystals," PECS VIII International Photonic and Electromagnetic Crystal Structures Meeting, Sydney, Australia, 2009.

D. J. Kan, A. A. Asatryan, C. G. Poulton, and L. C. Botten, "Multipole method for modeling linear defects in photonic woodpiles," ACOFT ACOLS 2009, Australasian Conference on Optics, Lasers and Spectroscopy and Australian Conference on Optical Fibre Technology in association with the International Workshop on Dissipative Solitons, Adelaide, Australia, 2009.

D. J. Kan, K. B. Dossou, A. A. Asatryan, C. G. Poulton, and L. C. Botten, "Modeling lossless waveguides in photonic woodpiles using the fictitious source superposition method," PECS IX International Photonic and Electromagnetic Crystal Structures Meeting, Granada, Spain, 2010.

D. J. Kan, C. G. Poulton, L. C. Botten, A. A. Asatryan, and K. B. Dossou, "Semianalytical Formulations for the Surface Modes of Photonic Woodpiles," IQEC/CLEO Pacific Rim 2011, The International Quantum Electronics Conference and The Conference on Lasers and Electro-Optics, Sydney, 2011.

Contents

List of Figures

List of Tables

Abstract

New semi-analytical methods are presented for modelling the electromagnetic fields of three-dimensional photonic crystals that are composed of orthogonal layers of cylindrical rods. Firstly, the *multipole method* is extended so that cylindrical defects, which act as optical waveguides, can be introduced into such 'woodpile' structures. These waveguides are important because they offer greater control over the mode dispersion and optical losses than conventional waveguides do. The multipole method forms the basis of all of the techniques presented in this thesis, and is employed here because it is considerably faster than the pre-existing methods for modelling woodpile waveguides.

Two approaches for modelling linear defects are presented. The first approach uses a grating super-cell to approximate a localised defect, and results are presented for both a coupled resonator optical waveguide and for a linear waveguide, where each waveguide is embedded in a finite woodpile cladding. The existence of waveguiding modes is inferred from the transmission spectra, and is verified by numerically reconstructing the fields. Furthermore, low loss waveguiding is observed for the linear waveguide.

To complement the super-cell approach, we have generalised the two-dimensional *fictitious source superposition* method, whereby the defect modes of a woodpile are computed directly. The principal advantage of this approach is that it is particularly efficient, making this approach well-suited to the task of tuning the dispersion relationships of the defect states; however, the performance gains are achieved by forgoing the ability to deal with finite structures. The dependence of the dispersion on the refractive index and size of the defect is investigated, and it is shown that tuning these parameters is an effective method for optimising the waveguide for operation in the slow-light regime.

Lastly, a comprehensive analysis of the surface modes of photonic woodpiles is performed. Specifically, the surface modes of both finite and semi-infinite woodpiles are characterised using transfer matrix and plane wave matrix formulations. In the case of finite structures, a general mathematical description of the modes that propagate simultaneously along the top and bottom surfaces is given. It is shown that when the number of layers is even, such 'double-interface' modes only exist for specific directions of the Brillouin zone. However, when the number of layers is odd, every surface mode is a double-interface mode and, in this case, the direction of propagation plays an important role in determining the coupling strength between the two surfaces: for certain directions, the coupling is negligible even when the number of layers is small. The dispersion curves

of two different double-interface modes can anticross or be interwoven, depending on the symmetry of the modes. A Fabry-Pérot cavity comprising two woodpile barrier regions is also considered. In particular, the conditions required in order for coupled surface modes to exist in these ‘compound woodpile’ structures are described.

Introduction

Over the last half-century, few of the advances made in the material sciences have had more far-reaching effects on society than the advent of semiconductor based technology, which ushered in the digital era. However, this technology is beginning to reach its physical limits, and so there is an increasing need to develop optical materials that are capable of operating at far greater speeds than semiconductor components. Such 'photonic' materials are exemplified by optical fibres, which, because of their unprecedented bandwidth, enabled the rapid growth of the telecommunication industry. One of the fundamental designs to emerge from the fibre optics revolution was the *fibre Bragg grating* (FBG), which was first demonstrated by Hill in 1978 [1], and which, due to the periodic variation of the refractive index along the length of the fibre, was able to transmit light selectively.

The mechanism underlying the selectivity of one-dimensional periodic systems like the FBG was elucidated by Lord Rayleigh in 1887 [2]: By adjusting the period, and thereby the amount of refraction, one can, as a result of the multiple scattering events, reflect target wavelengths while allowing the remaining light to be guided down the fibre. The extension of this idea to higher dimensional systems has its origins in the pioneering work on X-ray diffraction in crystals that was conducted by Sir William Lawrence Bragg, and for which he was awarded the Nobel prize in physics in 1915. Although Bragg's work was concerned with atomic lattices, it has since been realised that his findings are also applicable to macroscopic lattices, which, like FBGs, are periodic on a wavelength scale. The defining feature of these types of macroscopic optical crystals, or *photonic crystals* (PCs), is the periodic nature of their refractive index. Thus, an FBG is an example of a one-dimensional PC in that its refractive index varies periodically in only one direction and, hence, Bragg scattering only occurs for light travelling parallel to the axis of the fiber. For certain wavelengths, this Bragg scattering results in the formation of gaps in the optical frequency bands; a phenomenon that is referred to as a *photonic bandgap*. Simply put, the multiple scattering conspires, through destructive interference, to suppress the longitudinal propagation of light inside the fibre, leading to *Bragg reflection*.

This thesis describes new semi-analytic methods for modelling a type of photonic crystal that is known as a *photonic woodpile*, and results that were obtained using these methods are presented herein. Woodpiles are layered structures in which each layer comprises a one-dimensional array of parallel rods, with the rods in each layer aligned orthogonally to those of the layer below, as illustrated in Fig. 1. Unlike FBGs, woodpiles are three-dimensional (3D) PCs in that their refractive index varies periodically along the three axes of the structure. The one-dimensionality of FBGs means that bandgaps can only exist for light propagating down the length of the fibre. Similarly, bandgaps in 2D PCs only exist for directions lying in the plane of periodicity. Woodpiles, however, can possess a photonic bandgap that is capable of suppressing light of certain wavelengths from propagating inside the crystal, irrespective of wave vector and polarisation (the photonic density of states vanishes). Such a bandgap is said to be *complete*, a property that is unique to 3D PCs, and results in omnidirectional reflection over the wavelengths spanned by the complete bandgap. Under certain conditions, periodic 1D dielectric stacks can also exhibit omnidirectional polarisation-insensitive reflection [3]. However, unlike 3D PCs, this phenomenon cannot be used to localise light in three dimensions since it relies on the translational symmetry of the 1D PC. While 2D PCs can be used to localise light in three dimensions, such confinement is not omnidirectional since it only occurs for directions that lie above the critical angle for total internal reflection – a point that is discussed in the next chapter.

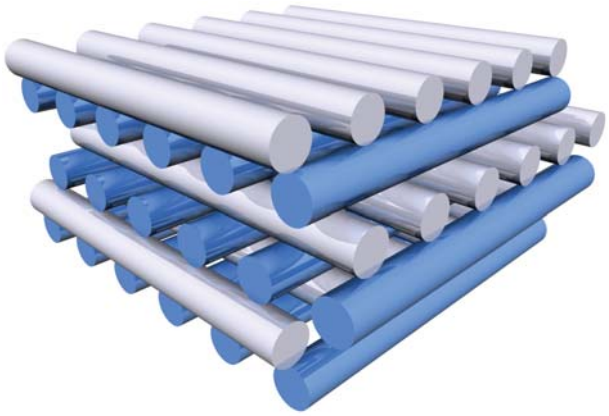

Figure 1: The geometry of the photonic woodpile.

The earliest investigations into the properties of 3D PCs were made during the 1970s by Vladamir Bykov [4] and Kazuo Ohtaka [5]. However, these papers went largely unnoticed at the time, and it wasn't until Eli Yablonovitch and Sajeev John, in 1987, pub-

lished seminal papers on the subject that interest in 3D PCs was rekindled [6, 7]. Both Yablonovitch and John were motivated by the prospect of using 3D PCs to control light in a manner analogous to the transport of electrons in semiconductors. In his paper [6], Yablonovitch demonstrated that 3D periodic systems made from lossless materials, such as dielectrics, could in principle be used to inhibit the spontaneous emission process in semiconductors. At the same time, John realised, by way of analogy with Anderson localisation [8] in amorphous semiconductors, that photons could be localised to defects in disordered dielectric 3D 'super-lattices' [7]. This implied that it might be possible to steer light along designed defects within the lattice. Thus, PCs can be thought of as 'semiconductors for light'. Yablonovitch's and John's papers generated an intense interest in PCs, and the first PCs with complete bandgaps were fabricated [9, 10] not long after these two papers were published.

Many uses for PCs have since been discovered. Compelling applications for PCs now include the creation of, *e.g.*, resonant cavities that have ultra-high quality-factors [11], slow-light waveguides [12] and directional couplers [13], and also include the study of non-linear processes such as third-harmonic generation [14]. Moreover, PCs need not be made from just dielectric materials; it has been shown that metallic and metallo-dielectric PCs are capable of low-loss guiding at long wavelengths [15], and also give rise to novel optical phenomena such as waveguide-plasmon polaritons [16].

While designs based on 2D periodicity have been tremendously successful, so far only a very small number of these designs have been realised using structures that are periodic in three dimensions [17–20]. This is because fabricating high-quality 3D PCs, as well as endowing these structures with functionality, is relatively difficult. Furthermore, successful designs are often motivated by theoretical predictions; however, modelling artificial defects in 3D PCs usually requires enormous amounts of computational power and memory, and it is likely that this computational barrier has hindered the development of functionalised 3D PC structures.

The woodpile is one of the most promising 3D PC geometries because it is amenable to several nanoscale fabrication techniques, each with its own advantages, and each capable of accurately incorporating defects into the structure. There are two general approaches for fabricating photonic woodpiles. The first involves using lithographic techniques to construct the woodpile in a layer-by-layer fashion, and is exemplified by the wafer bonding method [21], which has been used to create high-quality defect structures within the woodpile [17–19]. In addition, with this approach, incorporating layers made from active materials (*e.g.*, in the control of spontaneous emission processes) is straight-

forward [17]. The woodpiles produced using wafer bonding are already of sufficient quality and size for them to be used as optical interconnects. The other prominent fabrication approach utilises high-speed lasers to write the entire woodpile at once [22]. These 'direct writing' methods are fast, accurate (though not yet as accurate as lithography) and can been used to create fairly arbitrary defects [23].

Modelling woodpiles that contain defects is performed exclusively using the finite difference time domain [37] and planewave expansion methods [24]. These methods are important because the constraints they impose on the geometry are minimal. Furthermore, there are publicly available implementations that are moderately simple to use. The generality of such methods comes at the cost of efficiency; typically, simulations are limited to a small region of the parameter space. This shortcoming is addressed in this thesis. Specifically, new semi-analytical methods for modelling defect layers in photonic woodpiles are presented. The methods described herein significantly reduce the computational burden of modelling woodpile waveguides. In addition, we use semi-analytical methods to perform a comprehensive study of the waves that propagate along the top and bottom surfaces of woodpiles.

Overview of the Thesis

The structure of this thesis is as follows. Chapter 1 provides some context for this work. To this end, a review of the literature pertaining to woodpiles is provided. Although this thesis concerns methods for modelling photonic woodpiles, we nonetheless include woodpile fabrication methods in the review because woodpiles are not as yet commonplace in the study of photonic crystals, and so the reader might not be aware of the practicalities of the geometry. By also including a review of the experimental and theoretical investigations in which the woodpile is the novel optical element, we aim to give the reader an understanding of the types of applications that the woodpile is well-suited for. Chapter 1 concludes with a brief discussion of how the pre-existing methods for modelling photonic woodpiles compare with the semi-analytical methods that we have developed for modelling these structures.

Chapter 2 explains the basic theoretical framework for the methods described in later chapters. Firstly, a brief account of the general optical modes of PCs is given. These properties are essential to the understanding of the methods and results presented in later chapters. However, because the layers of the woodpile usually do not interpenetrate, it is better to regard the structure as an assemblage of diffraction gratings. The problem of

determining the modes then becomes one of determining the amplitudes of the diffracted fields generated by each layer. For circular rods, the diffracted fields can be found by applying the *multipole method*, whereby the fields in the vicinity of each rod are expanded in terms of cylindrical harmonics. The multipole method is the most efficient basis in which to compute the scattered fields produced by circular rods because very few basis functions are required in order to obtain well converged approximations for the fields[1]. For this reason, the multipole method is employed in all of the techniques that we have developed for modelling woodpiles.

Chapter 3 describes a new generalisation of the pre-existing multipole framework for woodpiles [25, 26]. It is shown how a grating super-cell can be incorporated into the existing framework, thereby allowing periodic defects to be introduced into the lattice. Super-cells are frequently employed in the study of PCs because they can be used to simulate localised defects, provided that the super-cell is sufficiently large. In addition, super-cells preserve the periodicity of the structure and, by doing so, effectively reduce the size of the problem domain. For 3D problems, the running time and memory requirements increase rapidly as the size of the super-cell increases, making this approach as much an exercise in computing as it is in mathematical modelling. We use the method to model a coupled-resonator optical waveguide, as well as a linear waveguide, where each waveguide comprises a defect layer embedded in a finite woodpile cladding.

Although the super-cell method is capable of approximating local defects, it is only of utility when the fields along the waveguide layer can be approximated using a small super-cell. If the fields require a large super-cell, as sometimes happens for linear waveguides, the computational load can be high, and in such instances one should look for more germane methods. To this end, we have generalised the *Fictitious Source Superposition* (FSS) method, described in Chapter 4, so that it can be used to model woodpile waveguides. This method obviates the need for a super-cell, and instead proceeds by placing an artificial source inside each rod of the defect layer and then subsequently taking an appropriate field superposition to remove all but one of these sources. The remaining source can then be used to mimic the fields that would be produced by a defect rod. This can be done efficiently because the multipole formulation lets one manipulate the outgoing fields directly; however, the FSS method forgoes the ability to deal with a finite number of layers. The FSS method is utilised in the study of 2D PCs [27] because it is one of the few methods that models local defects exactly, and that can thus cope with highly-extended fields, such as those that result from shallow structural perturbations. Here, the

[1]The multipole method is semi-analytical because the basis functions are defined using infinite series.

FSS method is employed because its running time compares extremely favourably with that of other methods, including our super-cell code, making it possible to investigate a large area of the parameter space of the defect. It is shown that the waveguide can be optimised for operation in the slow-light regime by simply tuning either the size or refractive index of the defect.

Lastly, an immediate application of the basic multipole framework is described in Chapter 5. Specifically, a comprehensive study of the surface waves that are supported by finite and semi-infinite woodpiles is carried out. Much of the chapter is devoted to surface modes that propagate simultaneously along both the top and bottom layers of the woodpile, and it is shown that the behaviour of such coupled surface modes is highly anisotropic. We also investigate the basic properties of coupled surface-modes of compound woodpiles, which comprise two half-stacks that are separated by a homogeneous region.

Chapter 1

Background

This chapter serves to put the methods and results presented in later chapters in a practical context by way of a literature review, wherein the fabrication methods (Sec. 1.1), applications (Sec. 1.2) and theoretical studies (Sec. 1.3) are discussed in turn. In the course of the review, it will become apparent that the woodpile, which is a relatively new geometry, is highly relevant not only in the area of 3D bandgap confinement for optical wavelengths, but also as a transparent material that offers 3D control over the optical dispersion. The chapter concludes with a short comparison between the various methods for modelling photonic woodpiles (Sec. 1.4), including the methods that we have developed for modelling these structures. The principle advantages of the multipole method employed that is employed in this thesis, are that it is considerably faster than conventional methods (which are purely numerical) for modelling linear defects contained within woodpiles, and it often provides greater physical insight into the problem at hand.

1.1 Fabrication

The woodpile geometry was proposed in 1994 by a number of authors [28, 29] and, in 1994, the first woodpile (indeed, one of the first 3D PCs) to be reported was constructed from macroscopic alumina rods. Transmission measurements showed that the structure possessed a complete bandgap in the microwave region [30]. This structure was also the first in which light was successfully localised to intentional defects [15, 31]; however, this work did not address the main technical challenge, which was to develop fabrication methods that could be used to create woodpiles capable of operating at optical wavelengths ($< 100\mu m$) and, most significantly, near the telecommunications band at 1.5μm. To this end, Noda *et al.* employed 2D lithographic techniques to print individual lay-

ers, which were then bonded together [32]. The rods can be made from gallium arsenide (GaAs), or other III-V semiconductors, making these woodpiles relevant in the field of optoelectronics. Importantly, the wafer bonding process is epitaxial in that the woodpile is assembled layer by layer, allowing defects or active materials to be incorporated into the structure in an extremely precise manner. Not long after this milestone, the same group, in 1998, used the wafer bonding method to fabricate a four-layer GaAs (refractive index of $n \approx 3.38$) woodpile that had a rod spacing of just $d = 4\mu$m, resulting in a predicted and observed photonic bandgap (PBG) that spanned the wavelengths $5 < \lambda < 10\mu\mathrm{m}$ [21].

At the same time, Lin and Fleming [33] developed an epitaxial method for creating high-quality silicon woodpiles ($n = 3.6$) that have complete PBGs in the infrared (10-14.5μm). An SEM image of such a woodpile is shown in Fig. 1.1. One of the appealing features of these woodpiles is that, being made of silicon, they can be made using existing microelectronics fabrication facilities. The silicon woodpiles can also be used as a template for fabricating metallic woodpiles, e.g., those made from tungsten by Fleming *et al.* [34]. Although these tungsten woodpiles absorb light at shorter wavelengths ($< 6\mu$m), there is a large region of low absorption, and this region coincides with a PBG that spans the infrared wavelengths from $8 < \lambda < 20\mu$m. Within the PBG, the attenuation of electromagnetic fields inside the tungsten structure is greater than that typically observed in dielectric PCs. Hence, compared to dielectric PCs, metallic woodpiles require fewer layers and smaller rod volumes relative to the rod spacing (*i.e.*, metallic woodpiles can be smaller and lighter) — a four-layer tungsten woodpile can exhibit high omnidirectional reflectivity. The presence of a strong absorption peak at $\lambda \approx 6\mu$m led Fleming *et al.* to propose that such tungsten woodpiles could be used as selective emitters in thermophotovoltaic applications, where the PBG suppresses broadband thermal (infrared) radiation.

In 1999, Lin and Fleming used these same fabrication techniques to create the first 3D PC, a woodpile made from silicon [35], to have a complete bandgap in the near-infrared (near-IR). In particular, the PBG covered the telecommunications wavelengths of greatest importance ($\lambda \approx 1.55\mu$m). Shortly thereafter, the wafer bonding method was used to fabricate a GaAs woodpile that possessed an appreciable complete gap in the near IR [36]. When 8 GaAs layers were used, the bandgap covered the wavelengths from 1.3-1.55μm (99.99% or better reflection measured over this region); the rod spacing used to achieve this was $d = 0.7 \pm 0.03\mu$m. The first woodpile to contain a designed, submicron sized defect was also presented in [36]. The defect was a high quality 90° bend that had a predicted transmittance of 95% over a substantial frequency range. (This prediction was determined numerically using finite difference time domain simulations [37].) The fact

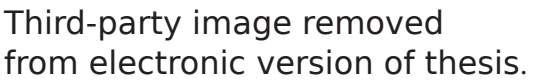

Figure 1.1: An SEM image of a silicon woodpile, which was fabricated in a layer-by-layer fashion using photolithography. Image taken from Lin *et al.* [33].

that the structure was made from GaAs, an important semiconductor in optoelectronics, was also seen as a desirable feature because it meant that the waveguide could conceivably be used as an interconnect betwen optical and electronic components.

The latter two methods for creating woodpiles involve mask lithography. An alternative microfabrication technique was reported in 2000 by Feigel *et al.* [38], and employs maskless holography in order to overcome the technological demands of the lithographic approaches. Two lasers are used to generate a sinusoidal interference pattern inside a chalcogenide glass photoresist. The underexposed regions are then removed chemically, leaving behind a grating whose period is determined by periodicity of the interference fringes (in this instance, $d \approx 1\mu$m, however, $d = 0.75\mu$m structures have also been made in this way [39]). This procedure exploits both the photosensitivity and the non-linear optical response of chalcogenide glasses; the latter property ensures that the grating has a binary profile, rather than a profile that varies smoothly. The significance of these structures is that chalcogenide has a high refractive index (n as large as ~ 3) compared to other glasses, and it is also highly non-linear, making these woodpiles relevant in the area of optical signal processing [40]. Furthermore, the layers are deposited one at a time, and so introducing a defect would be quite straightforward. A drawback of this approach is that the rod width is strongly dependent on the rod spacing. In addition, some surface roughness is inevitable because spurious reflections from the substrate interfere with the writing beams.

Holographic techniques can also be used to write many layers at once by using a phase mask to split a single beam into many writing beams (typically four or more beams). The

beams are then used to create a three-dimensionally periodic interference pattern inside the photoresist. These fringes determine the lattice type of the woodpile [41]. While holography is less suitable for producing artificial defects than the epitaxial appraches are, it is much faster and has modest technological requirements in comparison. Typically, polymers are used as the photoresist, and so the index of the resulting woodpile is usually too low ($n \approx 1.6$) for there to be a complete bandgap, although the low index woodpiles can, in principle, be used as a template for making high index structures. The polymer structures also show varying degrees of distortion. It has been suggested that using an alternative photoresist, such as a gelatin emulsion [42], will alleviate this problem. Holography can also be used to produce orthorhombic lattices, whereby each layer is rotated by an amount $\alpha \neq 90^\circ$ about the stacking axis relative to the layer below [43]. It was shown theoretically that when $\alpha = 55^\circ$ the size of the bandgap of the polymer woodpiles could be up to twice as large as the bandgap of the face-centred tetragonal ($\alpha = 90^\circ$) configuration.

More recently, 'direct laser-writing' (DLW) methods have been attracting attention because they can be used to fabricate fairly arbitrary 3D geometries [44]. A high-speed (femtosecond) laser is focused to a spot inside the photoresist, thereby initiating two-photon polymerisation in the vicinity of the focal point. The structure is then written by dragging the focal spot through the sample, and the unexposed volume is subsequently removed via a selective chemical etching process. This procedure can be used to inscribe woodpiles directly into both low- and high-index materials, e.g., chalcogenide glass [45, 46] using this approach. Furthermore, DLW can be used to write features, such as cavities and elaborate channels [23], that are as small as 100nm in diameter. However, the focal spot of the writing beam tends to be elongated in the direction parallel to the beam, and this can lead to longitudinal distortion in the features, especially when a high-index material is used. Wong *et al.* (2006) [47] showed that this aberration can be partially compensated for by overlapping two writing elements and, by doing this, the authors were able to fabricate chalcogenide glass woodpiles whose rods were largely free of distortion (see Fig. 1.2). Direct laser writing methods are not yet as accurate as lithographic techniques, and so the scattering losses inside woodpiles that are created using DLW are expected to be greater than in woodpiles created using, e.g., the wafer bonding method. Another drawback of the DLW method is that active materials can not be incorporated precisely into the sample.

Direct laser writing has also been employed to make 'inverse' woodpiles (low-index rods in a high-index background). In the simplest case, DLW is used to construct a

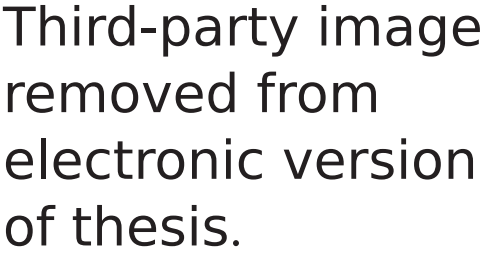

Figure 1.2: An SEM image of chalcogenide (As_2S_3) woodpile, which was fabricated using direct laser writing techniques. Image taken from Wong *et al.* [47].

polymer template, which is then infiltrated with the higher-index material, e.g., TiO_2 ($n \approx 2.7$), and the polymer is subsequently removed [48]. It is also possible to make inverse woodpiles made from germanium ($n = 4.1$) [49], and silicon ($n = 3.95$) [50]. The advantage of using an inverse structure is that it scatters light much more strongly than the complement structure does and, hence, will usually have a much wider bandgap. For example, the germanium inverse woodpile fabricated by Garcia-Santamaria *et al.* [49] had a complete bandgap that had a predicted width (*i.e.*, gap-to-midgap ratio) of 25% (verified experimentally for one direction), while a silicon inverse woodpile having elliptical rods can, in theory, have a bandgap that is as large as 28% [28].

1.2 Applications

Woodpiles have already been used successively in a number of applications, which fall roughly into two categories: applications that exploit the selective opacity of the PC, e.g., waveguiding and the control of the spontaneous emission of light, and applications that exploit the transmission properties, e.g., superprism effects and optical cloaking.

One of the earliest demonstrations of the woodpile's ability to suppress spontaneous emission was reported by de Dood *et al.* in 2003 [51]. Erbium ions were distributed throughout an Si woodpile, which was fabricated using the lithographic techniques devel-

oped by Lin et al. [33]. Despite being only five layers high, the woodpile suppressed the radiative rate of the Er^{3+} ions by 25% at wavelengths near 1.53μm, and there was strong evidence to suggest that the reduced emission was due to the presence of a PBG that covered this wavelength region. Similar experiments have been performed using quantum dots (QD), *i.e.*, semiconducting nanoparticles. For instance, direct laser writing was used to fabricate a woodpile out of a low-index QD composite consisting of a polymer resin doped with PbSe QDs [52]. The PbSe QDs had an emission band at 1.6μm that coincided with the partial PBG of the woodpile, resulting in a 50% suppression rate in the stacking direction.

The behaviour of light-emitting structures embedded inside a woodpile has also been examined (2004) [17]. Both five- and nine-layer GaAs woodpile structures were fabricated using the wafer-bonding approach [36], where the rods of the middle layer were multiple-quantum-wells (MQW; three-layer laminar structures made from semiconductors, in this case InGaAsP) having an emission peak near 1.55μm. Since GaAs has a high refractive index ($n \approx 3.38$), the field attenuation due to complete PBG was high, leading to a strong suppression of light emission from the MQW layer. In the case of the 9-layer woodpile, the suppression was as much as -20 dB from 1.45-1.6μm, and was in agreement with numerical modelling. When a cavity consisting of the InGaAsP MQW material was introduced into the MQW layer, the emission from the cavity was enhanced for wavelengths inside the PBG because of the presence of cavity modes, suggesting that the PBG inhibits other leakage mechanisms. As the size of the cavity was decreased, the spectral features sharpened until a critical cavity size was reached, at which point the cavity modes became indistinguishable from one another, and a single emission peak was observed. It was shown, both experimentally and using numerical modelling, that the Q factor, which is defined as the wavelength of the spectral line divided by the linewidth (full width at half maximum), and which is inversely proportional to the optical losses, is a constant function of the cavity size. By comparison, the Q factors of the cavity modes of 2D PCs decrease as the size of the cavity increases, since total internal reflection does not confine light as strongly as the complete PBG of the woodpile does. The results of finite difference time domain modelling (FDTD) suggested that a 17-layer structure would have a cavity Q factor of over 3,000. In fact, very recently a woodpile cavity having a Q factor of 38,500 was realised and, by coupling one of the cavity modes to a quantum dot layer, was used to create the first 3D PC laser [20].

A cavity has also been created on the top layer of a GaAs woodpile by inorporating a 2D PC, which contained a dielectric strip that served as the cavity, into the top layer. A Q

factor of 9,000 was attained by choosing the parameters of the top layer so that there was 'a bandgap for surface modes' [53]. In theory, the *Q* factor of such surface cavities can be made to exceed 100,000 simply by increasing the number of layers of the woodpile.

For wavelengths outside of the PBG, photonic crystals are useful as dispersive optical media that offer some control over the dispersion. Woodpiles are especially interesting in this regard as they are both three-dimensional and highly anisotropic. A striking example of the novel tranmission properties of PCs is the superprism effect [54], which is analogous to the wavelength dependent refraction that occurs in homogeneous dispersive prisms; however, the effect can be markedly stronger in PCs. Superprism phenomena have been observed in polymer woodpiles [55], where the angle of refraction was found to vary by 60° as the wavelength was increased from 860-960nm, with both positive and negative refraction occuring in this wavelength range. This change in deflection is two orders of magnitude higher than that of conventional prisms.

One of the most astonishing instances of a woodpile being used to manipulate optical dispersion was the creation of a 3D 'carpet cloak' for optical wavelengths [56]. The cloak causes irregularities on the surface of the object of interest to become indistinguishable from the rest of the object when they are viewed through the cloak. In the case of the woodpile cloak, a gold sheet containing a small bump was placed under a polymer woodpile. The rods of the woodpile were arranged into an face-centred cubic lattice so that the woodpile would behave as though it were isotropic for wavelengths $\lambda \gtrsim 1.6\mu$m, *i.e.*, for wavelengths longer than about twice the period $d = 0.8\mu$m of one of the layers. This measure ensured that the cloak operated for a wide cone of viewing directions. In the vicinity of the bump, the average ε of each unit cell was chosen so as to cause the reflected fields generated by the bump to be cancelled inside the woodpile. The presence of a marked 3D cloaking effect for the wavelengths $1.6 - 2.6\mu$m was confirmed by using a microscope to collect the reflected fields over a 60° field of view.

Waves that propagate on the surface of a woodpile are also important since, in principle, they can be engineered to improve the coupling efficiency between an external source and a defect embedded inside a woodpile, or to improve the directivity of antennas placed on a woodpile substrate [57], for example. So far, experimental progress towards manipulating woodpile surface waves has been limited to the excitation of surface waves and of the modes of cavity resonators situated on the surface of a woodpile [53].

The type of woodpile structure that has attracted the most interest (and which concerns this thesis) is the woodpile waveguide. The principal advantage of this structure is that, because the waveguide is surrounded by a woodpile cladding, it does not rely on total

internal reflection at all and, therefore, scattering losses are much less of a problem. In addition, such a waveguide offers three-dimensional control over the waveguide modes, and is relatively easy to fabricate. As we have already touched upon, much work has been done towards reducing the dimensions of the structure, with the aim of making a waveguide small enough to function at telecommunications wavelengths. In 2006, Imada *et al.* reported the first woodpile waveguide to be operated successfully at the telecommunications band near 1.55μm [18] (this was also a first for any 3D PC). The waveguide was formed by increasing the width of a single rod of the middle layer of a 9 layer GaAs woodpile. Adding dielectric in this way also increased the confinement strength in the stacking direction. The band structure[1] calculations showed that there were several waveguide modes, some of which were *slow-light* modes, *i.e.*, modes having a very low group velocity $v_g = \partial\omega/\partial k_x$ in the waveguiding (x) direction. The propagation lengths inside the waveguide were found experimentally to be as large as $\sim 30\mu$m for the 9 layer structure, and were in good agreement with FDTD simulations. Moreover, the presence of both low and high v_g modes could be inferred from the propagation lengths, which are proportional to both v_g and Q. Numerical modelling was used to confirm that the Q factors increased exponentially as the number of layers increases (an intrinsic property of all PCs); while a 9 layer waveguide has a Q of about 300, which corresponds to 10% transmittance after 50μm of propagation, a 25 layer waveguide has an expected Q of 3×10^5, which corresponds to lossless propagation over distances in excess of 500μm.

In 2009, the same group demonstrated vertical and L-shaped waveguides operating at $\sim 1.5\mu$m [19]. The vertical waveguide comprised an empty channel that extended downwards through a 4 layer GaAs woodpile. The channel was able to guide light efficiently, irrespective of the polarisation of the incident laser beam. The vertical wavegude was then bonded to a horizontal waveguide, which was created by removing half a rod from the top layer of a 5-layer stack, resulting in a 9 layer L-shaped waveguide. Numerical modelling showed that the horizontal arm of the bend had guided modes that, potentially, could couple to those of the vertical arm, and these predictions were borne out in practice; the compound structure was able to transmit light efficiently for one polarisation. A vertical waveguide, similar to the one just described, was fabricated recently (2011) by using direct laser writing [23]. The waveguide spanned 22 layers of a silicon woodpile, illustrating the suitability of DLW for producing many-period structures, and had computed and measured resonances near 1.75μm.

[1] The band structure is discussed in the next chapter.

1.3 Theoretical and Numerical Studies

Amongst the literature on woodpiles, there are a number of purely theoretical studies in which the behaviour of light inside existing or new woodpile designs is elucidated. In this section, we review these studies so that we may, in section Sec. 1.4, delineate our work from the pre-existing theoretical studies.

Much of the early work devoted to woodpiles was theoretical. The woodpile geometry was proposed independently by Ho *et al.* [28] and Sözüer and Dowling [29] in 1994 (although, according to the latter authors, priority probably belongs to John Pendry). These groups used Fourier expansion techniques to demonstrate theoretically that diamond lattice configurations (*i.e.*, a four layer stacking unit in which the first pair of gratings is offset laterally by half a period with respect to the second pair, as in Fig. 1) possessed complete bandgaps when the dielectric rods were rectangular or cylindrical. Both Ho and Sözüer judged correctly that fabricating and incorporating defects into these type of structures would be relatively simple.

Linear waveguides based on the woodpile geometry were first analysed in 1999 by Chutinan [58], who modelled the types of structures that would be fabricated later using the wafer bonding method [18, 36]. In the study, plane wave expansion (PWE) [59] and FDTD methods [37] were used to show that the removal of a single rod from the middle layer of the woodpile would result in a channel that supported several waveguide modes. Two different 90° bend waveguides were also examined, and it was found that removing half a rod in each of two successive layers would result in a bend that would outperform conventional sharp-bend waveguides; reflection calculations for a 12 layer stack suggested that such a bend would be capable of guiding light with 95% efficiency over a large frequency range. A limitation of the study was that, due to the enormous computional cost (at the time) of the numerical models, the error in the estimates of the mode frequencies was quite large (about 15% of the size of the bandgap).

The same methods were used to study the interactions between the linear waveguide just mentioned and a cavity that was created by attaching a small dielectric block to one of the rods in, or just above, the waveguide layer (2003) [60]. The waveguide layer, in turn, was sandwiched between two woodpiles. It was shown that the Q factor of the uncoupled cavity increased exponentially as the number of periods in either the lateral or stacking direction increased (Q as large as 10^6 for a 29 layer stack). When the waveguide was present, coupling between the two defects occurred for asymmetric configurations only, and the patterns of the uncoupled modes were used to explain the oscillatory dependence

of coupling strength on the in-plane distance between the defects. Also, the effect of the number of layers and waveguide position on the efficiency of light extraction was quantified.

Kawashima *et al.* (2005) proposed that adding dielectric (a 'donor-defect') to create a linear waveguide would allow for stronger light-matter interactions [61]. Several designs were examined and, of these, 'cross-rod' defects, whereby the defect rod interpenetrates the other rods of the waveguide layer, offered the greatest control over the dispersion and, especially, the field distribution. For a single crossed rod, the position of the rods immediately above and below the waveguide were arranged to produce a large single-mode bandwidth as well as a strongly localised single-lobed field pattern that Kawashima *et al.* speculated would improve the coupling efficiency to the waveguide. One such arranged cross-rod waveguide possessed slow-light modes, and so could, in principle, be used as an optical delay line. The addition of a second crossed-rod increased the bandwidth of the linear waveguide without increasing the modal volumes. By constructing the defects from non-linear or light-emitting materials, such a waveguide should afford some control over the dispersion, since donor-defects result in modes that tend to be strongly confined to the waveguide.

This group also proposed that a combination of donor-defects and acceptor-defects (removal of dielectric) might be used to create a linear waveguide for which light-matter interactions and, therefore, non-linearities are suppressed [62]. The waveguide comprised an acceptor defect (created by removing a single rod) and two crossed-rod defects that were situated immediately above and below the acceptor defect. The compound defect had an extremely large single-mode bandwidth, which could be made to span 90% of the PBG by adjusting the positions of the nearby rods, and outperformed 2D PC slabs in this regard. Moreover, the fields concentrated inside the acceptor defect, and had smaller volumes than the fields that would be produced by the acceptor defect without the donor defects. This meant that the group velocities of the waveguide modes were relatively large, and so light travelling along the acceptor defect would have little time to interact with the walls of the waveguide.

Another functional defect that is of practical significance is the planar defect [63], where the rods of the waveguide layer are modified uniformly. Detailed numerical studies of four classes of planar defects were performed by Chen *et al.* [64]. While donor defects resulted in resonances associated with defect states, acceptor defects caused band-edge states to shift into the PBG, resulting in band-edge resonances that were signified by the presence of standing waves. Typically, high symmetry configurations resulted in higher

Q factors of a resonances. The reflectances were, however, computed for a small stack (9 layers) so as to avoid the lengthy computations that would be necessary in order to locate very high Q resonances. Consequently, there were slight discrepancies between the frequencies of some of the resonances and the frequencies of the corresponding defect states.

Most defects, however, are undesirable artefacts of the fabrication process, and constitute structural disorder. (Although, disorder is sometimes introduced intentionally, namely in the study of Anderson localization of light [65].) For 3D PCs, the effect that incoherent disorder has on the optical properties is particularly difficult to model. Fortunately, the most significant fabrication flaws tend to be systematic, at least for epitaxial processes. The most common extrinsic defects that such processes result in are layer misalignment and rod dimensions varying across different layers. Of these, layer misalignment has the greatest effect on the size and position of the PBG [66], yet numerical models show that an alignment error as large as $20 - 30\%$ can be tolerable [66–68]. If the lateral disorder in the positions of individual rods is such that the gratings have superstructure, as can happen for the woodpiles produced using the methods of Lin and Fleming [33], then the size and position of the PBG of the disordered woodpile will be the same as that of the ideal woodpile. In this case, the frequency bands of the former woodpile can be obtained from the bands of the latter by applying a folding procedure that preserves the extrema of the bands [69].

Due to the successes in developing woodpile fabrication methods, there has been a surge of interest in woodpiles recently. The scope of the theoretical work on woodpiles is no longer limited to defect structures and optical frequencies. Some examples are, briefly: models for describing negative refraction in woodpile slabs [70], optimising the surface for use as a substrate for antennas [57] and as an optical sensor [71], and the design of woodpiles for operation at terahertz frequencies [72].

1.4 Methods for Modelling Woodpiles

The prevailing approaches for computing the frequency bands of the optical modes of infinite woodpiles[2] are the plane wave expansion (PWE) method [24, 59, 73] and, to a lesser extent, the FDTD and transfer matrix methods [74–76]. Numerical approaches for which the spatial domain is discretised, like the FDTD and PWE methods, are the most

[2]In this thesis, the terms ‘finite woodpile’ and ‘infinite woodpile’ refer to woodpiles that have a finite and an infinite number of layers, respectively.

important aids at the disposal of experimentalists because such methods impose minimal restrictions on the geometry. This flexibility comes at the expense of efficiency; a tradeoff that becomes apparent when modelling defects in woodpiles because these structures necessitate a 3D super-cell (the simulated defect is replicated periodically in three dimensions), which must be large in order to minimise the coupling between the fields of different super-cells. Whatever method is used, modelling woodpile defect structures invariably requires supercomputing resources; however, the computational demands of purely numerical methods can be prohibitive, and sometimes the only recourse is to sacrifice accuracy for speed.

Modelling finite woodpiles is usually performed using FDTD, and encompasses computing the reflection and transmission spectra, the scattered fields, and, sometimes, the time evolution of the fields in response to a source of excitation. For structures that rely on the PBG in order to confine light to a defect within a woodpile, many layers are usually required if the field attenuation inside the woodpile is to be strong. For example, it is expected that 25 layers are needed for lossless waveguiding through a 500μm long linear defect within a woodpile [18], yet such large computational domains can be impractical to model using FDTD. The method is relatively inefficient at computing steady state properties, such as reflectance, because the FDTD simulations must still be performed in the time domain. This makes even one dimensional (planar) defects computationally intractable unless the number of layers is reduced [64].

Semi-analytical approaches have been developed to make the problem of modelling woodpiles more tractable. These methods rely on the observation that, for certain rod shapes, the solutions can be constructed using basis functions that are tailored to the geometry, leading to solutions that converge rapidly. One such approach, by Gralak *et al.*, is applicable when the rods of the woodpile have rectangular profiles [77], and extends the *method of exact eigenfunctions*, which was originally developed for stacks of lamellar gratings [78, 79]. Within each layer, Maxwell's equations are reduced to two independent scalar equations, allowing the fields to be expressed in terms of the eigenvalues and eigenfunctions of simple self-adjoint operators. The fields for the entire stack, which may have a finite or infinite number of layers (as specified by the boundary conditions), are then determined by solving the resulting system of scalar equations.

Methods also exist for obtaining semi-analytical solutions when the rods are cylindrical. These include Dirichlet-to-Neumann (DtN) map and multipole methods. The former approach entails constructing field operators for the first layer of the woodpdile, and then updating the operators as they are 'marched' through the remaining layers of

the structure [80]. The operators are expressed in terms of DtN maps, which map the fields on the boundary of the unit-cell to their normal derivatives, and which depend only on the structure of the grating. (The DtN maps need only be constructed once for each unique layer.) For cylindrical scatterers, the DtN maps can be constructed using cylindrical waves and, therefore, do not require the unit-cell to be discretised. Dirichlet-to-Neumann maps are somewhat analogous to the notion of the scalar wave impedance Z of a homogeneous isotropic medium. This impedance relates the transverse component $E_\parallel$ of the electric field to the transverse component $H_\parallel$ of the magnetic field according to $E_\parallel = ZH_\parallel$. The connection between Z and DtN maps becomes evident by observing that, for harmonic waves propagating in a homogeneous isotropic medium, the 'normal' derivative of $E_\parallel$ (*i.e.*, the derivative in the direction of propagation) is simply a scalar multiple of $H_\parallel$. Thus, using the definition of impedance, one can derive a relationship of the form $dH_\parallel/\partial z = \Lambda H_\parallel$, where Λ can be regarded as a scalar DtN map for the homogeneous medium. The notion of impedance was generalised for PCs by Lawrence et al. [81], whereby a matrix $\mathbf{Z}$ relating the magnetic field vector to the electric field vector is constructed, and serves as a multi-channel impedance.

Multipole methods, which form the basis of our work, are another class of methods for which the fields are expanded in terms of cylindrical harmonics. One advantage is that the boundary conditions are satisfied exactly since the method does not require the cylinder boundaries to be discretised. Unlike the DtN map method, the multipole expansions account explicitly for the mutual scattering that occurs between the cylinders of a grating [25, 26, 82]. This feature can be exploited to create defect cylinders within the woodpile, either by adding substructure to the unit-cell of a grating (described in Chapter 3), or by manipulating individual cylinders directly (described in Chapter 4). The ability to model fabricated structures, however, is limited because of the constraints that the method imposes on the shape of the rods (although the method is more compatible with the geometry of inverse woodpiles, and can be used in conjunction with numerical methods to handle non-cylindrical scatterers, as has been done previously for conical mountings of finite 2D arrays [83]). Nevertheless, the multipole method is well-suited for studying some of the general properties of woodpiles. It is able to deal with linear waveguides embedded inside large stacks, and, so far, is the only method capable of locating woodpile waveguide modes without the need for a super-cell. Dispensing with the super-cell results in large performance gains, making it possible to explore contiguous regions of the parameter space (something that is lacking in literature). Also, material dispersion and absorption can be accounted for easily; dispersion can be modelled by using a re-

fractive index that is appropriate for the frequency, while absorption can be modelled by using a complex-valued refractive index, with the imaginary part of the refractive index used to control the lossiness of the material.

Another advantage that is unique to the multipole method is that, in instances where the symmetry of the lattice is more significant than the shape of the rods, certain fundamental properties can be deduced readily from the field identities. For example, in Chapter 5 the basic properties of the surface waves of woodpiles are derived from the multipole expressions, and these considerations have bearing on the coupling efficiency between external optics and waveguides or emitters embedded in the woodpile, and on the efficiency of optical structures placed on the surface [53, 57].

Lastly, we remark that a 'multipole type' method was developed by Adams et al. [84] to model the electromagnetic fields of a two-layer lamellar crossed-grating structure (such a structure constitutes two consecutive layers of a woodpile whose rods have a rectangular profile), whereby the fields immediately above and below each layer are expanded in terms of diffracted plane waves. A Green's function approach, similar to that used in the multipole method (discussed in Sec. 3.2.1 of Chapter 3 of this thesis), is then used to obtain the fields between the grooves of a given layer. In principle, the fields generated by a woodpile composed of lamellar gratings can be computed in this fashion, although this has approach has never been employed in the study of woodpiles

Chapter 2

Theoretical Formulation

This chapter describes the basic concepts that underlie the methods presented in the chapters to follow. We begin with a summary of the general properties of the optical modes of photonic crystals (Sec. 2.1). (Detailed explanations of these properties can be found in standard textbooks [3, 85].) The modes of woodpiles are most naturally formulated using diffraction grating theory, the basic principles of which are described in Secs. 2.2 and 2.3. There are several ways to solve the diffraction problem for a grating [25, 26, 86–88]. For this step we have opted to use the multipole method [25, 26, 88] to compute generalised reflection and transmission coefficients of the layer. This approach is outlined in Secs. 2.4 and 2.5. Lastly, the transfer matrix method for computing the modes of a woodpile is described in Sec. 2.6.

2.1 Modes of Photonic Crystals

For simplicity, the discussion in this section is limited to photonic crystals (PCs) comprised of simply-connected homogeneous regions of isotropic dielectric material. The material properties at any point $\mathbf{r} = (x, y, z)$ are specified by the refractive index $n(\mathbf{r}) = \sqrt{\mu(\mathbf{r})\,\varepsilon(\mathbf{r})}$, where, under the given assumptions, the magnetic permeability μ and electric permittivity ε are positive step functions. The electric (**E**) and magnetic (**H**) fields obey Maxwell's equations:

$$\nabla \times \mathbf{H} - \frac{\partial \mathbf{D}}{\partial t} = \mathbf{J}, \tag{2.1}$$

$$\nabla \times \mathbf{E} + \frac{\partial \mathbf{B}}{\partial t} = 0, \tag{2.2}$$

$$\nabla \cdot \mathbf{B} = 0, \tag{2.3}$$

$$\nabla \cdot \mathbf{D} = \rho, \tag{2.4}$$

where $\mathbf{D}$ and $\mathbf{B}$ are the electric and magnetic flux densities, respectively, and ρ and $\mathbf{J}$ are the free charge and current densities. That is, ρ and $\mathbf{J}$ are produced by external sources (charges), and so do not include bound currents and charges. In this thesis, we make the standard assumptions that there are no external charges ($\rho = 0$ and $\mathbf{J} = \mathbf{0}$) and the field intensities are small enough so that the constitutive relations are given by the linear relationships

$$\mathbf{D} = \varepsilon \mathbf{E} \tag{2.5}$$

and

$$\mathbf{B} = \mu \mathbf{H}. \tag{2.6}$$

The electromagnetic fields inside a PC can be expanded in terms of harmonic modes, whose functional forms are given by

$$\mathbf{E}(\mathbf{r}, t) = \mathbf{E}(\mathbf{r}) \exp(-i\omega t) \tag{2.7}$$

and

$$\mathbf{H}(\mathbf{r}, t) = \mathbf{H}(\mathbf{r}) \exp(-i\omega t). \tag{2.8}$$

Here, and throughout the rest of the thesis, we adopt the common practice of representing the electromagnetic fields as complex numbers, thereby simplifying many of the mathematical manipulations. Note that the complex fields are not the same as the physical fields, which can be obtained from the real part of the complex representations [Eqs. (2.7) and (2.8)].

The periodicity of the PC imposes the following spatial dependence on the modes:

$$\mathbf{H}(\mathbf{r}) = e^{i\mathbf{k}\cdot\mathbf{r}} \mathbf{u}_{\mathbf{H}}(\mathbf{r}, \mathbf{k}), \tag{2.9}$$

and

$$\mathbf{E}(\mathbf{r}) = e^{i\mathbf{k}\cdot\mathbf{r}} \mathbf{u}_{\mathbf{E}}(\mathbf{r}, \mathbf{k}), \tag{2.10}$$

where $\mathbf{u}_{\mathbf{E}}(\mathbf{r}, \mathbf{k})$ and $\mathbf{u}_{\mathbf{H}}(\mathbf{r}, \mathbf{k})$ are envelope functions that have the same periodicity as the crystal lattice, and the parameter $\mathbf{k} = (k_x, k_y, k_z)$ is referred to as the Bloch vector. Equations (2.9) and (2.10) are Bloch's theorem, which states that the PC modes are planewaves modulated by periodic envelope functions $\mathbf{u}_{\mathbf{E}}(\mathbf{r}, \mathbf{k})$ and $\mathbf{u}_{\mathbf{H}}(\mathbf{r}, \mathbf{k})$ [3, 85], and such modes are referred to as Bloch modes. A photonic bandgap (PBG) is then a frequency range for which there are no propagating Bloch modes. A bandgap is *complete* if it spans all of $\mathbf{k}$-

space, irrespective of the polarisation of the modes. Inside the bandgap the Bloch modes are evanescent, in that they decay exponentially inside the crystal. This implies that the Bloch vector of any evanescent mode has at least one complex component. Figure 2.1 shows the frequency bands (referred to as the *band structure*) of the Bloch modes of a woodpile, where **k** traverses the high-symmetry directions of the first Brillouin zone (first BZ: the central primitive cell of the reciprocal lattice). A sizeable complete bandgap that spans the high-symmetry directions of the BZ is clearly evident. Searching for a PBG amounts to locating the local extrema in the frequency bands of the Bloch modes. These extrema correspond to standing wave solutions inside the PC, and are usually the result of an underlying symmetry. Thus, even though only the high-symmetry directions of the BZ are considered in Fig. 2.1, the bandgap is complete.

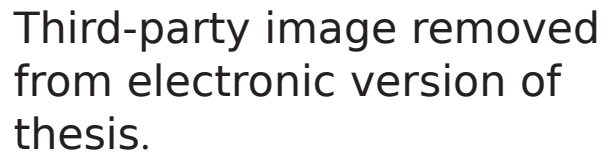

Figure 2.1: Band structure of a woodpile whose rods form a face-centred tetragonal lattice. The inset depicts the high-symmetry points of the first Brillouin zone. Figure taken from Chen *et al.* [64].

These observations lead to a conceptually simple method for using PCs to confine light. An evanescent mode decays at a rate proportional to $\exp(-\alpha x)$ for some $\alpha > 0$, where the x axis corresponds to one of the periodic directions of the PC. In an idealised

PC, *i.e.*, one that is free from defects and that extends infinitely in all directions, the evanescent modes are spatially unbounded, and so their magnitudes diverge as x becomes increasingly negative. While it is physically impossible to realise modes that behave this way, these modes are mathematically valid solutions of Maxwell's equations [Eqs. (2.1)-(2.4)] and are required in order to give a complete mathematical description of the fields. Indeed, for each wavelength, a PC will have an infinite number of evanescent Bloch modes but will only support a finite number of propagating modes. In any real PC the evanescent modes are terminated at the edges of the PC, namely at the surface layer or defect. Inside a bandgap, all fields that result when an edge is introduced must be evanescent in the bulk region. Such a mode can still propagate along the surface or defect, however. The mode is, in effect, confined to the edge, and is often referred to as a surface mode or defect mode, accordingly.

Typically, defects are created by either changing the size or shape of some of the scatterers. Examples of common defects are shown in Fig. 2.2. The boundary of a PC also constitutes a defect, as in Fig. 2.2(a), and it is possible to excite *surface* modes that propagate along such boundaries. An inherent limitation of 2D PC geometries is that the light that is not travelling in the plane of periodicity must be guided via total internal reflection. If this light is travelling at angles smaller than the critical angle for internal reflection, then the light will be lost from the waveguide. In contrast, 3D PCs, which are the concern of this thesis, can possess a bandgap for all possible directions and polarisations. Thus, 3D PCs can be used to guide or trap light without restrictions on the direction and polarisation. For this reason, 3D PC waveguides are thought to be able to guide light with greater efficiency than 2D PC geometries because, in practice, unavoidable structural imperfections, such as surface roughness, will cause some of the light to be scattered in directions that lie below the critical angle.

Evidently, the parameters of the PC must be chosen so that the bandgap, or a perhaps just a particular band, covers the range of frequencies and Bloch vectors of interest. To this end, the parameter of greatest practical significance is the scale of the PC, since scaling the dimensions of the crystal simply has the effect of scaling the band structure. Similarly, scaling ε uniformly has a similar effect (at least for non-dispersive materials), although this is of less utility because the refractive index is determined by the materials available. (In principle, scaling μ will also change the frequency of the bands; however, for most dielectrics of interest $\mu \approx 1$.) Increasing the contrast between the refractive indices of neighbouring dielectric regions tends to increase the frequency between successive bands, and is a relatively simple way of increasing the size of a bandgap. Alter-

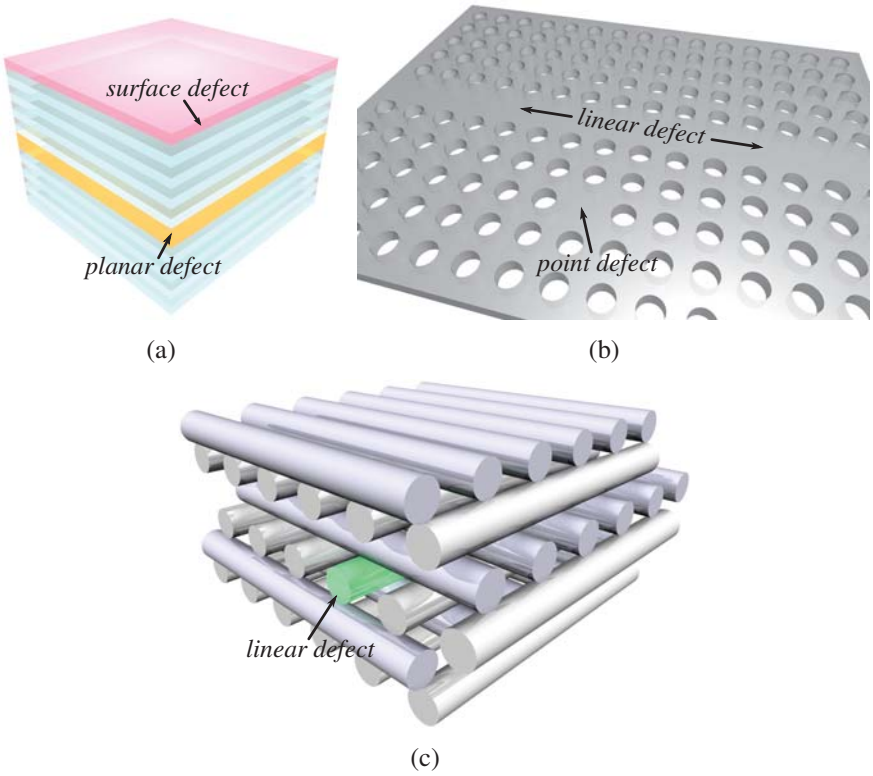

Figure 2.2: Typical defects for (a) 1D, (b) 2D and (c) 3D photonic crystals.

natively, a bandgap can be enlarged by optimising the lattice spacings and sizes of the scatterers, although the geometrical constraints on the mode (especially mode orthogonality) mean that manipulating the geometry will alter the band structure in a way that is less predictable than simply changing the material indices. Lattices that are 'approximately isotropic', in that their Brillouin zone is roughly circular or spherical in shape (this happens for face-centred cubic and diamond lattices, in particular) are more likely to possess complete bandgaps than less symmetrical PCs. The reasoning is that for such PCs, one direction through the structure is 'roughly equivalent' to any other direction, and so if there is a bandgap for some value of $\mathbf{k}$, then the bandgap is likely to remain open for all other values of $\mathbf{k}$. Clearly, there is considerable trial and error involved in choosing suitable parameters for a PC, hence the need for efficient ways of computing the band structure.

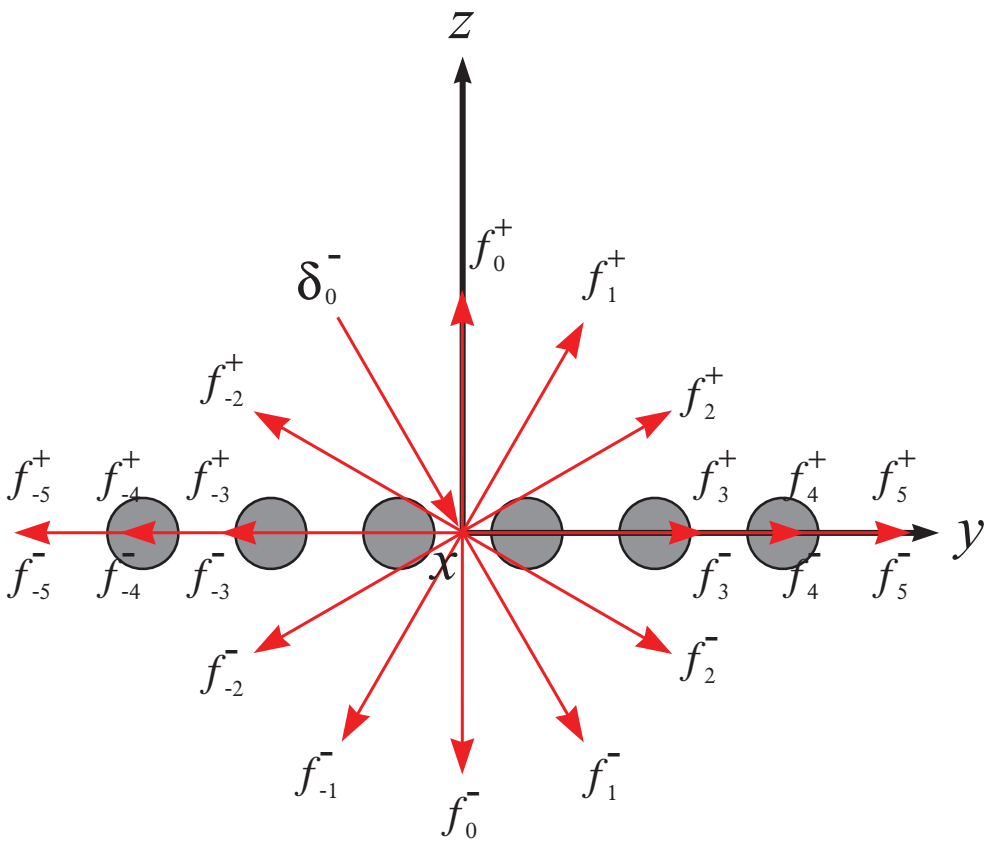

Figure 2.3: The reflected (f_q^+) and transmitted (f_q^-) plane wave diffraction orders that are generated when an incoming planewave δ_0^- impinges on a diffraction grating. Above (below) a certain cutoff order, the positive (negative) orders become evanescent in the z direction, and so are only able to propagate in the xy plane.

2.2 Diffraction Gratings

Each layer of the woodpile is periodic in one-dimensionally and, thus, acts as a diffraction grating. When illuminated by a monochromatic plane wave δ_0^-, a diffraction grating will generate a countably infinite number of reflected f_q^+ and transmitted plane waves f_q^- (or simply diffraction orders), each travelling in a different direction, as determined by the period of the grating, and the wavelength λ and direction of δ_0^- (see Fig. 2.3). The rods of the layer are infinitely long, and the coordinate system is chosen so that the rods are parallel to the x axis. The z axis is defined as the direction normal to the plane of the grating, and the y axis specifies the direction of the grating, as shown in Fig. 2.4. This convention is adopted throughout this thesis, except in a few instances where the roles of x and y must be interchanged to unify the treatment of successive woodpile layers. The incoming plane wave δ_0^- can be represented by the wave vector

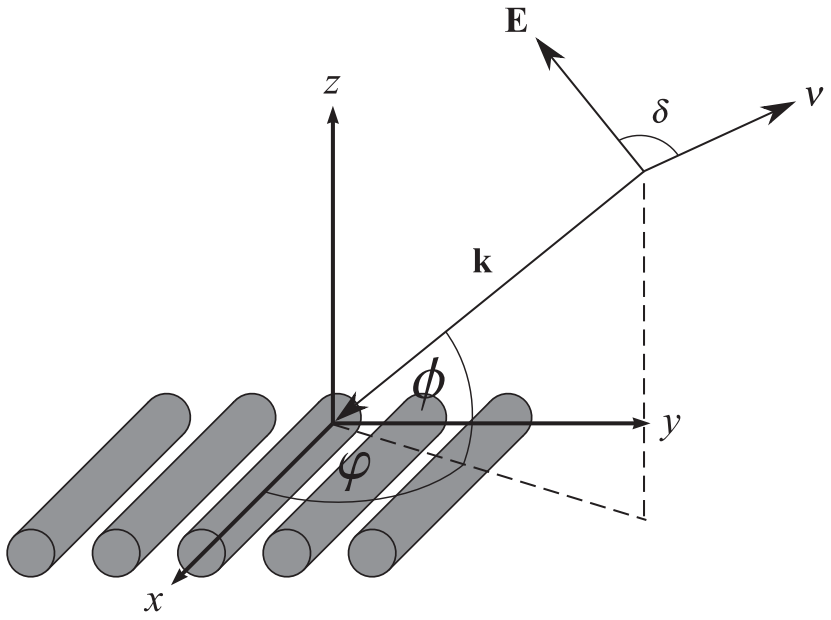

Figure 2.4: Configuration of the incident field with wave vector $\mathbf{k}$. The polarisation angle δ is defined as the angle between the vector $\boldsymbol{\nu} = \mathbf{k} \times \hat{\mathbf{z}}/(k \sin\theta)$ and the direction of the electric field $\mathbf{E}$, with $\delta = 0, \pi/2$ corresponding to *TE* and *TM* polarisation, respectively.

$\mathbf{k} = (\alpha_0, \beta_0, -\gamma_0)$, wavelength λ and polarisation angle δ (defined in Fig. 2.4), and we choose $\delta = 0$ and $\delta = \pi/2$ to be the principle polarisations, which will be referred to as *TE* and *TM* polarisation, respectively. An arbitrarily polarised incident field can always be expressed as a superposition of these two polarisations. It is often convenient to define the components of $\mathbf{k}$ in terms of the propagation angles ϕ and φ (see Fig. 2.4), so that $\alpha_0 = kn_b \sin\varphi\cos\phi$, $\beta_0 = kn_b \sin\varphi \sin\phi$ and $\gamma_0 = kn_b \cos\varphi$, where $n_b = \sqrt{\mu_b \varepsilon_b}$ is the refractive index of the background, and $k = 2\pi/\lambda$ is free-space wavenumber.

In this thesis, the longitudinal (x) components of the electric ($\mathbf{E}$) and magnetic ($\mathbf{H}$) fields[1] are determined using the multipole method. Having obtained E_x and H_x, the remaining field components can be recovered using Maxwell's equations [Eqs. (2.1)-(2.4)]. The longitudinal components of the incoming field are simply

$$\begin{bmatrix} \delta^-_{E,0} \\ \delta^-_{H,0} \end{bmatrix} e^{i\mathbf{k}\cdot\mathbf{r}}, \tag{2.11}$$

where $\mathbf{r} = (x, y, z)$, and $\delta^-_{E,0}$ and $\delta^-_{H,0}$ are amplitudes of the x components of the electric and magnetic fields, respectively.

[1]Throughout this thesis, $\mathbf{H}$ denotes the normalised magnetic field obtained by multiplying the magnetic field by the free-space impedance $Z_0 = \sqrt{\mu_0/\varepsilon_0}$.

For a grating having a period of d, the y dependency of the q^{th} diffraction is $\exp(i\beta_q y)$, where β_q specifies the direction of the order and is given by the *grating equation*:

$$\beta_q = \beta_0 + 2\pi q/d. \tag{2.12}$$

The x components of the q^{th} diffraction order are then

$$f_{E,q}^{\pm} e^{i\beta_q y} e^{\pm i\chi_q z} e^{i\alpha_0 x} \tag{2.13}$$

where

$$\chi_q = \sqrt{(kn_b)^2 - (\beta_q^2 + \alpha_0^2)} \tag{2.14}$$

and $f_{E,q}^{\pm}$ are the field amplitudes associated with the q^{th} order. Here and elsewhere, the superscript $+$ $(-)$ is used to denote an upward (downward) travelling wave (as in Fig. 2.3), and the z coordinate is relative to the plane of the grating. The $\exp(i\alpha_0 x)$ term arises from the fact that the fields propagating in the x direction do not diffract, since the layer is homogeneous with respect to the x coordinate, thus the x dependence of the incoming field δ^- [see Eq. (2.11)] is preserved in the diffracted fields. For $\beta_q^2 + \alpha_0^2 < (kn_b)^2$, χ_q is real, so in this case Eq. (2.13) describes a propagating planewave. However, for $\beta_q^2 + \alpha_0^2 > (kn_b)^2$, χ_q is imaginary, and in this case the wave is evanescent in that it decays exponentially in either the positive or negative z-direction. More specifically, for each diffraction order $q \geq 0$ there is a wavelength λ_q' known as the Rayleigh wavelength, below which all orders m such that $0 \leq m \leq q$ are propagating. Note that the value of λ_q' depends on the angle of incidence and on the period of the grating, and can be determined from the grating equation [Eq. (2.12)] and Eq. (2.14) by setting $\chi_q = 0$ and $k = 2\pi/\lambda_q$. When $\lambda = \lambda_q'$, the q^{th} order propagates in the direction parallel to the axis of the grating (the order becomes evanescent). Furthermore, at this wavelength, all orders $m \geq q$ are evanescent, as depicted in Fig. 2.3. Further increasing λ (so that $\lambda > \lambda_q'$) causes the orders $m \geq q$ to become increasingly evanescent. Similarly, there is a Rayleigh wavelength λ_q' for each order $q < 0$ such that for $\lambda \geq \lambda_q'$ all orders $m \leq q$ are evanescent.

It follows immediately from Eqs. (2.11) and (2.13) that the total fields (incoming and diffracted) are

$$\begin{bmatrix} E_x \\ H_x \end{bmatrix} = \begin{bmatrix} \delta_{E,0}^- \\ \delta_{H,0}^- \end{bmatrix} e^{i\mathbf{k}\cdot\mathbf{r}} + \sum_{q\in\mathbb{Z}} \begin{bmatrix} f_{E,q}^+ \\ f_{H,q}^+ \end{bmatrix} e^{i\beta_q y} e^{i\chi_q z} e^{i\alpha_0 x} \tag{2.15}$$

above the grating, and

$$\begin{bmatrix} E_x \\ H_x \end{bmatrix} = \sum_{q\in\mathbb{Z}} \begin{bmatrix} f^-_{E,q} \\ f^-_{H,q} \end{bmatrix} e^{i\beta_q y} e^{-i\chi_q z} e^{i\alpha_0 x} \tag{2.16}$$

below the grating. If the rods of the grating were instead oriented parallel to the y-axis, the grating equation would be

$$\alpha_p = \alpha_0 + 2\pi p/d, \tag{2.17}$$

where $p \in \mathbb{Z}$ indexes the diffraction orders associated with the x direction. In this case we would have derived for the longitudinal components (y) of the fields:

$$\begin{bmatrix} E_y \\ H_y \end{bmatrix} = \begin{bmatrix} \delta^-_{E,0} \\ \delta^-_{H,0} \end{bmatrix} e^{i\mathbf{k}\cdot\mathbf{r}} + \sum_{p\in\mathbb{Z}} \begin{bmatrix} f^+_{E,p} \\ f^+_{H,p} \end{bmatrix} e^{i\alpha_p x} e^{i\chi'_p z} e^{i\beta_0 y} \tag{2.18}$$

above the layer, and

$$\begin{bmatrix} E_y \\ H_y \end{bmatrix} = \sum_{p\in\mathbb{Z}} \begin{bmatrix} f^-_{E,p} \\ f^-_{H,p} \end{bmatrix} e^{i\alpha_p x} e^{-i\chi'_p z} e^{i\beta_0 y} \tag{2.19}$$

below the layer, with $\chi'_p = \sqrt{(kn_b)^2 - (\beta_0^2 + \alpha_p^2)}$. That is, the roles of α_0 and β_0 are merely swapped.

2.3 Diffraction by a Woodpile

The diffraction orders of the woodpile are determined by the diffraction orders of the constituent gratings. As before, one only needs to consider the longitudinal components of the fields. (Later, we will explain how to express the fields in terms of *TE* and *TM* components, since the effects of polarisation are of practical significance.) To begin with, we consider a grating that is illuminated from above by the field δ^- given in Eq. (2.11), so that the diffracted fields generated by the grating are simply given by Eqs. (2.15) and (2.16). When an identical layer is then placed below the first layer, each of the downwards diffraction orders produced by first layer [*i.e.*, the individual terms in Eq. (2.16)] will be diffracted upon reaching the second layer, thereby producing secondary diffracted fields that are analogous to Eqs. (2.15) and (2.16), with the term involving δ^- instead representing the incoming order. Since the two layers are identical, the grating equation, Eq. (2.12), is the same for both layers. Consequently, the diffracted orders

above and below the two layer stack are the same as those that are produced by a single layer, except that the amplitudes of the orders of the two structures will differ. The same reasoning shows that the directions of the diffracted fields produced by a single layer are the same as those produced by a 2D stack consisting of an arbitrary number of such layers.

If instead the rods of the top layer were oriented parallel to the y axis, then the bottom layer would cause the p^{th} downwards diffraction order of the top layer to diffract into the following upwards and downwards orders:

$$f_{E,s}^{\pm} e^{i\beta_q y} e^{\pm i\gamma_s z} e^{i\alpha_p x}, \tag{2.20}$$

[cf. Eq. (2.20)], where

$$\gamma_s = \sqrt{(kn_b)^2 - (\alpha_p^2 + \beta_q^2)}, \tag{2.21}$$

and, for notational convenience, each pair $(p, q) \in \mathbb{Z} \times \mathbb{Z}$ is mapped to a unique integer s, so that the subscript s denotes quantities associated with the $(p, q)^{\text{th}}$ diffraction order. Note that the s^{th} woodpile order is propagating if γ_s^2 is positive, and is evanescent if γ_s^2 is negative. Evidently, the diffracted orders given by Eq. (2.20) propagate in different directions from the orders of a 2D grating stack. Although the upwards orders $f_{E,s}^{+}$ of the bottom layer diffract upon reaching the top layer, they diffract in the same directions as the fields generated by the bottom layer [Eq. (2.20)]. More generally, the diffracted fields produced by stack consisting of an arbitrary number both x and y aligned gratings will propagate in the same directions as the orders in Eq. (2.20), irresepective of the ordering of the layers, so long as any two layers of the same orientation have the same period. Thus, s represents a single diffraction order of the woodpile. The fields above and below an arbitrary layer of the 3D stack are

$$\begin{bmatrix} E_x \\ H_x \end{bmatrix} = \sum_{s\in\mathbb{Z}} \left\{ \begin{bmatrix} \delta_{E,s}^{-} \\ \delta_{H,s}^{-} \end{bmatrix} e^{-i\gamma_s z} + \begin{bmatrix} f_{E,s}^{+} \\ f_{H,s}^{+} \end{bmatrix} e^{i\gamma_s z} \right\} e^{i\alpha_p x} e^{i\beta_q y} \tag{2.22}$$

and

$$\begin{bmatrix} E_x \\ H_x \end{bmatrix} = \sum_{s\in\mathbb{Z}} \left\{ \begin{bmatrix} \delta_{E,s}^{+} \\ \delta_{H,s}^{+} \end{bmatrix} e^{i\gamma_s z} + \begin{bmatrix} f_{E,s}^{-} \\ f_{H,s}^{-} \end{bmatrix} e^{-i\gamma_s z} \right\} e^{i\alpha_p x} e^{i\beta_q y}, \tag{2.23}$$

respectively. Note that for the top layer, $\delta_{E,s}^{-} = 0$ and $\delta_{H,s}^{-} = 0$ for all orders s other than the specular order ($p = q = 0$), while for the bottom layer $\delta_{E,s}^{+} = \delta_{H,s}^{+} = 0$ for all orders.

If the longitudinal component of the incoming field is zero ('classical incidence') and the incoming fields are either *TE* or *TM* polarised, then the diffracted fields produced by

2D stacks possess the same polarisation as the incoming fields. For arbitrary incidence ('conical incidence'), the polarisation states of the input and output fields will usually differ. Nevertheless, it is often useful to express the fields in terms of *TE* and *TM* polarised resolutes. The *TE* and *TM* directions determined by the s^{th} diffracted order are

$$\mathbf{R}_s^E = \left(-\beta_q \hat{\mathbf{x}} + \alpha_p \hat{\mathbf{y}}\right) / \left(\alpha_p^2 + \beta_q^2\right)^{1/2} \tag{2.24}$$

and

$$\mathbf{R}_s^M = \left(\alpha_p \hat{\mathbf{x}} + \beta_q \hat{\mathbf{y}}\right) / \left(\alpha_p^2 + \beta_q^2\right)^{1/2} \tag{2.25}$$

respectively. Let $\mathbf{E_t}$ and $\mathbf{H_t}$ denote the transverse components (*i.e.*, the components parallel to the xy plane) of the electric and magnetic fields, respectively. Above the grating, one may write for the transverse components:

$$\begin{aligned}\mathbf{E_t} = (\mu_b/\varepsilon_b)^{1/4} \sum_s \xi_s^{-1/2} \left[E_{I,s}^- e^{-i\gamma_s z} + E_{D,s}^+ e^{i\gamma_s z}\right] e^{i(\alpha_p x + \beta_q y)} \mathbf{R}_s^E \\ + \xi_s^{1/2} \left[F_{I,s}^- e^{-i\gamma_s z} + F_{D,s}^+ e^{i\gamma_s z}\right] e^{i(\alpha_p x + \beta_q y)} \mathbf{R}_s^M,\end{aligned} \tag{2.26}$$

and

$$\begin{aligned}\hat{\mathbf{z}} \times \mathbf{H_t} = (\varepsilon_b/\mu_b)^{1/4} \sum_s \xi_s^{1/2} \left[E_{I,s}^- e^{-i\gamma_s z} - E_{D,s}^+ e^{i\gamma_s z}\right] e^{i(\alpha_p x + \beta_q y)} \mathbf{R}_s^E \\ + \xi_s^{-1/2} \left[F_{I,s}^- e^{-i\gamma_s z} - F_{D,s}^+ e^{i\gamma_s z}\right] e^{i(\alpha_p x + \beta_q y)} \mathbf{R}_s^M,\end{aligned} \tag{2.27}$$

where the subscript I is used to denote the incoming fields, the subscript D denotes the diffracted fields, and $\xi_s = \gamma_s / (k n_b)$. (As before, s indexes the woodpile diffraction orders, and the superscripts $+$ and $-$ are used to discriminate between upward and downwards fields.) The factors ξ_s and μ_b/ε_b have been included to normalise the energy of the reflected and transmitted fields relative to the input field [*i.e.*, $\delta_{E,0}^-$ and $\delta_{H,0}^-$ in Eq. (2.15)] so that the reflectance and transmittance can be computed. Expressions analogous to Eq. (2.26) and (2.27) also hold for the fields below the grating.

A change of coordinate systems must be applied to any field that is expressed in the form given in Eqs. (2.26) and (2.27) before the multipole method can be used to determine the field amplitudes of the longitudinal components [*i.e.*, $f_{E,s}^{\pm}$ and $f_{H,s}^{\pm}$ in Eqs. (2.22) and (2.23)]. For gratings whose rods are parallel to the x axis, the longitudinal components can be obtained using $E_x = \mathbf{E_t} \cdot \hat{\mathbf{x}}$ and $H_x = -\hat{\mathbf{z}} \times (\hat{\mathbf{z}} \times \mathbf{H_t}) \cdot \hat{\mathbf{x}}$. For example, one finds that the longitudinal components of the diffracted fields are related to the *TE* and

TM components of the diffracted fields according to (in matrix notation)

$$\boldsymbol{\mathcal{F}}^{+} = \mathbf{Z}\mathbf{X}^{+}\boldsymbol{\mathcal{F}}_{D}^{+} \quad \text{and} \quad \boldsymbol{\mathcal{F}}^{-} = \mathbf{Z}\mathbf{X}^{-}\boldsymbol{\mathcal{F}}_{D}^{-}, \tag{2.28}$$

with

$$\boldsymbol{\mathcal{F}}^{\pm} = \begin{bmatrix} [f_{E,s}^{\pm}] \\ [f_{H,s}^{\pm}] \end{bmatrix}, \boldsymbol{\mathcal{F}}_{D}^{\pm} = \begin{bmatrix} [E_{D,s}^{\pm}] \\ [F_{D,s}^{\pm}] \end{bmatrix}, \tag{2.29}$$

$$\mathbf{X}^{+} = \begin{bmatrix} -\boldsymbol{\xi}_{\beta} & \boldsymbol{\xi}_{\alpha} \\ -\boldsymbol{\xi}_{\alpha} & -\boldsymbol{\xi}_{\beta} \end{bmatrix}, \mathbf{X}^{-} = \begin{bmatrix} -\boldsymbol{\xi}_{\beta} & \boldsymbol{\xi}_{\alpha} \\ \boldsymbol{\xi}_{\alpha} & \boldsymbol{\xi}_{\beta} \end{bmatrix}, \tag{2.30}$$

$$\mathbf{Z} = \begin{bmatrix} \mathrm{diag}\left[(\mu_b/\varepsilon_b)^{1/4}\right] & \mathbf{0} \\ \mathbf{0} & \mathrm{diag}\left[(\varepsilon_b/\mu_b)^{1/4}\right] \end{bmatrix}, \tag{2.31}$$

$$\boldsymbol{\xi}_{\beta} = \mathrm{diag}[\xi_s^{-1/2}\beta_q/(\alpha_p^2+\beta_q^2)^{1/2}] \tag{2.32}$$

and[2]

$$\boldsymbol{\xi}_{\alpha} = \mathrm{diag}[\xi_s^{1/2}\alpha_p/(\alpha_p^2+\beta_q^2)^{1/2}]. \tag{2.33}$$

Analogous expressions relationships exist between the longitudinal and the *TE* and *TM* components of the incoming fields. Equations (2.28)-(2.32) are also applicable for gratings whose rods are parallel to the y axis; however, in this case a rotated coordinate system (x', y', z') must be used. This is achieved by making the following substitutions:

$$x \to x', \quad y \to y', \quad \text{and} \quad z \to z', \tag{2.34}$$

$$\alpha_p \to \alpha_p', \quad \beta_q \to \beta_q', \quad \text{and} \quad \gamma_s \to \gamma_s', \tag{2.35}$$

with the correspondences $x' = y$, $y' = -x$, and $z' = z'$. The propagation constants α_p', β_q', and γ_s' for the rotated system are defined analogously to α_p, β_q and γ_s. It follows immediately from Eqs. (2.12), (2.17) and (2.21) that

$$\alpha_p' = \beta_p, \quad \beta_q' = -\alpha_{-q} \quad \text{and} \quad \gamma_{(p,q)}' = \gamma_{(-q,p)}. \tag{2.36}$$

2.4 Basics of the Multipole Method

In this thesis, the amplitudes $f_{E,s}^{\pm}$ and $f_{H,s}^{\pm}$ of the diffracted orders above and below a single layer [see Eqs. (2.22) and (2.23)] are determined using the multipole method. The

[2]Here and elsewhere, the notation $\mathrm{diag}[]$ denotes a diagonal matrix.

basic approach is as follows (more detail is given in the next chapter). We suppose that the rods are parallel to the x axis, and that, for the purposes of this Chapter, there is only one cylinder per unit-cell. If the rods are parallel to the y axis, then one instead uses the rotated coordinate system defined in Eqs. (2.34)-(2.36). Each incoming order can be represented using the wave vector $\mathbf{k} = (\alpha_p, \beta_q, \gamma_s)$. Since the layer is homogeneous in the x direction, the fields will have an x dependency of $\exp(i\alpha_p x)$, and so one may project the problem onto the yz plane, see Fig. 2.5. The longitudinal components of both the incoming order and the resulting scattered fields satisfy the Helmholtz equation:

$$[\nabla_\perp^2 + k_\perp^2]V(\boldsymbol{\rho}) = 0, \tag{2.37}$$

for $V = E_x$ and $V = H_x$, where $\nabla_\perp$ acts on the in-plane coordinates y and z [or $\boldsymbol{\rho} = (\rho, \theta)$ in cylindrical coordinates, see Fig. 2.5], and $\mathbf{k}_\perp = (\beta_q, \gamma_s)$ is the projection of the wave vector. Observe that $k_\perp^2 = (kn_b)^2 - \alpha_p^2$ and, thus, Eq. (2.37) does not depend on the β_q of the incoming order. This means that for each α_p, one can simultaneously determine the fields excited by all incoming orders $\{\cdots, \beta_{-1}, \beta_0, \beta_1, \cdots\}$.

For cylindrical geometries, Eq. (2.37) reduces to Bessel's equation and, consequently, the fields at any point $\boldsymbol{\rho}$ exterior to the cylinder can be expanded in terms of cylindrical harmonics [89]. That is,

$$V(\boldsymbol{\rho}) = \sum_{n=-\infty}^{\infty} \left[A_n^V J_n(k_\perp \rho) + B_n^V H_n(k_\perp \rho)\right] e^{in\theta}, \tag{2.38}$$

where there is an assumed x dependence of $\exp(i\alpha_p x)$. Here, J_n are Bessel functions, which represent incoming waves, and H_n are Hankel functions of the first kind, which represent outgoing waves emanating from the boundary of the cylinder. Equation (2.38) is valid for points inside any annular region A (white region in Fig. 2.5) extending from the cylinder boundary, so long as the region does not contain any other cylinders. Similarly, the multipole expansion for points $\boldsymbol{\rho}$ inside the cylinder is

$$V(\boldsymbol{\rho}) = \sum_{n=-\infty}^{\infty} C_n^V J_n(k_\perp \rho)\, e^{in\theta}. \tag{2.39}$$

If the cylinders of the layer are identical, then the multipole coefficients have the same quasiperiodicity as the diffracted planewave fields. That is, the multipole coefficients for the j^{th} unit-cell along the layer are $A_n^V \exp(i\beta_0 jd)$, $B_n^V \exp(i\beta_0 jd)$, and $C_n^V \exp(i\beta_0 jd)$.

To determine the multipole coefficients, one uses Green's function methods to obtain

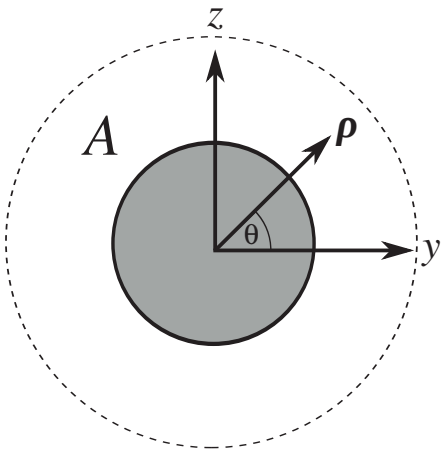

Figure 2.5: Local coordinate system for the multipole expansion given by Eq. (2.38).

the *Wijngaard expansion*, which is a second expression for local fields in Eq. (2.38) whereby the incoming fields A_n^V of the $j = 0$ unit-cell of the layer are expanded in terms of the outgoing fields $B_m^V \exp(i\beta_0 jd)$ of all other cylinders $j \neq 0$. In the next chapter, it is shown how the Wijngaard expansion can be derived for a grating unit-cell that contains multiple cylinders. By equating Eq. (2.38) with the Wijngaard expansion, one can eliminate V to give an equation that relates A_n^V to each B_m^V. This equation can then be solved for the outgoing fields B_n^V by applying the boundary conditions, which state that the tangential components (*i.e.*, E_θ, H_θ, E_x and H_x) are continuous across the cylinder boundaries. [This is a general condition imposed by Maxwell's equations, see Eqs. (2.1)-(2.4), and can be derived by applying the Gauss divergence theorem to a suitable volume that crosses the boundary [90].] Having obtained B_n^V, the amplitudes $f_{E,s}^{\pm}$ and $f_{H,s}^{\pm}$ of the diffracted orders in Eqs. (2.15) and (2.16) can be determined in a manner similar to the derivation of the Wijngaard expansion.

2.5 Reflection and Transmission Matrices

The multipole method allows one to establish the following linear relationships between the diffracted fields and the incoming fields impinging on a layer:

$$\begin{bmatrix} \boldsymbol{\mathcal{F}}_D^- \\ \boldsymbol{\mathcal{F}}_D^+ \end{bmatrix} = \begin{bmatrix} \boldsymbol{\mathcal{T}}_a & \boldsymbol{\mathcal{R}}_b \\ \boldsymbol{\mathcal{R}}_a & \boldsymbol{\mathcal{T}}_b \end{bmatrix} \begin{bmatrix} \boldsymbol{\mathcal{F}}_I^- \\ \boldsymbol{\mathcal{F}}_I^+ \end{bmatrix}, \tag{2.40}$$

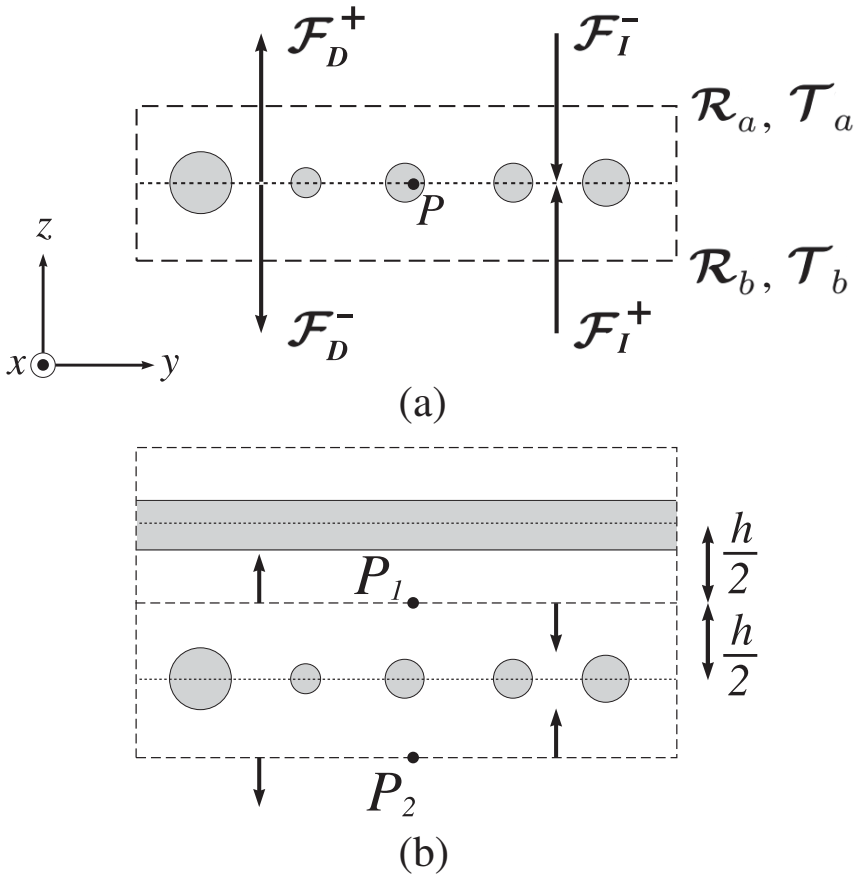

Figure 2.6: (a) The incoming and diffracted fields, with phase origin at P, and the reflection and transmission matrices associated with the fields above and below the unit cell. (b) The unit cell with phase origins P_1 and P_2 adjusted to give the grating a total thickness of h.

where the diffracted fields $\boldsymbol{\mathcal{F}}_D^{\pm}$ and the incoming fields $\boldsymbol{\mathcal{F}}_I^{\pm}$ are expressed in terms of *TE* and *TM* components. That is, $\boldsymbol{\mathcal{F}}_D^{\pm}$ are given by Eq. (2.29), and $\boldsymbol{\mathcal{F}}_I^{\pm}$ are given by

$$\boldsymbol{\mathcal{F}}_I^{\pm} = \begin{bmatrix} [E_{I,s}^{\pm}] \\ [F_{I,s}^{\pm}] \end{bmatrix}. \tag{2.41}$$

The matrices $\boldsymbol{\mathcal{R}}$ and $\boldsymbol{\mathcal{T}}$, which are determined using the multipole method, act as reflection and transmission matrices, respectively, with the subscript *a* (*b*) used to denote matrices that act on the fields that are incident from above (below) the layer, see Fig. 2.6(a).

Recurrence relationships for the scattering matrices for a stack of $(s+1)$ non-interpenetrating gratings are then found readily from Eq. (2.40) by expressing the fields incident to the s and $(s+1)^{\text{th}}$ layer in terms of $\boldsymbol{\mathcal{R}}$ and $\boldsymbol{\mathcal{T}}$ of the $(s+1)^{\text{th}}$ layer and $\boldsymbol{\mathcal{R}}^s$

and $\boldsymbol{\mathcal{T}}^s$ of the s layer stack beneath it (also see Sec. IIIB of [26]):

$$\boldsymbol{\mathcal{R}}_a^{s+1} = \widetilde{\boldsymbol{\mathcal{R}}}_a + \widetilde{\boldsymbol{\mathcal{T}}}_b \boldsymbol{\mathcal{R}}_a^s \left(\boldsymbol{\mathcal{I}} - \widetilde{\boldsymbol{\mathcal{R}}}_b \boldsymbol{\mathcal{R}}_a^s\right)^{-1} \widetilde{\boldsymbol{\mathcal{T}}}_a, \tag{2.42}$$

$$\boldsymbol{\mathcal{T}}_a^{s+1} = \boldsymbol{\mathcal{T}}_a^s \left(\boldsymbol{\mathcal{I}} - \widetilde{\boldsymbol{\mathcal{R}}}_b \boldsymbol{\mathcal{R}}_a^s\right)^{-1} \widetilde{\boldsymbol{\mathcal{T}}}_a, \tag{2.43}$$

$$\boldsymbol{\mathcal{R}}_b^{s+1} = \boldsymbol{\mathcal{R}}_b^s + \boldsymbol{\mathcal{T}}_a^s \widetilde{\boldsymbol{\mathcal{R}}}_b \left(\boldsymbol{\mathcal{I}} - \boldsymbol{\mathcal{R}}_a^s \widetilde{\boldsymbol{\mathcal{R}}}_b\right)^{-1} \boldsymbol{\mathcal{T}}_b^s, \tag{2.44}$$

$$\boldsymbol{\mathcal{T}}_b^{s+1} = \widetilde{\boldsymbol{\mathcal{T}}}_b \left(\boldsymbol{\mathcal{I}} - \boldsymbol{\mathcal{R}}_a^s \widetilde{\boldsymbol{\mathcal{R}}}_b\right)^{-1} \boldsymbol{\mathcal{T}}_b^s. \tag{2.45}$$

Here, the change in phase that occurs for fields propagating between successive layers has been incorporated into $\widetilde{\boldsymbol{\mathcal{R}}}_{a/b}$ and $\widetilde{\boldsymbol{\mathcal{T}}}_{a/b}$ by applying a padding $\boldsymbol{\mathcal{P}}$ symmetrically above and below the layer. This gives the grating a thickness h that accounts for the distance between adjacent layers [see Fig. 2.6(b)]. (All distances are expressed in units of d.) For woodpiles, it is necessary to offset the layers, as shown in Fig. 2.8(a), in order for the bandgap to be complete [29]. Hence, a lateral shift transform $\boldsymbol{\mathcal{Q}}$ that effects either a shift of δ_x in the x direction or a shift δ_y in the y direction (usually $\delta_x = \delta_y = d/2$) is applied to the gratings of every second pair:

$$\begin{bmatrix} \widetilde{\boldsymbol{\mathcal{R}}}_a & \widetilde{\boldsymbol{\mathcal{T}}}_b \\ \widetilde{\boldsymbol{\mathcal{T}}}_a & \widetilde{\boldsymbol{\mathcal{R}}}_b \end{bmatrix} = \begin{bmatrix} \boldsymbol{\mathcal{Q}}\boldsymbol{\mathcal{P}} & \mathbf{0} \\ \mathbf{0} & \boldsymbol{\mathcal{Q}}\boldsymbol{\mathcal{P}} \end{bmatrix} \begin{bmatrix} \boldsymbol{\mathcal{R}}_a & \boldsymbol{\mathcal{T}}_b \\ \boldsymbol{\mathcal{T}}_a & \boldsymbol{\mathcal{R}}_b \end{bmatrix} \begin{bmatrix} \boldsymbol{\mathcal{P}}\boldsymbol{\mathcal{Q}}^{-1} & \mathbf{0} \\ \mathbf{0} & \boldsymbol{\mathcal{P}}\boldsymbol{\mathcal{Q}}^{-1} \end{bmatrix}, \tag{2.46}$$

where $\boldsymbol{\mathcal{P}} = \mathrm{diag}\begin{bmatrix} \mathbf{P} & \mathbf{P} \end{bmatrix}$, $\mathbf{P} = \mathrm{diag}\left[e^{i\gamma_s h/2}\right]$, $\boldsymbol{\mathcal{Q}} = \mathrm{diag}\begin{bmatrix} \mathbf{Q} & \mathbf{Q} \end{bmatrix}$ and

$$\mathbf{Q} = \begin{cases} \mathrm{diag}\left[e^{i\alpha_p \delta_x}\right], \text{ for an } x \text{ shift}, \\ \mathrm{diag}\left[e^{i\beta_q \delta_y}\right], \text{ for a } y \text{ shift}, \\ \mathbf{I}, \text{ for no shift}, \end{cases} \tag{2.47}$$

in which $\mathbf{I}$ denotes the identity matrix.

The requirement that the layers of the woodpile be non-interpenetrating follows from the fact that if the rods of a layer were to overlap with the rods of an adjacent layer, as in Fig. 2.7(a), then the annular region A in Fig. 2.5 would always intersect one of the cylinders. Hence, the exterior multipole expansion [Eq. (2.38)] would not be valid anywhere. The situation for 2D PCs is more complicated. To see this, consider the perforated 2D PC (air-holes in a dielectric background) shown in Fig. 2.7(b), where the bottom boundary I_2 of the top row of holes lies below the top boundary I_1 of the bottom row of holes. In this case, the layers interpenetrate without the holes overlapping, and so a multipole

field expansion is valid in the vicinity of each hole. The question arises as to whether, at the boundaries I_1 and I_2, the interpentration invalidates a field expansion in terms of planewave diffraction orders [namely Eqs. (2.22) and (2.23)]. Botten *et al.* [91] showed numerically, using the methods in described in the previous sections, that while the non-interpenetration condition is sufficient, it is not necessary. This question is closely related to Lord Rayleigh's conjecture (known as the Rayleigh hypothesis) that a field expansion in terms of planewave orders is possible inside the grating [92, 93] – a matter that has been subject to much debate since it was first suggested in 1897, and that is still controversial. It has been shown that the Rayleigh hypothesis is correct for gratings having shallow groove depths [94]. It is also known that a field expansion in terms of diffraction orders is valid within its domain of convergence, which is determined by the refractive index and radius of the cylinders [95]. While a number of studies have demonstrated that in general the Rayleigh hypothesis is incorrect (see, e.g., ref. [96]), it has been suggested quite recently by Tishchenko [97] that the reason the Rayleigh hypothesis produced the wrong results in these studies was that the evaluation of the field expansion was prone numerical instability. Indeed, Tishchenko found strong numerical evidence in favour of the Rayleigh hypothesis for arbitrarily deep grooves.

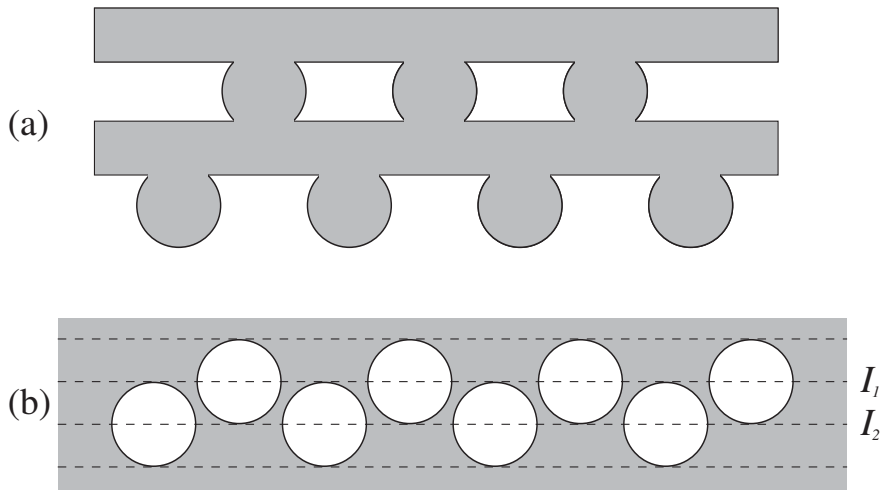

Figure 2.7: (a) A four-layer woodpile whose layers are interpenetrating. (b) A perforated 2D PC comprising two rows of air-holes in a dielectric background. The layers of the 2D PC interpenetrate in that the bottom boundary I_2 of the top row of holes is below the top boundary I_1 of the second row. The holes do not overlap, however.

The matrices $\boldsymbol{\mathcal{R}}_a^s$, $\boldsymbol{\mathcal{R}}_b^s$, $\boldsymbol{\mathcal{T}}_a^s$ and $\boldsymbol{\mathcal{T}}_b^s$ for an s layer stack can be viewed as Fabry-Pérot

reflection and transmision coefficients [98] for the top and bottom surfaces. Let

$$\mathbf{d} = \begin{bmatrix} [E^-_{I,s}] \\ [F^-_{I,s}] \end{bmatrix} \tag{2.48}$$

represent the input planewave (expressed in *TE* and *TM* components), so that

$$E^-_{I,s} = \delta_{s0} \cos\delta \tag{2.49}$$

and

$$F^-_{I,s} = \delta_{s0} \sin\delta \tag{2.50}$$

where $s = 0$ specifies the specular channel (*i.e.*, $p = q = 0$), δ is the polarisation angle, and δ_{ij} is the Kronecker delta:

$$\delta_{ij} = \begin{cases} 1, \text{ for } i = j\,, \\ 0, \text{ otherwise.} \end{cases} \tag{2.51}$$

The field reflected back by the top surface is, by construction, $\mathbf{r} = \boldsymbol{\mathcal{R}}^s_a \mathbf{d}$. Similarly, the field $\mathbf{t}$ transmitted through to the bottom surface of the woodpile is $\mathbf{t} = \boldsymbol{\mathcal{T}}^s_a \mathbf{d}$. The vectors $\mathbf{r}$ and $\mathbf{t}$ have the same form as Eq. (2.48), namely

$$\mathbf{r} = \begin{bmatrix} [E^+_{D,s}] \\ [F^+_{D,s}] \end{bmatrix}, \quad \text{and} \quad \mathbf{t} = \begin{bmatrix} [E^-_{D,s}] \\ [F^-_{D,s}] \end{bmatrix}. \tag{2.52}$$

The reflectance R and transmittance T are defined as

$$R = \sum_s |E^+_{D,s}|^2 + |F^+_{D,s}|^2, \qquad T = \sum_s |E^-_{D,s}|^2 + |F^-_{D,s}|^2, \tag{2.53}$$

where the sum is taken over only the propagating diffraction orders [refer to the discussion regarding Eq. (2.21)]. One test of the correctness of any implementation is that the energy conservation relationships

$$T_{TE} + R_{TE} = 1, \quad \text{and} \quad T_{TM} + R_{TM} = 1 \tag{2.54}$$

should hold for lossless materials (*i.e.*, when the refractive indexes are real). For the multipole method, Eqs. (2.54) obtain irrespective of the number of multipole orders that are used [99]. By comparing the energy flux through the top and bottom surfaces of a

layer or, more generally, a stack of layers, the following energy conservation relationshps can be derived (see Appendix C 2 of [25]):

$$\boldsymbol{\mathcal{T}}_a^H \boldsymbol{\mathcal{I}}_r \boldsymbol{\mathcal{T}}_a + \boldsymbol{\mathcal{R}}_a^H \boldsymbol{\mathcal{I}}_r \boldsymbol{\mathcal{R}}_a = \boldsymbol{\mathcal{I}}_r - i\boldsymbol{\mathcal{I}}_e \boldsymbol{\mathcal{R}}_a + i\boldsymbol{\mathcal{R}}_a^H \boldsymbol{\mathcal{I}}_e, \tag{2.55}$$

$$\boldsymbol{\mathcal{T}}_a^H \boldsymbol{\mathcal{I}}_r \boldsymbol{\mathcal{R}}_b + \boldsymbol{\mathcal{R}}_a^H \boldsymbol{\mathcal{I}}_r \boldsymbol{\mathcal{T}}_b = -i\boldsymbol{\mathcal{I}}_e \boldsymbol{\mathcal{T}}_b + i\boldsymbol{\mathcal{T}}_a^H \boldsymbol{\mathcal{I}}_e, \tag{2.56}$$

$$\boldsymbol{\mathcal{R}}_b^H \boldsymbol{\mathcal{I}}_r \boldsymbol{\mathcal{T}}_a + \boldsymbol{\mathcal{T}}_b^H \boldsymbol{\mathcal{I}}_r \boldsymbol{\mathcal{R}}_a = -i\boldsymbol{\mathcal{I}}_e \boldsymbol{\mathcal{T}}_a + i\boldsymbol{\mathcal{T}}_b^H \boldsymbol{\mathcal{I}}_e, \tag{2.57}$$

$$\boldsymbol{\mathcal{R}}_b^H \boldsymbol{\mathcal{I}}_r \boldsymbol{\mathcal{R}}_b + \boldsymbol{\mathcal{T}}_b^H \boldsymbol{\mathcal{I}}_r \boldsymbol{\mathcal{T}}_b = \boldsymbol{\mathcal{I}}_r - i\boldsymbol{\mathcal{I}}_e \boldsymbol{\mathcal{R}}_b + i\boldsymbol{\mathcal{R}}_b^H \boldsymbol{\mathcal{I}}_e, \tag{2.58}$$

where[3] $\boldsymbol{\mathcal{I}}_r = \mathrm{diag}[\mathbf{I}_r, \mathbf{I}_r]$, $\boldsymbol{\mathcal{I}}_e = \mathrm{diag}[\mathbf{I}_e, \mathbf{I}_e]$, and $\mathbf{I}_r$ and $\mathbf{I}_e$ are diagonal matrices that select the propagating and evanescent diffraction orders, respectively. That is, $[\mathbf{I}_r]_s = 1$ if the s^{th} order is propagating, and $[\mathbf{I}_r]_s = 0$ otherwise, so that if $\mathbf{I}$ denotes the identity matrix, then $\mathbf{I}_e = \mathbf{I} - \mathbf{I}_r$.

2.6 Band Structure and the Transfer Matrix

To calculate the band structure of a woodpile, one must compute the Bloch modes, which were introduced in Sec. 2.1. For the Bloch analysis, either a stacking unit comprising a pair of orthogonal layers can be used, or a four-layer stacking unit comprising two such pairs can be used. Since the layers of the woodpile must be interleaved in order for there to be a complete bandgap, the lattice generated by the two-layer stacking unit will be oblique, whereas the four-layer stacking unit results in an orthogonal lattice. For the two-layer stacking unit, the phase origins of the fields incident to the pair must be offset, as in Fig. 2.8(a), in order to effect an interleaving of the structure. This is achieved by applying a lateral shear transform to the reflection matrices $\boldsymbol{\mathcal{R}}^{(2)}_{\text{a/b}}$ and transmission matrices $\boldsymbol{\mathcal{T}}^{(2)}_{\text{a/b}}$ of the pair, which are computed from the recurrence relationships given by Eqs. (2.42). The transformed scattering matrices for the pair are:

$$\begin{bmatrix} \widetilde{\boldsymbol{\mathcal{R}}}_a^{(2)} & \widetilde{\boldsymbol{\mathcal{T}}}_b^{(2)} \\ \widetilde{\boldsymbol{\mathcal{T}}}_a^{(2)} & \widetilde{\boldsymbol{\mathcal{R}}}_b^{(2)} \end{bmatrix} = \begin{bmatrix} \boldsymbol{\mathcal{Q}} & \mathbf{0} \\ \mathbf{0} & \boldsymbol{\mathcal{Q}}^{-1} \end{bmatrix} \begin{bmatrix} \boldsymbol{\mathcal{R}}_a^{(2)} & \boldsymbol{\mathcal{T}}_b^{(2)} \\ \boldsymbol{\mathcal{T}}_a^{(2)} & \boldsymbol{\mathcal{R}}_b^{(2)} \end{bmatrix} \begin{bmatrix} \boldsymbol{\mathcal{Q}}^{-1} & \mathbf{0} \\ \mathbf{0} & \boldsymbol{\mathcal{Q}} \end{bmatrix}, \tag{2.59}$$

where $\boldsymbol{\mathcal{Q}} = \mathrm{diag}\begin{bmatrix} \mathbf{Q} & \mathbf{Q} \end{bmatrix}$, with $\mathbf{Q} = \mathrm{diag}\left[e^{i(\alpha_p+\beta_q)d/4}\right]$. Note that the transform $\boldsymbol{\mathcal{Q}}$ that appears here is different from the $\boldsymbol{\mathcal{Q}}$ appearing in Eq. (2.46). The above transform is not required if a four-layer stacking unit is used.

[3] The superscript H denotes the conjugate transpose.

For an arbitrary Bloch mode of the (infinite) woodpile, Bloch's theorem [Eqs. (2.9) and (2.10)] implies that the fields $\boldsymbol{\mathcal{F}}_{\mathbf{1}} = \left[\left(\boldsymbol{\mathcal{F}}_{\mathbf{1}}^{-}\right)^{T} \left(\boldsymbol{\mathcal{F}}_{\mathbf{1}}^{+}\right)^{T}\right]^{T}$ impinging on the top surface of a constituent grating pair[4], and the fields $\boldsymbol{\mathcal{F}}_{\mathbf{2}} = \left[\left(\boldsymbol{\mathcal{F}}_{\mathbf{2}}^{-}\right)^{T} \left(\boldsymbol{\mathcal{F}}_{\mathbf{2}}^{+}\right)^{T}\right]^{T}$ impinging on the bottom surface satisfy

$$\boldsymbol{\mathcal{F}}_{\mathbf{2}} = \mu \boldsymbol{\mathcal{F}}_{\mathbf{1}}, \tag{2.60}$$

where $\mu = \exp(-i\mathbf{k} \cdot \mathbf{a}_3)$, $\mathbf{k} = (k_x, k_y, k_z)$ is the Bloch vector and $\mathbf{a}_3$ is the lattice replication vector in the stacking direction [see Fig. 2.8(a)]. Bloch's theorem can be recast as an eigenvalue problem for the inter-layer transfer matrix $\mathbf{T}$, which propagates the fields across the pair (*i.e.*, $\mathbf{T}\boldsymbol{\mathcal{F}}_{\mathbf{1}} = \boldsymbol{\mathcal{F}}_{\mathbf{2}}$), and which is readily deduced from the reflection and transmission matrices of the stacking unit and from Eq. (2.40). Specifically,

$$\mathbf{T}\boldsymbol{\mathcal{F}}_{\mathbf{1}} = \mu \boldsymbol{\mathcal{F}}_{\mathbf{1}}, \tag{2.61}$$

where

$$\mathbf{T} = \begin{bmatrix} \widetilde{\boldsymbol{\mathcal{T}}}_{a}^{(2)} - \widetilde{\boldsymbol{\mathcal{R}}}_{b}^{(2)} (\widetilde{\boldsymbol{\mathcal{T}}}_{b}^{(2)})^{-1} \widetilde{\boldsymbol{\mathcal{R}}}_{a}^{(2)} & \widetilde{\boldsymbol{\mathcal{R}}}_{b}^{(2)} (\widetilde{\boldsymbol{\mathcal{T}}}_{a}^{(2)})^{-1} \\ -(\widetilde{\boldsymbol{\mathcal{T}}}_{b}^{(2)})^{-1} \widetilde{\boldsymbol{\mathcal{R}}}_{a}^{(2)} & (\widetilde{\boldsymbol{\mathcal{T}}}_{b}^{(2)})^{-1} \end{bmatrix}. \tag{2.62}$$

In practice, one does not solve the above eigenproblem but instead computes the eigenvalues of a derived form of Eq. (2.61) that is more numerically robust (see, e.g., [100] or Sec. III of [25]). From Eq. (2.61), we can conclude that modes for which $|\mu| \neq 1$ are evanescent, while for propagating modes $|\mu| = 1$.

The scattering matrices $\widetilde{\boldsymbol{\mathcal{R}}}_{a/b}^{(2)}$ and $\widetilde{\boldsymbol{\mathcal{T}}}_{a/b}^{(2)}$ are functions of α_0 and β_0. For the Bloch analysis, we may regard α_0 and β_0 as being the components of the Bloch vector that are associated with the x and y directions, respectively, *i.e.*, $\alpha_0 \equiv k_x$ and $\beta_0 \equiv k_y$, and the diffraction orders s can be interpreted as being the Fourier components of the corresponding Bloch mode. Thus, Eq. (2.61) can be used to determine the set of allowable k_z's for each combination of k_x, k_y and wave number k. To compute the band structure, it suffices to use Eq. (2.61) to recover the propagating modes for each distinct $\mathbf{k_t} = (k_x, k_y)$ along the boundary of the surface Brillouin zone [101] [Γ-X-M path shown in Fig. 2.8(b)]. Effectively, the band structure is projected onto the k_x-k_y plane. This procedure was used to compute the band diagram in Sec. 3.3 of the next chapter.

[4]Here and elsewhere, the superscript T denotes the vector or matrix transpose.

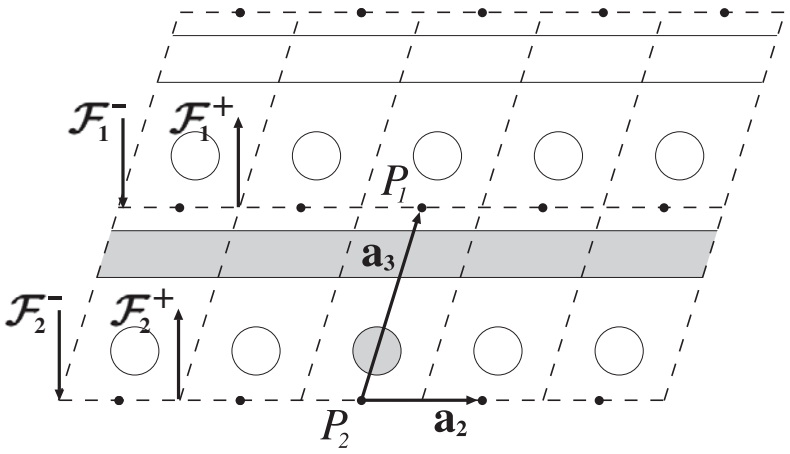

(a)

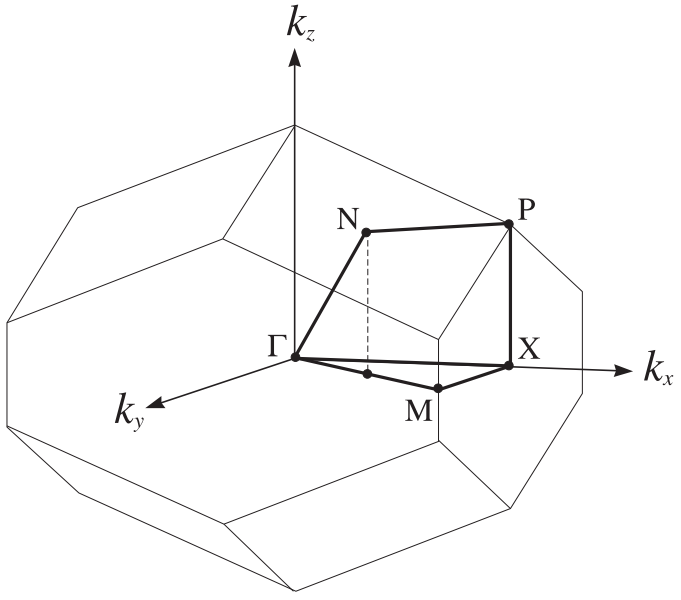

(b)

Figure 2.8: (a) For the Bloch analysis, a pair of orthogonal rods constitutes a single point of a body-centred tetragonal (BCT) lattice for which the primitive vectors are $\mathbf{a_1} = d\hat{\mathbf{x}}$ (not shown), $\mathbf{a_2} = d\hat{\mathbf{y}}$ and $\mathbf{a}_3 = (d/2)\,\hat{\mathbf{x}} + (d/2)\,\hat{\mathbf{y}} + 2h\hat{\mathbf{z}}$. Offsetting the phase origins P_1 and P_2 laterally, as indicated above, has the effect of interleaving the layers of an infinite stack. (b) The boundaries of the first Brillouin zone (thin lines) and the high-symmetry directions (thick lines) of a prolate BCT lattice, such as the lattice shown in part (a). The Γ-X-M path corresponds to the surface Brillouin zone of the woodpile [101].

Chapter 3

Multipole Super-cell Formulation

3.1 Introduction

In this chapter, the first of two methods that we have developed for modelling defects inside woodpiles is described. Section 3.2 explains how the existing multipole theory for woodpiles [26] can be generalised by allowing for a grating unit-cell that contains multiple cylinders. These methods are used to compute the transmittance of a 28 layer woodpile that contains a single defect layer (see Sec. 3.3), where parameters of the woodpile are chosen so that the cladding region possesses a complete photonic band gap (PBG). Two defect structures are considered: A coupled resonator optical waveguide (CROW) and a linear waveguide. The CROW is created by perturbing every second cylinder in the defect layer. A related structure was studied by Gralak *et al.* [77], although in that study the two-period defect was present in every layer of the woodpile, whereas here the defect is introduced expressly to create a functional layer, like the structure shown in Fig. 3.1. The dispersion curves for the waveguide modes of the CROW are inferred from the transmittance spectra by varying the angle of incidence. The second defect that is considered is the more computationally demanding case of a linear waveguide formed by perturbing the central cylinder of the unit cell, as in Fig. 3.1. In this case, the computational demands make inferring the dispersion curves from the transmission resonances of the linear waveguide impractical.

3.2 Theory

In this section, we outline how the theory in [25] can be generalised to allow for gratings that contain more than one cylinder per unit cell, like the unit cell shown in Fig. 3.2(a).

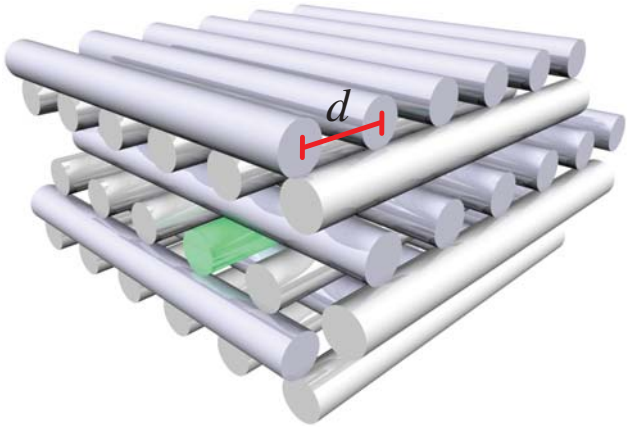

Figure 3.1: Schematic of a photonic woodpile. The rods within each layer are spaced apart by an amount d. A linear waveguide can be created by altering the properties of a single cylinder (green).

Our treatment is analogous to that of [25]; the key difference lies in the form of the associated Green's function. When there is only a single cylinder, the polar representation of the Green's function is expressed in terms of *global* lattice sums that represent the field contribution due to the periodic replicates of the cylinder. For $N_c > 1$ cylinders per unit cell, the polar representation also involves *local* lattice sums that derive from multiple contributions from all other cylinders in the unit cell and their periodic replicates. A 2D treatment of the $N_c > 1$ case was given in [88]. We remark that [88] differs from the 3D treatment in that, for classical incidence, the electric and magnetic problems completely decouple, and the grating reflection and transmission matrices, $\boldsymbol{\mathcal{R}}$ and $\boldsymbol{\mathcal{T}}$, can be formulated to act directly on the longitudinal components of the electric and magnetic fields (*i.e.*, the components parallel to the cylinders). For conical incidence, it is convenient to express the fields as a superposition of *TE* and *TM* polarised components, as in [25], and $\boldsymbol{\mathcal{R}}$ and $\boldsymbol{\mathcal{T}}$ must be formulated accordingly. In all other respects, the derivation of the scattering matrices presented here parallels that of [88], with the exception that we do not require the magnetic permeabilities (μ) of the cylinders and the background region to be unity. This permits the study of magnetic materials and, interestingly, metamaterials [102, 103].

Section 3.2.1 describes the procedure for obtaining multipole expressions for the fields produced by an up-down symmetric grating. The derivation of the single layer reflection and transmission matrices $\boldsymbol{\mathcal{R}}$ and $\boldsymbol{\mathcal{T}}$, which were introduced in Sec. 2.5, is given in Sec. 3.2.2.

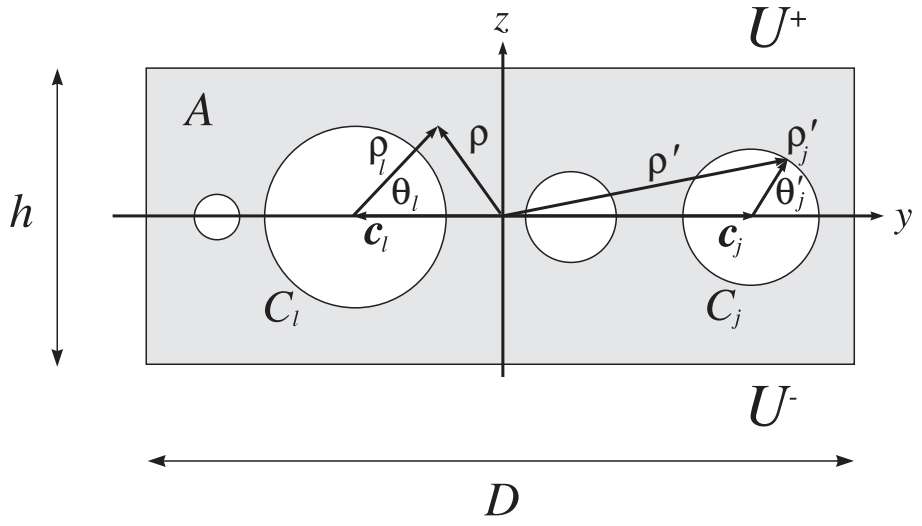

Figure 3.2: An up-down symmetric super-cell consisting of multiple cylinders that are aligned parallel to the x axis and whose centers lie along the y-axis. The surfaces U^+ and U^- must be chosen so that the cylinders are completely contained inside the interior region A.

3.2.1 Multipole Fields for a Grating

For this section, it is assumed that the cylinders of the layer are parallel to the x axis, and the y axis defines the grating direction, so that z is the direction normal to the grating. As was discussed in Sec. 2.4, the Helmholtz equation

$$[\nabla_\perp^2 + k_\perp^2]V(\boldsymbol{\rho}) = 0, \tag{3.1}$$

is solved for each incoming planewave order, where $V = E_x$ or $V = H_x$, $\mathbf{k} = (\alpha_p, \beta_q, \gamma_s)$ is the wave vector of the incoming wave, $\mathbf{k}_\perp = (\beta_q, \gamma_s)$ is the projection of the wave vector onto the yz plane, and $k_\perp = \sqrt{(kn_b)^2 - \alpha_p^2}$ is the wave number of the projection. For an arbitrary cylinder l of the super-cell, the local fields are given by an equation analogous to Eq. 2.38:

$$V_l(\boldsymbol{\rho}_l) = \sum_{n=-\infty}^{\infty} \left[A_n^{l,V} J_n(k_\perp \rho_l) + B_n^{l,V} H_n(k_\perp \rho_l)\right] e^{in\theta_l} \tag{3.2}$$

where there is an assumed x dependency of $\exp(i\alpha_p x)$, and where $\boldsymbol{\rho}_l = (\rho_l, \theta_l)$ is the position vector of $\boldsymbol{\rho}$ relative to the cylinder centre $\mathbf{c}_l$ (as shown in Fig. 3.2), and $A_n^{l,V}$ and $B_n^{l,V}$ are, respectively, the incoming and outgoing multipole coefficients for cylinder l.

By defining the Green's function G implicitly by

$$[\nabla_\perp^2 + k_\perp^2]G(\boldsymbol{\rho}) = \sum_{n=-\infty}^{\infty} \delta(\boldsymbol{\rho} - nD\hat{\mathbf{y}}) \exp(i\beta_0 nD), \tag{3.3}$$

the fields at any point $\boldsymbol{\rho}$ in region exterior to the cylinders and bounded by U^+ and U^- (*i.e.*, the region *A* of the super-cell, as in Fig. 3.2) can be expressed as

$$V(\boldsymbol{\rho}) = \int_A \left[V(\boldsymbol{\rho}')\nabla_{\boldsymbol{\rho}'}^2 G(\boldsymbol{\rho} - \boldsymbol{\rho}') - G(\boldsymbol{\rho} - \boldsymbol{\rho}')\nabla_{\boldsymbol{\rho}'}^2 V(\boldsymbol{\rho}')\right] d\boldsymbol{\rho}' \tag{3.4}$$

$$= \oint_{\partial C} \left[V(\boldsymbol{\rho}')\frac{\partial}{\partial n'}G(\boldsymbol{\rho} - \boldsymbol{\rho}') - G(\boldsymbol{\rho} - \boldsymbol{\rho}')\frac{\partial}{\partial n'}V(\boldsymbol{\rho}')\right] d\boldsymbol{\rho}', \tag{3.5}$$

where $\partial C = U^+ \bigcup U^- \bigcup_{j=1}^{N_c} C_j$, with C_j denoting the boundary of cylinder j. Note that the phase-factors $\exp(i\beta_0 nD)$ in Eq. (3.3) account for the field quasi-periodicity in the direction of the grating, where D is the grating period (*i.e.*, the length of the super-cell, as shown in Fig. 3.2). As a result of these phase factors, the left and right boundaries of the super-cell do not need to be considered in the line integral in Eq. (3.5). Equation (3.5) follows from Eq. (3.4) by applying Green's theorem to the super-cell.

The line integral in Eq. (3.5) can be evaluated in the local coordinate system of cylinder l by substituting Eq. (3.2) into Eq. (3.5), and using the appropriate representations of G (see also [88]). The following polar representation of G should be used for source points $\boldsymbol{\rho}' = (\rho', \theta')$ on the boundary C_l:

$$G(\boldsymbol{\rho} - \boldsymbol{\rho}') = -\frac{i}{4}\sum_{m=-\infty}^{\infty} H_m(k_\perp\rho)J_m(k_\perp\rho')\exp(im\theta)\exp(-im\theta') + \sum_{n=-\infty}^{\infty} J_n(k_\perp\rho)\exp(in\theta)\sum_{s=-\infty}^{\infty} S_{n-s}J_s(k_\perp\rho')\exp(-is\theta'), \tag{3.6}$$

where

$$S_m = \sum_{n\neq 0} H_m(k_\perp|\mathbf{c}_n|)\, e^{i\beta_0 nD}\exp[im\arg(\mathbf{c}_n)] \tag{3.7}$$

are the *global lattice sums*, and $\mathbf{c}_n = nD\hat{\mathbf{x}}$. The global lattice sums are conditionally convergent, and sophisticated techniques must be used to evaluate S_m stably and efficiently (see, e.g., [104]). For source points $\boldsymbol{\rho}_j' = (\rho_j', \theta_j')$ on the boundary C_j $(j \neq l)$ (refer to Fig.

3.2), the following polar representation of G should instead be used:

$$G(\boldsymbol{\rho}-\boldsymbol{\rho}') = G(\boldsymbol{\rho}_l - \boldsymbol{\rho}'_j - \mathbf{c}_j + \mathbf{c}_l) = -\frac{i}{4}\sum_{m=-\infty}^{\infty} J_m(k_\perp \rho_l)\exp(im\theta_l) \times \sum_{s=-\infty}^{\infty} S_{m-s}^{lj} J_s(k_\perp \rho'_j)\exp(-is\theta'_j), \quad (3.8)$$

where

$$S_m^{lj} = \sum_{n=-\infty}^{\infty} H_m\left(k_\perp \left|\mathbf{c}_n^{lj}\right|\right) e^{i\beta_0 nD}\exp\left[im\arg(\mathbf{c}_n^{lj})\right], \quad (3.9)$$

are the *local lattice sums* [88], with $\mathbf{c}_n^{lj} = \mathbf{c}_j - \mathbf{c}_l + \mathbf{c}_n$. The evaluation of the line integral over the boundaries U^+ and U^- of the super-cell requires the Cartesian form of G, which is given by

$$G(y,z) = \frac{1}{2iD}\sum_{q=-\infty}^{\infty}\frac{1}{\gamma_s}e^{i(\beta_q y + \gamma_s|z|)}. \quad (3.10)$$

Upon evaluating the line integral in Eq. (3.5), one obtains the Wijngaard expansion, which is a second local representation of the exterior fields in the vicinity of cylinder l:

$$V_l(\boldsymbol{\rho}_l) = \sum_{n=-\infty}^{\infty} B_n^{l,V} H_n(k_\perp\rho_l)\, e^{in\theta_l} + \sum_{n=-\infty}^{\infty} J_n(k_\perp\rho_l)\, e^{in\theta_l} \times \left[\sum_{j=1}^{N_c}\sum_{m=-\infty}^{\infty} B_m^{j,V} S_{n-m}^{lj} + \sum_{s=-\infty}^{\infty}\left(J_{ns}^{l,-}\delta_{V,s}^{-} + J_{ns}^{l,+}\delta_{V,s}^{+}\right)\right], \quad (3.11)$$

where $\delta_{V,s}^{\pm}$ are the longitudinal components of the incoming fields [see Eqs. (2.22) and (2.23)], and

$$J_{ns}^{l,\pm} = (\pm 1)^n \exp\left[\pm in\arg(\gamma_s + i\beta_q)\right]\exp(i\beta_q c_l) \quad (3.12)$$

change the basis of the incident field from plane waves to multipoles. (The expression for $J_{ns}^{l,\pm}$ is derived by comparing the incoming plane waves with the generating function for the Bessel functions, see, e.g., [88].) Here, p is fixed, and so the summation over s in Eq. (3.11) is merely a summation over q only. As before, there is an assumed x dependence of $\exp(i\alpha_p x)$. Note that the diffraction in the grating direction is incorporated into the Cartesian form Green's [Eq. (3.10)], in that the summation is over all of the β_q's. Consequently, the Wijngaard expansion accounts for diffraction in the grating direction. Evidently, the initial restriction that β_q be fixed was redundant.

The only difference between the two field representations, Eqs. (3.2) and (3.11), is

that the sources of the incoming fields in Eq. (3.11) are made explicit. Specifically, the terms involving global lattice sums represent the fields sourced by the periodic replicates of cylinder l, the terms involving local lattice sums represent the fields sourced by the cylinders $j \neq l$ and their periodic replicates, and the term involving $\delta^{\pm}_{V,s}$ is the multipole representation of the incoming diffraction orders. By equating the two representations of the local fields, one can express the incoming multipole coefficients in terms of the outgoing coefficients so that, using matrix notation,

$$\boldsymbol{\mathcal{A}} = \boldsymbol{\mathcal{S}}\boldsymbol{\mathcal{B}} + \boldsymbol{\mathcal{J}}^{-}\boldsymbol{\mathcal{D}}^{-} + \boldsymbol{\mathcal{J}}^{+}\boldsymbol{\mathcal{D}}^{+}. \tag{3.13}$$

Equation (3.13) is known as the Rayleigh identity, in which $\boldsymbol{\mathcal{A}}$ and $\boldsymbol{\mathcal{B}}$ are, respectively, the coefficients of the incoming and outgoing multipole fields impinging on the boundary of cylinder l, $\boldsymbol{\mathcal{S}}\boldsymbol{\mathcal{B}}$ represents the scattered fields sourced by each cylinder, and $\boldsymbol{\mathcal{J}}^{-}\boldsymbol{\mathcal{D}}^{-}$ ($\boldsymbol{\mathcal{J}}^{+}\boldsymbol{\mathcal{D}}^{+}$) is the multipole representation of the incoming field above (below) the layer. That is,

$$\boldsymbol{\mathcal{A}} = \begin{bmatrix} [\mathbf{A}^{l,E}] \\ [\mathbf{A}^{l,H}] \end{bmatrix}, \quad \boldsymbol{\mathcal{B}} = \begin{bmatrix} [\mathbf{B}^{l,E}] \\ [\mathbf{B}^{l,H}] \end{bmatrix}, \tag{3.14}$$

$\mathbf{A}^{l,E/H} = \left[A_n^{l,E/H}\right]$, $\mathbf{B}^{l,E/H} = \left[B_n^{l,E/H}\right]$, $\boldsymbol{\mathcal{S}} = \operatorname{diag}[\mathbf{S},\mathbf{S}]$, $\mathbf{S} = \left[\mathbf{S}^{lj}\right]$, $\mathbf{S}^{lj} = \left[S^{lj}_{n-m}\right]$, $\boldsymbol{\mathcal{J}}^{\pm} = \operatorname{diag}\begin{bmatrix} [\mathbf{J}^{l,\pm}] & [\mathbf{J}^{l,\pm}] \end{bmatrix}$, $\mathbf{J}^{l,\pm} = [J^{l,\pm}_{ns}]$, $\boldsymbol{\mathcal{D}}^{\pm} = [(\mathbf{D}^{\pm,E})^T\,(\mathbf{D}^{\pm,H})^T]^T$, and $\mathbf{D}^{\pm,E/H} = [\delta^{\pm}_{E/H,s}]$, where $s = (p,q)$ with p fixed.

The fields for points inside cylinder l can also be expressed in terms of cylindrical harmonics; if n_l is the refractive index of cylinder l, then the interior fields are:

$$V_l(\boldsymbol{\rho}_l) = \sum_{n=-\infty}^{\infty} C_n^{l,V} J_n(k_{\perp,l}\rho_l)\, e^{in\theta_l}, \tag{3.15}$$

where the x dependence is $\exp(i\alpha_p x)$, and where $k_{\perp,l} = \sqrt{(kn_l)^2 - \alpha_p^2}$ is the wave number of the interior fields. Equations (3.2) and (3.15), along with the boundary condition, which states that the tangential components (E_θ, H_θ, E_x and H_x) be continuous across the cylinder boundary, lead to

$$\boldsymbol{\mathcal{A}} = -\boldsymbol{\mathcal{M}}\boldsymbol{\mathcal{B}}, \tag{3.16}$$

in which the matrix $\boldsymbol{\mathcal{M}}$ encapsulates the material properties of cylinder l. Expressions for $\boldsymbol{\mathcal{M}}$ can be found in Appendix 3.A. In general, $\boldsymbol{\mathcal{M}}$ is not diagonal, hence Eq. (3.16) causes the electric and magnetic problems to become coupled. Solving (3.13) and (3.16)

for the outgoing multipole coefficients $\boldsymbol{\mathcal{B}}$ gives

$$\boldsymbol{\mathcal{B}} = -(\boldsymbol{\mathcal{M}} + \boldsymbol{\mathcal{S}})^{-1}\boldsymbol{\mathcal{J}}\boldsymbol{\mathcal{D}}, \tag{3.17}$$

with $\boldsymbol{\mathcal{J}} = \begin{bmatrix} \boldsymbol{\mathcal{J}}^- & \boldsymbol{\mathcal{J}}^+ \end{bmatrix}$ and $\boldsymbol{\mathcal{D}} = \begin{bmatrix} (\boldsymbol{\mathcal{D}}^-)^T & (\boldsymbol{\mathcal{D}}^+)^T \end{bmatrix}^T$. Equation (3.17) can be used to construct the reflection and transmission matrices for the layer.

3.2.2 Scattering Matrices for a Grating

The diffracted fields $f^{\pm}_{E,s}$ and $f^{\pm}_{H,s}$ in Eqs. (2.22) and (2.23) can be recovered by again evaluating Eq. (3.5), this time taking $\boldsymbol{\rho}$ to lie above and below the boundaries U^+ and U^- in turn, and using the Cartesian representation of the Green's function [Eq. (3.10)]. Consequently, the diffracted fields will be expressed in terms of the outgoing multipole coefficients $\boldsymbol{\mathcal{B}}$ [Eq. (3.17)]. The longitudinal components of diffracted fields are found to be [88]

$$\boldsymbol{\mathcal{F}} = \boldsymbol{\mathcal{D}} + \frac{2}{D}\boldsymbol{\mathcal{G}}\boldsymbol{\mathcal{K}}\boldsymbol{\mathcal{B}}, \tag{3.18}$$

where

$$\boldsymbol{\mathcal{F}}^{\pm} = \begin{bmatrix} \left[f^+_{E,s}\right] \\ \left[f^+_{H,s}\right] \end{bmatrix}, \tag{3.19}$$

and $\boldsymbol{\mathcal{K}}$ reverts to the plane wave basis from the multipole basis, and is defined analogously to $\boldsymbol{\mathcal{J}}$:

$$\boldsymbol{\mathcal{K}} = \begin{bmatrix} (\boldsymbol{\mathcal{K}}^-)^T & (\boldsymbol{\mathcal{K}}^+)^T \end{bmatrix}^T, \tag{3.20}$$

$$\boldsymbol{\mathcal{K}}^{\pm} = \begin{bmatrix} \mathbf{K}^{1,\pm} & \cdots & \mathbf{K}^{N_c,\pm} & \mathbf{0} & \cdots & \mathbf{0} \\ \mathbf{0} & \cdots & \mathbf{0} & \mathbf{K}^{1,\pm} & \cdots & \mathbf{K}^{N_c,\pm} \end{bmatrix},$$

$\mathbf{K}^{l,\pm} = [K^{l,\pm}_{sn}]$ and $K^{l,\pm}_{sn} = (\pm 1)^n \exp\left[\mp in \arg(\gamma_s + i\beta_q)\right] \times \exp(-i\beta_q c_l)$. Equation (3.18) includes a pre-factor $\boldsymbol{\mathcal{G}}$ that serves to normalise the reflected and transmitted energy:

$$\boldsymbol{\mathcal{G}} = \begin{bmatrix} \boldsymbol{\mathfrak{G}} & \mathbf{0} \\ \mathbf{0} & \boldsymbol{\mathfrak{G}} \end{bmatrix}, \tag{3.21}$$

$\boldsymbol{\mathfrak{G}} = \operatorname{diag}[1/\gamma_s]$, and $s = (p, q)$ with p fixed. (Refer to the discussions regarding Eqs. (2.24) and (2.25), see also Eqs. (31) and (47) of [26].)

In view of Eqs. (3.17) and (3.18), the longitudinal components of the diffracted

planewaves generated by the incoming field $\boldsymbol{\mathcal{D}}$ are

$$\boldsymbol{\mathcal{F}} = \boldsymbol{\mathcal{D}} - \frac{2}{D}\boldsymbol{\mathcal{G}}\boldsymbol{\mathcal{K}}\boldsymbol{\mathcal{L}}\boldsymbol{\mathcal{J}}\boldsymbol{\mathcal{D}}, \tag{3.22}$$

where $\boldsymbol{\mathcal{L}} = (\boldsymbol{\mathcal{M}} + \boldsymbol{\mathcal{S}})^{-1}$ is the multipole scattering operator. This result can be restated in terms of *TE* and *TM* polarised components be making use of Eq. (2.28) and the analogous expression for the incoming fields. One finds that

$$\begin{bmatrix} \boldsymbol{\mathcal{F}}_D^- \\ \boldsymbol{\mathcal{F}}_D^+ \end{bmatrix} = \left[\boldsymbol{\mathcal{I}} - \frac{2}{D}\hat{\boldsymbol{\mathcal{X}}}^{-1}\boldsymbol{\mathcal{Z}}^{-1}\boldsymbol{\mathcal{G}}\boldsymbol{\mathcal{K}}\boldsymbol{\mathcal{L}}\boldsymbol{\mathcal{J}}\boldsymbol{\mathcal{Z}}\hat{\boldsymbol{\mathcal{X}}}\right]\begin{bmatrix} \boldsymbol{\mathcal{F}}_I^- \\ \boldsymbol{\mathcal{F}}_I^+ \end{bmatrix}, \tag{3.23}$$

where the *TE* and *TM* polarised fields, $\boldsymbol{\mathcal{F}}_D^{\pm}$ and $\boldsymbol{\mathcal{F}}_I^{\pm}$, are given by Eqs. (2.29) and (2.41), respectively, $\boldsymbol{\mathcal{Z}} = \mathrm{diag}\left[\begin{array}{cc} \mathsf{Z}, & \mathsf{Z} \end{array}\right]$ and $\hat{\boldsymbol{\mathcal{X}}} = \mathrm{diag}\left[\begin{array}{cc} \mathsf{X}^-, & \mathsf{X}^+ \end{array}\right]$. Note that, unlike Eqs. (2.28), (2.29) and (2.41), p is fixed in Eq. (3.23).

The single-layer scattering matrices can be inferred by identifying the coefficient matrix in Eq. (3.23) with that in Eq. (2.40). When the grating is up-down symmetric, the size of the multipole scattering operator can be halved using a folding procedure, thereby reducing the cost of evaluating the matrix inversion in the expression for $\boldsymbol{\mathcal{L}}$. We proceed by rewriting Eq. (3.23) in terms of quantities that are symmetric and antisymmetric (denoted using the superscripts s and a) with respect to the z coordinate:

$$\begin{bmatrix} \boldsymbol{\mathcal{F}}_D^- \\ \boldsymbol{\mathcal{F}}_D^+ \end{bmatrix} = \begin{bmatrix} \boldsymbol{\mathcal{F}}_I^- \\ \boldsymbol{\mathcal{F}}_I^+ \end{bmatrix} - \frac{kn_b}{{k_\perp}^2 D}\boldsymbol{\mathcal{T}}^{-1}\boldsymbol{\mathcal{X}}\boldsymbol{\mathcal{Z}}^{-1} \times \begin{bmatrix} \boldsymbol{\mathcal{K}}^s\boldsymbol{\mathcal{L}}\boldsymbol{\mathcal{J}}^s & \boldsymbol{\mathcal{K}}^s\boldsymbol{\mathcal{L}}\boldsymbol{\mathcal{J}}^a \\ \boldsymbol{\mathcal{K}}^a\boldsymbol{\mathcal{L}}\boldsymbol{\mathcal{J}}^s & \boldsymbol{\mathcal{K}}^a\boldsymbol{\mathcal{L}}\boldsymbol{\mathcal{J}}^a \end{bmatrix}\boldsymbol{\mathcal{Z}}\boldsymbol{\mathcal{X}}\boldsymbol{\mathcal{T}}\begin{bmatrix} \boldsymbol{\mathcal{F}}_I^- \\ \boldsymbol{\mathcal{F}}_I^+ \end{bmatrix} \tag{3.24}$$

[cf. Eq. (52) of [25]] where $\boldsymbol{\mathcal{X}} = \mathrm{diag}\left[\begin{array}{cc} \mathsf{X}^-, & \mathsf{X}^- \end{array}\right]$,

$$\boldsymbol{\mathcal{T}} = \begin{bmatrix} \mathsf{I} & \mathsf{I} \\ \mathsf{I} & -\mathsf{I} \end{bmatrix}, \tag{3.25}$$

and I is the identity matrix. It can be shown that $\boldsymbol{\mathcal{K}}^s\boldsymbol{\mathcal{L}}\boldsymbol{\mathcal{J}}^a$ and $\boldsymbol{\mathcal{K}}^a\boldsymbol{\mathcal{L}}\boldsymbol{\mathcal{J}}^s$ vanish for up-down symmetric gratings. Furthermore, for $\boldsymbol{\mathcal{K}}^s\boldsymbol{\mathcal{L}}\boldsymbol{\mathcal{J}}^s$ and $\boldsymbol{\mathcal{K}}^a\boldsymbol{\mathcal{L}}\boldsymbol{\mathcal{J}}^a$ the rows that correspond to the negative multipole orders are redundant, and this allows one to truncate $\boldsymbol{\mathcal{K}}^{a/s}$, $\boldsymbol{\mathcal{J}}^{a/s}$ and $\boldsymbol{\mathcal{L}}$ by retaining only the rows and columns corresponding to the multipole orders $n, m \geq 0$. Using a tilde to denote such a truncated matrix, the scattering matrices for an

up-down symmetric grating are then

$$\boldsymbol{\mathcal{R}}_{a,p} = \boldsymbol{\mathcal{R}}_{b,p} = -\frac{kn_b}{2k_\perp^2 D}\mathbf{X}^{-}\mathbf{Z}^{-1}\left(\widetilde{\boldsymbol{\mathcal{K}}}^s\boldsymbol{\epsilon}^s\widetilde{\boldsymbol{\mathcal{L}}}^s\widetilde{\boldsymbol{\mathcal{J}}}^s - \widetilde{\boldsymbol{\mathcal{K}}}^a\boldsymbol{\epsilon}^a\widetilde{\boldsymbol{\mathcal{L}}}^a\widetilde{\boldsymbol{\mathcal{J}}}^a\right)\mathbf{Z}\mathbf{X}^{-}, \tag{3.26}$$

and

$$\boldsymbol{\mathcal{T}}_{a,p} = \boldsymbol{\mathcal{T}}_{b,p} = \boldsymbol{\mathcal{I}} - \frac{kn_b}{2k_\perp^2 D}\mathbf{X}^{-}\mathbf{Z}^{-1}\left(\widetilde{\boldsymbol{\mathcal{K}}}^s\boldsymbol{\epsilon}^s\widetilde{\boldsymbol{\mathcal{L}}}^s\widetilde{\boldsymbol{\mathcal{J}}}^s + \widetilde{\boldsymbol{\mathcal{K}}}^a\boldsymbol{\epsilon}^a\widetilde{\boldsymbol{\mathcal{L}}}^a\widetilde{\boldsymbol{\mathcal{J}}}^a\right)\mathbf{Z}\mathbf{X}^{-}, \tag{3.27}$$

where the subscript p has been used to emphasise the fact that the reflection and transmission matrices so defined act on fields that have an x dependence of $\exp(i\alpha_p x)$. The definitions of the terms on the right-hand sides of Eqs. (3.26) and (3.27) are provided in Appendix 3.B.

The natural way to construct the reflection matrix $\boldsymbol{\mathcal{R}}_a$ that acts on all of the components of the downward incoming fields is by using the implied ordering

$$\boldsymbol{\mathcal{R}}_a = \mathrm{diag}\left[\boldsymbol{\mathcal{R}}_{a,p}\right] \tag{3.28}$$

Note that this imposes a global ordering on the fields in Eq. (2.40). The remaining scattering matrices are then $\boldsymbol{\mathcal{R}}_b = \mathrm{diag}\left[\boldsymbol{\mathcal{R}}_{b,p}\right]$, $\boldsymbol{\mathcal{T}}_a = \mathrm{diag}\left[\boldsymbol{\mathcal{T}}_{a,p}\right]$, and $\boldsymbol{\mathcal{T}}_b = \mathrm{diag}\left[\boldsymbol{\mathcal{T}}_{b,p}\right]$. A complication arises because the scattering matrices for gratings whose rods are parallel to the y-axis are computed in a rotated rotated coordinate system [refer to Eqs. (2.34)-(2.36)]. In particular, $\gamma'_{(p,q)} = \gamma_{(-q,p)}$, which means that the woodpile order $s = (p, q)$ for the rotated coordinate system corresponds to the order $s = (-q, p)$ in the unrotated system. Consequently, the entries of the scattering matrices for the rotated system must be permuted so that they are consistent with global the channel order given by Eq. (3.28).

3.3 Woodpile Waveguides

We now use the techniques described in the preceding sections to compute the reflectances and transmittances of two woodpile waveguides, which are each embedded within finite woodpiles. In both cases, the waveguide is created by changing the size of selected cylinders of the 15^{th} layer of a 28 layer woodpile, where the bottom layer is taken to be the first layer. The radii and refractive index of the cylinders are $r = 0.15d$ and $n_l = 2.68$ (chalcogenide glass), respectively, where d is the pitch of the constituent gratings (as in Fig. 3.1). The background refractive index is air ($n_b = 1$) and, thus, the thicknesses of the layers comprising the bulk must be chosen so that adjacent layers are touching. To

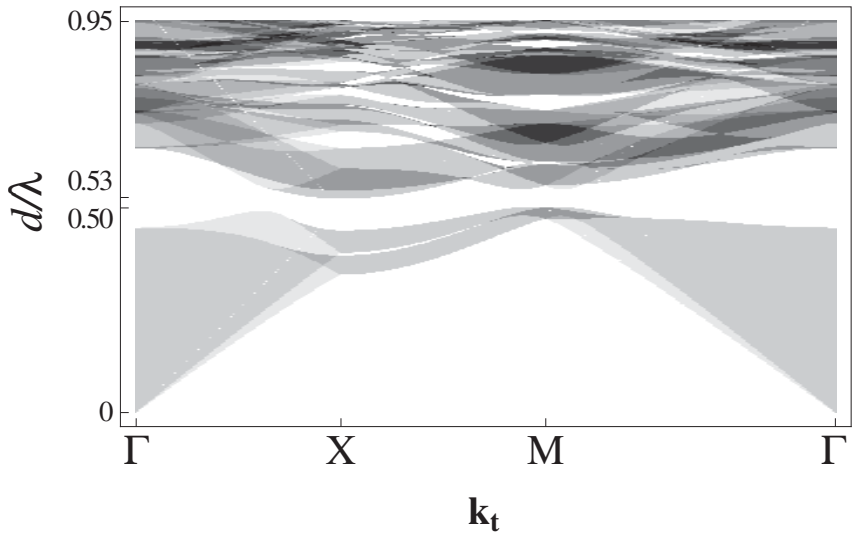

Figure 3.3: Plot of the number of propagating Bloch modes for each (normalized) frequency d/λ as the in-plane Bloch vector $\mathbf{k_t} = (k_x, k_y)$ traverses the boundary of the surface Brillouin zone shown in Fig. 2.8(b). White indicates the absence of propagating states. The structural parameters of the woodpile are given in Sec. 3.3.

achieve this, a layer thickness of $h = 0.3002d$ is used. The band structure of the homogeneous infinite woodpile was computed using the method outlined in Section 2.6, and is shown in Fig. 3.3. It can be seen that a complete PBG spans the normalised frequencies $0.50 \lesssim d/\lambda \lesssim 0.53$, which correspond to the normalised wavelengths $1.9 \leq \lambda/d \leq 2.0$.

The woodpile waveguides considered in this thesis rely on the fact that the 28-layer woodpile cladding strongly attenuates light for wavelengths that fall within the bandgap. Ideally, the field attenuation should be strong for all directions, in order to minimise the scattering losses due to extrinsic factors such as surface roughness. To investigate the field attenuation inside the cladding, we have computed the transmission spectra of an 8-, 14- and 28-layer woodpile, for *TE* and *TM* polarised incidence, see Fig. 3.4. The spectra are computed for the irreducible Brillouin zone (BZ) of the waveguide. Since the rods of the waveguide layer are taken to be oriented parallel to the x axis, the irreducible BZ of the waveguide spans the Bloch vectors $0 \leq k_x \leq \pi/d$ with $k_y = 0$, or, equivalently, it spans the $\mathbf{\Gamma}-\mathbf{X}$ path along the horizontal axis of Fig. 3.3. The value of k_x is changed by letting the α_0 component of the wave vector $\mathbf{k} = (\alpha_0, \beta_0, -\gamma_0)$ of the incident planewave vary over the values $0 < \alpha_0 < \pi/d$, with $\beta_0 = 0$. [The value of γ_0 changes implicitly according to Eq. (2.21).] This corresponds to an incident field that changes from normal incidence to glancing incidence as α_0 increases. Note that for these value of α_0 and β_0, a *TE* polarised incident field is one for which $E_x = E_z = H_y = 0$, while for a *TM* polarised

incident field, $E_y = H_x = H_z = 0$. In the context of transmission, we will simply refer to α_0 and β_0 as k_x and k_y, respectively. (When the structure has infinitely many layers, α_0 and β_0 are precisely k_x and k_y, as noted in Sec. 2.6.)

As the number of layers increases, it can be seen in Fig. 3.4 that the transmittace [as computed using Eq. (2.53)] decreases for both *TE* and *TM* incidence. When there are 14 layers, the transmittance over the bandgap wavelengths is low for most of the BZ, while for 28 layers, the transmittance vanishes entirely for these wavelengths, irrespective of k_x. In the next two sections, the waveguiding modes of the 28-layer CROW and linear waveguide are located by looking for transmission resonances inside the PBG. These resonances occur when the incident field excites a defect mode.

3.3.1 A Coupled Resonator Optical Waveguide

Of the two waveguide geometries considered in this chapter, the CROW is the more computationally tractable one because the size of the super-cell is small. For this structure, the super-cell comprises two cylinders separated by a distance d equal to the pitch of the gratings, and the length of the super-cell is $D = 2d$. The waveguide is created by decreasing the radius r_w of the second cylinder of the super-cell of the defect layer, thereby resulting in a periodic defect that repeats every two cylinders, as illustrated schematically in Fig. 3.5. The CROW can guide light along either the longitudinal (x) direction, or in the transverse (y) direction via resonant coupling.

The top panels in Figs. 3.6(a)-(c) show the positions of the transmission peaks for *TM* incidence for $r_w = 0$, $r_w = 0.5r$ and $r_w = 0.8r$. In each case, one or more strong transmission peaks sweep through frequencies corresponding to the PBG of the host woodpile. These resonances can be attributed to the waveguide layer, as they are not present in the transmission spectrum of the regular 28 layer woodpile (see Fig. 3.4). No such peaks were found for *TE* incidence, however. In general, the fields inside the defect rod will have a lower spatial frequency than the fields in the neighbouring air region. Thus, as the radius of the defect rod increases, the resonance shifts to longer wavelengths. The bottom panels of Figs. 3.6(a)-(c), show the corresponding quality factors $Q = \omega/\Delta\omega$ of the transmission resonances, where $\omega = k/c$ is the resonant frequency, and $\Delta\omega$ is the linewidth (full width at half maximum of the peak). As with any PC defect mode, the Q factors tend to be higher for wavelengths near the middle of the PBG [3]. In each of Figs. 3.6(a) and 3.6(b), one of the resonances seemingly gets cutoff as it approaches the middle of the bandgap. In reality, the linewidth of the peak becomes too fine for the peak to be easily resolved.

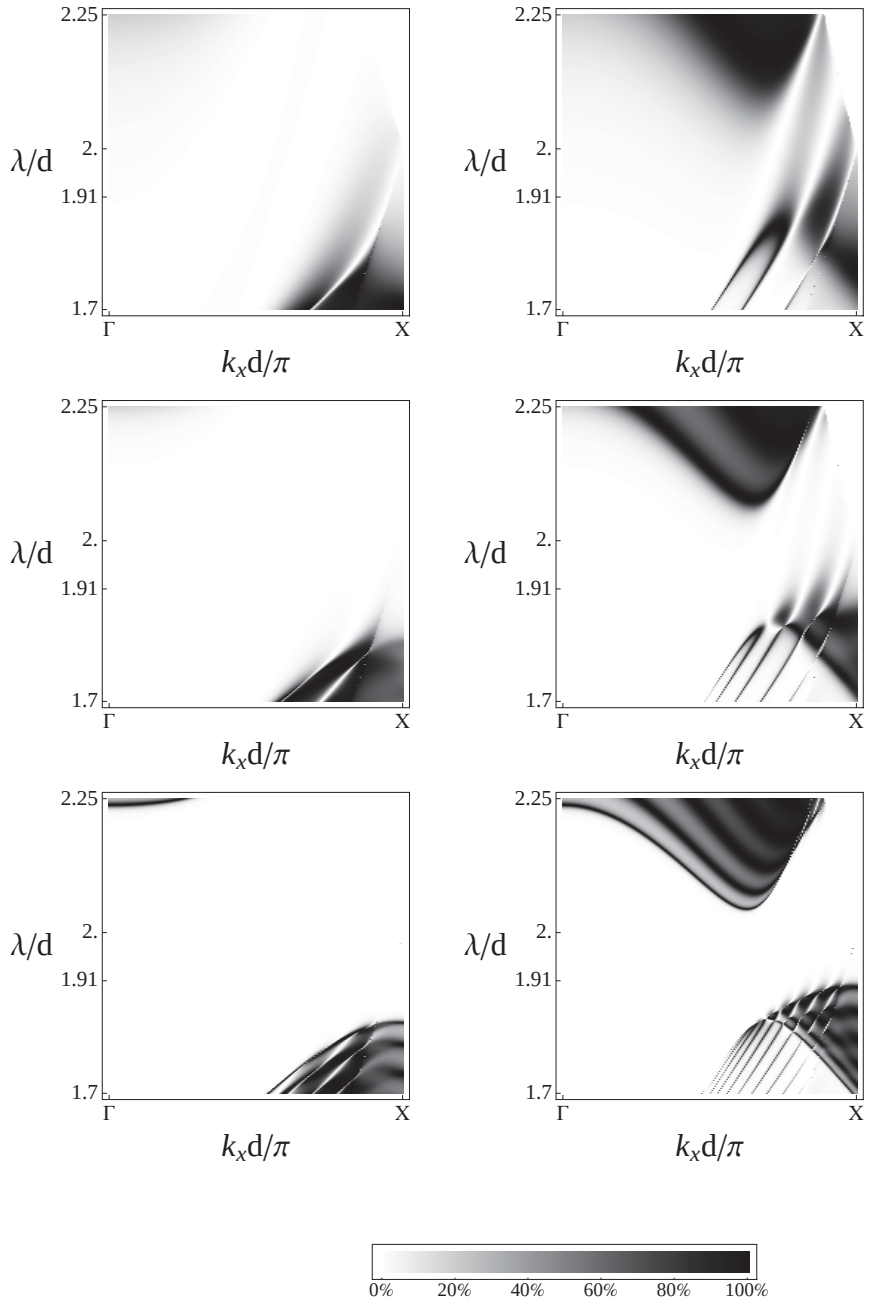

Figure 3.4: Rows 1-3 show, respectively, the transmittance $\%$ for an 8-, 14-, and 28-layer woodpile. Left column: *TE* incidence. Right column: *TM* incidence. The complete of the corresponding infinite woodpile spans the wavelengths $1.9 \lesssim \lambda \lesssim 2.0$.

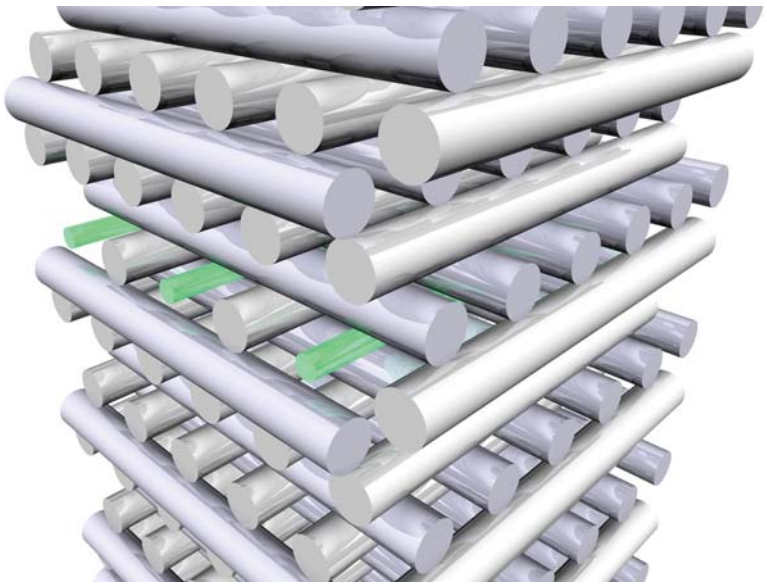

Figure 3.5: Geometry of the coupled resonator optical waveguide. The waveguide is created by reducing the size of every second rod of the defect layer uniformly (green rods).

The fields at one of the resonances are shown in Fig. 3.7, and are localised to the waveguide layer, indicative of a defect mode. Note that the fields in Fig. 3.7 are plotted on a compressed colour scale to show a greater dynamic range of the lower-intensity field components. Also, throughout this thesis all fields, such as those shown in Fig. 3.7, are plotted in arbitrary units because the energy is defined relative to energy of the incident planewave. Moreover, as is the convention in the study of photonic crystals, the dimensions of the woodpile are defined relative to the period d. The field plots in this thesis are therefore inherently unitless – the energy of the mode, in absolute terms, depends on power of the incident field.

Cusps occur at the contact points of the rods, as illustrated in Fig. 3.8, causing the E_z component of the fields at these points to exhibit singular behaviour, especially near the defect layer, *i.e.*, where the field is concentrated. (The existence of singularities at cusps was reported by, e.g., Meixner [105] in 1972.) The magnetic permeability of the rods is the same as that of the background region, and so the magnetic field must be continuous and, therefore, regular at the cusps. Similarly, the continuity of the tangential components E_x and E_y across the boundaries ensures that these components are regular at the cusps. Recall that for $k_y = 0$, a *TM* polarised incident field is one for which $H_y \neq 0$ and, by implication, $E_y = H_x = H_z = 0$ (also see Fig. 2.4). The singular nature of the E_z component means that the diffracted fields will therefore always have a '*TM*-like'

character in that E_y, H_x and H_z are small relative to E_z, and this appears to be why the transmission resonances of the CROW (Fig. 3.6) only occur for a *TM*-polarised incident field.

3.3.2 A Linear Waveguide

Ideally, a linear waveguide would be modelled by perturbing a single cylinder in the defect layer. In this chapter we have approximated such a structure by using a super-cell of length $D = 11d$ comprising 11 cylinders spaced equally along the axis of the grating, and then decreasing the radius r_w of the central cylinder of the waveguide layer. Essentially, the structure being modelled is the same as the CROW depicted in Fig. 3.5, except that the defect repeats every 11 cylinders. This approach relies on the PBG to prevent significant coupling between the fields of any two super-cells. In the next chapter we use an alternative formulation to investigate the validity of this assumption. In particular, it will be shown that a super-cell of 10 cylinders adequately isolates the linear waveguide from its periodic replicates.

For the linear waveguide, the length of the super-cell and the fineness of the spectral features make the super-cell approach particularly demanding, and computing the transmittance for the entire Brillouin zone (BZ) proved to be impractical. Instead, the transmittance was computed for three values of k_x near the edge of the BZ. Figure 3.9 shows the transmittance for $k_x = 0.86(\pi/d)$, $k_x = 0.92(\pi/d)$ and $k_x \approx \pi/d$, with the defect radius $r_w = 0.5r$ fixed. As was for the CROW, the linear defect causes prominent resonances to appear inside the PBG, while no such resonances are present for *TE* incidence (for the reasons discussed in Sec. 3.3.1). As k_x increases, the resonance shifts to shorter wavelengths, and the Q factor gradually increases from $13,000$ to $23,000$. Near the edge of the BZ ($k_x \approx \pi/d$), the resonance becomes a doublet because there are a pair of defect modes that become degenerate precisely at $k_x = 1$. The existence of such a degenerate pair can be attributed to the fact the waveguide has glide reflection symmetry [106], *i.e.*, the waveguide is invariant under the transformation

$$z \to -z, \quad x \to x + d/2. \tag{3.29}$$

To try and improve the Q-factors, we changed the radius of the defect, while keeping $k_x \approx \pi/d$ fixed. The transmittances for *TM* incidence for $r_w = 0.0$, $r_w = 0.5r$, and $r_w = 0.8r$ are shown in Fig. 3.10. Increasing the radius causes the resonance to shift

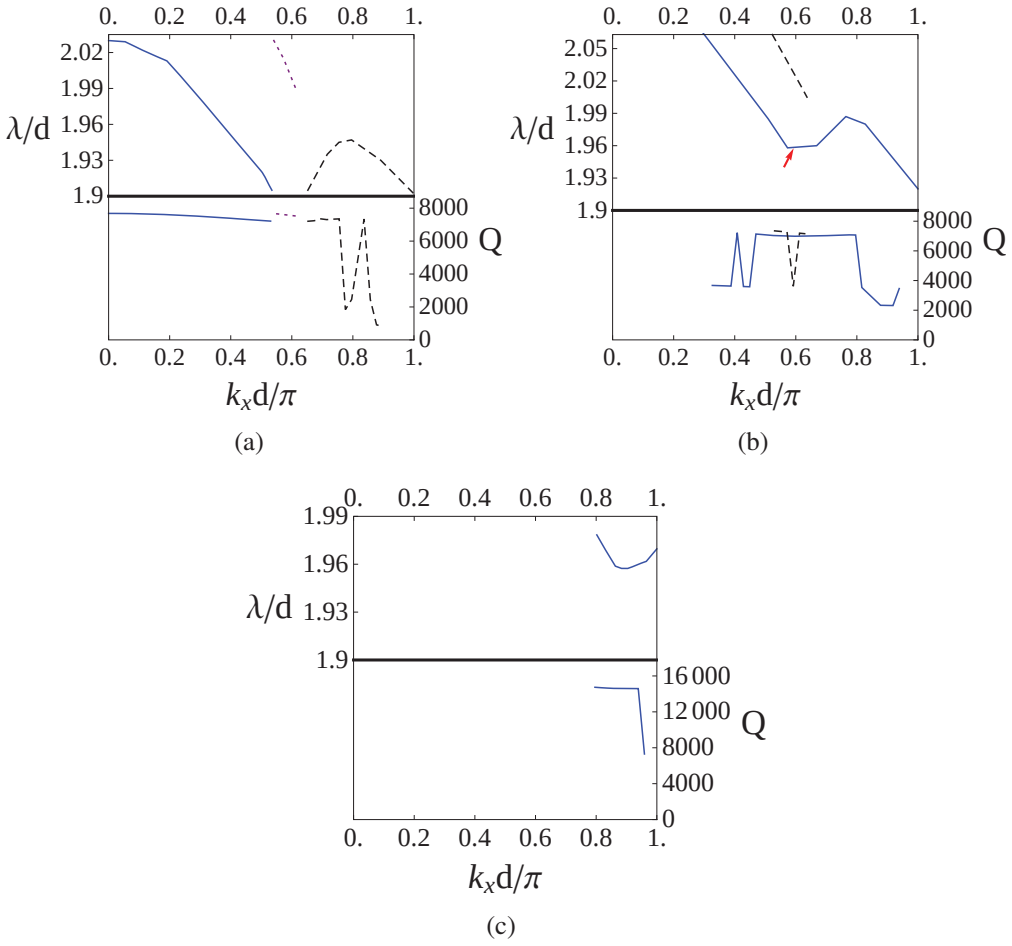

Figure 3.6: Location of transmission maxima (top panels) for *TM* incidence and the corresponding *Q*-factors (bottom panels) for the CROW using defect sizes of (a) $r_w = 0$, (b) $r_w = 0.5r$ and (c) $r_w = 0.8r$ as k_x varies. Inside the bandgap, the transmittance is negligible except near the resonances. As r_w increases, the resonances move to longer wavelengths. Fields at the point indicated (arrow) in part (b) are shown in Fig. 3.7.

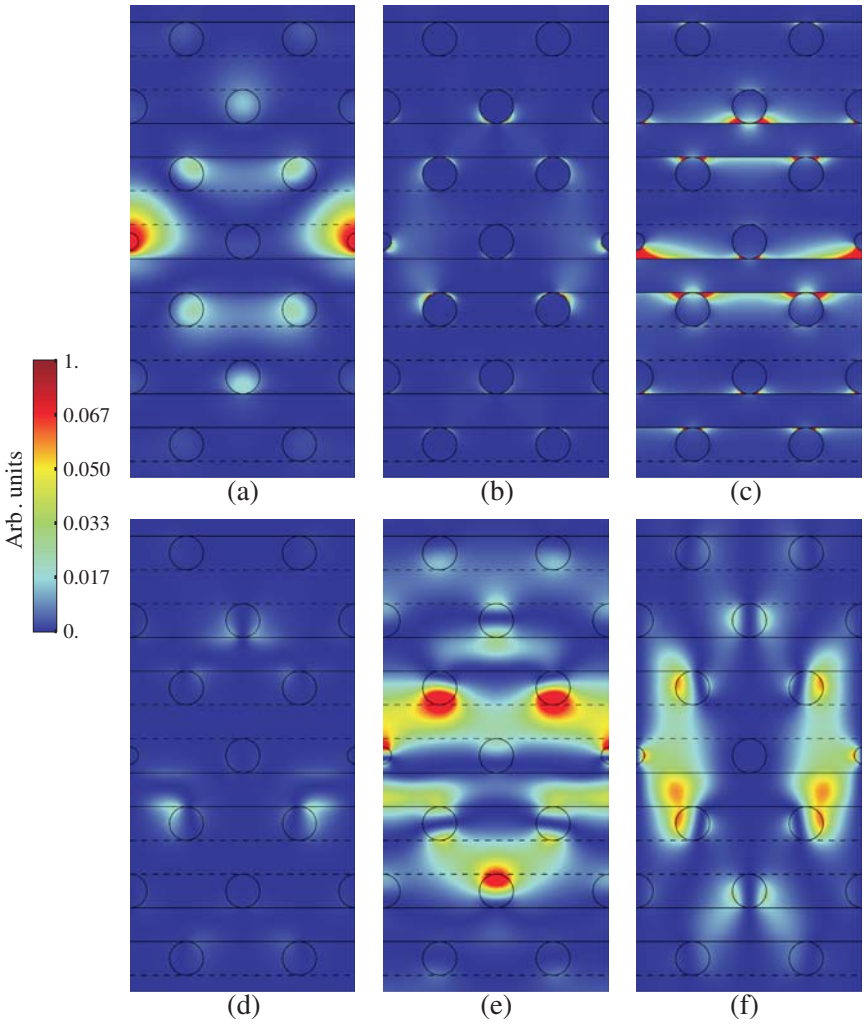

Figure 3.7: Componentwise field intensity in the vicinity of the waveguide layer of the CROW (only one period in the horizontal direction is shown): (a) $|E_x|^2$, (b) $|E_y|^2$, (c) $|E_z|^2$, (d) $|H_x|^2$, (e) $|H_y|^2$ and (f) $|H_z|^2$. The view looks down the rods of the waveguide layer. The radius of the defect rods (smaller circles) is $r_w = 0.5r$, and the parameters of the incident *TM*-polarised field are $k_x d/\pi = 0.59$, $k_y = 0$ and $\lambda/d = 1.958$, which correspond to the point indicated in Fig.3.6(b).

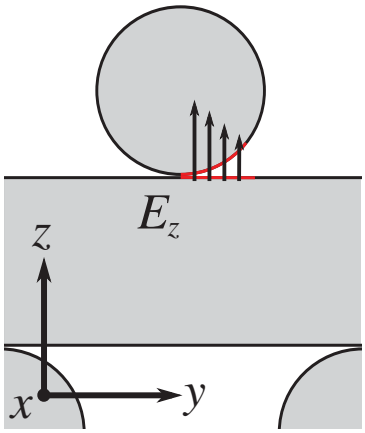

Figure 3.8: The magnitude of the E_z component of the fields increases in the vicinity of the contact points of the rods. The E_z component becomes singular precisely at the cusp, while all other field components are continuous at this point.

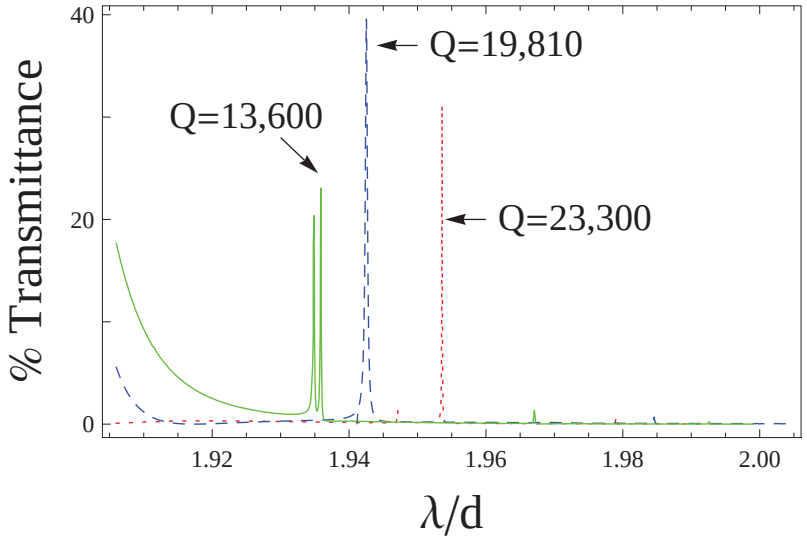

Figure 3.9: Transmittance and Q-factors for a linear waveguide for TM incidence with $r_w = 0.5r$ and $k_y = 0$ fixed and $k_x d/\pi = 0.86$ (red/dotted), 0.92 (blue/dashed) and 1.0 (green/solid). The resonance shifts to shorter wavelengths as k_x increases.

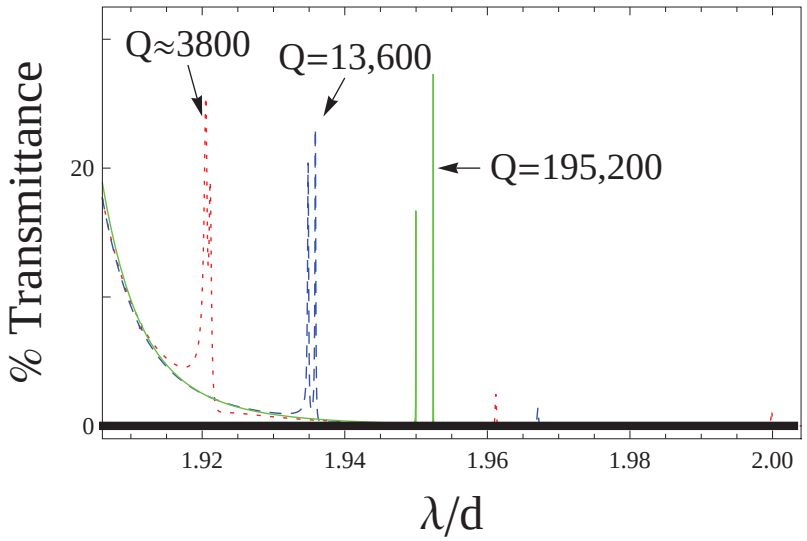

Figure 3.10: Transmittance and Q-factors for a linear waveguide for TM incidence with $k_x d/\pi \sim 1$ and $k_y = 0$ fixed. The defect size is $r_w = 0.0$ (red/dotted), *i.e.*, cylinder completely removed, $r_w = 0.5r$ (blue/dashed), $r_w = 0.8r$ (green/thin) and $r_w = r$, *i.e.*, no defect (black/thick). The resonances shift to longer wavelengths as r_w increases.

to longer wavelengths (as was for the CROW), and also causes the Q-factors to increase rapidly. The increase in the Q-factors is understandable because the resonance is moving closer to the middle of the bandgap, where the field attenuation inside the cladding is strongest. The resonances in Fig. 3.10 are always doublets because there are two nearly-degenerate modes when Bloch vector is close the BZ edge. When $r_w = 0.8r$, the Q-factor is $\sim 200,000$, which might be sufficiently high for low-loss waveguiding over useful distances. However, quantifying the propagation efficiency requires greater resolution in the k_x domain than can be achieved with the super-cell approach.

The fields for the $Q = 13,600$ resonance in Fig. 3.10 are shown in Fig. 3.11. Again, the E_z component was found to exhibit singular behaviour near the contact points of the rods near the defect, thereby giving the fields a *TM*-like character. Interestingly, the central lobe of the longitudinal component of the electric field (E_x) resembles a typical LP_{01} waveguiding mode of a PC fibre. The distribution of the electric field intensity of a representative LP_{01} mode of a hollow-core PC fibre is shown in Fig. 3.12 for comparison (images taken from [107]). (The compressed colour scale used in 3.11(a) exaggerates the intensity of the side lobes of the woodpile mode.) This similarity suggests that the light inside the woodpile waveguide is indeed propagating along the defect rod. The lower symmetry of the woodpile waveguide mode is due to the fact that, for the cross-section shown Fig. 3.11 ($x = 0.25d$), the woodpile waveguide only has two-fold rotational symmetry,

whereas the PC fibre mode has six-fold rotational symmetry in the plane transverse to the axis of the fibre. In addition, the normalised volumes of the two modes are comparable – they are both about five periods in diameter.

3.4 Discussion

In this chapter, a super-cell method for modelling woodpile defect structures was presented, and the existence of defect modes in a CROW and a linear waveguide embedded in a woodpile cladding was inferred from the corresponding transmission spectra. It was also found that the waveguides discriminate strongly between the polarisation states of the excitation field. Changing the size of the defect rod proved to be an effective way of controlling the Q-factors of both of the waveguides that we considered here. Furthermore, the linear waveguide supports waveguide modes that might be suitable for low-loss waveguiding over useful distances. We found that the woodpile required $\sim$28 layers in order for it to exhibit strong, omnidirectional field attenuation for the frequencies inside the bandgap. This observation is similar to that made by Imada et al. [18], who estimated for a GaAs woodpile ($n \approx 3.38$) that about 25 layers are needed to achieve lossless waveguiding over a length of 500 μm. However, locating the transmission resonances for these stack sizes is particularly difficult because the Q-factors increase exponentially with increasing stack size [18].

The results for the linear waveguide were obtained using a super-cell of length $D = 11$. This imposes a lower bound of $p_{\max} \approx 11$ on the number of plane wave orders to be retained, since the number of propagating orders is approximately equal to D. The results that were presented were for $p_{\max} = 15$, which was the upper bound imposed by the amount of computational memory and power that was available when the study was performed. Table 3.1 shows how the normalized frequency d/λ of the transmission resonance for $r_w = 0.5r$, with $k_x = 0.86\pi/d$ (as shown by the dotted/red curve in Fig. 3.9) varies as $p_{\max}$ is increased from 12 to 15, and suggests that the frequency estimate is converged to about two decimal places. Considerations on the size of the super-cell will be deferred until the next chapter, wherein an approach for computing the waveguide modes directly is described. That approach complements the methods explained in this chapter, and will be used to demonstrate that a super-cell of 11 cylinders adequately isolates the defect from the fields of neighbouring cells.

The principal difficulty with the super-cell approach is that the computational demands grow quickly with increasing size of the super-cell. While the plane wave and multipole

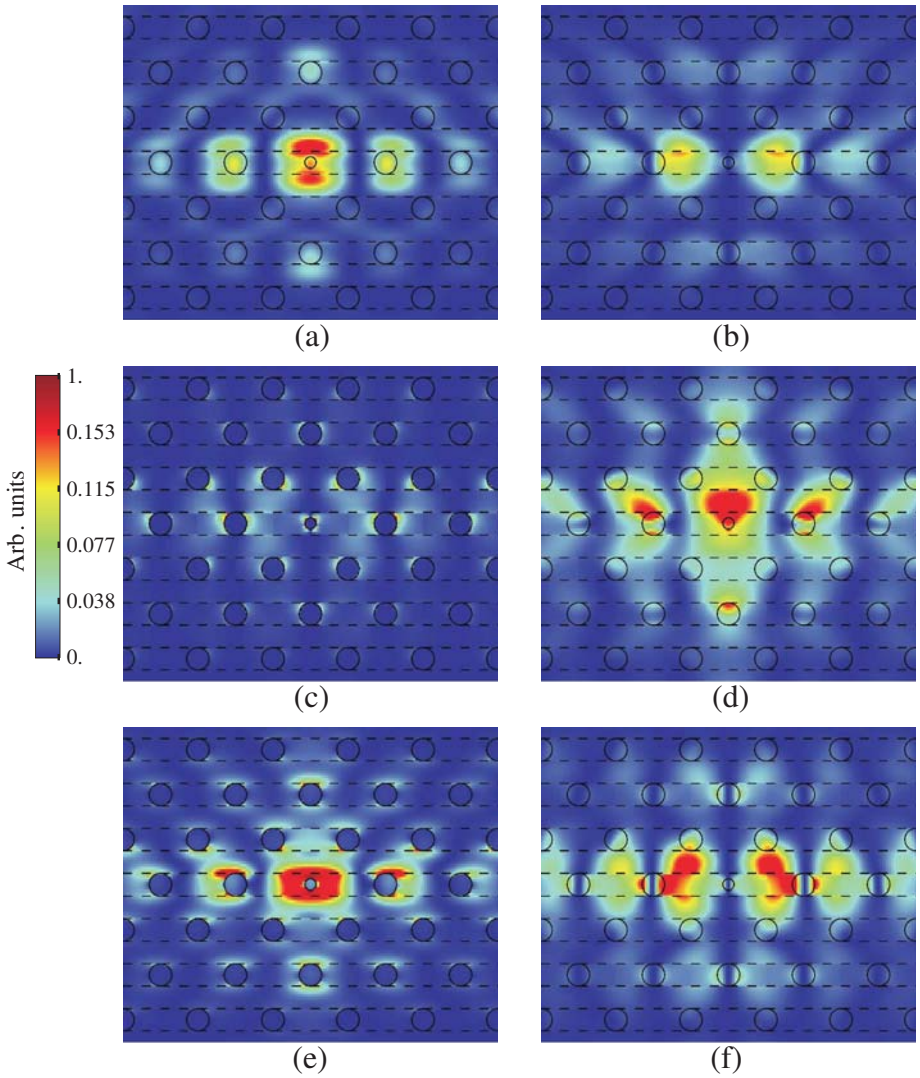

Figure 3.11: Componentwise field intensity in the vicinity of the linear waveguide: (a) $|E_x|^2$, (c) $|E_y|^2$, (e) $|E_z|^2$, (b) $|H_x|^2$, (d) $|H_y|^2$ and (f) $|H_z|^2$. The view looks down the defect rod (smaller circle), which has a radius of $r_w = 0.5r$. The parameters of the incident field are $k_x\pi/d \sim 1$, $k_y = 0$ and $\lambda/d = 1.936$, which correspond to the $Q = 13,600$ resonance indicated in Fig. 3.10.

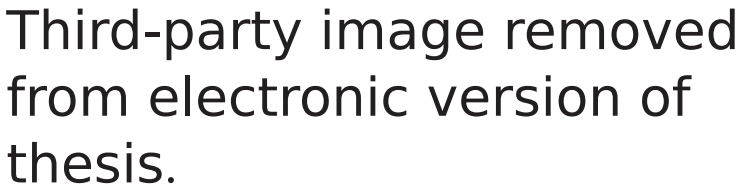

Figure 3.12: (a) Micrograph of a hollow-core photonic crystal fibre and (b) the electric field intensity of the LP_{01} mode of the fibre. Images taken from [107].

Table 3.1: *Frequency estimates of the resonance of the linear waveguide as the planewave truncation parameter $p_{\max}$ is increased. The frequencies were determined using a super-cell containing $N_c = 11$ cylinders, with $k_x = 0.86\pi/d$ and $r_w = 0.5r$ fixed.*

$p_{\max}$	d/λ
12	0.512104
13	0.512033
14	0.511968
15	0.511876

field expansions are expressed in terms of infinite series [see Eqs. (2.26) and (2.27) and Eq. (3.2)], these series must be truncated in any implementation. The natural way to do this is to discard the higher-order terms, so that if $s = (p, q)$ is an arbitrary woodpile diffraction order, then one imposes the condition $-p_{\max} \leq p, q \leq p_{\max}$, for some choice of $p_{\max}$. Similarly, only the multipole orders $-n_{\max} \leq n \leq n_{\max}$ are retained, for some $n_{\max}$. (Consequently, the matrices appearing in the above discourse are all finite.) The justification for this choice is that the higher orders correspond to higher frequency components of the respective Fourier expansions and are, thus, less significant. It follows that the degree of convergence of the numerical fields will improve as $p_{\max}$ and $n_{\max}$ are increased. Of these parameters, $n_{\max}$ is of much less significance since the overall running time of the super-cell approach scales only as $O((n_{\max})^3)$, and, moreover, $n_{\max}$ is small because the solution converges rapidly in the multipole basis. In contrast, the method scales as $O((p_{\max})^6)$, and this is problematic because the solution converges relatively slowly in the planewave basis ($p_{\max} > n_{\max}$). This is particularly evident for woodpiles because adjacent layers of the stack are touching, resulting in strong evanescent coupling between the layers. In 2D PCs, the scatterers are spaced relatively far apart, and so $p_{\max}$ is comparable to the number of propagating orders, which carry most of the energy of the optical field. For a woodpile, $p_{\max}$ must be large enough so as to include not only the propagating orders but also a considerable number of the evanescent orders.

3.A Expressions for the Boundary Condition Matrix

The matrix $\boldsymbol{\mathcal{M}}$ encapsulating the boundary conditions [see Eq. (3.16)] is a 2 by 2 block matrix and we use superscripts E and H to label the blocks so that

$$\boldsymbol{\mathcal{M}} = \begin{bmatrix} \mathbf{M}^{EE} & \mathbf{M}^{EH} \\ \mathbf{M}^{HE} & \mathbf{M}^{HH} \end{bmatrix}. \tag{3.30}$$

Each block is diagonal with N_c partitions, where N_c is the number of cylinders in the grating unit cell. We use integers l to index the cylinders, and n to index the elements of the partition. In addition, the label 'II' denotes quantities that depend on the material properties of cylinder l while 'I' denotes quantities that depend on the properties of the background region. If the radius of cylinder l is a_l, then the entries on the diagonal of

each block are

$$\mathsf{M}^{EE}_{l,n} = \frac{\eta_2(\mathrm{I})\,\eta_3(\mathrm{I})\,H_n(k_{\perp\mathrm{I}}r_l)\,J_n(k_{\perp\mathrm{I}}r_l)}{\Delta} \times \left\{ \frac{\left[\eta_1(\mathrm{I}) - \eta_1(\mathrm{II})\right]^2}{\eta_2(\mathrm{I})\,\eta_3(\mathrm{I})} - J_2 H_3 \right\}, \tag{3.31}$$

$$\mathsf{M}^{HH}_{l,n} = \frac{\eta_2(\mathrm{I})\,\eta_3(\mathrm{I})\,H_n(k_{\perp\mathrm{I}}r_l)\,J_n(k_{\perp\mathrm{I}}r_l)}{\Delta} \times \left\{ \frac{\left[\eta_1(\mathrm{I}) - \eta_1(\mathrm{II})\right]^2}{\eta_2(\mathrm{I})\,\eta_3(\mathrm{I})} - J_3 H_2 \right\}, \tag{3.32}$$

$$\mathsf{M}^{EH}_{l,n} = \frac{\left[\eta_1(\mathrm{I}) - \eta_1(\mathrm{II})\right]\eta_2(\mathrm{I})\,\eta_3(\mathrm{I})}{\Delta} \times \frac{2k\mu_{\mathrm{I}}}{\pi k^2_{\perp\mathrm{I}} r_l}, \tag{3.33}$$

$$\mathsf{M}^{HE}_{l,n} = -\left(\varepsilon_{\mathrm{I}}/\mu_{\mathrm{I}}\right)\mathsf{M}^{EH}_{l,n}, \tag{3.34}$$

with $k^2_{\perp i} = k^2\varepsilon_i\mu_i - \alpha_p^2$, $\eta_1(j) = -\alpha_p n/\left[(k_{\perp j})^2 r_l\right]$, $\eta_2(j) = -ik\mu_j/k_{\perp j}$, $\eta_3(j) = ik\varepsilon_j/k_{\perp j}$,

$$\Delta = J_n(k_{\perp\mathrm{I}}r_l)^2\,\eta_2(\mathrm{I})\,\eta_3(\mathrm{I}) \times \left\{ \frac{\left[\eta_1(\mathrm{I}) - \eta_1(\mathrm{II})\right]^2}{\eta_2(\mathrm{I})\,\eta_3(\mathrm{I})} - J_2 J_3 \right\}, \tag{3.35}$$

$$J_j = \frac{J'_n(k_{\perp\mathrm{I}}r_l)}{J_n(k_{\perp\mathrm{I}}r_l)} - \frac{\eta_j(\mathrm{II})\,J'_n(k_{\perp\mathrm{II}}r_l)}{\eta_j(\mathrm{I})\,J_n(k_{\perp\mathrm{II}}r_l)}$$

and

$$H_j = \frac{H'_n(k_{\perp\mathrm{I}}r_l)}{H_n(k_{\perp\mathrm{I}}r_l)} - \frac{\eta_j(\mathrm{II})\,J'_n(k_{\perp\mathrm{II}}r_l)}{\eta_j(\mathrm{II})\,J_n(k_{\perp\mathrm{II}}r_l)}.$$

3.B Elaboration of the Rayleigh Identity and Scattering Matrix Expressions

The symmetrised versions of the multipole transformation matrices [see Eq. (3.24)] are

$$\boldsymbol{\mathcal{J}}^{s/a} = \mathrm{diag}\left[\begin{array}{cc} \boldsymbol{\mathcal{J}}^- \pm \boldsymbol{\mathcal{J}}^+ & \boldsymbol{\mathcal{J}}^- \mp \boldsymbol{\mathcal{J}}^+ \end{array}\right] \tag{3.36}$$

and

$$\boldsymbol{\mathcal{K}}^{s/a} = \mathrm{diag}\left[\begin{array}{cc} \boldsymbol{\mathcal{K}}^- \pm \boldsymbol{\mathcal{K}}^+ & \boldsymbol{\mathcal{K}}^- \mp \boldsymbol{\mathcal{K}}^+ \end{array}\right]. \tag{3.37}$$

As was discussed in Section 3.2.2, the above matrices appear as folded quantities in the final expressions for the scattering matrices [Eqs. (3.26) and (3.27)]. Specifically,

$$\widetilde{\mathcal{L}}^{s/a} = \begin{bmatrix} \widetilde{\mathbf{M}}^{EE} + \widetilde{\mathbf{S}}^{s/a}\boldsymbol{\epsilon}^{s/a} & \widetilde{\mathbf{M}}^{EH} \\ \widetilde{\mathbf{M}}^{HE} & \widetilde{\mathbf{M}}^{HH} + \widetilde{\mathbf{S}}^{a/s}\boldsymbol{\epsilon}^{a/s} \end{bmatrix}^{-1}, \tag{3.38}$$

$\widetilde{\mathbf{S}}^{s/a} = \left[\widetilde{\mathbf{S}}^{lj,s/a}\right]$, $\widetilde{\mathbf{S}}^{lj,s/a} = \left[S^{lj}_{n-m} \pm (-1)^m S^{lj}_{n+m}\right]$, $\boldsymbol{\epsilon}^s = \mathrm{diag}\left[\mathrm{diag}\left[\begin{array}{cc} \boldsymbol{\epsilon}, & \mathbf{I} \end{array}\right]\right]$, $\boldsymbol{\epsilon}^a = \mathrm{diag}\left[\mathrm{diag}\left[\begin{array}{cc} \mathbf{I}, & \boldsymbol{\epsilon} \end{array}\right]\right]$, $\boldsymbol{\epsilon} = \mathrm{diag}\left[\epsilon_m\right]$,

$$\epsilon_m = \begin{cases} 1/2, \text{ for } m = 0\,, \\ 1, \text{ for } m > 0 \end{cases}$$

and $\mathbf{M}^{EE/HH}$ are the blocks of $\mathcal{M}$. See also Appendix B of [25].

Chapter 4

The Fictitious Source Superposition Method

4.1 Introduction

In this chapter we describe how the *fictitious source superposition* (FSS) method can be applied to the problem of modelling a cylindrical defect contained in a woodpile cladding (such a structure is illustrated schematically in Fig. 3.1). While the super-cell method described in the previous chapter proved to be an efficient way of modelling the coupled resonator optical waveguide, generating the dispersion curves for the linear waveguide remained difficult because of the narrow linewidth of the spectral features. Further, the method required a moderately large super-cell in the grating direction, and this partly offset the benefits of expressing the electromagnetic field identities in a natural basis for the problem. Indeed, as was mentioned in Sec. 1.4, the pre-existing methods for modelling rod defects in woodpiles all necessitate a super-cell [24, 37], whereby periodic boundary conditions are imposed at an arbitrary distance from the defect. The super-cell is used to artificially reduce the modelled domain to a size that can be computed within a reasonable time. Regardless of which method is used, increasing the size of the super-cell, thereby making the structure more similar to the physical structure being modeled, leads to rapidly increasing demands on computing time and memory.

In earlier work, 2D FSS methods, which do not rely on a super-cell, were used to compute modes that were highly extended, such as happens when near cutoff [27, 108]. Here, those techniques are generalised in order to avoid the computational overhead associated with a super-cell. The FSS method entails placing sources inside each cylinder of the waveguide layer, and then taking an appropriate superposition of fields to mimic a finite

number of defects in an infinite array of cylinders. This can be done efficiently because the multipole formulation lets one manipulate the outgoing fields directly; however, the FSS method forgoes the ability to deal with a finite number of layers. In the context of woodpiles, this is a new method capable of producing accurate results when the fields of the defect mode extend great distances into the 3D structure. The substantial performance gains realised by the FSS method mean that it is possible to obtain well-resolved dispersion curves for the linear waveguide, and also allow us to optimise the geometry for use as a slow-light waveguide. This regime occurs when the group velocity, $\mathbf{v}_g \stackrel{\text{def}}{=} \nabla_{\mathbf{k}}\omega(\mathbf{k})$, is small along the waveguiding direction, *i.e.*, when $v_x = \partial\omega/\partial k_x \ll c$, where x is the direction parallel to the linear waveguide, ω is the angular frequency, $\mathbf{k}$ is the Bloch vector, and c is the speed of light in a vacuum.

In Section 4.2 it is shown how the FSS formulation of [27, 108], originally developed for 2D grating arrays, can be generalised to model linear defects in 3D woodpiles; the principal difference being that there is now a set of grating diffraction orders associated with the x direction in addition to the usual ones associated with the y direction (see [109] for a list of references to early work on the use of fictitious sources in the study of 2D systems of diffracting rods). For this chapter, the nomenclature introduced in Chapter 3 is slightly modified to accommodate the extensions to the theory (where appropriate, the correspondences with the equations of Chapter 3 are noted). The measures that were taken to validate our code are outlined in Section 4.3, along with implementation notes. Results are presented for a chalcogenide woodpile waveguide, where the radius and refractive index of the defect rod were allowed to vary in turn, see Section 4.4.

4.2 Theory

4.2.1 Overview

The theory in this section is organised as follows. In Section 4.2.2, multipole expressions for the fields produced by a single grating are given, where a fictitious source is now placed inside each cylinder of the grating. Using the fictitious sources to manipulate the outgoing fields of each cylinder independently from those of the other cylinders in the grating is impractical if not impossible. Instead, the array of sources is chosen so that it quasi-periodic. Hence, all of the multipole expressions for the fields produced by the grating remain the same as those in the previous chapter, except possibly for the appearance of an additional term representing the contribution of the fictitious sources to

the fields. In particular, it will become apparent that the presence of fictitious sources does not affect the expressions for the grating reflection and transmission matrices $\boldsymbol{\mathcal{R}}$ and $\boldsymbol{\mathcal{T}}$.

Section 4.2.3 describes how the expressions derived in Sec. 4.2.2 can be used to simulate a linear waveguide. This entails expressing the fictitious source coefficients as the solutions of a homogeneous system of equations. Integrating the fields with respect to the quasi-periodic phase causes all but one fictitious source vanish. (The idea of integrating over the Brillouin zone in order to compute the defect modes of PCs is also employed in the resolvent approach [110].) The remaining source can then be used to mimic a cylinder that has a different radius and refractive index from the host cylinder. The field integration step amounts to taking an average of the multipole field coefficients and, consequently, the homogeneous system for the superposed problem is related trivially to the original homogeneous systems. The FSS method can also be used mimic compound defects comprising multiple defect rods; however, such structures are not discussed in this thesis (see [108] for the derivation of the FSS method for compound defects in 2D grating arrays).

4.2.2 FSS Grating Field Identities

We begin by considering a single grating whose rods are parallel to the x axis, with the y axis corresponding to the direction of the grating. Unlike the super-cell approach, the refractive indices and radii of the cylinders of the grating must uniform. In order to discriminate between different unit-cells, an integer j is used to index the cylinders in order of increasing horizontal displacement, with $j = 0$ denoting the central cylinder of the layer, see Fig. 4.1. The multipole expansion for the longitudinal components E_x and H_x of the fields at a point $\boldsymbol{\rho} = (\rho, \theta)$ exterior to cylinder j is then

$$V(\boldsymbol{\rho}) = \sum_{n=-\infty}^{\infty} \left[A_n^{j,V} J_n(k_{e\perp}\rho) + B_n^{j,V} H_n(k_{e\perp}\rho) \right] e^{in\theta} \tag{4.1}$$

with $V = E_x$ and $V = H_x$ in turn, where $k_{e\perp} = \sqrt{(kn_b)^2 - \alpha_p^2}$ is the transverse wavenumber of the exterior fields [*cf.* Eq. (2.38)], and where there is an assumed x dependence of $\exp(i\alpha_p x)$. Note that the periodicty of the grating means that the multipole coefficients $A_n^{j,V}$ and $B_n^{j,V}$ must be quasiperiodic, *i.e.*, $A_n^{j,V} = A_n^{0,V}\exp(i\beta_0 jd)$ and $B_n^{j,V} = B_n^{0,V}\exp(i\beta_0 jd)$. Equation (4.1) holds whether or not fictitious sources are

present. When there are no fictitious sources, the fields inside cylinder j are simply

$$V(\boldsymbol{\rho}) = \sum_{n=-\infty}^{\infty} C_n^{j,V} J_n(k_{i\perp}\rho)\, e^{in\theta}, \tag{4.2}$$

where $k_{i\perp} = \sqrt{(kn_c)^2 - \alpha_p^2}$ is the transverse wavenumber of the interior fields, and $C_n^{j,V} = C_n^{0,V}\exp(i\beta_0 jd)$.

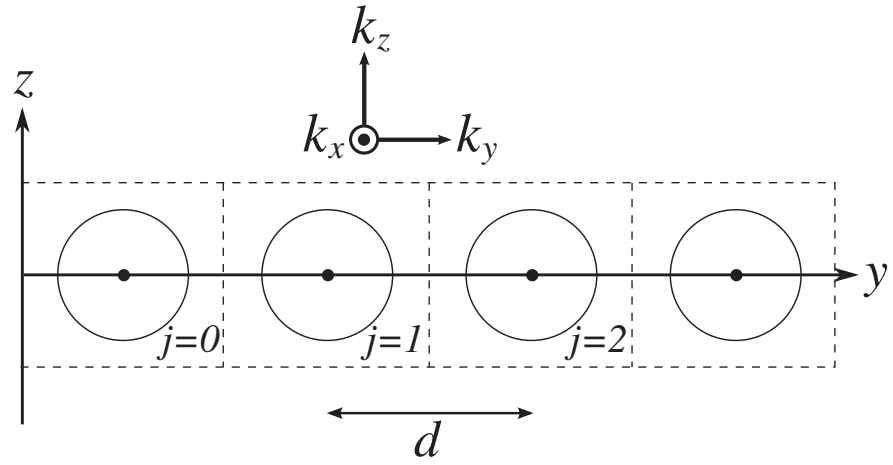

Figure 4.1: Successive unit-cells of a grating whose cylinders are parallel to the x-axis, with j indexing the cylinders in order of increasing displacement along the y-axis.

Before describing the modifications to the multipole theory, we recap the main steps of the derivation of the scattering matrices $\boldsymbol{\mathcal{R}}$ and $\boldsymbol{\mathcal{T}}$. For the moment we assume that $j = 0$. As in Chapter 3, the Rayleigh identity relates the incoming fields ($A_n^{0,V}$) to the outgoing fields ($B_n^{0,V}$) according to

$$\boldsymbol{\mathcal{A}} = \boldsymbol{\mathcal{S}}\boldsymbol{\mathcal{B}} + \boldsymbol{\mathcal{J}}^{-}\mathbf{ZX}^{-}\boldsymbol{\mathcal{F}}_I^{-} + \boldsymbol{\mathcal{J}}^{+}\mathbf{ZX}^{+}\boldsymbol{\mathcal{F}}_I^{+}. \tag{4.3}$$

[cf. Eq. (3.13)], where $\boldsymbol{\mathcal{J}}^{\pm}\mathbf{ZX}^{\pm}$ converts the incoming planewave orders $\boldsymbol{\mathcal{F}}_I^{\pm}$ into multipoles. The definitions of the terms in Eq. (4.3) that appear in calligraphic font can be found in Sec. 3.2.1. In this chapter, all planewave fields are expressed in terms of *TE* and *TM* components, hence the incoming plane waves must first be expressed in Cartesian coordinates. This is achieved by the terms $\mathbf{ZX}^{\pm}$ [refer to the discussion near Eq. (2.28)]. By requiring that the tangential components E_θ, H_θ, E_x and H_x be continuous across the

cylinder boundaries, a second equation relating $\boldsymbol{\mathcal{A}}$ to $\boldsymbol{\mathcal{B}}$ is obtained:

$$\boldsymbol{\mathcal{A}} = -\boldsymbol{\mathcal{M}}\boldsymbol{\mathcal{B}}, \tag{4.4}$$

[cf. Eq. (3.16)] where $\boldsymbol{\mathcal{M}}$ completely encapsulates the material properties of the cylinders, *i.e.*, the refractive index and radius. Expressions for $\boldsymbol{\mathcal{M}}$ are given in Appendix 3.A. Equations (4.3) and (4.4) allow $\boldsymbol{\mathcal{B}}$ to be expressed purely in terms of the incoming fields:

$$\boldsymbol{\mathcal{B}} = -\boldsymbol{\mathcal{L}}\boldsymbol{\mathcal{J}}^{-}\mathbf{ZX}^{-}\boldsymbol{\mathcal{F}}_I^{-} - \boldsymbol{\mathcal{L}}\boldsymbol{\mathcal{J}}^{+}\mathbf{ZX}^{+}\boldsymbol{\mathcal{F}}_I^{+}, \tag{4.5}$$

where $\boldsymbol{\mathcal{L}} = (\boldsymbol{\mathcal{M}} + \boldsymbol{\mathcal{S}})^{-1}$ is the multipole scattering operator.

The diffracted planewave fields $\boldsymbol{\mathcal{F}}_D^{\pm}$ produced by the grating are then expressed in terms of the incoming planewave orders and the outgoing multipole fields:

$$\boldsymbol{\mathcal{F}}_D^{-} = \boldsymbol{\mathcal{F}}_I^{-} + (2/d)\boldsymbol{\mathcal{G}}(\mathbf{ZX}^{-})^{-1}\boldsymbol{\mathcal{K}}^{-}\boldsymbol{\mathcal{B}} \tag{4.6}$$

and

$$\boldsymbol{\mathcal{F}}_D^{+} = \boldsymbol{\mathcal{F}}_I^{+} + (2/d)\boldsymbol{\mathcal{G}}(\mathbf{ZX}^{+})^{-1}\boldsymbol{\mathcal{K}}^{+}\boldsymbol{\mathcal{B}}, \tag{4.7}$$

[*cf.* Eq. (3.18)] where $(\mathbf{ZX}^{\pm})^{-1}\boldsymbol{\mathcal{K}}^{\pm}$ converts the multipole fields back into planewaves, and $\boldsymbol{\mathcal{G}}$ is the normalisation factor. Substituting the multipole fields of Eq. (4.5) into the two equations above yields following the relationships between the incoming and diffracted fields incident on the grating:

$$\boldsymbol{\mathcal{F}}_D^{-} = \boldsymbol{\mathcal{T}}_{a,p}\boldsymbol{\mathcal{F}}_I^{-} + \boldsymbol{\mathcal{R}}_{b,p}\boldsymbol{\mathcal{F}}_I^{+} \tag{4.8}$$

and

$$\boldsymbol{\mathcal{F}}_D^{+} = \boldsymbol{\mathcal{R}}_{a,p}\boldsymbol{\mathcal{F}}_I^{-} + \boldsymbol{\mathcal{T}}_{b,p}\boldsymbol{\mathcal{F}}_I^{+}, \tag{4.9}$$

where $\boldsymbol{\mathcal{R}}_p$ and $\boldsymbol{\mathcal{T}}_p$ are the usual reflection and transmission matrices associated with the fields incoming from above (subscript a) and below (subscript b) the grating [*cf.* Eqs. (3.26) and (3.27)]. The subscript p is used here to emphasise the fact that the expressions apply to the p^{th} diffraction order associated with the x direction.

When fictitious sources are placed inside each cylinder, the fields inside cylinder j are instead

$$V(\boldsymbol{\rho}) = \sum_{n=-\infty}^{\infty} \left[C_n^{j,V} J_n(k_{i\perp}\rho) + Q_n^{j,V} H_n(k_{i\perp}\rho)\right] e^{in\theta}, \tag{4.10}$$

[cf. Eq. (4.2)], where $Q_n^{j,V}$ are the fictitious source coefficients, and represent a line

source that coincides with the axis of the cylinder. Further, the sources are chosen so that they are quasi-periodic, *i.e.*, $Q_n^{j,V} = Q_n^{0,V}\exp(i\beta_0 jd)$. This ensures that the exterior fields retain their quasi-periodicity, and, hence, the presence of the fictitious sources does not affect the form of the Rayleigh identity [Eq. (4.3)]. Equation (4.4) and, thus, Eq. (4.5) gain an additional term involving the fictitious sources

$$\boldsymbol{\mathcal{Q}} = \begin{bmatrix} [Q_n^{0,E}] \\ [Q_n^{0,H}] \end{bmatrix} \tag{4.11}$$

so that instead

$$\boldsymbol{\mathcal{A}} = -(\boldsymbol{\mathcal{M}}\boldsymbol{\mathcal{B}} + \boldsymbol{\mathcal{N}}\boldsymbol{\mathcal{Q}}) \tag{4.12}$$

and

$$\boldsymbol{\mathcal{B}} = \boldsymbol{\mathcal{Y}}^{-}\boldsymbol{\mathcal{F}}_I^{-} + \boldsymbol{\mathcal{Y}}^{+}\boldsymbol{\mathcal{F}}_I^{+} + \boldsymbol{\mathcal{Y}}^{\text{fs}}\boldsymbol{\mathcal{Q}}, \tag{4.13}$$

where, for convenience, we define

$$\boldsymbol{\mathcal{Y}}^{\text{fs}} = -\boldsymbol{\mathcal{L}}\boldsymbol{\mathcal{N}} \tag{4.14}$$

and

$$\boldsymbol{\mathcal{Y}}^{\pm} = -\boldsymbol{\mathcal{L}}\boldsymbol{\mathcal{J}}^{\pm}\mathbf{ZX}^{\pm}. \tag{4.15}$$

Expressions for $\boldsymbol{\mathcal{N}}$ are given in Appendix 4.A. Equations (4.6) and (4.7) remain valid, with $\boldsymbol{\mathcal{B}}$ now given by Eq. (4.13). Thus, Eqs. (4.8) and (4.9) can be generalised to

$$\boldsymbol{\mathcal{F}}_D^{-} = \boldsymbol{\mathcal{T}}_{a,p}\boldsymbol{\mathcal{F}}_I^{-} + \boldsymbol{\mathcal{R}}_{b,p}\boldsymbol{\mathcal{F}}_I^{+} + \boldsymbol{\mathcal{Q}}_p^{-}\boldsymbol{\mathcal{Q}} \tag{4.16}$$

and

$$\boldsymbol{\mathcal{F}}_D^{+} = \boldsymbol{\mathcal{R}}_{a,p}\boldsymbol{\mathcal{F}}_I^{-} + \boldsymbol{\mathcal{T}}_{b,p}\boldsymbol{\mathcal{F}}_I^{+} + \boldsymbol{\mathcal{Q}}_p^{+}\boldsymbol{\mathcal{Q}}, \tag{4.17}$$

with

$$\boldsymbol{\mathcal{Q}}_p^{\pm} = -(2/d)(\mathbf{ZX}^{\pm})^{-1}\boldsymbol{\mathcal{K}}^{\pm}\boldsymbol{\mathcal{L}}\boldsymbol{\mathcal{N}} \tag{4.18}$$

for the channel p.

In order to (uniformly) change the material parameters of the cylinders of the grating when there are no fictitious sources, we need only change the boundary condition matrix $\boldsymbol{\mathcal{M}}$ appearing in Eq. (4.4). Hence, if $\hat{\boldsymbol{\mathcal{M}}}$ is the matrix for the new parameters of the cylinders, Eq. (4.4) becomes

$$\boldsymbol{\mathcal{A}} = -\hat{\boldsymbol{\mathcal{M}}}\boldsymbol{\mathcal{B}}. \tag{4.19}$$

Evidently, if we instead wish to use the fictitious sources to mimic these new parameters, then $\boldsymbol{\mathcal{Q}}$ must be chosen in a way so as to satisfy both Eq. (4.12) and Eq. (4.19). This leads to the first of two main relationships between the outgoing fields, *i.e.*, $\boldsymbol{\mathcal{B}}$, and the sources $\boldsymbol{\mathcal{Q}}$:

$$\boldsymbol{\mathcal{B}} = \boldsymbol{\mathcal{H}}\boldsymbol{\mathcal{Q}}, \tag{4.20}$$

where

$$\boldsymbol{\mathcal{H}} = (\hat{\boldsymbol{\mathcal{M}}} - \boldsymbol{\mathcal{M}})^{-1}\boldsymbol{\mathcal{N}}\boldsymbol{\mathcal{Q}}. \tag{4.21}$$

The cylinders can be removed altogether by either choosing the radius so that it is vanishingly small, or by choosing the refractive index of the cylinders to be the same as the background refractive index n_b. Removing a cylinder in this manner is equivalent to setting $\boldsymbol{\mathcal{H}} = \mathbf{0}$ so that, in this case, Eq. (4.20) simply becomes

$$\boldsymbol{\mathcal{B}} = \mathbf{0}. \tag{4.22}$$

Coupling of the fields between adjacent layers of the woodpile occurs via $\boldsymbol{\mathcal{F}}_I^{\pm}$ and $\boldsymbol{\mathcal{F}}_D^{\pm}$, *i.e.*, via Eqs. (4.8) and (4.9), for cladding layers, and Eqs. (4.16) and (4.17), for layers containing fictitious sources (see Fig. 4.2). Further, mixing occurs between different channels, so that the incoming fields $\boldsymbol{\mathcal{F}}_I^{\pm}$ result from scattered fields produced by all other layers, where these scattered fields are radiating in all channels, rather than just in channel p (this is because channel p for x-aligned gratings is physically different from channel p for y-aligned gratings). The field equations for different values of p are thus coupled and must be solved simultaneously. All of the expressions derived so far can be generalised systematically to take this channel mixing into account.

Starting with Eqs. (4.8) and (4.9), it is apparent that analogous relationships must also hold between the total diffracted and incoming fields (*i.e.*, when p is no longer fixed). For example, if we define

$$\boldsymbol{\mathcal{R}}_a = \mathrm{diag}\,[\boldsymbol{\mathcal{R}}_{a,p}], \tag{4.23}$$

with $\boldsymbol{\mathcal{R}}_b$, $\boldsymbol{\mathcal{T}}_a$ and $\boldsymbol{\mathcal{T}}_b$ similarly defined, then the Eqs. (4.8) and (4.9) generalise to

$$\boldsymbol{\mathcal{F}}_D^- = \boldsymbol{\mathcal{T}}_a\boldsymbol{\mathcal{F}}_I^- + \boldsymbol{\mathcal{R}}_b\boldsymbol{\mathcal{F}}_I^+ \tag{4.24}$$

and

$$\boldsymbol{\mathcal{F}}_D^+ = \boldsymbol{\mathcal{R}}_a\boldsymbol{\mathcal{F}}_I^- + \boldsymbol{\mathcal{T}}_b\boldsymbol{\mathcal{F}}_I^+. \tag{4.25}$$

(Once $\boldsymbol{\mathcal{R}}$ and $\boldsymbol{\mathcal{T}}$ have been constructed, $\boldsymbol{\mathcal{R}}_p$ and $\boldsymbol{\mathcal{T}}_p$ can be discarded.) For the global

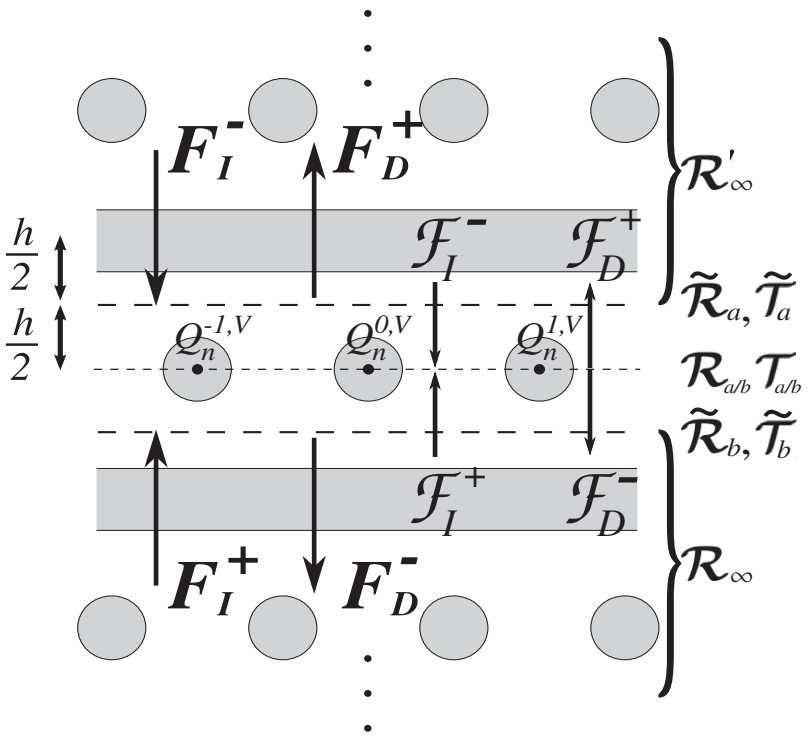

Figure 4.2: The incoming and diffracted fields ($\boldsymbol{\mathcal{F}}_I^{\pm}$ and $\boldsymbol{\mathcal{F}}_D^{\pm}$), as well as the reflection and transmission matrices ($\boldsymbol{\mathcal{R}}_a$, $\boldsymbol{\mathcal{R}}_b$, $\boldsymbol{\mathcal{T}}_a$, $\boldsymbol{\mathcal{T}}_b$) associated with the waveguide layer. Each cylinder of the layer contains a fictitious source ($Q_n^{j,V}$). The phases of $\boldsymbol{\mathcal{F}}_I^{\pm}$ and $\boldsymbol{\mathcal{F}}_D^{\pm}$ must be adjusted in order to give the waveguide layer an artificial thickness h equal to the distance between adjacent layers. The phase-adjusted fields are given by $\boldsymbol{F}_I^{\pm}$ and $\boldsymbol{F}_D^{\pm}$. The scattering matrices for the top (bottom) surfaces of the waveguide are $\widetilde{\boldsymbol{\mathcal{R}}}_a$ and $\widetilde{\boldsymbol{\mathcal{T}}}_a$ ($\widetilde{\boldsymbol{\mathcal{R}}}_b$ and $\widetilde{\boldsymbol{\mathcal{T}}}_b$). The semi-infinite cladding regions below and above the waveguide layer are characterised by the $\boldsymbol{\mathcal{R}}_\infty$ and $\boldsymbol{\mathcal{R}}'_\infty$ reflection matrices.

channel ordering implied by Eq. (4.23), Eqs. (4.16), (4.17), (4.13) and (4.20) generalise to

$$\boldsymbol{\mathcal{F}}_D^- = \boldsymbol{\mathcal{T}}_a \boldsymbol{\mathcal{F}}_I^- + \boldsymbol{\mathcal{R}}_b \boldsymbol{\mathcal{F}}_I^+ + \boldsymbol{\mathcal{Q}}^- \boldsymbol{\mathcal{Q}}, \tag{4.26}$$

$$\boldsymbol{\mathcal{F}}_D^+ = \boldsymbol{\mathcal{R}}_a \boldsymbol{\mathcal{F}}_I^- + \boldsymbol{\mathcal{T}}_b \boldsymbol{\mathcal{F}}_I^+ + \boldsymbol{\mathcal{Q}}^+ \boldsymbol{\mathcal{Q}}, \tag{4.27}$$

$$\boldsymbol{\mathcal{B}} = \boldsymbol{\mathcal{Y}}^- \boldsymbol{\mathcal{F}}_I^- + \boldsymbol{\mathcal{Y}}^+ \boldsymbol{\mathcal{F}}_I^+ + \boldsymbol{\mathcal{Y}}^{\text{fs}} \boldsymbol{\mathcal{Q}}, \tag{4.28}$$

and

$$\boldsymbol{\mathcal{B}} = \boldsymbol{\mathcal{H}} \boldsymbol{\mathcal{Q}}. \tag{4.29}$$

Equations (4.26)-(4.29) appear to be identical to Eqs. (4.16), (4.17), (4.13) and (4.20), however p is no longer fixed, so that

$$\boldsymbol{\mathcal{Q}} = [\boldsymbol{\mathcal{Q}}_p], \tag{4.30}$$

$$\boldsymbol{\mathcal{B}} = [\boldsymbol{\mathcal{B}}_p], \tag{4.31}$$

where the vector $\boldsymbol{\mathcal{Q}}_p$ is given by Eq. (4.11), and $\boldsymbol{\mathcal{B}}_p$ is defined analogously to $\boldsymbol{\mathcal{Q}}_p$. The matrices $\boldsymbol{\mathcal{H}}$ and $\boldsymbol{\mathcal{Y}}^{\text{fs}}$ are simply

$$\boldsymbol{\mathcal{H}} = \text{diag}\left[\boldsymbol{\mathcal{H}}_p\right] \quad \text{and} \quad \boldsymbol{\mathcal{Y}}^{\text{fs}} = \text{diag}\left[\boldsymbol{\mathcal{Y}}_p^{\text{fs}}\right], \tag{4.32}$$

with $\boldsymbol{\mathcal{H}}_p$ and $\boldsymbol{\mathcal{Y}}_p^{\text{fs}}$ given by Eqs. (4.21) and (4.14), respectively. Similarly, for layers whose rods are parallel to the x axis, the matrices $\boldsymbol{\mathcal{Q}}^{\pm}$ and $\boldsymbol{\mathcal{Y}}^{\pm}$ are constructed as:

$$\boldsymbol{\mathcal{Q}}^{\pm} = \text{diag}\left[\boldsymbol{\mathcal{Q}}_p^{\pm}\right], \quad \text{and} \quad \boldsymbol{\mathcal{Y}}^{\pm} = \text{diag}\left[\boldsymbol{\mathcal{Y}}_p^{\pm}\right], \tag{4.33}$$

with $\boldsymbol{\mathcal{Q}}_p^{\pm}$ and $\boldsymbol{\mathcal{Y}}_p^{\pm}$ given by Eqs. (4.18) and (4.15), respectively.

For layers whose rods are parallel to the y-axis, Eqs. (4.24)-(4.29) are constructed using a rotated coordinate system [refer to the discussion regarding Eq. (3.28)] in which the woodpile order $s = (p, q)$ corresponds to the order $s = (-q, p)$ in the unrotated system. Since the matrices $\boldsymbol{\mathcal{Q}}^{\pm}$ convert multipole fields to plane wave orders, the rows of $\boldsymbol{\mathcal{Q}}^{\pm}$ (for y-aligned gratings) must be permuted so that the row order is consistent with the global order implied by Eq. (4.23). Similarly, the matrices $\boldsymbol{\mathcal{Y}}_p^{\pm}$ convert plane waves into multipoles, and so the columns of $\boldsymbol{\mathcal{Y}}_p^{\pm}$ must be permuted accordingly.

Equations (4.26)-(4.29) are the main results of this section, and they generalise the corresponding FSS expressions for 2D grating stacks reported in Section 2.D of [27]. These relationships, along with Eqs. (4.24) and (4.25) allow one to find the incoming

fields (now the modes of an infinite structure) in Eq. (4.28) in terms of $\boldsymbol{\mathcal{Q}}$, establishing a second linear relationship, $\boldsymbol{\mathcal{B}} = \mathbf{Z}\boldsymbol{\mathcal{Q}}$, between $\boldsymbol{\mathcal{B}}$ and $\boldsymbol{\mathcal{Q}}$, and thus determining $\boldsymbol{\mathcal{Q}}$.

4.2.3 Formulation for a Linear Waveguide

The simplest defect that can be modelled using the FSS method is one where the properties of just a single cylinder of the woodpile are changed (as in Fig. 3.1). Fictitious sources are first placed in each cylinder of the waveguide layer, using the procedure just described. Thus, initially, the defect is one-dimensional in that the sources modify the entire row of cylinders uniformly to create a defect that is localised only in the z direction. While this means that the woodpile is no longer periodic in this direction, the periodicity in the x and y directions is preserved. Hence, a field expansion in terms of woodpile diffraction orders is still valid, and α_0 and β_0 can be regarded as the k_x and k_y as components of the Bloch vector (see Fig. 4.1). Similarly, the diffraction orders s can be thought of as the Fourier components of the corresponding Bloch mode. The fields of the woodpile are then integrated over one dimension of the Brillouin zone, thereby removing the fictitious sources from all but one of the rods.

Let $k = 2\pi/\lambda$ be the free-space wave number, and let k_x and k_y be fixed. The incoming fields must first be expressed in terms the fictitious sources $\boldsymbol{\mathcal{Q}}$ of Eq. (4.30). A symmetrical padding must first be applied to the waveguide layer, giving the layer an artificial thickness of h equal to the distance between adjacent layers. The phase origin of the fields incident above (below) the grating must, thus, be shifted upwards (downwards) by an amount $h/2$. This is achieved by using the phase adjusted fields

$$\boldsymbol{F}_I^{\pm} = \boldsymbol{\mathcal{P}}^{-1}\boldsymbol{\mathcal{F}}_I^{\pm} \quad \text{and} \quad \boldsymbol{F}_D^{\pm} = \boldsymbol{\mathcal{P}}\boldsymbol{\mathcal{F}}_D^{\pm} \tag{4.34}$$

in Eqs. (4.26) and (4.27), with $\boldsymbol{\mathcal{P}}$ as defined in Eq. (2.46). These phase-adjusted fields satisfy relationships analogous to Eqs. (4.26) and (4.27). Specifically, it follows immediately from Eqs. (4.26), (4.27) and (4.34) that

$$\boldsymbol{F}_D^{-} = \widetilde{\boldsymbol{\mathcal{T}}}_a\boldsymbol{F}_I^{-} + \widetilde{\boldsymbol{\mathcal{R}}}_b\boldsymbol{F}_I^{+} + \boldsymbol{\mathcal{P}}\boldsymbol{\mathcal{Q}}^{-}\boldsymbol{\mathcal{Q}}, \tag{4.35}$$

and

$$\boldsymbol{F}_D^{+} = \widetilde{\boldsymbol{\mathcal{R}}}_a\boldsymbol{F}_I^{-} + \widetilde{\boldsymbol{\mathcal{T}}}_b\boldsymbol{F}_I^{+} + \boldsymbol{\mathcal{P}}\boldsymbol{\mathcal{Q}}^{+}\boldsymbol{\mathcal{Q}}, \tag{4.36}$$

where $\widetilde{\boldsymbol{\mathcal{R}}}_{a/b} = \boldsymbol{\mathcal{P}}\boldsymbol{\mathcal{R}}_{a/b}\boldsymbol{\mathcal{P}}$ and $\widetilde{\boldsymbol{\mathcal{T}}}_{a/b} = \boldsymbol{\mathcal{P}}\boldsymbol{\mathcal{T}}_{a/b}\boldsymbol{\mathcal{P}}$ are the corresponding reflection and transmission matrices. The phase origins of the fields $\boldsymbol{\mathcal{F}}_{I/D}^{\pm}$ and $\boldsymbol{F}_{I/D}^{\pm}$ are depicted in Fig.

(4.2), along with the scattering matrices associated with each surface of the waveguide layer. Note that for up-down symmetric layers, $\boldsymbol{\mathcal{R}}_a = \boldsymbol{\mathcal{R}}_b$ and $\widetilde{\boldsymbol{\mathcal{R}}}_a = \widetilde{\boldsymbol{\mathcal{R}}}_b$ (and similarly for the transmission matrices).

The reflection from the cladding is characterised by the $\boldsymbol{\mathcal{R}}_\infty$ reflection matrx, which is found from a Bloch mode analysis of the bulk woodpile. The derivation of $\boldsymbol{\mathcal{R}}_\infty$ is performed in Secs. 5.2 and 5.3 of the next chapter [specifically, see Eq. (5.9)]. In order for there to be a complete bandgap, consecutive pairs of gratings must be interleaved (the stacking unit comprises four layers rather than two). Consequently, the reflection matrix $\boldsymbol{\mathcal{R}}_\infty$ for the cladding below the waveguide layer is different from the reflection matrix $\boldsymbol{\mathcal{R}}'_\infty$ for the cladding above the layer. The fields reflected back by the cladding are simply

$$\boldsymbol{F}_I^+ = \boldsymbol{\mathcal{R}}_\infty \boldsymbol{F}_D^- \quad \text{and} \quad \boldsymbol{F}_I^- = \boldsymbol{\mathcal{R}}'_\infty \boldsymbol{F}_D^+. \tag{4.37}$$

Equations (4.35)-(4.37) are then solved for the incoming fields, which are found to be

$$\boldsymbol{F}_I^\pm = \mathbf{D}^\pm \boldsymbol{\mathcal{Q}}, \tag{4.38}$$

where

$$\mathbf{D}^\pm = (\mathbf{I} - \mathbf{G}^\mp \widetilde{\boldsymbol{\mathcal{T}}} \mathbf{G}^\pm)^{-1} (\mathbf{G}^\mp \widetilde{\boldsymbol{\mathcal{T}}} \mathbf{G}^\pm \boldsymbol{\mathcal{Q}}^\pm + \mathbf{G}^\mp \boldsymbol{\mathcal{Q}}^\mp), \tag{4.39}$$

$\mathbf{G}^- = (\mathbf{I} - \boldsymbol{\mathcal{R}}_\infty \widetilde{\boldsymbol{\mathcal{R}}})^{-1} \boldsymbol{\mathcal{R}}_\infty$, $\mathbf{G}^+ = (\mathbf{I} - \boldsymbol{\mathcal{R}}'_\infty \widetilde{\boldsymbol{\mathcal{R}}})^{-1} \boldsymbol{\mathcal{R}}'_\infty$, and where we have made use of the fact that for up-down symmetric gratings $\widetilde{\boldsymbol{\mathcal{R}}}_a = \widetilde{\boldsymbol{\mathcal{R}}}_b \stackrel{\text{def}}{=} \widetilde{\boldsymbol{\mathcal{R}}}$ and $\widetilde{\boldsymbol{\mathcal{T}}}_a = \widetilde{\boldsymbol{\mathcal{T}}}_b \stackrel{\text{def}}{=} \widetilde{\boldsymbol{\mathcal{T}}}$. Equations (4.28), (4.34) and (4.38) allow $\boldsymbol{\mathcal{B}}$ to be expressed in the form

$$\boldsymbol{\mathcal{B}} = \mathbf{Z} \boldsymbol{\mathcal{Q}}, \tag{4.40}$$

with

$$\mathbf{Z} = (\boldsymbol{\mathcal{Y}}^- \boldsymbol{\mathcal{P}} \mathbf{D}^- + \boldsymbol{\mathcal{Y}}^+ \boldsymbol{\mathcal{P}} \mathbf{D}^+ + \boldsymbol{\mathcal{Y}}^{\text{fs}}) \boldsymbol{\mathcal{Q}}. \tag{4.41}$$

Equations (4.29) and (4.40) completely determine the fictitious source coefficients, which are the solutions of

$$(\mathbf{Z} - \boldsymbol{\mathcal{H}})\, \boldsymbol{\mathcal{Q}} = \mathbf{0}. \tag{4.42}$$

Suppose that the cylinders of the waveguide layer are aligned parallel to the x-axis, hence k_x and k_y are the components of the Bloch vector that are associated with the direction parallel to the cylinders of the layer and with the grating direction, respectively, as in Fig. 4.1 (*i.e.*, $k_x \equiv \alpha_0$ and $k_y \equiv \beta_0$). When an average of the fields of the entire woodpile is taken with respect to k_y, where k_y lies in the first Brillouin zone, the FSS multipole

field expansions for the waveguide layer [Eqs. (4.1) and (4.10)] remain valid (as $k_{e\perp}$ and $k_{i\perp}$ do not depend on β_0), except with the averaged coefficients $\langle A_n^{j,V}\rangle$, $\langle B_n^{j,V}\rangle$, $\langle C_n^{j,V}\rangle$ and $\langle Q_n^{j,V}\rangle$ used in place of $A_n^{j,V}$, $B_n^{j,V}$, $C_n^{j,V}$ and $Q_n^{j,V}$, where the averaging operator $\langle\cdot\rangle$ is defined as

$$\langle\cdot\rangle = \frac{d}{2\pi}\int_{-\frac{\pi}{d}}^{\frac{\pi}{d}} \cdot \,\mathrm{d}\beta_0.$$

The fictitious source coefficients $Q_n^{0,V}$ for the $j=0$ cylinder are chosen to be constant with respect to k_y. This constraint, along with the quasi-periodicity requirement $Q_n^{j,V} = Q_n^{0,V}\exp(i\beta_0 jd)$, ensures that all fictitious sources in cylinders $j\neq 0$ disappear as a result of the averaging procedure, while the source in cylinder $j=0$ is unaffected, since

$$\begin{aligned}\langle Q_n^{j,V}\rangle &= Q_n^{0,V}\langle e^{i\beta_0 jd}\rangle \\ &= Q_n^{0,V}\frac{d}{2\pi}\int_{-\frac{\pi}{d}}^{\frac{\pi}{d}} e^{i\beta_0 jd}\mathrm{d}\beta_0 \qquad (4.43)\\ &= \begin{cases} Q_n^{0,V}, \text{ for } j=0\,, \\ 0, \text{ for } j\neq 0\,. \end{cases} \qquad (4.44)\end{aligned}$$

It follows that

$$\langle \boldsymbol{\mathcal{Q}}\rangle = \boldsymbol{\mathcal{Q}},$$

see Eq. (4.30). Consequently, $\boldsymbol{\mathcal{Q}}$ can be used to control the outgoing fields $\langle B_n^{0,V}\rangle$ (or, equivalently, $\langle\boldsymbol{\mathcal{B}}\rangle$) emanating from the $j=0$ cylinder. Applying the averaging operator to Eq. (4.29) yields

$$\langle\boldsymbol{\mathcal{B}}\rangle = \langle\boldsymbol{\mathcal{H}}\boldsymbol{\mathcal{Q}}\rangle = \boldsymbol{\mathcal{H}}\boldsymbol{\mathcal{Q}},$$

where the second equality relies on the fact that the boundary conditions do not depend on β_0, and so $\boldsymbol{\mathcal{H}} = \langle\boldsymbol{\mathcal{H}}\rangle$. Similarly, applying the averaging operator to Eq. (4.40) yields

$$\langle\boldsymbol{\mathcal{B}}\rangle = \langle\mathbf{Z}\boldsymbol{\mathcal{Q}}\rangle = \langle\mathbf{Z}\rangle\boldsymbol{\mathcal{Q}}.$$

Hence, the choices of $\boldsymbol{\mathcal{Q}}$ that produce the outgoing fields $\langle\boldsymbol{\mathcal{B}}\rangle$ of the defect being mimicked are given by the solutions of

$$\langle\mathbf{Z}(k,k_x) - \boldsymbol{\mathcal{H}}(k,k_x)\rangle\,\boldsymbol{\mathcal{Q}} = \mathbf{0}, \qquad (4.45)$$

cf. Eq. (4.42). Evidently, searching for the defect modes of the linear waveguide amounts to determining the values of k and k_x for which Eq. (4.45) has non-trivial solutions.

In principle, the solutions can be found by locating the zeroes of the determinant of $\langle \mathbf{Z} - \boldsymbol{\mathcal{H}} \rangle$; however, we have found that a more numerically stable method is to locate the vanishing singular values of this matrix.

4.3 Implementation and Verification

In this section we discuss the practicalities of the FSS method. In addition, we compare our super-cell formulation against our FSS code, and investigate the rate of convergence of the FSS method. The most important aspect of any FSS implementation is the discretisation of the integral in Eq. (4.45). For simplicity, we used the trapezoidal rule to carry out the integration. However, as an artefact of using the trapezoidal rule, fictitious sources $\pm\boldsymbol{\mathcal{Q}}$ are left in every N unit-cells, where N is the number sub-intervals used for the numerical integration. Thus, a super-cell spanning N cylinders is imposed onto the defect layer. (This artefact can be avoided by using a different integration rule, e.g., Gaussian quadrature.) Consequently, N must be large enough to ensure that the amount of coupling between the fields of adjacent super-cells is negligible. In practice, this is of little importance because the integration step is relatively fast even for large values of N. When N is even, the sign of $\boldsymbol{\mathcal{Q}}$ is positive, resulting in a defect that is repeated every N cylinders. In other words, a coupled resonator optical waveguide is modelled (CROW). This behaviour provides a means for testing the correctness of our implementation because this type of structure can be modelled directly, albeit much less efficiently, using the super-cell formulation presented in Chapter 3. Using Eqs. (4.24), (4.25) and (4.37), it is straightforward to demonstrate that the outgoing fields $\boldsymbol{F}_D^{\pm}$ emanating from the waveguide layer satisfy

$$(\mathbf{I} - \mathbf{E}^{\mp}\mathbf{E}^{\pm})\boldsymbol{F}_D^{\pm} = \mathbf{0} \tag{4.46}$$

with

$$\mathbf{E}^{-} = (\mathbf{I} - \widetilde{\boldsymbol{\mathcal{R}}}_a \boldsymbol{\mathcal{R}}'_{\infty})^{-1} \widetilde{\boldsymbol{\mathcal{T}}}_b \boldsymbol{\mathcal{R}}_{\infty},$$

$$\mathbf{E}^{+} = (\mathbf{I} - \widetilde{\boldsymbol{\mathcal{R}}}_b \boldsymbol{\mathcal{R}}_{\infty})^{-1} \widetilde{\boldsymbol{\mathcal{T}}}_a \boldsymbol{\mathcal{R}}'_{\infty},$$

and where $\widetilde{\boldsymbol{\mathcal{R}}}_{a/b}$ and $\widetilde{\boldsymbol{\mathcal{T}}}_{a/b}$, which are computed using the super-cell method, are now the scattering matrices for a grating whose every N_s^{th} cylinder has been perturbed. To find the modes of this CROW, one searches for values of k and k_x for which Eq. (4.46) has non-trivial solutions ($k_y = 0$ in this case).

Figure 4.3 compares the solutions found using the super-cell method with those found

using our FSS implementation, which uses the trapezoidal rule. The size of the super-cell is $N_s = 4$, and the number of integration intervals is $N = 4$. (The computational cost in evaluating $\boldsymbol{\mathcal{R}}_\infty$ for larger values of N_s is prohibitive.) The parameters of the cladding are the same as those used in Chapter 3. There is good agreement between the two methods because, when $N = 4$, the structure modelled using the FSS method is identical to a CROW that has a period of four cylinders. Figure 4.3 also shows the solutions that were found when $N = 10$ and $N = 40$ integration intervals are used. Using $N = 10$ intervals effectively models a grating super-cell containing 10 cylinders, yet there is still good agreement with the values obtained for $N = 40$ intervals. From this it can be concluded that the field confinement in the grating direction is strong enough for a super-cell containing 10 cylinders to accurately approximate a linear waveguide. (Recall that a super-cell comprising 11 cylinders was used in the previous chapter.)

The running time of the FSS method is determined by the cost of computing $\langle \mathbf{Z} - \boldsymbol{\mathcal{H}} \rangle$ in Eq. (4.45), and this cost, in turn, is determined largely by the cost of constructing $\boldsymbol{\mathcal{R}}_\infty$ and $\boldsymbol{\mathcal{R}}'_\infty$ for each integration point. The overall running time of the FSS method is therefore linearly proportional to the number of mesh points. This cost can be halved by making use of the fact that the top cladding is identical to the bottom cladding up to a shift of $d/2$ (or more generally by an amount δ) in either the x or y direction, and a reflection about the plane of the waveguide. This observation leads to the following relationship between $\boldsymbol{\mathcal{R}}_\infty$ and $\boldsymbol{\mathcal{R}}'_\infty$:

$$\boldsymbol{\mathcal{R}}'_\infty = \boldsymbol{\mathcal{Q}} \boldsymbol{\mathcal{R}}_\infty \boldsymbol{\mathcal{Q}}^{-1}, \tag{4.47}$$

with $\boldsymbol{\mathcal{Q}}$ as in Eq. (2.46) (which is not to be confused with the $\boldsymbol{\mathcal{Q}}$ that represents the fictitious sources). The similarity transform simply displaces the rods of the upper cladding by a distance $\delta = d/2$ in the direction parallel to the defect rod.

Many of the matrices appearing in the preceding theory are sparse (e.g., the boundary condition matrices used to construct $\boldsymbol{\mathcal{H}}$) and so the matrix algebra routines that are used can be optimised to take advantage of this. Moreover, the matrix $\boldsymbol{\mathcal{H}}$, which encapsulates the parameters of the defect, is easily computed, and once $\langle \mathbf{Z} \rangle$ has been computed $\langle \mathbf{Z} - \boldsymbol{\mathcal{H}} \rangle \boldsymbol{\mathcal{Q}} = \mathbf{0}$ can be solved for very little additional cost. Effectively, changing the parameters of defect incurs almost no computational penalty, making the woodpile FSS method the only practical method for investigating large regions of the parameter space of the defect.

The dispersion curves for the linear waveguide are presented in the next section. These were computed with the FSS method, where the integration step was carried out using the trapezoidal rule with $N = 40$ integration intervals, and where the diffraction orders

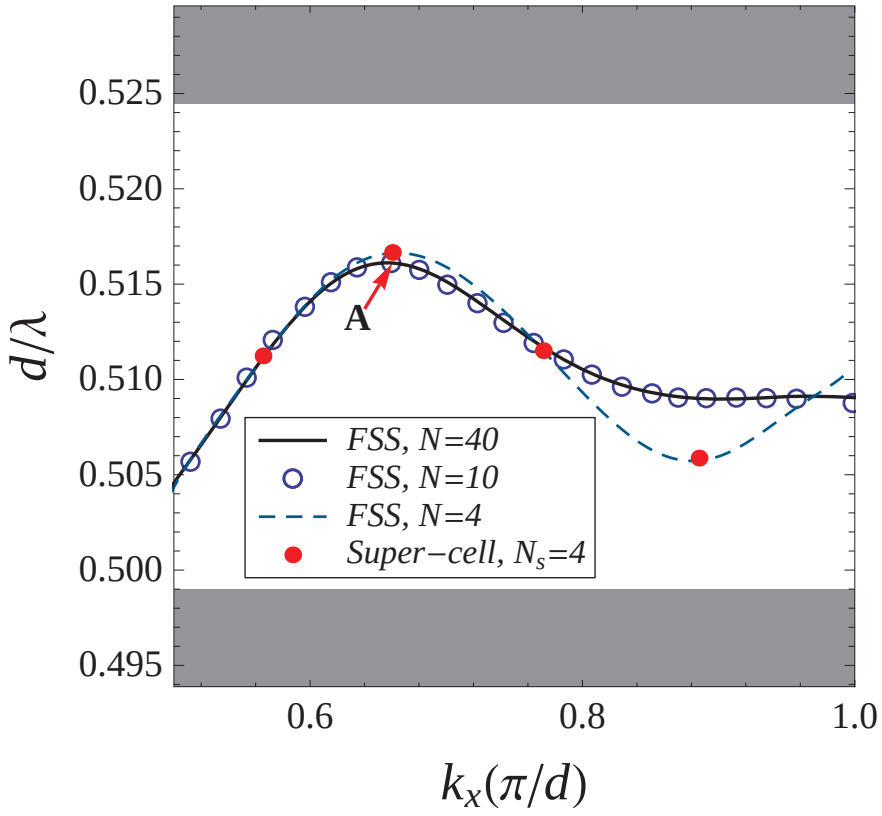

Figure 4.3: Dispersion curves for the linear waveguide that were computed using the FSS method with $N = 4, 10$ and 40 integration intervals. The radius of the defect rod is $0.5r$, where r is the radius of the cladding rods. (Parameters of the cladding are given in Sec. 4.4.) The frequency at the point A ($k_x = 2.075/d$) is listed in Table 4.1 for different multipole and plane wave truncation values, and for different values of N. Mode frequencies computed using Eq. (4.46) with a super-cell containing $N_s = 4$ cylinders are shown for comparison with the $N = 4$ curve for the FSS method. If the trapezoidal rule is used to carry out the integration (as it is here), then the FSS method is equivalent to the super-cell method when $N_s = N$.

and multipole orders were truncated to $p_{\max} = 5$ and $n_{\max} = 5$, respectively. That is, $-p_{\max} \leq p, q \leq p_{\max}$ and $-n_{\max} \leq n \leq n_{\max}$, with n as defined in Eq. (4.1). (These parameters were discussed in more detail at the end of Chapter 3.) Table 4.1 shows how the frequency of the mode at point A ($k_x = 2.075/d$) in Fig. 4.3 varies for different choices of $p_{\max}$, $n_{\max}$ and N. For $p_{\max} = 5$, $n_{\max} = 5$, and $N = 40$, the error is less than 1% of the width of the complete bandgap, which spans the normalised frequencies $0.4990 \leq d/\lambda \leq 0.5245$. (The structural parameters of the woodpile are given in the next section.) It can be seen for $p_{\max} = 5$ and $n_{\max} = 5$ that the frequency estimate of the mode converges rapidly with respect the the number of integration intervals N. This is consistent with the results for the $N = 10$ and $N = 40$ curves shown in Fig. 4.3. Obtaining more accurate frequency estimates for higher values of $p_{\max}$ and $n_{\max}$ would require using a different $n_{\max}$ for each plane wave order $-p_{\max} \leq p \leq p_{\max}$, and is therefore impractical. We found that an upper limit of $p_{\max} \approx 6$ must be imposed in order to obtain well resolved dispersion curves in a reasonable amount of time.

It has been observed for 2D FSS implementations that the results produced by Gaussian quadrature and the trapezoidal numerical integration are the same, except possibly for a difference in the rate at which the two methods converge [27]. A general feature of Gaussian quadrature is that, for certain functions, highly accurrate estimates of the integral can be obtained using very few sample points. This is to be compared with the trapezoidal rule, which typically requires a relatively large number of integration points. Nevertheless, we found the trapezoidal rule to be efficient and not limiting in this respect. The reason for its surprisingly good performance might be due to the fact that the error term of the trapezoidal rule tends to be much smaller when the integrand is a smooth peridioc function [111], such as the integrand in Eq. (4.45). Another advantage of the trapezoidal rule is that the rate of convegence can be improved by choosing the number of integration points to be $N = 2^n m$, for some integers n and m, and then applying Romberg's method to the estimates of $\langle \mathbf{Z}(k, k_x) - \boldsymbol{\mathcal{H}}(k, k_x) \rangle$ for $N = m, 2m, 4m, ..., 2^n m$. Such a numerical optimisation would not be possible if Gaussian integration were instead used.

4.4 Results

For the following, the radius and refractive index of each cylinder of the cladding are $r = 0.15d$ and $n_c = 2.68$ (chalcogenide glass), and the background refractive index is $n_b = 1$. The inter-layer spacing is $h = 0.3002d$, so that the cylinders in adjacent layers are almost touching, and each pair of consecutive layers is offset laterally by a distance

Table 4.1: Convergence of the (normalised) frequencies d/λ near point A of Fig. 4.3, with $k_x = 2.075/d$ fixed.

d/λ	$p_{\max}$	$n_{\max}$	N
0.516643	3	9	80
0.516275	4	9	80
0.516158	5	5	10
0.516160	5	5	20
0.516160	5	5	40
0.516160	5	5	80
0.516160	5	5	160
0.516122	5	7	40
0.516120	5	9	40
0.516115	5	9	80
0.516059	6	7	80
0.516035	7	7	80

$d/2$ in both the x and y directions with respect to pairs immediately above and below it. The cladding has a complete bandgap that spans the normalised frequencies $0.4990 \leq d/\lambda \leq 0.5245$, and that lies just above the light line $kn_b = k_x$, with $0 \leq k_x \leq \pi/d$. Thus, the confinement of any mode propagating along the waveguide is due to the bandgap. In all cases, the Brillouin zone (BZ) integration was carried out using the trapezoidal rule with $N = 40$ integration intervals.

Figure 4.4 shows how the dispersion curves for the linear waveguide change as the radius r_d of the defect rod is decreased relative to the radius of the cladding rods. For each value of r_d there is a pair of defect modes inside the complete bandgap that become degenerate precisely at the edge of the BZ ($k_x d/\pi = 1.0$). This degeneracy has been observed before in woodpile waveguides structures [18, 19, 60–62], and can be attributed to the fact that the waveguide considered here is invariant under the transformation $(z \to -z)$, $(x \to x + d/2)$ [106] ('glide-reflection' symmetry). The behaviour of the modes for any given r_d is quite different from that of typical waveguiding modes of planar PC waveguides in that one of the two modes displays quartic dispersion. In particular, for $r_d = 0.5r$ there is a region near the edge of the Brillouin zone [from $k_x \approx 0.85(\pi/d)$ to $k_x = \pi/d$ – about 15% of the BZ] over which the frequency of the higher branch is almost constant, $d/\lambda \approx 0.5090$, and quite close to the middle of the bandgap. This region meets the slow-light criterion $v_x/c \ll 1$, where v_x is the group velocity in the direction of the waveguide. For this region, the speed at which light propagates through the waveguide

is reduced drastically, and non-linear optical processes, such as third harmonic generation [14], are enhanced because the light has more time to interact with the waveguide (especially since chalcogenide glass exhibits a strong non-linear response [40]). (The group velocity $\mathbf{v}_g \stackrel{\text{def}}{=} \nabla_{\mathbf{k}}\omega(\mathbf{k})$ of a wave propagating through a lossless weakly dispersive homogeneous medium corresponds to the energy transport velocity. This notion of group velocity is also applicable to the propagating Bloch modes of a photonic crystal, and it is therefore possible to define the group index n_g of a Bloch mode as $n_g = c/v_g$. The notion of phase velocity, however, is not easily extended to waves in photonic crystals because the complex spatial variation of the fields makes it difficult to define the wavefronts sensibly [3].) However, it can be seen that the group velocity dispersion (GVD) $\partial(1/v_x)/\partial\omega$ diverges when $k_x \gtrsim 0.85$ and, consequently, it would be difficult to utilise the waveguide for these values of k_x since a pulse travelling through the waveguide would be strongly dispersed. For $r_d = 0.5r$, the modes near $k_x \approx 0.85(\pi/d)$ are better suited for slow-light purposes, since the GVD is finite there and v_x is relatively small. By instead choosing the defect size to be $r_d = 0.404r$ the waveguide can be engineered so that it has both low GVD and low v_x over the region $0.85(\pi/d) \lesssim k_x \leq \pi/d$ because the dispersion is approximately linear for these values of k_x.

As was for the CROW and linear waveguide examined in the last chapter, decreasing r_d, thereby removing some dielectric, has the effect of increasing the frequency of the defect modes. Further, the frequency of the quartic mode decreases more rapidly than that of the quadratic mode as r_d increases. Thus, since the frequencies of these two modes must always be the same at the edge of the BZ, the dispersion curve of the quartic mode can be made to cross that of the quadratic mode simply by making r_d sufficiently large (specifically, by choosing $r_d/r \gtrsim 0.6$). We found that defect modes appeared as soon $r_d \neq r$, and that for shallow defects ($r_d/r \gtrsim 0.95$) the corresponding dispersion curves are flat and very close to the low-frequency edge of the bandgap (not shown). Note that for such small perturbations the defect modes necessarily become highly extended and, thus, it is extremely difficult, if not impossible, to use a super-cell approach to model a shallow defect, whereas the FSS method is well-suited for the task. (Shallow defects are best modelled using perturbation theory [112]; however, to our knowledge such methods haven't been applied to photonic woodpiles.)

The electric and magnetic energy densities for the point B ($k_x d/\pi = 1.0$, $d/\lambda \approx 0.5091$, $r_d = 0.5r$) of Fig. 4.4 are shown in Fig. 4.5 for the planes $x/d = 0.0$ and $x/d = 0.25$, where x is the direction parallel to the defect rod. For both the lateral and stacking directions, there is strong localisation of the electric and magnetic fields. Point B

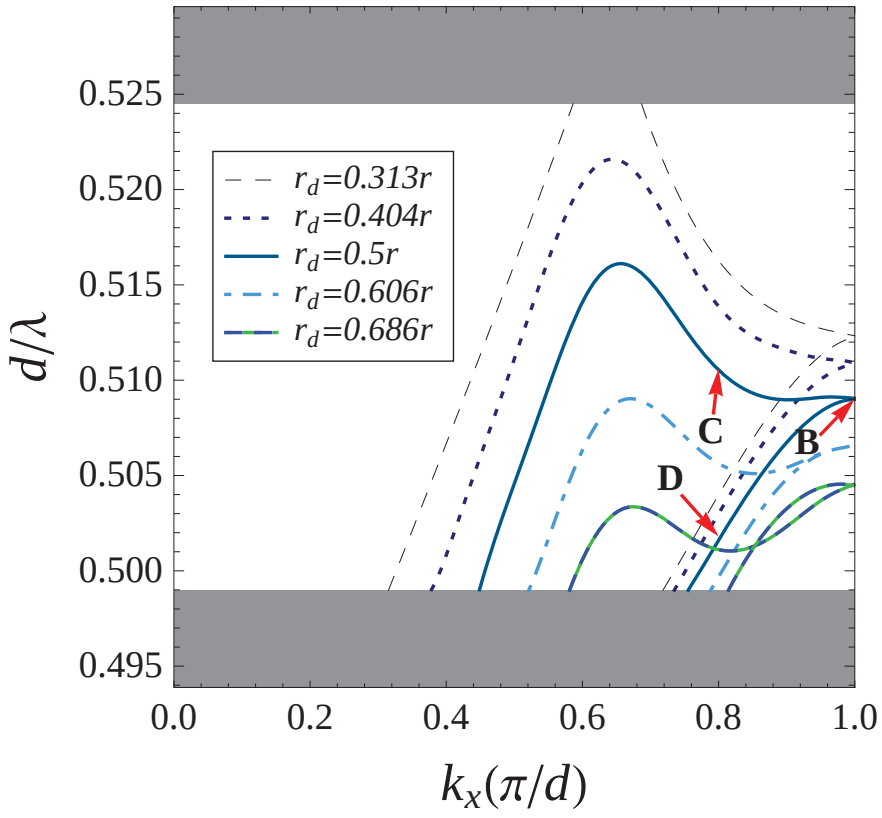

Figure 4.4: Dispersion curves for the linear waveguide for different values of r_d, which specifies the radius of the defect rod. The radius of the defect is specified relative to the radius r of the cladding rods. The dispersion curves are only shown for the frequencies that lie inside the complete bandgap of the cladding ($0.4990 \leq d/\lambda \leq 0.5245$).

lies inside the broad flat region of the frequency band for $r_d = 0.5$, and so corresponds to a slow-light mode. To further investigate this phenomenon, we have computed the energy flux S_x in the waveguiding direction, where $\mathbf{S} = \mathrm{Re}(\mathbf{E} \times \mathbf{H}^*)/2$ is the Poynting vector. Figures 4.6(a) and 4.6(b) show the flux at $x/d = 0.0$ and $x/d = 0.25$, respectively, for the point B. Much of the energy flow in the forward direction (blue) concentrates in the unit-cell containing the defect, whereas most of the energy flow in the backward direction (red) concentrates in an annular region that surrounds the central red lobe. We have verified that this power distribution does not change greatly as x changes (not shown), although the magnitude of S_x oscillates fairly uniformly over the woodpile as x increases. Moreover, S_x assumes positive values as often as it does negative ones, thus the net flux is small, leading to a low group velocity v_x along the waveguide.

Figures 4.5(c) and 4.5(d) show plots of S_x for the point C [$d/\lambda = 0.5105$, $k_x = 0.8(\pi/d)$] of Fig. 4.4. This point lies on the same dispersion curve as point B; however, unlike point B, point C does not lie inside the slow-light region, and it can be seen that S_x is largely negative when $x/d = 0.25$, resulting in a relatively large v_x. This time the flux in the backward direction is concentrated in a large central lobe, that is surrounded by smaller side lobes of energy flowing in the forward direction. Both points B and C lie on the quartic dispersion curve for $r_d = 0.5r$. In Fig. 4.5, we have also included plots of S_x for a point that lies on the quadratic dispersion curve for $r_d = 0.5r$ [specifally, for point D ($d/\lambda = 0.5102$, $k_x = 0.8\pi/d$) of Fig. 4.4]. The energy flux occurs primarily inside the waveguide layer, where there is considerable power in the side lobes, in addition to the central lobe.

Of the three modes (points A, B, and C), the slow-light mode (point B) has the smallest modal volume. The small volume and low group-velocity mean that this mode would elicit a stronger non-linear response from the chalcogenide defect than the other modes would. The fields of all three modes possess mirror symmetry about the z-axis. However, unlike modes A and C, mode B is very nearly four-fold rotationally symmetric about the defect rod when $x = 0.25d$. An inspection of the Bloch modes might yield insights into the origins of the increased symmetry of mode B. While the FSS method does not permit such an anlaysis, alternative approaches, such as the Bloch mode methods developed by Brownless *et al.* [113], might be used to explain the connection between the rotational symmetry of mode B and the low group-velocity. Such a study is a substantial task and is beyond the scope of this thesis.

We have also modelled a waveguide that was created by decreasing only the refractive index n_d of a single rod, while leaving the radius of the rod unchanged. The dispersion

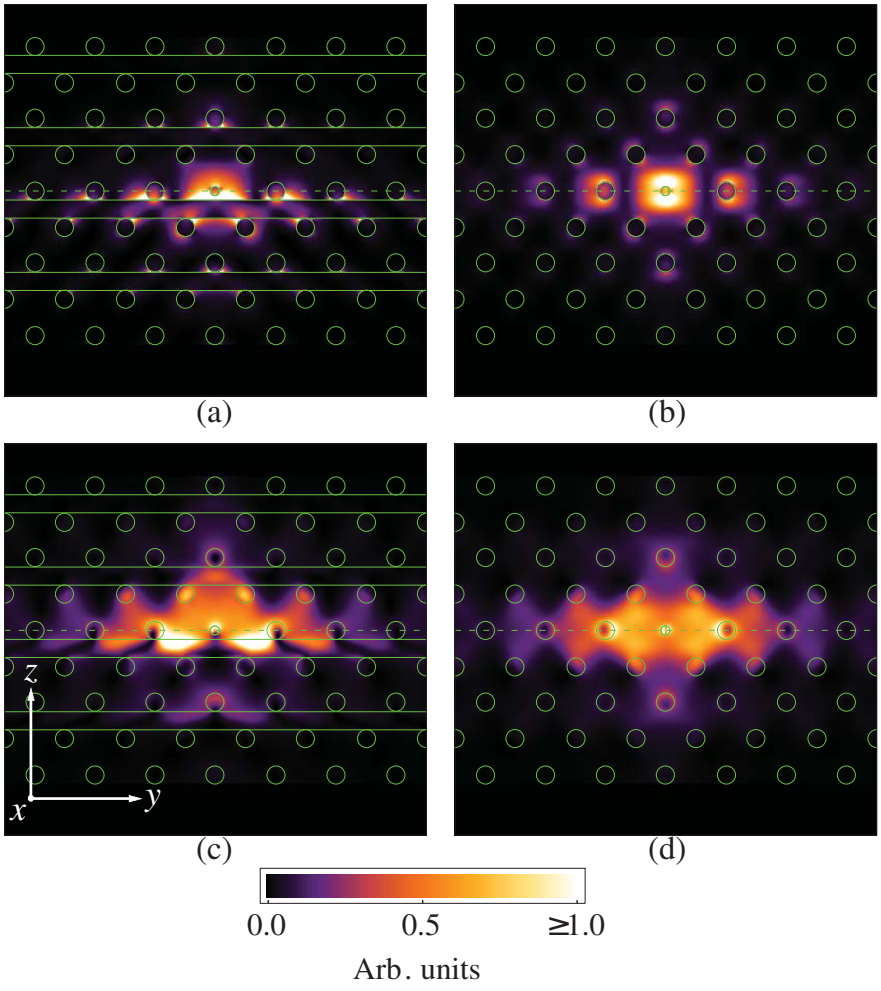

Figure 4.5: Plots of the energy density $\varepsilon\|\boldsymbol{E}\|^2$ of the electric field [(a) and (b)], and of the energy density $\mu\|\boldsymbol{H}\|^2$ of the magnetic field [(c) and (d)] at point B ($k_x = \pi/d$, $d/\lambda \approx 0.5091$) in Fig. 4.4. The permittiviy is specified by $\varepsilon(y,z)$, and the permeability $\mu(y,z)$ is unity. The view looks down the defect rod, the radius of which is $r_d = 0.5r$. Plots (a) and (c) are for the plane $x/d = 0.0$, and plots (b) and (d) are for the plane $x/d = 0.25$.

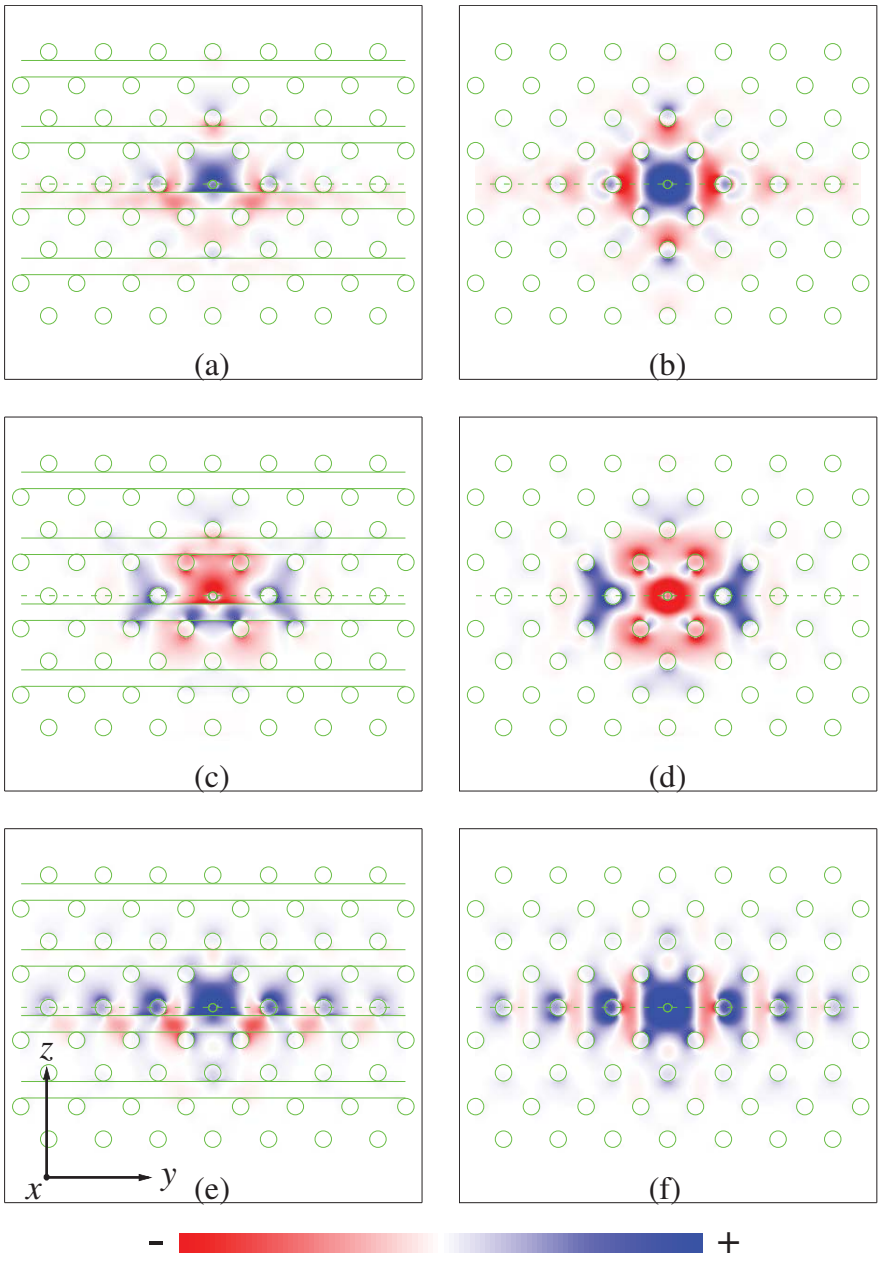

Figure 4.6: Plot of $\mathrm{Re}(S_x)$ for the points B [parts (a) and (b)], C [parts (c) and (d)], and D [parts (e) and (f)] of Fig. 4.4, where S_x is the x component of the Poynting vector. The view looks down the defect rod, the radius of which is $r_d = 0.5r$. The plots (a), (c) and (e) are for the plane $x/d = 0.0$, where x is the direction parallel to the defect rod, and the plots (b), (d) and (f) are for the plane $x/d = 0.25$.

curves for this structure are shown in Fig. 4.7. Decreasing n_d, so that $n_b < n_d < n_c$, has an effect similar to reducing the radius of the defect, with lower n_d resulting in a higher frequency (both types of defects are 'acceptor-type' defects, in that they are created by reducing the amount of dielectric [62]). Once again, there is a fairly large region of the BZ over which one of the frequency bands flattens. In particular, the breadth of the slow-light region is maximised for $n_d/n_c \approx 0.575$. For reasonably small perturbations ($0.90 \lesssim n_d/n_c < 1.0$) the defect modes have frequencies very close to the low-frequency edge of the bandgap, as was the case when $r_d \approx r$. The degeneracy of the defect modes at the edge of the BZ ($k_x = \pi/d$) is again evident because the defect preserves the glide-reflection symmetry of the waveguide.

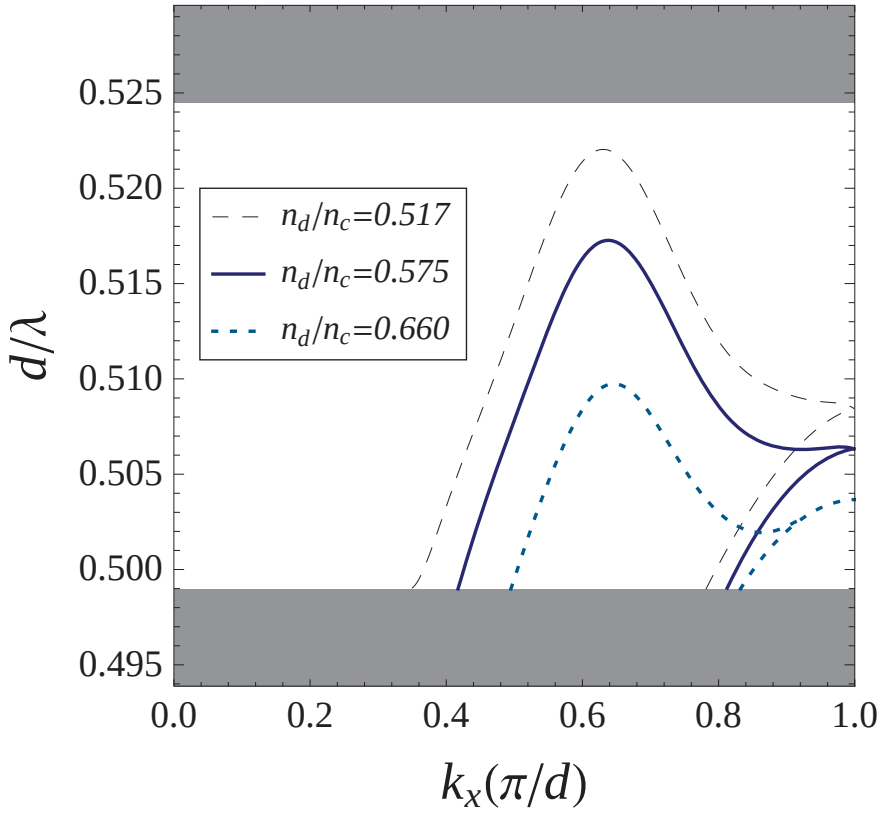

Figure 4.7: Dispersion curves for the linear waveguide for different values of n_d, which specifies the refractive index of the defect rod. The refractive index of the cladding rods is $n_c = 2.68$ (chalcogenide glass).

4.5 Discussion

We have generalised the FSS method so that we can model localised linear defects in woodpiles in a highly efficient manner. Our results suggest that creating a defect by decreasing the average refractive index of a single unit-cell, even by as little as 1%, always results in defect states. Further, the symmetry of the woodpile structure results in waveguiding modes that are always degenerate at the edge of the Brillouin zone. The method overcomes the performance limitations of the super-cell approach developed in Chapter 3, allowing the parameters of the defect rod to be changed in a continuous manner. It was found that choosing the radius of the defect to be half that of the cladding rods resulted in a waveguide having a low group-velocity (evidenced by flat dispersion) over $\sim 15\%$ of Brillouin zone. In this region, light entering the waveguide is slowed-down dramatically, leading to a host of compelling applications [114]. Fabricating slow-light waveguides based on planar PC geometries is challenging because scattering losses due to structural imperfections appear to scale inversely with group velocity [115, 116]. This is understandable because the light has more time to interact with the walls of the PC. For these geometries, most scattering losses are due to backscattering and out-of-plane scattering, where in-plane scattering can be mitigated by increasing the number of layers of the periodic pattern. If a woodpile geometry were used instead, then the complete bandgap of the woodpile cladding could be used to eliminate out-of-plane scattering, making this a compelling geometry for slow-light waveguides. So long as there are a sufficient number of layers, most of the losses in such a woodpile waveguide ought to be the result of backscattering, although this is an open question.

Another possibility that we have explored is to place fictitious sources in two successive layers, and then use a double integral during the superposition step, *i.e.*, integrate with respect to both the k_x and k_y directions, thereby leaving a single defect rod in each of the two layers. In principle, the resulting cross-shaped defect would act as an optical resonator. However, the FSS method does not appear to be applicable in this case because the multipole basis functions [J_n and H_n in Eqs. (4.1) and (4.10)] depend on α_0, and so after integrating Eqs. (4.1) and (4.10) with respect to α_0 there would be no clear choice of basis functions. It is possible, though, to mimic multiple defects if the defect rods are parallel; by generalising the techniques reported in [108], a finite set of parallel defects can be distributed arbitrarily throughout the woodpile.

4.A Expressions for FSS Boundary Condition Matrix

The matrix $\mathcal{N}$ encapsulating the boundary conditions for the fictitious sources [see Eq. (4.12)] is a 2 by 2 block matrix, where superscripts E and H are used to label the blocks so that

$$\mathcal{N} = \begin{bmatrix} \mathsf{N}^{EE} & \mathsf{N}^{EH} \\ \mathsf{N}^{HE} & \mathsf{N}^{HH} \end{bmatrix}. \tag{4.48}$$

Furthermore, each block is diagonal so we may use n to index the elements of a given block. The label 'I' denotes quantities that depend on the properties of the background region, while 'II' denotes quantities that depend on the material properties of the cylinder. Let r be the radius of the cylinder, and let ε_j and μ_j be the permittivity and permeability, respectively, of region j (*i.e.*, $j = \mathrm{I}$ or $j = \mathrm{II}$). If $k_{\perp j}$ is the transverse wavenumber inside region j, so that $k_{\perp j}^2 = k^2 \varepsilon_j \mu_j - \alpha_p^2$, then the diagonal entries of the blocks are

$$\mathsf{N}_n^{EE} = \eta_3\left(\mathrm{II}\right) J_2 H/\Delta, \tag{4.49}$$

$$\mathsf{N}_n^{HH} = \eta_2\left(\mathrm{II}\right) J_3 H/\Delta, \tag{4.50}$$

$$\mathsf{N}_n^{EH} = \eta_2\left(\mathrm{II}\right)\left[\eta_1\left(\mathrm{I}\right) - \eta_1\left(\mathrm{II}\right)\right] H/\Delta, \tag{4.51}$$

and

$$\mathsf{N}_n^{HE} = \eta_3\left(\mathrm{II}\right)\left[\eta_1\left(\mathrm{I}\right) - \eta_1\left(\mathrm{II}\right)\right] H/\Delta, \tag{4.52}$$

where $\eta_1\left(j\right) = -\alpha_p n/\left[\left(k_{\perp j}\right)^2 r\right]$, $\eta_2\left(j\right) = -ik\mu_j/k_{\perp j}$, $\eta_3\left(j\right) = ik\varepsilon_j/k_{\perp j}$,

$$\Delta = J_n\left(k_{\perp \mathrm{I}} r\right)^2 \left\{\left[\eta_1\left(\mathrm{I}\right) - \eta_1\left(\mathrm{II}\right)\right]^2 - J_2 J_3\right\},$$

$$J_j = \eta_j\left(\mathrm{I}\right)\left\{\frac{J_n'\left(k_{\perp \mathrm{I}} r\right)}{J_n\left(k_{\perp \mathrm{I}} r\right)} - \frac{\eta_j\left(\mathrm{II}\right) J_n'\left(k_{\perp \mathrm{II}} r\right)}{\eta_j\left(\mathrm{I}\right) J_n\left(k_{\perp \mathrm{II}} r\right)}\right\}$$

and

$$H = J_n\left(k_{\perp \mathrm{I}} r\right) H_n\left(k_{\perp \mathrm{II}} r\right) \times \left\{\frac{H_n'\left(k_{\perp \mathrm{II}} r\right)}{H_n\left(k_{\perp \mathrm{II}} r\right)} - \frac{J_n'\left(k_{\perp \mathrm{II}} r\right)}{J_n\left(k_{\perp \mathrm{II}} r\right)}\right\}.$$

Chapter 5

Woodpile Surface Modes

5.1 Introduction

The literature relating to the electromagnetic properties of infinitely extended woodpiles is quite extensive compared to that on the properties of the waves that can be trapped on the surfaces of woodpiles [53, 57, 71]. These *surface modes* are important for coupling to the woodpile from external sources, as well as for the radiation dynamics of sources, such as quantum dots, placed within the woodpile. In addition, it has been shown that the control of surface modes can be used to create resonant cavities that have high Q factors, and it is thought that such cavities could be relevant in the control of surface-plasmon polaritons [53].

The theory of surface states for periodic media was first considered for electrons in atomic lattices by Tamm in the 1930s [117], and later by Heine [118]. Perhaps the most important example of optical surface waves are *surface plasmons*, which propagate along metal-dielectric interfaces [119], and which can occupy particularly small volumes. Wood anomalies [120], whereby a grating diffracts light parallel to the grating axis, and the propagation of light along periodically-perforated thin sheets [121] are early examples of optical waves that are confined to a region that is thin with respect to the period of the patterning. The existence of electromagnetic waves that propagate along an interface between a dielectric photonic crystal (PC) and a homogeneous dielectric region (usually air) was first proposed by Meade *et al*. [122], and has been confirmed experimentally for both 2D [123] and 3D PCs [53]

To our knowledge, there are three other theoretical studies of surface modes in woodpile structures. The first treatment, by Ishizaki and Noda [53], was a numerical study performed to confirm experimental findings, in which the dispersion relation of the surface

modes were computed, and the propagation of surface modes was able to be suppressed by incorporating a 2D PC into the top layer of an 8-layer woodpile. This enabled the design of a high-Q resonant cavity ($Q \approx 9000$) on the surface of a woodpile. Ederra *et al*. [57] carried out a numerical study on the effect that the rod size of the top layer, as well as the addition of a quartz film, had on the dispersion relationships of the surface modes, with the aim of improving the directivity of antennas that use woodpile substrates. This study also investigated effects relating to the number of layers of a finite stack; however, the effects of stack size were minimal because the penetration depths of the surface modes were small relative to the thickness of the woodpiles, whose sizes ranged from 16-24 layers. Very recently, Su et al. [71] examined the effect that position and orientation of the surface, as well as index contrast, had on the optical sensing capabilities of woodpiles. None of those studies considered surface modes that propagate simultaneously along the top and bottom surfaces of the woodpile ('double-interface' modes).

In this chapter, transfer matrix and scattering matrix methods are used to perform a comprehensive analysis of the surface modes of both semi-infinite woodpiles (*i.e.*, that have only one surface, see Sec. 5.2) and woodpiles that consist of a finite number of layers (see Sec. 5.4). In the latter case, the existence of double-interface modes is demonstrated mathematically, and it is shown numerically that the strength of the coupling between the fields at the top surface and those at the bottom surface depends greatly on the direction of propagation. Interactions between such coupled modes are also observed. In particular, the dispersion curve of a double-interface mode can be intertwined with that of another double-interface mode. This phenomenon has also been observed in coupled photonic PC waveguides in hexagonal lattices [113]. We remark that in [57], the high-symmetry directions of the woodpile are not considered, while in [53] and [71], the band structure calculations are limited to semi-infinite woodpiles. The results in this chapter indicate that parameters such as stack-size, parity of the number of layers, and direction of propagation play an important role in the properties of the surface modes, and could be exploited to offer more precise control over the surface states of woodpiles.

In addition, the plane wave scattering matrix formulation [26, 88, 124] is used to obtain a basic description of the surface modes of 'compound' woodpiles, which are PC-air-PC arrangements in which the PC regions are woodpiles that may be either finite or semi-infinite. Specifically, we describe the conditions under which the surface modes are capable of propagating along two or more interfaces simultaneously (see Sec. 5.5).

Unlike earlier studies on the surface modes of woodpiles [53, 57, 71], the results presented here were obtained for circular rods, rather than rectangular ones, since our meth-

ods are most easily applied to circular geometries. However, the shape of the rods is not significant in this study because we only consider effects that are related to symmetry of the lattice.

5.2 Surface modes of semi-infinite woodpiles

We begin by deriving a simple analytical description of the modes that propagate along the surface of a truncated woodpile that extends infinitely in the half-space $z < 0$, and whose top layer lies in the plane $z = 0$. As before, d specifies the grating period. The woodpile can be regarded as a stack of pairs of orthogonal gratings, so that, for a woodpile whose layers are spaced apart by a distance h, and whose rods are aligned parallel to either the x- or y-axis, the primitive lattice vector in the stacking direction is given by $\mathbf{a}_3 = \delta_x\hat{\mathbf{x}} + \delta_y\hat{\mathbf{y}} + 2h\hat{\mathbf{z}}$, with δ_x and δ_y specifying the relative lateral displacement between successive pairs of gratings of the woodpile (all distances are expressed in units of d).

The fields impinging on the lower boundary of the l^{th} layer can be expanded in terms of upward $\boldsymbol{\mathcal{F}}_l^+$ and downward $\boldsymbol{\mathcal{F}}_l^-$ plane wave orders [which obey relationships analogous to Eq. (2.40)], as illustrated in Fig. 5.1. The surface modes of the semi-infinite structure, however, are best determined using Bloch mode field expansions. For a finite stack comprising n grating *pairs*, the plane wave fields immediately below the j^{th} pair can be re-expressed in the Bloch mode basis as [26, 124]

$$\begin{pmatrix} \boldsymbol{\mathcal{F}}_{2j}^- \\ \boldsymbol{\mathcal{F}}_{2j}^+ \end{pmatrix} = \mathbf{F}\boldsymbol{\Lambda}^j\mathbf{c}^- + \mathbf{F}'(\boldsymbol{\Lambda}')^{-(n-j)}\mathbf{c}^+, \tag{5.1}$$

cf. Eq. (44) of [26], where $\mathbf{c}^\pm$ are vectors denoting the amplitudes of the Bloch components, and where $\mathbf{F}$ is the matrix whose columns are the downward Bloch modes (*i.e.*, that travel into the PC) of the infinite woodpile. Similarly, the columns of $\mathbf{F}'$ are the upward Bloch modes. The matrices $\mathbf{F}$ and $\mathbf{F}'$ effect a change of basis from Bloch modes to plane waves, and, hence, $\mathbf{F}$ and $\mathbf{F}'$ are block matrices of the form

$$\mathbf{F} = \begin{pmatrix} \mathbf{F}_- \\ \mathbf{F}_+ \end{pmatrix} \quad \text{and} \quad \mathbf{F}' = \begin{pmatrix} \mathbf{F}'_- \\ \mathbf{F}'_+ \end{pmatrix}. \tag{5.2}$$

Following the nomenclature of [26] [see, in particular, Eqs. (40)-(43)], the columns of $\mathbf{F}$ and $\mathbf{F}'$ are the eigenvectors of the transfer matrix $\mathbf{T}$, which relates fields at the top surface of the unit-cell to those at the bottom surface of the unit-cell, as discussed in Sec. 2.6. That

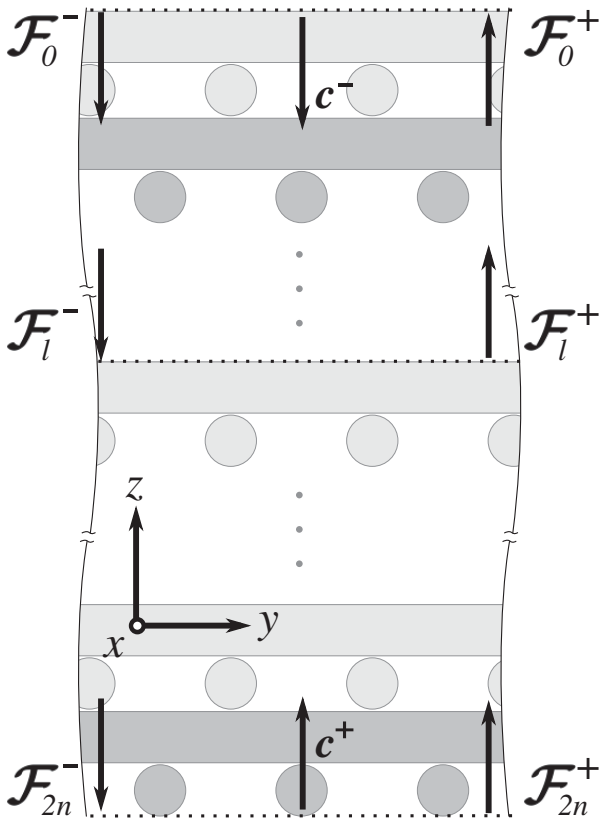

Figure 5.1: The phase origins (dotted horizontal lines) of the plane wave fields $\boldsymbol{\mathcal{F}}^{\pm}$ and Bloch modes $\mathbf{c}^{\pm}$ of a woodpile that comprises $2n$ pairs. The woodpile extends infinitely in the x and y directions.

is, the fields immediately below the j^{th} pair ($\boldsymbol{\mathcal{F}}^{\pm}_{2j}$) are related to the fields immediately below $(j+1)^{\text{th}}$ pair ($\boldsymbol{\mathcal{F}}^{\pm}_{2j+2}$) according to

$$\mathsf{T}\begin{pmatrix}\boldsymbol{\mathcal{F}}^{-}_{2j}\\ \boldsymbol{\mathcal{F}}^{+}_{2j}\end{pmatrix}=\begin{pmatrix}\boldsymbol{\mathcal{F}}^{-}_{2j+2}\\ \boldsymbol{\mathcal{F}}^{+}_{2j+2}\end{pmatrix}=\tilde{\mu}\begin{pmatrix}\boldsymbol{\mathcal{F}}^{-}_{2j}\\ \boldsymbol{\mathcal{F}}^{+}_{2j}\end{pmatrix}, \tag{5.3}$$

for some Bloch factor (eigenvalue) $\tilde{\mu}$. The matrices $\boldsymbol{\Lambda}$ and $\boldsymbol{\Lambda}'$ in Eq. (5.1) are, therefore, diagonal matrices whose diagonal entries are simply the corresponding Bloch factors of the columns of $\mathbf{F}$ and $\mathbf{F}'$, respectively, so that $\boldsymbol{\Lambda}=\operatorname{diag}[\mu]$ and $\boldsymbol{\Lambda}'=\operatorname{diag}[\mu']$, in which $\mu=\exp(-i\mathbf{k}\cdot\mathbf{a}_3)$ and $\mu'=\exp(-i\mathbf{k}'\cdot\mathbf{a}_3)$. Here, $\mathbf{k}=(k_x,k_y,k_z)$ and $\mathbf{k}'=(k_x,k_y,k_z')$ denote the Bloch vectors of the corresponding Bloch modes, with k_x, k_y known in advance. Furthermore, for propagating Bloch modes $|\mu|=1$ and $|\mu'|=1$, while for evanescent modes $|\mu|<1$ and $|\mu'|>1$.

In the limit as $n\to\infty$, the second term in Eq. (5.1) vanishes because, when there is

no bottom surface, upwards traveling Bloch modes can not be generated (*i.e.*, $\mathbf{c}^+ = \mathbf{0}$). Thus, the fields impinging on the surface ($\boldsymbol{\mathcal{F}}_0^{\pm}$) satisfy

$$\begin{pmatrix} \mathbf{0} \\ \boldsymbol{\mathcal{F}}_0^+ \end{pmatrix} = \begin{pmatrix} \mathbf{F}_- \\ \mathbf{F}_+ \end{pmatrix} \mathbf{c}^-, \tag{5.4}$$

where we have made use of the fact that there is no incoming field incident to the top layer, *i.e.*, $\boldsymbol{\mathcal{F}}_0^- = \mathbf{0}$. The dispersion curves of the surface modes can, therefore, be obtained by determining the wavelengths λ for which

$$(\mathbf{F}_-)\mathbf{c}^- = \mathbf{0} \tag{5.5}$$

has non-trivial solutions for a given choice of $\mathbf{k}_t = (k_x, k_y)$ (the in-plane Bloch vector), keeping in mind that, for surface modes, one only needs to consider wavelengths that lie below the light-line [122].

Figures 5.2(a) and 5.2(b) depict the surface of a semi-infinite woodpile, and the corresponding first Brillouin zone, respectively. The dispersion curves of the surface modes [computed using Eq. (5.5)] for a semi-infinite woodpile are shown in Fig. 5.2(c) for the values of $\mathbf{k}_t$ that lie along the high-symmetry directions of the Brillouin zone of the surface. Figure 5.2 also shows the band diagram (patterned region) of the corresponding infinite woodpile projected onto the surface Brillouin zone. The refractive indices of the background region and cylinders are $n_b = 1$ and $n_c = 2.68$ (chalcogenide glass), respectively, and the radius of each cylinder is $r = 0.15d$, with $\delta_x = \delta_y = d/2$, and with $h = 0.3002d$ chosen so that the rods of one layer are almost touching those of the adjacent layers (these values are used throughout this thesis). Note that the $\Gamma - \mathrm{X}_1$ direction is not equivalent to the $\Gamma - \mathrm{X}_2$ direction and, consequently, the surface modes in the $\mathrm{M} - \mathrm{X}_1$ direction differ from those in the $\mathrm{M} - \mathrm{X}_2$ direction. Above the light-line (solid shaded region), the frequencies of the modes are not quantised; hence, the surface modes appear to become cutoff as they cross the light-line. Similarly, the surface modes also appear to terminate abruptly as they leave the bandgap, although in reality the patterned region represents a continuum of solutions. Figure 5.3 shows the intensity of each field component of a representative surface mode [$\mathbf{k}_t = (0.54, 1) \times \pi/d$, $d/\lambda = 0.522$].

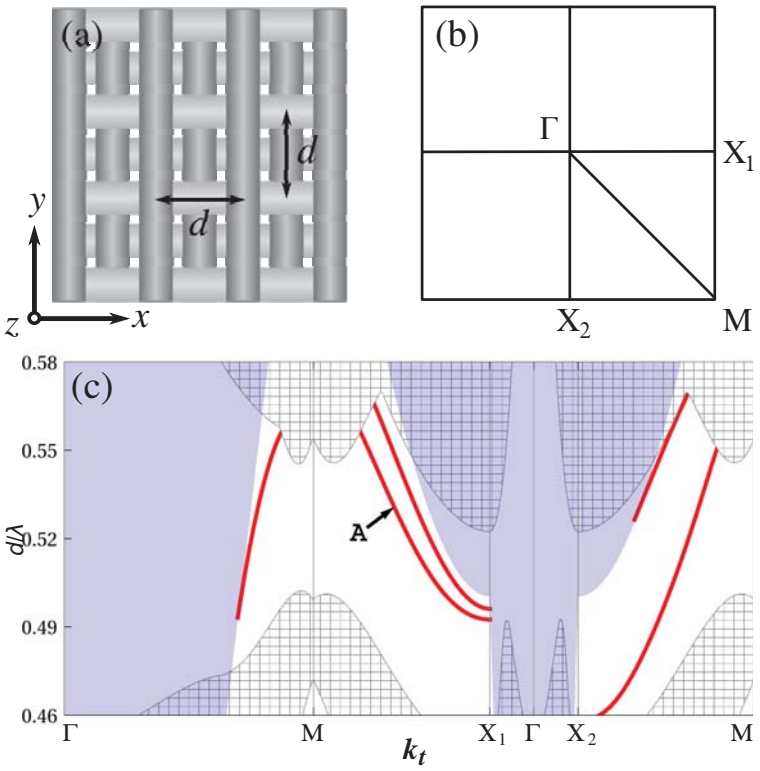

Figure 5.2: (a) Schematic of a semi-infinite woodpile (viewed from above), and (b) the high-symmetry directions of the first Brillouin zone of the semi-infinite woodpile. (c) Band diagram for an infinite woodpile. The patterned area indicates the normalized frequencies d/λ for which there are one or more propagating Bloch modes, while the solid shaded region (blue) denotes frequencies that lie above the light-line. The red (thick) curves denote the dispersion relationships of the surface modes of the corresponding semi-infinite woodpile. The fields for the mode at the point A are shown in Fig 5.3.

5.3 A heuristic for locating surface modes

Before discussing finite structures, we describe a simple heuristic that can be used to locate the surface modes of an arbitrary grating stack consisting of m layers, where m can be either even or odd. Later this heuristic will be used to relate the surface modes of finite and compound woodpiles to those of the corresponding semi-infinite woodpile. The plane wave scattering matrices relating the outgoing plane wave fields $\boldsymbol{\mathcal{F}}_0^+$ and $\boldsymbol{\mathcal{F}}_m^-$ sourced on the surfaces of an m layer grating stack to the incoming fields $\boldsymbol{\mathcal{F}}_0^-$ and $\boldsymbol{\mathcal{F}}_m^+$ incident to the top and bottom layers are computed using the stacking recurrences [see Eq. (2.42)]:

$$\boldsymbol{\mathcal{F}}_0^+ = \boldsymbol{\mathcal{R}}_m^a \boldsymbol{\mathcal{F}}_0^- + \boldsymbol{\mathcal{T}}_m^b \boldsymbol{\mathcal{F}}_m^+ \tag{5.6}$$

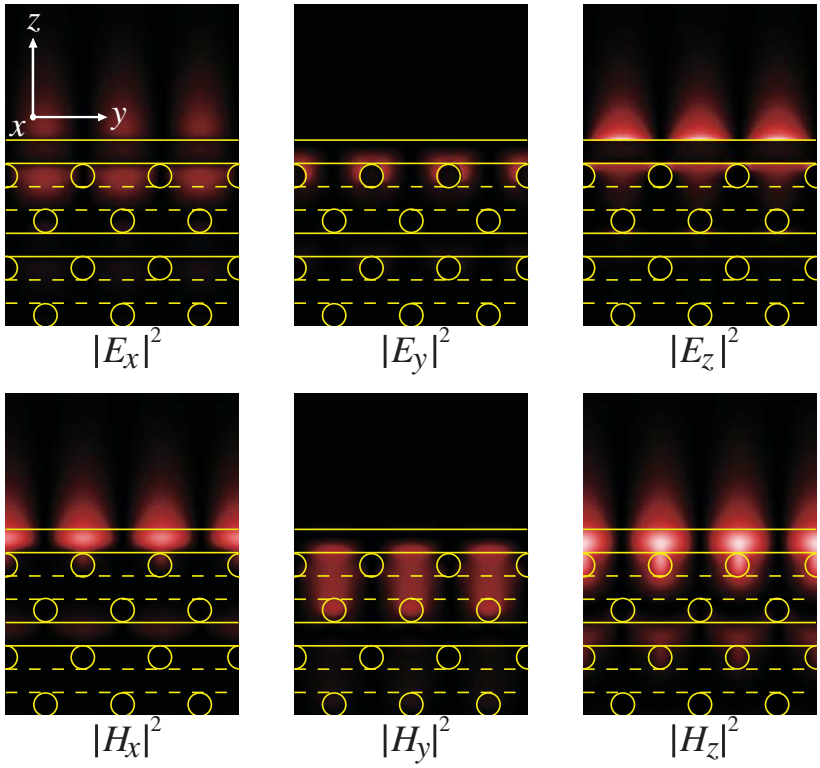

Figure 5.3: The intensities of the electric (**E**) and magnetic (**H**) field components for the mode at point A of Fig. 3(c) ($d/\lambda = 0.522$, $k_x = 0.54 \times \pi/d$, $k_y = \pi/d$). The dotted lines indicate the positions of cylinders that run parallel to the y-axis, and that do not intersect the plane of the plot.

and

$$\boldsymbol{\mathcal{F}}_m^- = \boldsymbol{\mathcal{R}}_m^b \boldsymbol{\mathcal{F}}_m^+ + \boldsymbol{\mathcal{T}}_m^a \boldsymbol{\mathcal{F}}_0^-, \tag{5.7}$$

where $\boldsymbol{\mathcal{R}}_m^a$ and $\boldsymbol{\mathcal{R}}_m^b$ are the reflection matrices for the top and bottom surfaces, respectively, and $\boldsymbol{\mathcal{T}}_m^a$ and $\boldsymbol{\mathcal{T}}_m^b$ are the corresponding transmission matrices. (Recall that $\boldsymbol{\mathcal{F}}_l^{\pm}$ denote the planewave fields impinging on the bottom boundary of the l^{th} grating of the stack, with $l = 0$ and $l = m$ specifying the top and bottom surfaces, respectively. See Fig. 5.1) The condition for a surface mode is that there is no incoming field, *i.e.*, $\boldsymbol{\mathcal{F}}_0^- = \boldsymbol{\mathcal{F}}_m^+ = \mathbf{0}$. From Eqs. (5.6) and (5.7), we conclude that surface modes exist precisely when either of $\boldsymbol{\mathcal{R}}_m^a$ or $\boldsymbol{\mathcal{T}}_m^b$ has a pole that coincides with a pole of either $\boldsymbol{\mathcal{R}}_m^b$ or $\boldsymbol{\mathcal{T}}_m^a$. In fact, it can be shown that the poles of all of the these matrices coincide (see Appendix 5.A) and, thus, one only needs to consider the poles of $\boldsymbol{\mathcal{R}}_m^a$. We reason that if $\boldsymbol{\mathcal{R}}_m^a$ has a pole, then $(\boldsymbol{\mathcal{R}}_m^a)^{-1}$ is singular, *i.e.*,

$$(\boldsymbol{\mathcal{R}}_m^a)^{-1} \boldsymbol{\mathcal{F}} = \mathbf{0}, \tag{5.8}$$

for some vector $\boldsymbol{\mathcal{F}}$. We will proceed formally, but before doing so we will demonstrate that Eq. (5.8) is consistent with Eq. (5.5).

A corollary of Eq. (5.8) is that the surface modes of a finite stack resemble the surface modes of the semi-infinite stack when m is large (assuming that there is periodicity in the stacking direction), since $\boldsymbol{\mathcal{R}}_m^a \to \boldsymbol{\mathcal{R}}_\infty$ as $m \to \infty$, where $\boldsymbol{\mathcal{R}}_\infty$ is the reflection matrix of a semi-infinite grating stack. Further, in the limit as $m \to \infty$, Eq. (5.8) is equivalent to Eq. (5.5) because

$$\boldsymbol{\mathcal{R}}_\infty = \mathbf{F}_+(\mathbf{F}_-)^{-1}, \tag{5.9}$$

which follows readily from Eq. (5.1) by setting $l = 0$ and $\mathbf{c}^+ = \mathbf{0}$ (see also [26] and [124]), and so

$$(\boldsymbol{\mathcal{R}}_\infty)^{-1}\boldsymbol{\mathcal{F}} = \mathbf{F}_-(\mathbf{F}_+)^{-1}\boldsymbol{\mathcal{F}} = \mathbf{0}. \tag{5.10}$$

Since $\mathbf{F}_+$ is invertible, it follows that surface modes exist for semi-infinite woodpiles when $\mathbf{F}_-$ has non-trivial null vectors, as before. Note that if instead the stack extended indefinitely in the upwards direction, then we would have derived

$$(\boldsymbol{\mathcal{R}}'_\infty)^{-1}\boldsymbol{\mathcal{F}} = \mathbf{0}, \tag{5.11}$$

where

$$\boldsymbol{\mathcal{R}}'_\infty = \mathbf{F}'_-(\mathbf{F}'_+)^{-1} \tag{5.12}$$

is the reflection matrix of a semi-infinite stack that extends upwards, *i.e.*, $\boldsymbol{\mathcal{R}}_m^b \to \boldsymbol{\mathcal{R}}'_\infty$ as $m \to -\infty$.

5.4 Surface modes of finite woodpiles

Next, we derive equations that determine the surface modes of a woodpile that consists of a finite number of layers. Unsurprisingly, the behaviour of the surface modes depends greatly on the alignment of the rods of the top layer relative to the rods of the bottom layer, *i.e.*, the behaviour depends on whether the number of layers m is even or odd. In each case, a general equation that governs the modes is derived, and this equation is then used to illustrate numerically the main features of the modes. It is then shown that the general equation leads to a factorisable form that better explains the behaviour of the modes.

5.4.1 Even number of layers

First, suppose that the number of layers $m = 2n$ is even. In this case, the number of unit-cells, n, in the stacking direction is an integer, which means that the plane wave fields immediately below the j^{th} layer of a stack of n grating pairs are still given by Eq. (5.1), with $j = 0$ and $j = n$ specifying the top and bottom surfaces of the woodpile, respectively (see Fig. 5.1). Equation (5.1) can be solved for the Bloch mode field expansions $\mathbf{c}^-$ and $\mathbf{c}^+$ by using the fact that $\boldsymbol{\mathcal{F}}_0^- = \boldsymbol{\mathcal{F}}_m^+ = \mathbf{0}$ for surface modes. One finds that

$$\mathbf{c}^- = \mathfrak{R}^a(\boldsymbol{\Lambda}')^{-n}\mathbf{c}^+ \quad \text{and} \quad \mathbf{c}^+ = \mathfrak{R}^b\boldsymbol{\Lambda}^n\mathbf{c}^-, \tag{5.13}$$

where

$$\mathfrak{R}^a = -(\mathbf{F}_-)^{-1}\mathbf{F}'_- \quad \text{and} \quad \mathfrak{R}^b = -(\mathbf{F}'_+)^{-1}\mathbf{F}_+ \tag{5.14}$$

serve as internal reflection coefficients for the top and bottom surfaces, respectively, and act directly on the Bloch modes. Solving Eqs. (5.13) for $\mathbf{c}^-$ gives

$$\begin{aligned}\left[\mathbf{I} - \mathfrak{R}^a(\boldsymbol{\Lambda}')^{-n}\mathfrak{R}^b\boldsymbol{\Lambda}^n\right]\mathbf{c}^- &\stackrel{\text{def}}{=} \mathfrak{B}\mathbf{c}^- \\ &= \mathbf{0},\end{aligned} \tag{5.15}$$

which has non-trivial solutions precisely when there are one or more surface modes.

Figures 5.4(a)-5.4(c) show the dispersion curves [computed using Eq. (5.15)] of the modes of an $m = 8$, $m = 6$ and an $m = 4$ layer woodpile (blue thin curves), respectively. For comparison, the dispersion curves for the surface modes of the semi-infinite woodpile are also shown in Fig. 5.4 (red thick curves), and are the same as those in Fig. 5.2(c). Three types of surface modes are evident for the finite structure: those that propagate along the top surface (solid curves), those propagating along the bottom surface (dotted curves), and double-interface modes (solid curves along the $\Gamma - \mathrm{M}$ direction, which corresponds to $k_x = k_y$). One can anticipate that for every mode propagating on the top surface with a certain frequency d/λ and Bloch vector (k_x, k_y), there must be a corresponding mode on the bottom surface that propagates with the same frequency, but whose Bloch vector is instead (k_y, k_x). Note that the rods of the top layers ($l = 0$) of both the semi-infinite and finite woodpiles were chosen to lie parallel to the y-axis, which is why there is a one-to-one correspondence between the red curves and the solid blue curves (not including the $\Gamma - \mathrm{M}$ direction). For $m \geq 6$, the deviation between these two sets of curves is small, indicating that the fields inside the woodpile decay quickly in the stacking direction. Observe that, in addition to surface modes, there are solutions that lie in-band

(*i.e.*, modes whose frequencies lie outside of the directional bandgap). They arise because in deriving Eq. (5.15) we did not rely on the existence of a bandgap. These modes always lie below the light-line and, thus, they are woodpile PC slab modes, which, as a result of total internal reflection, can only propagate within the woodpile region.

Along the $\Gamma - \mathrm{M}$ direction, the presence of the second surface causes the red curve to 'split' into a pair of double-interface modes (blue curves), one of which can be classified as *even*, and the other of which is *odd*. This splitting always occurs for this direction when the number of layers m is even (so long as $\delta_x = \delta_y = d/2$), and is clearly discernible for the 4- and 6-layer woodpiles, while for the 8-layer woodpile, the splitting is only appreciable when the modes are in-band. As m increases, the strength of the coupling between the top and bottom surface decreases (owing to the photonic bandgap) and, hence, the strength of the splitting decreases, where the splitting strength is defined as the amount the frequencies of the even and odd modes differ from that of the corresponding mode of the semi-infinite woodpile. Thus, for any double interface mode, we can conclude from Fig. 5.4(a) that when $m \geq 8$, the fields propagating along the top surface will be, in effect, decoupled from those propagating along the bottom surface. In general, the field of the even (odd) mode is not necessarily symmetric (antisymmetric), since the relationship between the fields on the top surface and those on the bottom surface depends on $\mathbf{k}_t$. Figure 5.5 shows the plots of the real and imaginary parts of E_z for the even mode ($\lambda/d = 0.535$) and for the odd mode ($\lambda/d = 0.548$) at $\mathbf{k}_t = (0.81, 0.81) \times (\pi/d)$ for the 6-layer stack. Note that for this value $\mathbf{k}_t$, E_z of the even mode is antisymmetric, while E_z of the odd mode is symmetric.

Equation (5.15) was previously derived in [125] for 2D PCs (see, in particular, Eq. (6) of [125]), although the approach used in that study instead relied on impedance matrices. In the case of 2D square and triangular lattices, the internal reflection matrices and Bloch factors satisfy $\mathfrak{R}^a = \mathfrak{R}^b$ and $(\mathbf{\Lambda}')^{-1} = s\mathbf{\Lambda}$ for some phase factor s, and so Eq. (5.15) can always be factorised, while for woodpiles such relationships do not hold in general. It will be shown that the existence of such a factorisation implies that the mode propagates on both the top and bottom surfaces simultaneously (a 'double-interface' mode), *i.e.*, the average magnitude of the fields along one surface will be comparable to the average magnitude along the opposing surface, with the fields decaying exponentially on either side of each surface. The reason why a factorisation of Eq. (5.15) is always possible for 2D PCs is that the top and bottom surfaces are equivalent (assuming that the 2D PC is terminated symmetrically) and so, in this case, every surface mode must be a double-interface mode. However, for finite woodpiles, Eq. (5.15) usually cannot be factorised

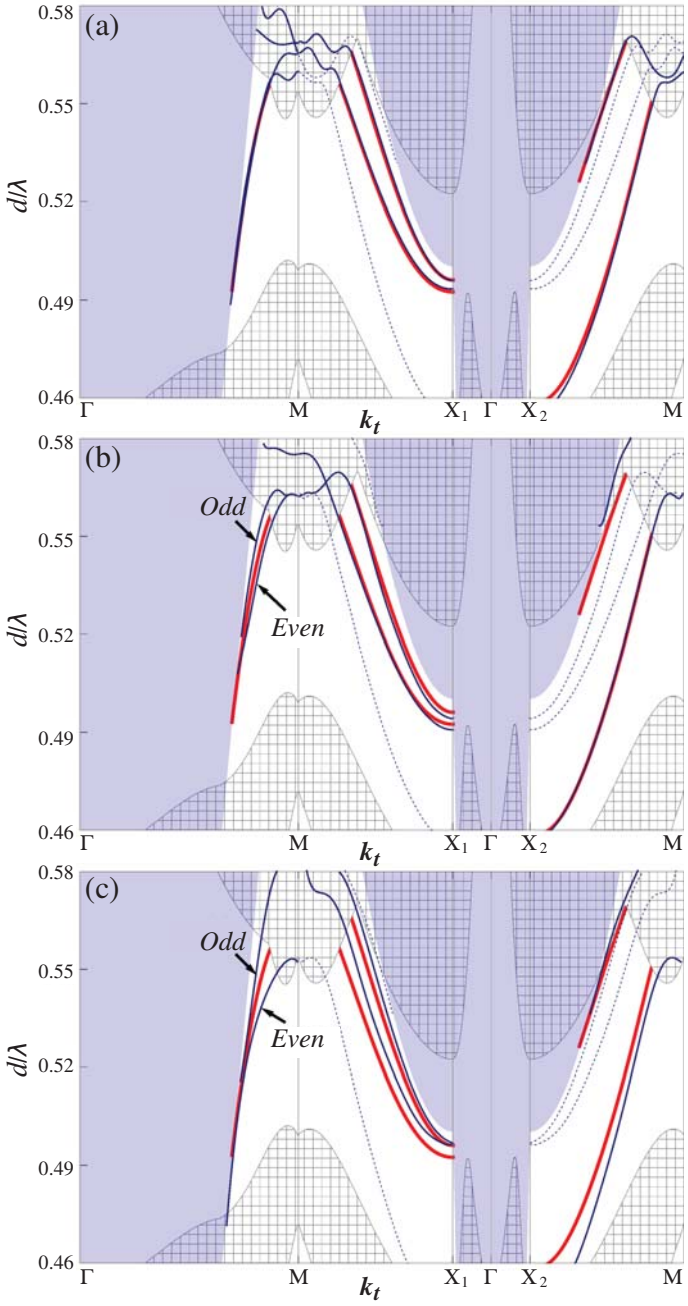

Figure 5.4: Dispersion curves (blue thin curves) for the surface modes an (a) $m = 8$, (b) $m = 6$ and (c) an $m = 4$ layer woodpile. The surface modes of the corresponding semi-infinite woodpile are shown for comparison (red thick curves). The solid (dotted) curves correspond to single-interface modes that propagate along the top (bottom) surface. The blue curves along the $\Gamma - \mathrm{M}$ direction are double-interface modes, *i.e.*, solutions of Eqs. (5.18) ('Even') and (5.20) ('Odd'). The strength of the splitting between the even and the odd double-interface mode of the 8-layer woodpile is not appreciable.

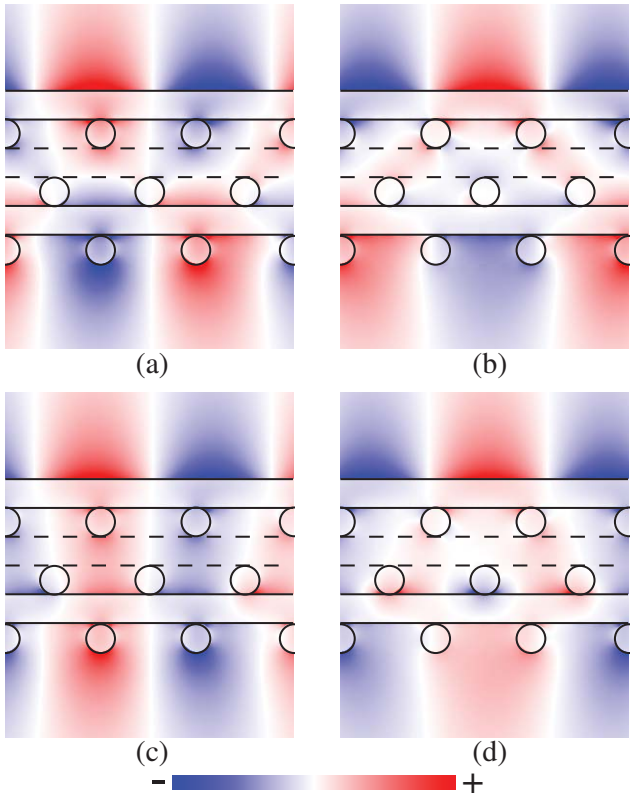

Figure 5.5: Plots of the z-component of the electric field of the even and odd double-interface modes of a 6-layer woodpile. The even and odd modes correspond to the points in Fig. 5.4(b) that are labelled 'Even' and 'Odd', respectively ($k_x = k_y = 0.81\pi/d$). (a) $\mathfrak{Re}(E_z)$ and (b) $\mathfrak{Im}(E_z)$ of the even mode ($\lambda/d = 0.535$). (c) $\mathfrak{Re}(E_z)$ and (d) $\mathfrak{Im}(E_z)$ of the odd mode ($\lambda/d = 0.548$). For this value of $\mathbf{k}_t = (k_x, k_y)$, E_z of the even mode has an odd field pattern, whereas E_z of the odd mode has an even pattern.

when m is even because, in this case, the top and bottom surfaces are physically distinct from one another in that the rods of the top layer are orthogonal to those of the bottom layer. Usually, then, a given surface mode will propagate predominantly along either the top or bottom surface of the woodpile, and the fields at the opposing surface will be much weaker.

However, when $k_x = k_y$ (*i.e.*, along the $\Gamma - \mathrm{M}$ direction of the Brillouin zone), the surface mode travels along an azimuth that makes a 45° angle with the rods of both the top and bottom surfaces, and so in this case the two surfaces are, in essence, equivalent. A surface mode propagating along this direction must, therefore, propagate along both surfaces simultaneously. Accordingly, the multipole field expansions for the scattering matrices [see Eqs. (3.26) and (3.27)] can be used to prove that, for the $\Gamma - \mathrm{M}$ direction,

the symmetry relationships

$$\mathfrak{R}^a = \mathfrak{R}^b \quad \text{and} \quad (\mathbf{\Lambda}')^{-1} = s\mathbf{\Lambda} \tag{5.16}$$

hold for woodpiles when $\delta_x = \delta_y = d/2$, with $s = \exp(-ik_x d)\exp(-ik_y d)$. The proofs of these relationships are given in Appendix 5.B. Equation (5.15) then becomes, after factorising,

$$(\mathbf{I} + s^{n/2}\mathfrak{R}^a\mathbf{\Lambda}^n)(\mathbf{I} - s^{n/2}\mathfrak{R}^a\mathbf{\Lambda}^n)\mathbf{c}^- = \mathbf{0}, \tag{5.17}$$

which implies that either

$$(\mathbf{I} - s^{n/2}\mathfrak{R}^a\mathbf{\Lambda}^n)\mathbf{c}^- = \mathbf{0}, \tag{5.18}$$

with

$$\mathbf{c}^- = s^{n/2}\mathbf{c}^+, \tag{5.19}$$

or

$$(\mathbf{I} + s^{n/2}\mathfrak{R}^a\mathbf{\Lambda}^n)\mathbf{c}^- = \mathbf{0}, \tag{5.20}$$

with

$$\mathbf{c}^- = -s^{n/2}\mathbf{c}^+. \tag{5.21}$$

For convenience, we refer to the modes that satisfy Eqs. (5.19) and (5.21) as *even* modes and *odd* modes, respectively, despite the appearance of the phase factor $s^{n/2}$, which depends on both k_x and the number of grating pairs. Such a partitioning of the double-interface modes is only possible because of the high structural symmetry along the $\Gamma - \mathrm{M}$ direction. Our choice of which solution is even and which is odd is somewhat arbitrary, since the phase factor $s^{n/2}$ depends on both k_x and the number of grating pairs. However, when $s^{n/2} = 1$ (e.g., at the M point of the Brillouin zone, that is, at $k_x = k_y = \pi/d$), Eqs. (5.19) and (5.21) reduce to $\mathbf{c}^- = \pm\mathbf{c}^+$, which are the usual notions of even and odd parity in that the fields of the even mode are in phase at the top and bottom surfaces, while the fields of the odd mode are out of phase by an amount π at the top and bottom surfaces.

An alternative formulation for the surface modes of a woodpile (m even) can be derived by solving Eq. (5.1) for the outgoing fields $\boldsymbol{\mathcal{F}}_0^+$ and $\boldsymbol{\mathcal{F}}_m^-$ at the surfaces. One finds that

$$(\boldsymbol{\mathcal{R}}_m^a)^{-1}\boldsymbol{\mathcal{F}}_0^+ = \mathbf{0}, \tag{5.22}$$

and

$$(\boldsymbol{\mathcal{T}}^a_m)^{-1}\boldsymbol{\mathcal{F}}^-_m = \mathbf{0}, \tag{5.23}$$

where the reflection and transmission matrices, $\boldsymbol{\mathcal{R}}^a_m$ and $\boldsymbol{\mathcal{T}}^a_m$ [see Eqs. (5.6) and (5.7)] are given by

$$\boldsymbol{\mathcal{R}}^a_m = \mathbf{F}'_+ \left[-\boldsymbol{\mathfrak{R}}^b + (\boldsymbol{\Lambda}')^{-n}\boldsymbol{\mathfrak{R}}^b\boldsymbol{\Lambda}^n\right]\boldsymbol{\mathfrak{B}}^{-1}(\mathbf{F}_-)^{-1} \tag{5.24}$$

and

$$\boldsymbol{\mathcal{T}}^a_m = \mathbf{F}_- \left[\mathbf{I} - \boldsymbol{\mathfrak{R}}^a\boldsymbol{\mathfrak{R}}^b\right]\boldsymbol{\Lambda}^n\boldsymbol{\mathfrak{B}}^{-1}(\mathbf{F}_-)^{-1}, \tag{5.25}$$

with $\boldsymbol{\mathfrak{B}}$ as in Eq. (5.15). Equations (5.24) and (5.25), which follow immediately from Eqs. (47) and (48) of [26], are the forms that the Airy formulae [98] assume in PC slabs. The post-factor $(\mathbf{F}_-)^{-1}$ converts downward plane wave fields into the Bloch basis, and the pre-factors $\mathbf{F}'_+$ and $\mathbf{F}_-$ convert the result back into upward and downward plane wave fields, respectively. Equation (5.22) is simply the heuristic described earlier [see Eq. (5.8)]. In addition, it can be seen that the poles of $\boldsymbol{\mathcal{R}}^a_m$ and $\boldsymbol{\mathcal{T}}^a_m$ coincide with the zeroes of $\boldsymbol{\mathfrak{B}}$ [*cf.* Eq. (5.15)], and, since $\boldsymbol{\mathcal{R}}^a_m$ and $\boldsymbol{\mathcal{T}}^a_m$ can be inverted analytically, either of Eqs. (5.22) and (5.23) is a sufficient condition for the existence of a surface mode. Similarly, by making the substitution $j \to -(n - j')$ in Eq. (5.1), so that $j' = 0$ and $j' = n$ correspond, respectively, to the bottom and top surfaces, it can be shown that the surface modes also coincide with the poles of $\boldsymbol{\mathcal{R}}^b_m$ and $\boldsymbol{\mathcal{T}}^b_m$. We have verified numerically that the zeroes of Eq. (5.22) are the same as the zeroes of Eqs. (5.18) and (5.20), and are also the same as those of Eq. (5.15).

We conclude that, for $k_x = k_y$, the modes of a finite stack that comprises $m = 2n$ layers appear as pairs of even and odd double-interface modes that can be regarded as a 'splitting' of a single mode of the corresponding semi-infinite stack into two distinct modes, with the strength of the splitting increasing as the number of layers decreases.

5.4.2 Odd number of layers

When m is odd, the top surface of the woodpile is truncated halfway through a stacking unit, making it difficult to express the fields as Bloch mode expansions. In this case, we instead formulate the problem entirely in the plane wave basis, and regard the woodpile as two stacks, each consisting of n layers, separated by a single layer, as illustrated in Fig. 5.6. Further, for this section we impose the constraint $\delta_x = \delta_y = d/2$, which results in a highly symmetrical woodpile that is invariant under the glide-reflection transformation

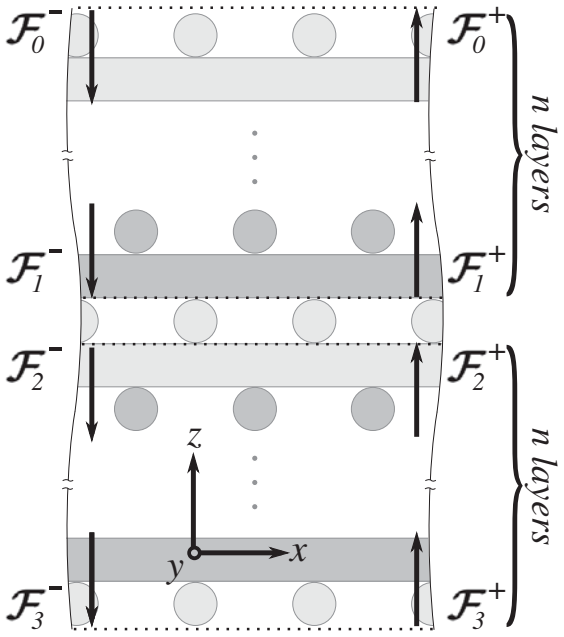

Figure 5.6: The phase origins (dotted horizontal lines) of the plane wave fields incident to the top surface ($\boldsymbol{\mathcal{F}}_0^{\pm}$), bottom surface ($\boldsymbol{\mathcal{F}}_3^{\pm}$), and the middle layer ($\boldsymbol{\mathcal{F}}_1^{\pm}$ and $\boldsymbol{\mathcal{F}}_2^{\pm}$) of a $2n+1$ layer woodpile.

$(y \to y + d/2)$, $(z \to -z)$, where the middle layer is taken to lie along $z = 0$, and which ensures the existence of double-interface modes.

We denote the plane wave fields above and below the middle layer by $\boldsymbol{\mathcal{F}}_1^{\pm}$ and $\boldsymbol{\mathcal{F}}_2^{\pm}$, respectively, and denote the fields at the surfaces by $\boldsymbol{\mathcal{F}}_0^{\pm}$ (top) and $\boldsymbol{\mathcal{F}}_3^{\pm}$ (bottom). The outgoing fields incident to the middle layer satisfy relationships analogous to Eqs. (5.6) and (5.7), specifically:

$$\boldsymbol{\mathcal{F}}_1^+ = \boldsymbol{\mathcal{R}}\boldsymbol{\mathcal{F}}_1^- + \boldsymbol{\mathcal{T}}\boldsymbol{\mathcal{F}}_2^+ \tag{5.26}$$

and

$$\boldsymbol{\mathcal{F}}_2^- = \boldsymbol{\mathcal{R}}\boldsymbol{\mathcal{F}}_2^+ + \boldsymbol{\mathcal{T}}\boldsymbol{\mathcal{F}}_1^-, \tag{5.27}$$

in which $\boldsymbol{\mathcal{R}}$ and $\boldsymbol{\mathcal{T}}$ are plane wave scattering matrices for the middle layer (only a single reflection and transmission matrix is required because the layer is up-down symmetric). Similarly, the incoming fields incident to the middle layer satisfy:

$$\boldsymbol{\mathcal{F}}_1^- = \boldsymbol{\mathcal{R}}_n^b \boldsymbol{\mathcal{F}}_1^+ + \boldsymbol{\mathcal{T}}_n^a \boldsymbol{\mathcal{F}}_0^- \tag{5.28}$$

and

$$\boldsymbol{\mathcal{F}}_2^+ = \boldsymbol{\mathcal{R}}_n'^a \boldsymbol{\mathcal{F}}_2^- + \boldsymbol{\mathcal{T}}_n'^b \boldsymbol{\mathcal{F}}_3^+. \tag{5.29}$$

Here, $\boldsymbol{\mathcal{R}}_n^b$ ($\boldsymbol{\mathcal{T}}_n^a$) is the reflection (transmission) matrix for the bottom (top) surface of the n-layer stack above the middle layer, and $\boldsymbol{\mathcal{R}}_n'^a$ ($\boldsymbol{\mathcal{T}}_n'^b$) is the reflection (transmission) matrix for the top (bottom) surface of the stack below the middle layer. Since the entire structure possesses glide-reflection symmetry (discussed below), the scattering matrices of the two 'half-stacks' are related via a similarity transform:

$$\boldsymbol{\mathcal{R}}_n'^a = \mathbf{Q}_y \boldsymbol{\mathcal{R}}_n^b \mathbf{Q}_y \quad \text{and} \quad \boldsymbol{\mathcal{T}}_n'^b = \mathbf{Q}_y \boldsymbol{\mathcal{T}}_n^a \mathbf{Q}_y, \tag{5.30}$$

where the similarity transform shifts the cylinders by an amount $d/2$ along the positive y-axis, and where $\mathbf{Q}_y$ is a diagonal matrix such that $\mathbf{Q}_y^{-1} = \mathbf{Q}_y$ [see Appendix 5.C]. Putting $\boldsymbol{\mathcal{F}}_0^- = \boldsymbol{\mathcal{F}}_3^+ = \mathbf{0}$, and then solving Eqs. (5.26)-(5.30) for the outgoing fields $\boldsymbol{\mathcal{F}}_1^+$ and $\boldsymbol{\mathcal{F}}_2^-$ gives

$$\boldsymbol{\mathcal{F}}_1^+ = \mathbf{D}_{12} \boldsymbol{\mathcal{F}}_2^- \tag{5.31}$$

and

$$\boldsymbol{\mathcal{F}}_2^- = \mathbf{D}_{21} \boldsymbol{\mathcal{F}}_1^+, \tag{5.32}$$

with

$$\mathbf{D}_{12} = (\mathbf{I} - \boldsymbol{\mathcal{R}} \boldsymbol{\mathcal{R}}_n^b)^{-1} \boldsymbol{\mathcal{T}} \mathbf{Q}_y \boldsymbol{\mathcal{R}}_n^b \mathbf{Q}_y \tag{5.33}$$

and

$$\mathbf{D}_{21} = (\mathbf{I} - \boldsymbol{\mathcal{R}} \mathbf{Q}_y \boldsymbol{\mathcal{R}}_n^b \mathbf{Q}_y)^{-1} \boldsymbol{\mathcal{T}} \boldsymbol{\mathcal{R}}_n^b. \tag{5.34}$$

Equations (5.31)-(5.34) determine $\boldsymbol{\mathcal{F}}_1^+$ and $\boldsymbol{\mathcal{F}}_2^-$.

The dispersion curves for the surface modes of a 9-, 7- and 5-layer woodpile are shown in Figs. 5.7(a)-5.7(c), respectively (blue/dark curves), along with the dispersion curves for the surface modes of the corresponding semi-infinite stack (red/thick curves). Unlike the m even case, every blue curve in Fig. 5.7 corresponds to a double-interface mode, since the top and bottom surfaces are essentially equivalent. The rods of both surfaces of the finite woodpile were taken to lie parallel to the y-axis, *i.e.*, parallel to the rods of the surface of the semi-infinite woodpile, thus, from the results of the Sec. 5.4.1, we can expect that the presence of a second surface will cause each red curve in Fig. 5.7 to 'split' into two new modes (blue curves), one of which will be quasi-even, and the other of which will be quasi-odd. This is evident in the $\mathrm{X}_2 - \mathrm{M}$ direction ($k_x = \pi/d$) for the 9- and 5-layer woodpiles [Figs. 5.7(a) and 5.7(c)]. However, along the $\mathrm{M} - \mathrm{X}_1$ direction (*i.e.*, when $k_y = \pi/d$), the quasi-even and quasi-odd modes correspond to degenerate symmetric and antisymmetric modes. This is because the symmetric and antisymmetric modes of any photonic crystal that is invariant under the glide-reflection transformation

$(y \to y + d/2)$, $(z \to -z)$, such as the 9- and 5-layer woodpiles considered here, become degenerate when $k_y = \pi/d$ [106]. Similarly, if the 'glide-direction' is parallel to the x-axis, as happens for the 7-layer woodpile, then the modes instead become degenerate when $k_x = \pi/d$ (*i.e.*, along the $\mathrm{X}_2 - \mathrm{M}$ direction), as can be seen in Fig. 5.7(b).

These degenerate modes are very similar in frequency to the corresponding modes of the semi-infinite woodpile. This is quite remarkable because the blue curves correspond to double-interface modes, while the red curves are single-interface modes. The similarity in frequency occurs because, for the degenerate modes, the coupling between the fields at the top surface and the fields at the bottom surface is particularly weak (the reasons for this are discussed in more detail in Section 5.4.3). Conversely, when there is no degeneracy, the difference between the blue curves and the red curves is sizeable because, in this case, the interaction between the mode on the top surface and the mode on the bottom surface is much stronger than for the degenerate double-interface modes. The splitting in the $\Gamma - \mathrm{M}$ direction only becomes appreciable when $m \leq 7$, and is markedly weaker than the splitting in the other directions (not including the degenerate modes), suggesting that the strength of the field confinement in the z-direction is stronger for modes for which $k_x = k_y$.

In general, the non-degenerate quasi-even and quasi-odd modes exhibit a stronger deviation from the red curves than do the single-interface modes of the m-even woodpiles because the mode on the top surface can couple to the mode on the bottom surface. When m is odd, the strength of the splitting in the $\Gamma - \mathrm{M}$ direction is weaker than when m is even, as can be seen in the dispersion curves for the 5- and 6-layer woodpiles [Figs. 5.7(c) and 5.4(b)]. Thus, the coupling strength between the field at the top surface and the field at the bottom surface depends not only on the number of layers, but also on the orientation of the rods of the top surface relative to those of the bottom surface. As was for the m-even case, modes that lie below the light-line but that do not lie inside a bandgap correspond to woodpile PC slab modes.

Figure 5.8 shows the plots of the real and imaginary parts of E_z for the quasi-even mode ($\lambda/d = 0.512$) and for the quasi-odd mode ($\lambda/d = 0.519$) at $\mathbf{k}_t = (1.0, 0.608) \times (\pi/d)$ for the 9-layer stack. Along the $x/d = 0.0$ plane, the fields of the quasi-even mode have 'TE-like' polarisation (*i.e.*, the dominant field components are the H_x, E_y and E_z components), and, while the E_y component has a symmetric field distribution, the H_x and E_z components have antisymmetric field distributions. Conversely, along the $x/d = 0.5$ plane, *i.e.*, halfway through the unit-cell, the quasi-even mode instead has 'TM-like' polarisation (*i.e.*, the dominant field components are the E_x, H_y and H_z components), with

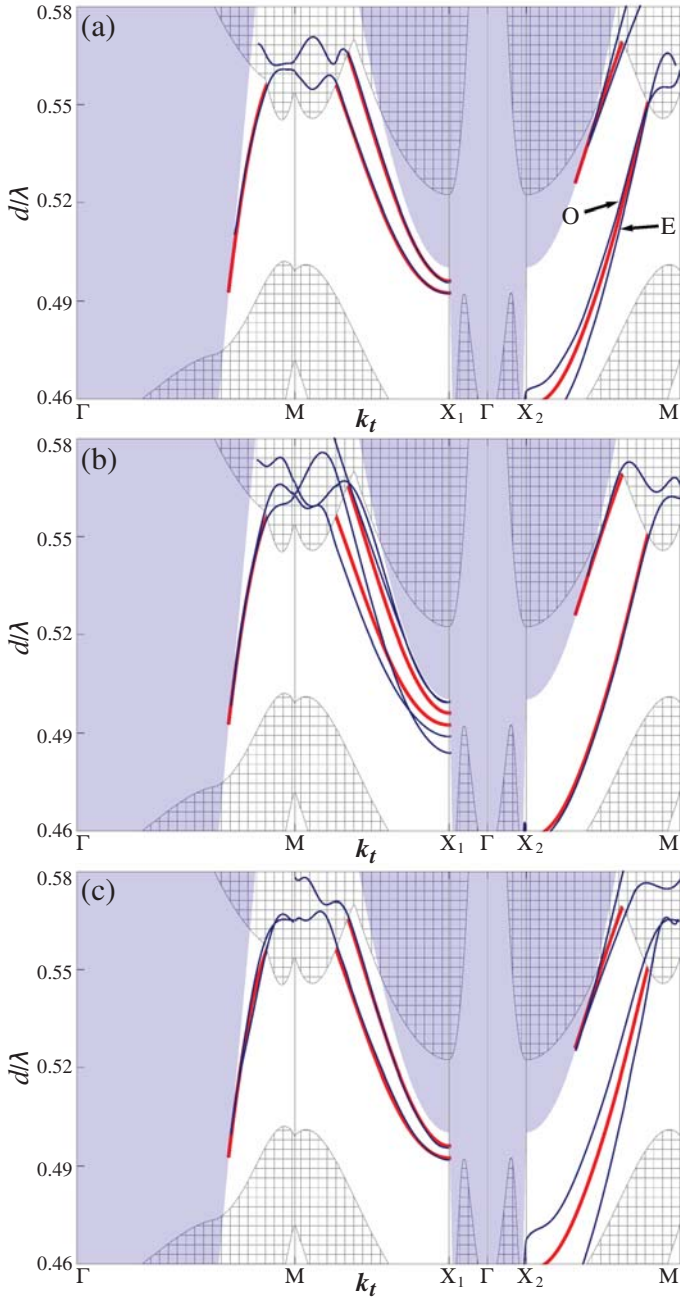

Figure 5.7: The dispersion curves (blue/dark) for the surface modes of an (a) $m = 9$, (b) $m = 7$ and (c) an $m = 5$ layer woodpile. The surface modes of the semi-infinite woodpile are also shown (red/thick). All surface modes of the finite woodpile are double-interface modes. The fields at the points labelled E (quasi-even) and O (quasi-odd) on the curves for the 9-layer woodpile are shown in Fig. 5.8.

the E_x and H_z components having symmetric patterns, and the H_y component having an antisymmetric pattern. As x/d increases, the fields of the quasi-even mode alternate smoothly between TE-like and TM-like polarisation (not shown). The polarisation pattern of the quasi-odd mode is the same as that of the quasi-even mode, except that each component of the quasi-odd mode is opposite in parity to the corresponding component of the quasi-even mode.

It can be anticipated from the results of the previous section that the mode splitting observed in Fig. 5.7 implies that Eqs. (5.31) and (5.32) can be expressed as a factorisation. By making use of the fact that

$$\boldsymbol{\mathcal{R}} = \mathbf{Q}_y \boldsymbol{\mathcal{R}} \mathbf{Q}_y \quad \text{and} \quad \boldsymbol{\mathcal{T}} = \mathbf{Q}_y \boldsymbol{\mathcal{T}} \mathbf{Q}_y, \tag{5.35}$$

(the middle layer is invariant under translations in the y-direction), one can express Equation (5.31) in the form

$$\boldsymbol{\mathcal{F}}_1^+ = \mathbf{Q}_y \mathbf{D}_{21} \mathbf{Q}_y \boldsymbol{\mathcal{F}}_2^-, \tag{5.36}$$

which, along with Eq. (5.32), allows $\boldsymbol{\mathcal{F}}_1^+$ to be expressed as the solutions of

$$(\mathbf{I} + \mathbf{Q}_y \mathbf{D}_{21})(\mathbf{I} - \mathbf{Q}_y \mathbf{D}_{21}) \boldsymbol{\mathcal{F}}_1^+ = \mathbf{0}. \tag{5.37}$$

Equation (5.37) admits two types of solutions, namely the solutions of

$$(\mathbf{I} - \sigma \mathbf{Q}_y \mathbf{D}_{21}) \boldsymbol{\mathcal{F}}_1^+ = \mathbf{0}, \tag{5.38}$$

with either $\sigma = 1$, which we refer to as the 'quasi-even' solution, or $\sigma = -1$ ('quasi-odd'). It follows that $\boldsymbol{\mathcal{F}}_1^+ = \sigma \mathbf{Q}_y \boldsymbol{\mathcal{F}}_2^-$, with the fields at the surfaces given by $\boldsymbol{\mathcal{F}}_0^+ = \boldsymbol{\mathcal{T}}_n^b \boldsymbol{\mathcal{F}}_1^+$ and $\boldsymbol{\mathcal{F}}_3^- = \boldsymbol{\mathcal{T}}_n'^a \boldsymbol{\mathcal{F}}_2^-$, where $\boldsymbol{\mathcal{T}}_n^b$ is the transmission matrix for the bottom surface of the sub-stack comprising the first n-layers, and $\boldsymbol{\mathcal{T}}_n'^a$ is the transmission matrix for the top surface of the sub-stack comprising the last n-layers. Since $\boldsymbol{\mathcal{T}}_n'^a = \mathbf{Q}_y \boldsymbol{\mathcal{T}}_n^b \mathbf{Q}_y$, we have the following relationship between the fields on either surface:

$$\boldsymbol{\mathcal{F}}_0^+ = \sigma \mathbf{Q}_y \boldsymbol{\mathcal{F}}_3^-. \tag{5.39}$$

The action of $\mathbf{Q}_y$ on a field can be understood by expressing $\mathbf{Q}_y$ in the form $\mathbf{Q}_y = s_y^{-1} \boldsymbol{\mathcal{Q}}_y$, with $\boldsymbol{\mathcal{Q}}_y = (s_y \mathbf{Q}_y)$ and $s_y = \exp(ik_y \delta_y)$. The operator $\boldsymbol{\mathcal{Q}}_y$ simply shifts the phases of the fields by an amount δ_y in the y-direction, thus, Eq. (5.39) states that the surface modes concentrate equally at the top and bottom surfaces. Unlike the factorisation for the m

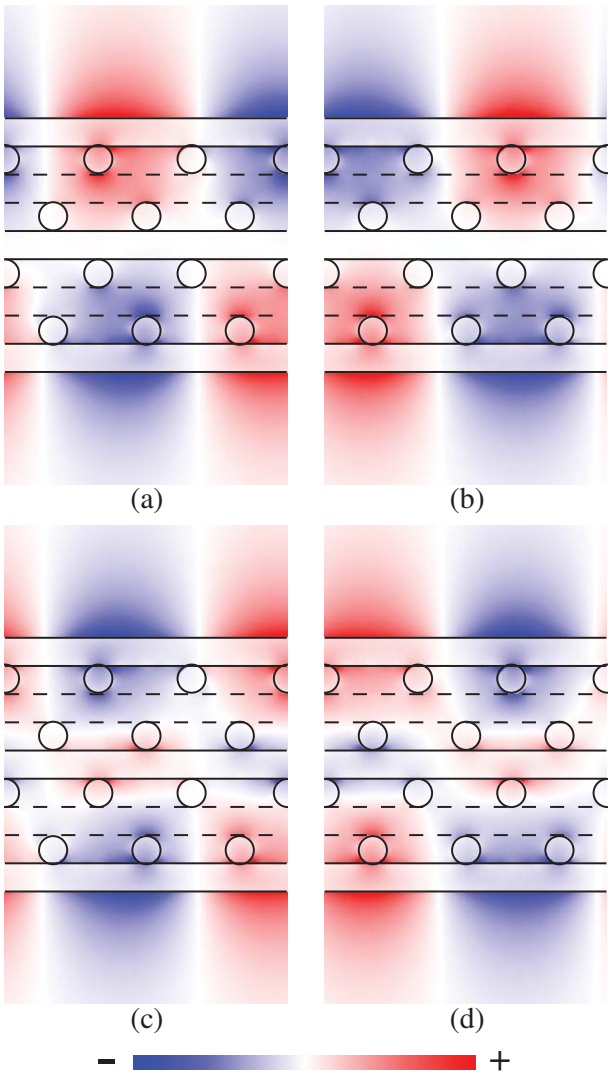

Figure 5.8: Plots of the z-component of the electric field of the quasi-even and quasi-odd double-interface mode of a 9-layer woodpile. (a) $\mathfrak{Re}(E_z)$ and (b) $\mathfrak{Im}(E_z)$ of the quasi-even mode ($\lambda/d = 0.512$). (c) $\mathfrak{Re}(E_z)$ and (d) $\mathfrak{Im}(E_z)$ of the quasi-odd mode ($\lambda/d = 0.519$). The quasi-even and quasi-odd mode correspond to point E and point O of Fig. 8(a), respectively ($k_x = \pi/d$, $k_y = 0.608\pi/d$).

even case, the factorisation given by Eq. (5.37) is possible at any point of the Brillouin zone when m is odd (so long as $\delta_x = \delta_y = d/2$). In short, under these conditions, the surface modes are always double-interface modes because the top and bottom surfaces are equivalent up to a shift by $d/2$ in the y-direction.

We have verified numerically that Eq. (5.38) is equivalent to finding the poles of $\boldsymbol{\mathcal{R}}^a_{2n+1}$ [see Eq. (5.8)], where $\boldsymbol{\mathcal{R}}^a_{2n+1}$ is the reflection matrix that is associated with the top surface of the woodpile. A practical limitation of Eq. (5.38) is that, as a result of the matrix product $\boldsymbol{\mathcal{T}}\boldsymbol{\mathcal{R}}^b_n$ in the definition of D_{21}, spurious numerical solutions appear when either of $\boldsymbol{\mathcal{T}}$ or $\boldsymbol{\mathcal{R}}^b_n$ has a pole. We have found that this behaviour can be avoided by instead determining the poles of the matrix $\boldsymbol{\mathcal{R}}^a_{2n+1}$ [this matrix can be computed iteratively using Eqs. (2.42)].

5.4.3 Interactions between double-interface modes

We have found that when the parities of two double-interface modes are the same, the dispersion curves of the two modes do not cross one another. Instead, an anti-crossing appears where a crossing point would be expected. However, almost all of the anti-crossings lie outside of the bandgap, since there are far more waveguiding modes (not shown in Figs. 5.4 and 5.7) than there are surface modes. These anti-crossings are analogous to those that occur between the lower- and higher-order modes of, e.g., PC waveguides [126], and of coupled PC waveguides [113], and they arise because the parity of each of the two modes is such that the two modes are able to couple to one another [126]. In instances where the strength of a splitting is sufficiently weak, the dispersion curve of the even mode will be intertwined with that of the corresponding odd mode. An example of this behaviour is shown in Fig. 5.9. The thick red curve corresponds to the (single-interface) surface mode of the semi-infinite woodpile. When the semi-infinite stack is truncated to give an 8-layer woodpile, the red curve 'splits' into two modes (thin blue curves), one even and the other odd, both of which begin to oscillate about the red curve as the Bloch-vector moves from the M point to the Γ point of the Brillouin zone (*i.e.*, as $k_x = k_y$ decreases). Further, the crossing points of the blue curves coincide with the red curve. This behaviour is characteristic of the modes of hexagonal coupled photonic crystal waveguides (CPCWs) [113]. That CPCW modes and double-interface modes behave similarly is not surprising since, in both cases, the fields are confined to narrow parallel channels. In the case of CPCWs, the channels are embedded inside a PC, and the fields decay on either side of each channel as a result of the photonic bandgap of the PC. For the double-interface modes considered in this chapter, the fields are bound to the surfaces because both the PC and free-space

regions lack propagating states.

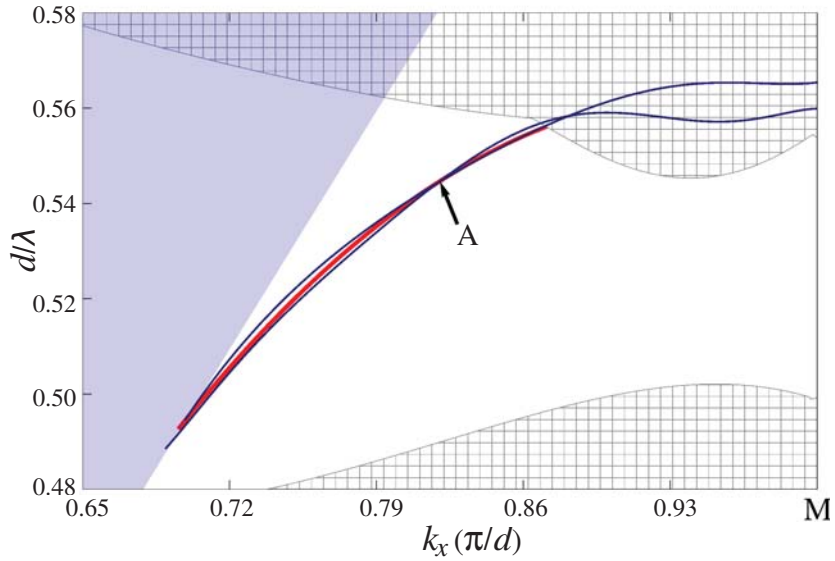

Figure 5.9: The 'braiding' between the dispersion curves of the even and the odd double-interface mode of the 8-layer woodpile (thin blue curves). The surface mode of the corresponding semi-infinite woodpile is also shown (thick red curves). The in-plane Bloch vector moves along the $\Gamma - \mathrm{M}$ direction, *i.e.*, $0 < k_x \leq \pi/d$ with $k_y = k_x$. The fields at the point labelled A on the curve for the semi-infinite structure are shown in Fig. 5.10.

The intuitive explanation for the intertwining of the modes of CPCWs is that, for certain values of k_x, the coupling between the modes of the two waveguides is particularly weak because the position of the second waveguide coincides with a nodal line of the mode of the first waveguide [113]. When this happens, the frequencies of the even and odd mode of the CPCW become degenerate, and are near that of the corresponding mode of the constituent waveguides. This can be seen in Fig. 5.10, which shows plots of the components of the electric field for the semi-infinite structure for the crossing point A [$d/\lambda = 0.544$ and $\mathbf{k}_t = (0.819, 0.819) \times \pi/d$] in Fig. 5.9. In the plots for both the E_x and E_y components, there is a pronounced node that runs parallel to the 9^{th} layer. This explains why the two double-interface modes of the 8-layer structure become degenerate for this value of k_x; each of the surfaces coincides with a nodal line of the corresponding mode of the semi-infinite woodpile, and, thus, the fields at the top surface do not couple strongly to the fields at the bottom surface. It has been proven that these nodal lines appear in hexagonal CPCWs because the two dominant evanescent Bloch modes of the PC that surrounds the waveguide do not decay monotonically, and so they will beat with one another [113]. Our results suggest that this phenomenon persists when each waveguide is

replaced with a surface.

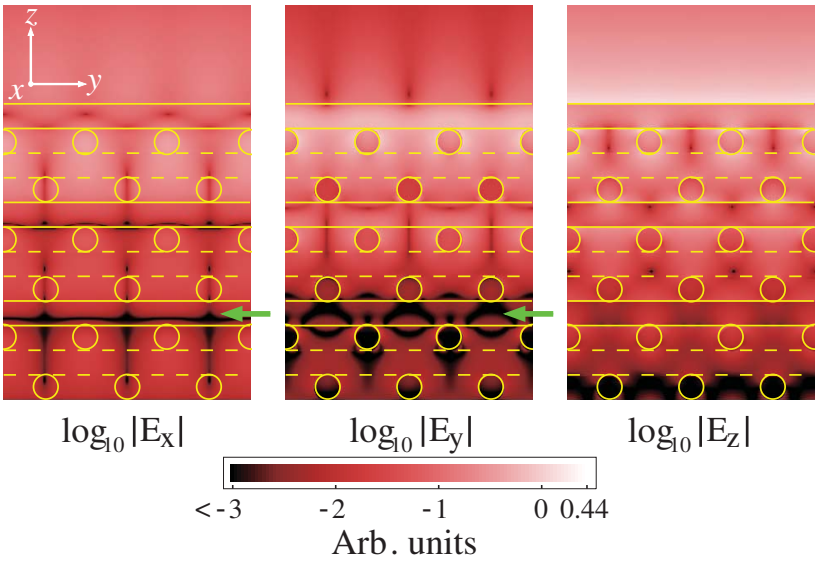

Figure 5.10: The components of the electric field for a semi-infinite woodpile. The fields are for the point labeled A ($d/\lambda = 0.544$, $k_x = k_y = 0.819\pi/d$) on the red curve of Fig. 5.9. For both the E_x and E_y components, a nodal line coincides with the 9^{th} layer (green arrows). Truncating the woodpile along the 9^{th} layer, thereby creating an 8-layer woodpile, would cause both top and bottom surfaces to lie along such a node. Hence, for this value of k_x, the fields at the top surface are weakly coupled to those at the bottom surface of the 8-layer structure.

5.5 Many-interface modes of compound woodpiles

In this section we consider the surface modes of composite structures consisting of two woodpiles that are separated by a distance Δ along the stacking (z) direction (see Fig. 5.11). Specifically, we are interested in the surface modes that travel along multiple surfaces at once. The approach used here is similar to that used in earlier work on 2D coupled PC waveguides [113, 127], except that here we are only concerned with modes that lie below the light-line. The general formulation for the surface modes is described in Section 5.5.1. A factorised form is then used to explain the behaviour of the 'many-interface' modes of both infinite (Sec. 5.5.2) and finite (Sec. 5.5.3) compound woodpiles.

5.5.1 General Formulation

The problem is most easily formulated using plane wave field expansions. The plane wave fields incident to the interior surfaces satisfy relationships analogous to Eqs. (5.26) and (5.27), *i.e.*,

$$\boldsymbol{\mathcal{F}}^{-} = \boldsymbol{\mathcal{R}}_n \boldsymbol{\mathcal{P}} \boldsymbol{\mathcal{F}}^{+} \quad \text{and} \quad \boldsymbol{\mathcal{F}}^{+} = \boldsymbol{\mathcal{R}}'_n \boldsymbol{\mathcal{P}} \boldsymbol{\mathcal{F}}^{-}, \tag{5.40}$$

where $\boldsymbol{\mathcal{F}}^{\pm}$ are the outgoing fields sourced on the interior surfaces, and $\boldsymbol{\mathcal{R}}_n$ and $\boldsymbol{\mathcal{R}}'_n$ are the reflection matrices for the top and the bottom interior surface, respectively (see Fig. 5.11). Note that unlike Eqs. (5.26) and (5.27), Eq. (5.40) does not contain a term describing the transmission through the PC regions as there are no external sources impinging on the exterior surfaces ($\boldsymbol{\mathcal{F}}_a^{-} = \boldsymbol{\mathcal{F}}_b^{+} = \mathbf{0}$). The block-diagonal matrix

$$\boldsymbol{\mathcal{P}} = \begin{bmatrix} \mathsf{P} & 0 \\ 0 & \mathsf{P} \end{bmatrix}, \tag{5.41}$$

in which $\mathsf{P} = \mathrm{diag}[i\gamma_s \Delta]$ simply shifts the phase origin of the fields by a distance Δ along the z-direction, with γ_s specifying the propagation constant in this direction for each woodpile diffraction order [see Eq. (2.21)]. The interior fields $\boldsymbol{\mathcal{F}}^{-}$ are then the solutions of

$$(\mathbf{I} - \boldsymbol{\mathcal{R}}_n \boldsymbol{\mathcal{P}} \boldsymbol{\mathcal{R}}'_n \boldsymbol{\mathcal{P}}) \boldsymbol{\mathcal{F}}^{-} = \mathbf{0}. \tag{5.42}$$

5.5.2 Infinite number of layers

Initially, suppose that the top and bottom half-stacks extend infinitely in the positive and negative z-directions, respectively, and that the structure is symmetric about the plane $z = 0$ (as in Fig. 5.11), *i.e.*, $\boldsymbol{\mathcal{R}}_n = \boldsymbol{\mathcal{R}}'_n = \boldsymbol{\mathcal{R}}_\infty$, where $\boldsymbol{\mathcal{R}}_\infty$ is given by Eq. (5.9). The dispersion curves of the surface modes of this structure are shown by the dark blue curves in Fig. 5.12, where the separation distance is $\Delta = 4h$ (the parameters of each of the PC regions are as before). For comparison, the dispersion curves for the surface modes of one of the semi-infinite half-stacks (thick red curves) are also shown in Fig. 5.12, and are the same as those in Fig. 5.2(c). The general behaviour of the modes can be understood by looking at the asymptotic behaviour of $\boldsymbol{\mathcal{P}}$. Rearranging Eq. (5.40) gives

$$\boldsymbol{\mathcal{R}}_n^{-1} \boldsymbol{\mathcal{F}}^{-} = \boldsymbol{\mathcal{P}} \boldsymbol{\mathcal{F}}^{+}. \tag{5.43}$$

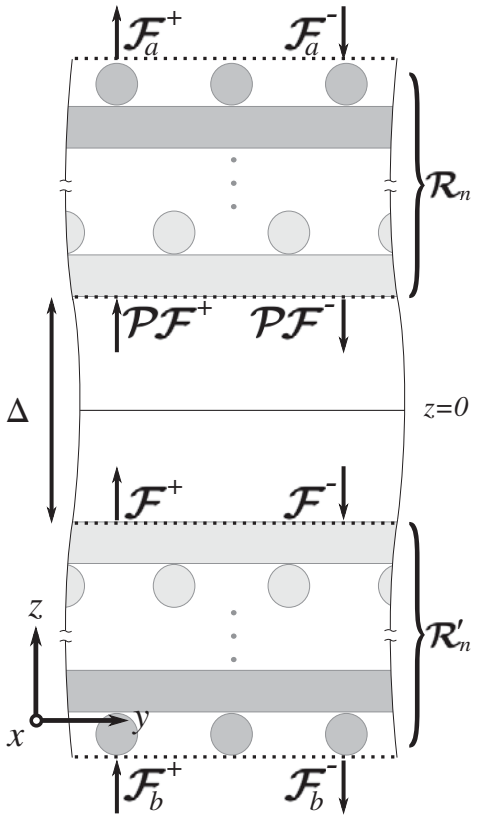

Figure 5.11: The phase origins (dotted horizontal lines) of the plane wave fields incident to the exterior ($\boldsymbol{\mathcal{F}}^{\pm}_{a/b}$) and interior ($\boldsymbol{\mathcal{F}}^{\pm}$) surfaces of a compound woodpile comprising two n-layer woodpiles that are separated by a distance Δ. A reflection matrix is associated with each of the interior surfaces ($\boldsymbol{\mathcal{R}}_n$ and $\boldsymbol{\mathcal{R}}'_n$). Field propagation between the interior surfaces is described by the matrix $\boldsymbol{\mathcal{P}}$.

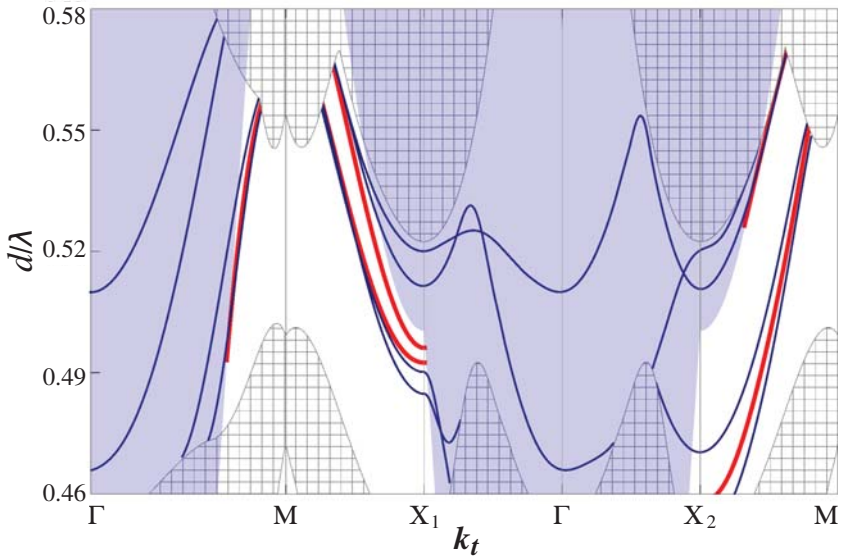

Figure 5.12: Dispersion curves (thin blue curves) for the surface-modes of a compound woodpile (*i.e.*, a PC-air-PC configuration) that has mirror symmetry about the $z = 0$ plane. The PC regions are semi-infinite, so that there are no exterior surfaces. Thus, every mode is a double-interface mode. The surface modes of one of the semi-infinite PC regions are also shown (thick red curves). The second PC causes the modes of the first PC to 'split' into two modes, one of which is even, the other of which is odd.

Equation (5.43) is the same form as the heuristic described earlier for locating the surface modes of individual woodpiles [see Eq. (5.8)], except for the appearance of the term $\boldsymbol{\mathcal{P}}\boldsymbol{\mathcal{F}}^{+}$, which acts as a perturbation term. For example, below the light-line, all of the propagation constants γ_s are imaginary (the fields decay exponentially in the region separating the two woodpiles), thus $\boldsymbol{\mathcal{P}} \to \mathbf{0}$ as $\Delta \to \infty$, and so the right-hand side of Eq. (5.43) vanishes. In this limit, the amount of overlap between the exponential tail of the field on one surface and the tail of the field at the opposing surface is negligible, and so the surface modes of the aggregate structure become indistinguishable from those of the constituent half-stacks. Similarly, for modes below the light-line, $\boldsymbol{\mathcal{P}} \to \mathbf{0}$ as either d/λ or $\mathbf{k}_t$ moves further away from the light-line, because $|\mathfrak{Im}(\gamma_s)|$ increases in this case.

Furthermore, below the light-line, each blue curve in Fig. 5.12 corresponds to a double-interface mode. In the previous section, it was shown that the existence of double-interface modes (or, more generally, many-interface modes) depends on the presence of certain symmetries. Since there is mirror symmetry about the plane $z = 0$, $\boldsymbol{\mathcal{R}}_n = \boldsymbol{\mathcal{R}}'_n$,

and, consequently, Eq. (5.42) factorises, implying that

$$(\mathbf{I} - \sigma\boldsymbol{\mathcal{R}}_n\boldsymbol{\mathcal{P}})\boldsymbol{\mathcal{F}}^- = \mathbf{0}, \tag{5.44}$$

where $\sigma = \pm 1$, and, thus,

$$\boldsymbol{\mathcal{F}}^- = \sigma\boldsymbol{\mathcal{F}}^+, \tag{5.45}$$

with $\sigma = 1$ corresponding to the even solution, and $\sigma = -1$ corresponding to the odd solution.

Note that Eq. (5.42) can also be factorised when the top half-stack is identical to the bottom half-stack, up to a translation along the z-axis, and up to a shift of $d/2$ along either of the x- and y-axes (when n is even, the constraint $k_x = k_y$ must also be imposed). Under these conditions, the matrix $\boldsymbol{\mathcal{R}}_n$ obeys a similarity transform that is analogous to Eq. (5.30), and that guarantees a factorisable form of Eq. (5.42) (also see Appendix 5.C). However, for argument's sake, we limit our discussion to compound woodpiles that have mirror symmetry about the $z = 0$ plane. It follows immediately from Eq. (5.45) that in the limit as $n \to \infty$, the surface modes are always double-interface modes that propagate along both of the interior surfaces. As was for the single-interface modes of the semi-infinite woodpile, the surface modes appear to become cutoff when they leave the bandgap (this happens because the frequencies of the propagating modes of the cladding regions form a continuum). There are also modes in Fig. 5.12 that lie above the light-line while remaining inside the bandgap of the PC. These modes are waveguide modes; the fields propagate inside the space separating the two woodpiles, but decay exponentially inside the semi-infinite PC regions. In this case, the fields are not confined to the surfaces.

In short, the introduction of the second woodpile causes each mode of the first woodpile to 'split' into an even mode and an odd mode (unless they are cut off by the light-line or by the edge of the bandgap), and that, in the case of surface modes, the strength of this splitting increases, *i.e.*, the coupling between the two surfaces becomes stronger, as Δ decreases, and also as d/λ and $\mathbf{k}_t$ move closer to the light-line.

5.5.3 Finite number of layers

When the number of layers, n, of each of the constituent half-stacks is finite, the outgoing fields $\boldsymbol{\mathcal{F}}_a^+$ and $\boldsymbol{\mathcal{F}}_b^-$ emanating from the exterior surfaces are related according to

$$\boldsymbol{\mathcal{F}}_a^+ = \boldsymbol{\mathcal{T}}_n\boldsymbol{\mathcal{P}}\boldsymbol{\mathcal{F}}^+ = \sigma\boldsymbol{\mathcal{T}}_n\boldsymbol{\mathcal{P}}\boldsymbol{\mathcal{F}}^- = \sigma\boldsymbol{\mathcal{F}}_b^-, \tag{5.46}$$

where $\mathcal{T}_n$ is the transmission matrix for the interior surfaces. It follows immediately from Eq. (5.45) and (5.46) that the surface modes are always either double-interface or quadruple-interface modes. In the former case, the modes propagate either along both of the interior surfaces or along both of the exterior surfaces, while in the latter case, the modes travel along all four surfaces simultaneously.

The dispersion curves for the surface modes of a compound woodpile in a 4 + 4 layer configuration, with $\Delta = 2h$ (*i.e.*, two four layer woodpiles separated by a distance of $2h$) are plotted (red solid curves) in Fig. 5.13. The black dotted curves are the modes of the constituent 4-layer woodpile, and are the same as those in Fig. 5.4(c). The rods of the interior surfaces of the compound structure were chosen to lie parallel to the rods of the top surface of the 4-layer woodpile. Thus, the single-interface modes that propagate along the top surface of the original woodpile (thick dotted curves, excluding the curves for the $\Gamma - \mathrm{M}$ direction) split into a pair of double-interface modes that propagate along the two interior surfaces (solid red curves). Similarly, the single-interface modes that propagate along the bottom surface of the 4-layer woodpile (thin dotted curves) split into a pair of double-interface modes that propagate along the two exterior surfaces (thin solid curves). Recall that along the $\Gamma - \mathrm{M}$ direction the 4-layer stack supports a pair of double-interface modes. The presence of the second (mirror-image) woodpile causes each of these modes to 'split' into two quadruple-interface modes (red solid curves). The quadruple-interface modes can be viewed as secondary splittings because each of the original double-interface modes is itself a (primary) splitting; hence, the quadruple-interface modes appear as groups of four modes. From the results of Sections 5.4.1 and 5.4.2, we can conclude that if the constituent woodpiles each have an odd number of layers, then every surface mode of the aggregate structure will be the result of a secondary splitting (*i.e.*, a quadruple-interface mode). Unlike the primary splittings, the secondary splittings will not necessarily be degenerate, since, unlike each of the two sub-stacks, the compound woodpile does not possess glide-reflection symmetry. If, instead, each of the two sub-stacks consists of an even number of layers, then only the modes whose Bloch vector lies along the $\Gamma - \mathrm{M}$ direction will be the result of secondary splittings.

As can be seen in Fig. 5.13, the strength of the splitting for the surface modes that propagate along the interior surfaces is stronger than that for the modes propagating along the exterior surfaces. If the field is concentrated on the exterior surfaces, then the fields $\boldsymbol{\mathcal{F}}^{\pm}$ on the inside surfaces are 'small', and so the perturbation term $\boldsymbol{\mathcal{P}}\boldsymbol{\mathcal{F}}^{+}$ on the right-hand side of Eq. (5.43) is also small. Conversely, if the field is concentrated on the interior surfaces, then the perturbation term is relatively large. This is understandable because, on

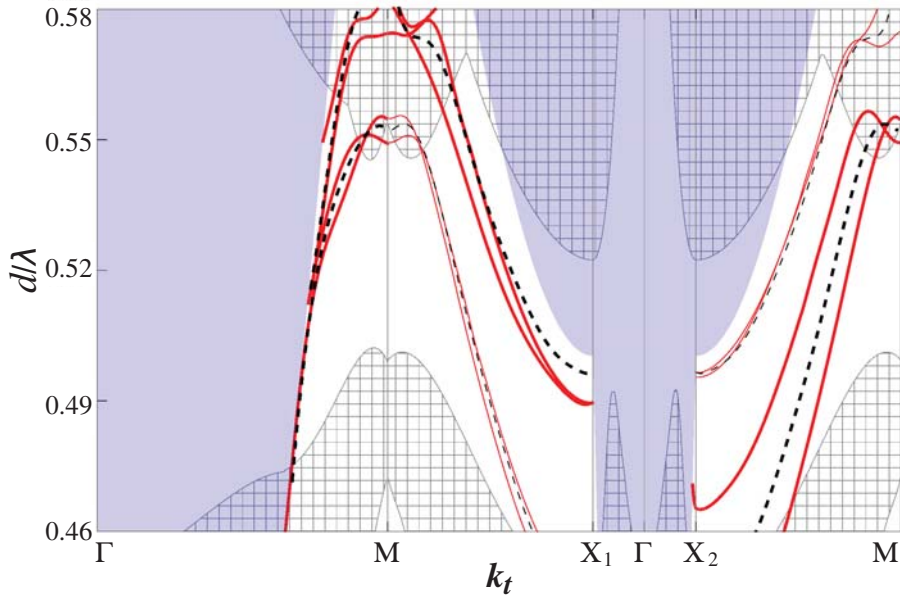

Figure 5.13: Modes of the $4+4$ layer compound woodpile (red curves), with $\Delta = 2h$, and the modes of the constituent 4-layer woodpile (blue curves). Along the $\Gamma - \mathrm{M}$ direction, the modes of the 4-layer woodpile are double-interface modes, and the modes of the compound woodpile are quadruple-interface modes. For the other directions, the modes of the 4-layer structure are single-interface modes that propagate along either the top surface (thick curves) or the bottom surface (thin curves), while the modes of the compound woodpile are double-interface modes that propagate along the interior surfaces (thick curves) or along the exterior surfaces (thin curves).

average, the outer surfaces are further away from all of the other surfaces than the inner surfaces are. Thus, modes bound to the outer surfaces more closely resemble the modes of the 4-layer woodpile than the modes bound to the inner surfaces do. This effect is enhanced by the fact that, for the structural parameters that we have used, the fields inside the cavity decay more slowly than the fields inside the PC regions.

Unlike the surface modes of the infinite compound woodpile (see Fig. 5.12), the surface modes of the truncated compound woodpile do not cross the light-line, *i.e.*, they do not become ideal waveguide modes. This is because, above the light-line, some of the light that leaks through the PC regions of the truncated structure will couple to radiation modes of the free-space regions. Any such waveguide mode would thus be lossy, and so would have a complex frequency. Another conspicuous difference between the surface modes of the finite and infinite structures is that the surface modes of the truncated compound woodpile do not become cutoff as they cross the edge of the bandgap, since the propagating modes of the cladding region are discrete when n is finite. We have also observed anti-crossings between the even and odd quadruple-interface modes, see Fig. 5.14. These anti-crossings are analogous to those that occur between the double-interface modes of regular woodpiles (see Sec. 5.4.3), and result from the symmetry of the compound woodpile. Plots of $\mathfrak{Re}(E_z)$ and $\mathfrak{Im}(E_z)$ for a representative *even* quadruple-interface mode, and for the corresponding *odd* mode are shown in Fig. 5.15.

5.6 Discussion

The control of electromagnetic waves on the surfaces of photonic woodpiles is important for a number of applications. For example, woodpiles can be used as a substrate to reduce optical losses because these structures can possess complete bandgaps; it has already been shown that, in the absence of surface modes, the properties of cavities on the surface of woodpiles differ from those of 2D PC cavities [53]. The results presented in this chapter indicate that the behaviour of the double-interface modes of finite woodpiles is more complicated than that of the double-interface modes of finite 2D PCs; the number of layers m, the parity of m, and direction all play important roles. We showed that coupling between the top and bottom surfaces can still occur when the number of layers is even, although in this case the coupled mode can only propagate along the high-symmetry directions of the surface. This property might be exploited to create, e.g., novel planar emitters that can act as either single- or double-sided emitters, depending on the orientation of the surfaces in relation to an external source. When m is odd, all surface modes are double-interface

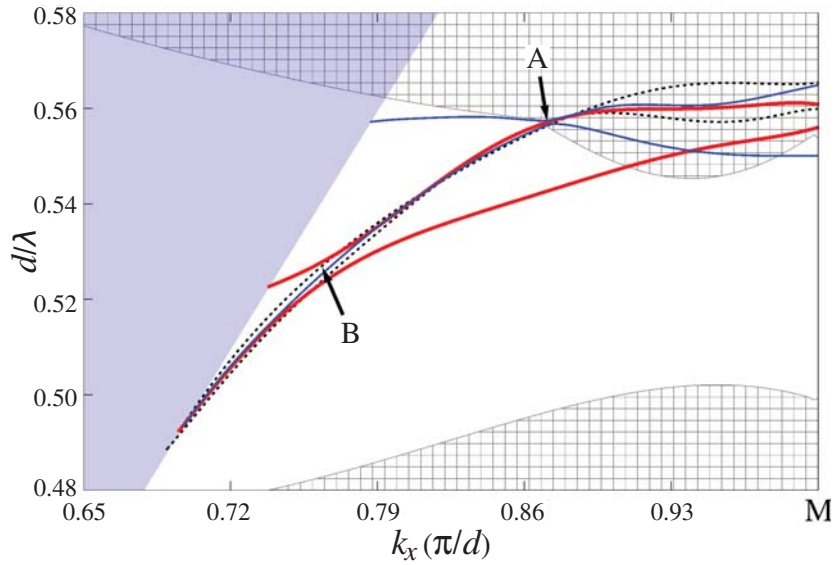

Figure 5.14: The two even (thin blue curves) and the two odd (thick red curves) quadruple-interface modes of an $8 + 8$ layer compound woodpile ($\Delta = 0.2d$) that result when the two double-interface modes of the 8-layer half-stack (dotted black curves) each 'split' into two modes. At the point labelled A, an anti-crossing occurs between the two even quadruple-interface modes. Similarly, at the point labelled B, an anti-crossing occurs between the two odd quadruple-interface modes. The Bloch vector lies along the $\Gamma - \mathrm{M}$ direction ($k_x = k_y$).

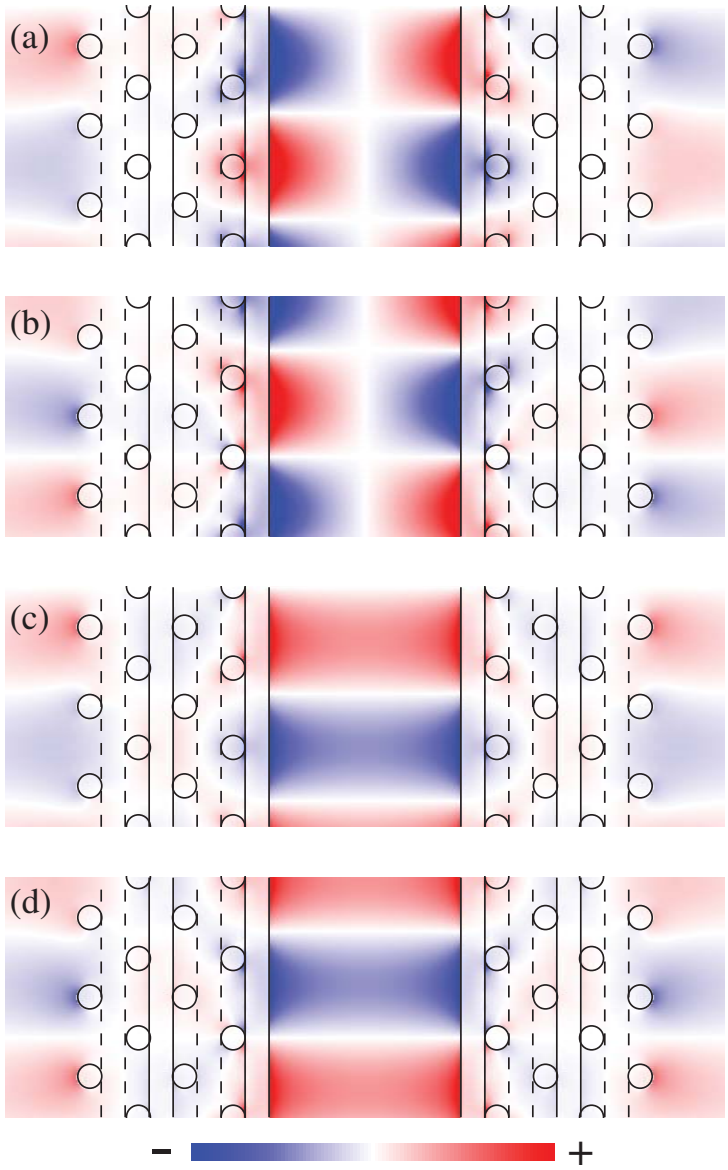

Figure 5.15: Plots of the z-component of the electric field of the even and odd quadruple-interface modes of an $8+8$ layer compound woodpile ($k_x = k_y = 0.752\pi/d$), with $\Delta = 8h$. (a) $\mathfrak{Re}(E_z)$ and (b) $\mathfrak{Im}(E_z)$ of the even mode ($\lambda/d = 0.524$). (c) $\mathfrak{Re}(E_z)$ and (d) $\mathfrak{Im}(E_z)$ of the odd mode ($\lambda/d = 0.517$). The fields concentrate more strongly at the interior surfaces than at the exterior surfaces.

modes, and so if one is trying to excite single-interface modes only, then an even number of layers should be used, and care should be taken in order to avoid the excitation of modes in the $\Gamma - \mathrm{M}$ direction.

In general, increasing the number of layers decreases the coupling strength between the top and bottom surfaces. However, if m is odd, then there are specific directions of the Brillouin zone for which the even and odd double-interface modes become degenerate and, hence, for these directions the coupling strength is largely insensitive to changes in m. The degeneracy in the double-interface modes at the edge of the Brillouin zone is also evident in finite 2D PCs [125], although in the case of finite 2D PCs the edge of the Brillouin zone represents just a single Bloch vector.

Lastly, double-interface modes of PCs are similar to the modes of hexagonal coupled PC waveguides in some respects. Most notably, the dispersion curve of an even mode can be intertwined with that of the corresponding odd mode, and this commonality is likely to be due to the similar way in which the dominant evanescent Bloch modes of each of these structures interact with the boundary of the surface or waveguide.

5.A Simultaneous Poles of the Reflection and Transmission Matrices

The heuristic given by Eq. (5.8) relies on the fact that the poles of the matrices $\boldsymbol{\mathcal{R}}^a_m$, $\boldsymbol{\mathcal{T}}^a_m$, $\boldsymbol{\mathcal{R}}^b_m$ and $\boldsymbol{\mathcal{T}}^b_m$ that appear in Eqs. (5.6) and (5.7) all coincide. This property follows immediately from the Bloch mode expressions for $\boldsymbol{\mathcal{R}}$ and $\boldsymbol{\mathcal{T}}$ when m is even, as discussed in Section 5.4.1 [see Eqs. (5.22) and (5.23)]. If m is odd, or, more generally, if the layers are not stacked in a periodic sequence, then the plane wave scattering matrices for the woodpile must instead be computed by using the recurrence relationships given by Eqs. 2.42 (repeated here for convenience):

$$\boldsymbol{\mathcal{R}}^a_m = \boldsymbol{\mathcal{R}}^a + \boldsymbol{\mathcal{T}}^b \boldsymbol{\mathcal{R}}^a_{m-1} \left(\mathbf{I} - \boldsymbol{\mathcal{R}}^b \boldsymbol{\mathcal{R}}^a_{m-1}\right)^{-1} \boldsymbol{\mathcal{T}}^a, \tag{5.47}$$

$$\boldsymbol{\mathcal{T}}^a_m = \boldsymbol{\mathcal{T}}^a_{m-1} \left(\mathbf{I} - \boldsymbol{\mathcal{R}}^b \boldsymbol{\mathcal{R}}^a_{m-1}\right)^{-1} \boldsymbol{\mathcal{T}}^a, \tag{5.48}$$

$$\boldsymbol{\mathcal{R}}^b_m = \boldsymbol{\mathcal{R}}^b_{m-1} + \boldsymbol{\mathcal{T}}^a_{m-1} \boldsymbol{\mathcal{R}}^b \left(\mathbf{I} - \boldsymbol{\mathcal{R}}^a_{m-1} \boldsymbol{\mathcal{R}}^b\right)^{-1} \boldsymbol{\mathcal{T}}^b_{m-1}, \tag{5.49}$$

$$\boldsymbol{\mathcal{T}}^b_m = \boldsymbol{\mathcal{T}}^b \left(\mathbf{I} - \boldsymbol{\mathcal{R}}^a_{m-1} \boldsymbol{\mathcal{R}}^b\right)^{-1} \boldsymbol{\mathcal{T}}^b_{m-1}, \tag{5.50}$$

where $\boldsymbol{\mathcal{R}}^a$, $\boldsymbol{\mathcal{T}}^a$, $\boldsymbol{\mathcal{R}}^b$ and $\boldsymbol{\mathcal{T}}^b$ are the scattering matrices for the top layer. The poles of the reflection and transmission matrices on the right-hand sides of Eqs. (5.47)-(5.50) only coincide with those of $\boldsymbol{\mathcal{R}}^a_m$, $\boldsymbol{\mathcal{T}}^a_m$, $\boldsymbol{\mathcal{R}}^b_m$ and $\boldsymbol{\mathcal{T}}^b_m$ at a finite number of points within the first Brillouin zone, hence, we can reasonably assume that the scattering matrices for the top layer and for the $(m-1)$-layer sub-stack do not have poles. Thus, the only way for $\boldsymbol{\mathcal{R}}^a_m$ and $\boldsymbol{\mathcal{T}}^a_m$ to have a pole is if $\left(\mathbf{I} - \boldsymbol{\mathcal{R}}^b \boldsymbol{\mathcal{R}}^a_{m-1}\right)$ is singular. Similarly, $\boldsymbol{\mathcal{R}}^b_m$ and $\boldsymbol{\mathcal{T}}^b_m$ have poles precisely when $\left(\mathbf{I} - \boldsymbol{\mathcal{R}}^a_{m-1} \boldsymbol{\mathcal{R}}^b\right)$ is singular. However,

$$\left(\mathbf{I} - \boldsymbol{\mathcal{R}}^a_{m-1} \boldsymbol{\mathcal{R}}^b\right) = \boldsymbol{\mathcal{R}}^a_{m-1} \left(\mathbf{I} - \boldsymbol{\mathcal{R}}^b \boldsymbol{\mathcal{R}}^a_{m-1}\right) \left(\boldsymbol{\mathcal{R}}^a_{m-1}\right)^{-1},$$

which implies that the poles of the scattering matrices of the m-layer stack coincide. When $\boldsymbol{\mathcal{T}}^{a,b}$ and $\boldsymbol{\mathcal{T}}^{a,b}_{m-1}$ have poles, the poles of Eqs. (5.48) and (5.50) correspond to spurious surface mode solutions; however, we have found that in practice, Eqs. (5.47) and (5.49) do not result in such spurious solutions, and so are better suited for locating the woodpile surface modes.

5.B Proof of Symmetry Relationships [Eqs. (5.16)] for the $k_x = k_y$ case.

Equations (5.16) stem from the fact that, when $k_x = k_y$,

$$\boldsymbol{\mathcal{R}}_y = \mathbf{A} \boldsymbol{\mathcal{R}}_x \mathbf{A} \quad \text{and} \quad \boldsymbol{\mathcal{T}}_y = \mathbf{A} \boldsymbol{\mathcal{T}}_x \mathbf{A}, \tag{5.51}$$

where $\boldsymbol{\mathcal{R}}_x$ ($\boldsymbol{\mathcal{R}}_y$) and $\boldsymbol{\mathcal{T}}_x$ ($\boldsymbol{\mathcal{T}}_y$) are the reflection and transmission matrices for a grating whose rods lie parallel to the x-axis (y-axis). The planewave fields appearing on the left-hand side of Eq. (5.1) can be partitioned into TE and TM polarised components, *i.e.*,

$$\boldsymbol{\mathcal{F}}^{\pm}_l = \begin{bmatrix} \boldsymbol{\mathcal{F}}^{\pm}_{l,\mathrm{TE}} \\ \boldsymbol{\mathcal{F}}^{\pm}_{l,\mathrm{TM}} \end{bmatrix}, \tag{5.52}$$

in which $\boldsymbol{\mathcal{F}}^{\pm}_{l,\mathrm{TE}}$ and $\boldsymbol{\mathcal{F}}^{\pm}_{l,\mathrm{TM}}$ are the vectors that consist of the TE and TM field coefficients, respectively. In principle these vectors are infinite; however, in practice they must be truncated so that they become vectors of length $M = N^2$, for some finite integers M and N. Consequently, $\boldsymbol{\mathcal{R}}$, $\boldsymbol{\mathcal{T}}$ and $\mathbf{A}$ are $2M \times 2M$ matrices. In particular, $\mathbf{A}$ is a 2×2

block-diagonal matrix:

$$\mathbf{A} = \begin{bmatrix} \boldsymbol{\mathcal{A}} & \mathbf{0} \\ \mathbf{0} & -\boldsymbol{\mathcal{A}} \end{bmatrix}, \tag{5.53}$$

where $\boldsymbol{\mathcal{A}}$ is an $N \times N$ block matrix such that

$$\boldsymbol{\mathcal{A}} = \begin{bmatrix} \boldsymbol{\mathcal{M}}_{1,1} & \cdots & \cdots & \cdots & \boldsymbol{\mathcal{M}}_{1,N} \\ \vdots & & & & \vdots \\ \vdots & & & & \vdots \\ \vdots & & & & \vdots \\ \boldsymbol{\mathcal{M}}_{N,1} & \cdots & \cdots & \cdots & \boldsymbol{\mathcal{M}}_{N,N} \end{bmatrix}, \tag{5.54}$$

in which $\boldsymbol{\mathcal{M}}_{p,q} = [\delta_{iq}\delta_{jp}]$, with $1 \leq i \leq N$ indexing the rows and $1 \leq j \leq N$ indexing the columns of $\boldsymbol{\mathcal{M}}_{p,q}$, and where $\delta_{ij} = 1$ if $i = j$, and $\delta_{ij} = 0$ otherwise. Note that $\boldsymbol{\mathcal{A}}$ is a permutation matrix (it has exactly one '1' in every column and in every row) and, thus $\mathbf{A}^{-1} = \mathbf{A}^{\mathrm{T}}$, where the superscript T denotes the matrix transpose. Since $\mathbf{A}$ is symmetrical, it follows that $\mathbf{A} = \mathbf{A}^{-1}$.

The reflection and transmission matrices in Eq. (5.51) are formulated so that they act on the fields at $z = \pm h/2$, with $z = 0$ specifying the plane of the grating, and so they give the grating an artificial thickness equal to h. Equations (5.51) can be derived from the multipole expressions for $\boldsymbol{\mathcal{R}}$ and $\boldsymbol{\mathcal{T}}$ [see Eqs. (3.26) and (3.27)]. The scattering matrices for the woodpile stacking unit, which consists of two gratings that are orthogonal to one another, satisfy

$$\boldsymbol{\mathcal{R}}_b = \mathbf{A}\boldsymbol{\mathcal{R}}_a\mathbf{A} \quad \text{and} \quad \boldsymbol{\mathcal{T}}_b = \mathbf{A}\boldsymbol{\mathcal{T}}_a\mathbf{A}, \tag{5.55}$$

where $\boldsymbol{\mathcal{R}}_a$ and $\boldsymbol{\mathcal{T}}_a$ are the scattering matrices that act on the fields that are incident from above the stacking unit, and $\boldsymbol{\mathcal{R}}_b$ and $\boldsymbol{\mathcal{T}}_b$ act on fields that are incident from below. The relationships (5.55) follow immediately from Eqs. (5.51) and the stacking recurrences [Eqs. (5.47)-(5.50)]. In order to effect an interleaving of the grating pairs of the woodpile, a shear transform must be applied to $\boldsymbol{\mathcal{R}}_a$, $\boldsymbol{\mathcal{R}}_b$, $\boldsymbol{\mathcal{T}}_a$ and $\boldsymbol{\mathcal{T}}_b$, which then become

$$\begin{aligned} \begin{bmatrix} \boldsymbol{\mathcal{T}}'_a & \boldsymbol{\mathcal{R}}'_b \\ \boldsymbol{\mathcal{R}}'_a & \boldsymbol{\mathcal{T}}'_b \end{bmatrix} &= \begin{bmatrix} \boldsymbol{\mathcal{Q}}^{-1}\boldsymbol{\mathcal{T}}_a\boldsymbol{\mathcal{Q}}^{-1} & \boldsymbol{\mathcal{Q}}^{-1}\boldsymbol{\mathcal{R}}_b\boldsymbol{\mathcal{Q}} \\ \boldsymbol{\mathcal{Q}}\boldsymbol{\mathcal{R}}_a\boldsymbol{\mathcal{Q}}^{-1} & \boldsymbol{\mathcal{Q}}\boldsymbol{\mathcal{T}}_b\boldsymbol{\mathcal{Q}} \end{bmatrix} \\ &= \begin{bmatrix} \boldsymbol{\mathcal{Q}}^{-1}\boldsymbol{\mathcal{T}}_a\boldsymbol{\mathcal{Q}}^{-1} & \boldsymbol{\mathcal{Q}}^{-1}\mathbf{A}\boldsymbol{\mathcal{R}}_a\mathbf{A}\boldsymbol{\mathcal{Q}} \\ \boldsymbol{\mathcal{Q}}\boldsymbol{\mathcal{R}}_a\boldsymbol{\mathcal{Q}}^{-1} & \boldsymbol{\mathcal{Q}}\mathbf{A}\boldsymbol{\mathcal{T}}_a\mathbf{A}\boldsymbol{\mathcal{Q}} \end{bmatrix}, \end{aligned} \tag{5.56}$$

where the second equality follows from Eq. (5.55). The shear transform operator, $\boldsymbol{\mathcal{Q}}$, is a

block-diagonal matrix of the form

$$\boldsymbol{\mathcal{Q}} = \begin{bmatrix} \mathbf{Q} & \mathbf{0} \\ \mathbf{0} & \mathbf{Q} \end{bmatrix}, \tag{5.57}$$

with

$$\mathbf{Q} = \begin{bmatrix} \ddots & & & & \\ & \boldsymbol{\mathcal{Q}}_{-1} & \mathbf{0} & \mathbf{0} & \\ & \mathbf{0} & \boldsymbol{\mathcal{Q}}_{0} & \mathbf{0} & \\ & \mathbf{0} & \mathbf{0} & \boldsymbol{\mathcal{Q}}_{1} & \\ & & & & \ddots \end{bmatrix}, \tag{5.58}$$

such that $\{\boldsymbol{\mathcal{Q}}_p\}$ are diagonal matrices. The q^{th} entry along the diagonal of the block $\boldsymbol{\mathcal{Q}}_p$ is given by $\boldsymbol{\mathcal{Q}}_{p,q} = \exp(-i\alpha_p\delta_x/2)\exp(-i\beta_q\delta_y/2)$, where α_p and β_p are the grating diffraction orders [see Eqs. (2.12) and (2.17)].

We now use the methods described in Sec. II of [124] to show that the downward Bloch vectors $\mathbf{F}$ and the downward Bloch factors $\boldsymbol{\Lambda}$ are related trivially to the upward Bloch vectors $\mathbf{F}'$ and upward Bloch factors $\boldsymbol{\Lambda}'$ [see Eq. (5.1)]. By definition,

$$\begin{bmatrix} \boldsymbol{\mathcal{F}}_2^- \\ \boldsymbol{\mathcal{F}}_1^+ \end{bmatrix} = \begin{bmatrix} \boldsymbol{\mathcal{T}}'_a & \boldsymbol{\mathcal{R}}'_b \\ \boldsymbol{\mathcal{R}}'_a & \boldsymbol{\mathcal{T}}'_b \end{bmatrix} \begin{bmatrix} \boldsymbol{\mathcal{F}}_1^- \\ \boldsymbol{\mathcal{F}}_2^+ \end{bmatrix}, \tag{5.59}$$

in which $\boldsymbol{\mathcal{F}}_1^{\pm}$ are the upward (+) and downward (-) planewave fields incident from above the grating pair, and $\boldsymbol{\mathcal{F}}_2^{\pm}$ are the planewave fields incident from below. Suppose that

$$\begin{bmatrix} \boldsymbol{\mathcal{F}}_1^- \\ \boldsymbol{\mathcal{F}}_1^+ \end{bmatrix}$$

is a downwards traveling Bloch mode (expressed in the planewave basis), whose corresponding Bloch factor is μ, with μ as described in Sec. 5.2. Bloch's theorem implies that

$$\begin{bmatrix} \boldsymbol{\mathcal{F}}_2^- \\ \boldsymbol{\mathcal{F}}_2^+ \end{bmatrix} = \mu \begin{bmatrix} \boldsymbol{\mathcal{F}}_1^- \\ \boldsymbol{\mathcal{F}}_1^+ \end{bmatrix}, \tag{5.60}$$

which can be combined with Eq. (5.59) to give

$$\mathbf{W}(\mu)\boldsymbol{\mathcal{F}} = \mathbf{0}, \tag{5.61}$$

with

$$\mathbf{W}(\mu) = \begin{bmatrix} \boldsymbol{\mathcal{T}}'_a - \mu\mathbf{I} & \boldsymbol{\mathcal{R}}'_b \\ \boldsymbol{\mathcal{R}}'_a & \boldsymbol{\mathcal{T}}'_b - \mu^{-1}\mathbf{I} \end{bmatrix} \quad \text{and} \quad \boldsymbol{\mathcal{F}} = \begin{bmatrix} \boldsymbol{\mathcal{F}}_1^- \\ \boldsymbol{\mathcal{F}}_2^+ \end{bmatrix}.$$

Thus, the eigenvalues μ (*i.e.*, Bloch factors) correspond to the solutions of $\det\mathbf{W}(\mu) = 0$. Substituting Eq. (5.56) into the expression for $\mathbf{W}(\mu)$ gives

$$\begin{aligned} \mathbf{W}(\mu) &= \begin{bmatrix} \boldsymbol{\mathcal{Q}}^{-1}\boldsymbol{\mathcal{T}}_a\boldsymbol{\mathcal{Q}}^{-1} - \mu\mathbf{I} & \boldsymbol{\mathcal{Q}}^{-1}\mathbf{A}\boldsymbol{\mathcal{R}}_a\mathbf{A}\boldsymbol{\mathcal{Q}} \\ \boldsymbol{\mathcal{Q}}\boldsymbol{\mathcal{R}}_a\boldsymbol{\mathcal{Q}}^{-1} & \boldsymbol{\mathcal{Q}}\mathbf{A}\boldsymbol{\mathcal{T}}_a\mathbf{A}\boldsymbol{\mathcal{Q}} - \mu^{-1}\mathbf{I} \end{bmatrix} \\ &= \mathbf{B}\widetilde{\mathbf{W}}(\mu)\mathbf{B}, \end{aligned} \tag{5.62}$$

with

$$\mathbf{B} = \begin{bmatrix} \mathbf{I} & \mathbf{0} \\ \mathbf{0} & \boldsymbol{\mathcal{Q}}^2 \end{bmatrix}$$

and

$$\begin{aligned} \widetilde{\mathbf{W}}(\mu) &= \begin{bmatrix} \boldsymbol{\mathcal{Q}}^{-1}\boldsymbol{\mathcal{T}}_a\boldsymbol{\mathcal{Q}}^{-1} - \mu\mathbf{I} & \boldsymbol{\mathcal{Q}}^{-1}\mathbf{A}\boldsymbol{\mathcal{R}}_a\mathbf{A}\boldsymbol{\mathcal{Q}}^{-1} \\ \boldsymbol{\mathcal{Q}}^{-1}\boldsymbol{\mathcal{R}}_a\boldsymbol{\mathcal{Q}}^{-1} & \boldsymbol{\mathcal{Q}}^{-1}\mathbf{A}\boldsymbol{\mathcal{T}}_a\mathbf{A}\boldsymbol{\mathcal{Q}}^{-1} - \mu^{-1}\boldsymbol{\mathcal{Q}}^{-4} \end{bmatrix} \\ &= \begin{bmatrix} \boldsymbol{\mathcal{Q}}^{-1}\boldsymbol{\mathcal{T}}_a\boldsymbol{\mathcal{Q}}^{-1} - \mu\mathbf{I} & \boldsymbol{\mathcal{Q}}^{-1}\mathbf{A}\boldsymbol{\mathcal{R}}_a\mathbf{A}\boldsymbol{\mathcal{Q}}^{-1} \\ \boldsymbol{\mathcal{Q}}^{-1}\boldsymbol{\mathcal{R}}_a\boldsymbol{\mathcal{Q}}^{-1} & \boldsymbol{\mathcal{Q}}^{-1}\mathbf{A}\boldsymbol{\mathcal{T}}_a\mathbf{A}\boldsymbol{\mathcal{Q}}^{-1} - s^{-1}\mu^{-1}\mathbf{I} \end{bmatrix}. \end{aligned}$$

In the second equality, we have used the fact that $\boldsymbol{\mathcal{Q}}^{-4} = s^{-1}\mathbf{I}$ when $\delta_x = \delta_y = d/2$, with $s = \exp(-ik_x d)\exp(-ik_y d)$. It follows that

$$\mathbf{W}(s^{-1}\mu^{-1}) = \mathbf{B}\mathbf{C}\widetilde{\mathbf{W}}(\mu)\mathbf{C}\mathbf{B}, \tag{5.63}$$

where

$$\mathbf{C} = \begin{bmatrix} \mathbf{0} & \mathbf{A} \\ \mathbf{A} & \mathbf{0} \end{bmatrix}. \tag{5.64}$$

Note that equation (5.63) relies on the fact that $\mathbf{A}$ commutes with $\boldsymbol{\mathcal{Q}}$ and $\boldsymbol{\mathcal{Q}}^{-1}$. Equations (5.61) and (5.62) imply that $\det\widetilde{\mathbf{W}}(\mu) = 0$, and, hence $\det\mathbf{W}(s^{-1}\mu^{-1}) = 0$. That is, if μ is an eigenvalue, then $s^{-1}\mu^{-1}$ is also an eigenvalue (we have also verified this numerically). Since μ was chosen to be a 'downward' eigenvalue, $s^{-1}\mu^{-1}$ must be an 'upward' eigenvalue, and so the entries of $\boldsymbol{\Lambda}'$ can always be arranged so that $(\boldsymbol{\Lambda}')^{-1} = s\boldsymbol{\Lambda}$, which is the desired result.

Since $s^{-1}\mu^{-1}$ is an eigenvalue, Bloch's theorem implies that there exists an (upward)

Bloch vector

$$\begin{bmatrix} \boldsymbol{\mathcal{F}}_1'^{-} \\ \boldsymbol{\mathcal{F}}_1'^{+} \end{bmatrix}$$

such that

$$\begin{bmatrix} \boldsymbol{\mathcal{F}}_2'^{-} \\ \boldsymbol{\mathcal{F}}_2'^{+} \end{bmatrix} = s^{-1}\mu^{-1} \begin{bmatrix} \boldsymbol{\mathcal{F}}_1'^{-} \\ \boldsymbol{\mathcal{F}}_1'^{+} \end{bmatrix}, \tag{5.65}$$

where $\boldsymbol{\mathcal{F}}_1'^{\pm}$ and $\boldsymbol{\mathcal{F}}_2'^{\pm}$ are defined analogously to $\boldsymbol{\mathcal{F}}_1^{\pm}$ and $\boldsymbol{\mathcal{F}}_2^{\pm}$, respectively. Further, $\boldsymbol{\mathcal{F}}_1'^{\pm}$ and $\boldsymbol{\mathcal{F}}_2'^{\pm}$ satisfy an eigenvalue problem similar to Eq. (5.61), namely

$$\mathbf{W}(s^{-1}\mu^{-1})\boldsymbol{\mathcal{F}}' = \mathbf{0}, \tag{5.66}$$

with

$$\boldsymbol{\mathcal{F}}' = \begin{bmatrix} \boldsymbol{\mathcal{F}}_1'^{-} \\ \boldsymbol{\mathcal{F}}_2'^{+} \end{bmatrix}. \tag{5.67}$$

Equation (5.61) and (5.62) imply that

$$\widetilde{\mathbf{W}}(\mu)\mathbf{B}\boldsymbol{\mathcal{F}} = \mathbf{0}, \tag{5.68}$$

and so if one chooses

$$\boldsymbol{\mathcal{F}}' = a_\mu \mathbf{B}^{-1}\mathbf{C}\mathbf{B}\boldsymbol{\mathcal{F}}, \tag{5.69}$$

for an arbitrary scalar a_μ, then

$$\mathbf{W}(s^{-1}\mu^{-1})\boldsymbol{\mathcal{F}}' = \mathbf{0}. \tag{5.70}$$

Hence, this choice of $\boldsymbol{\mathcal{F}}'$ gives the components of the (upward) Bloch vector that corresponds to $s^{-1}\mu^{-1}$, where it is assumed that there is no degeneracy in the Bloch factors. We can conclude that

$$\begin{bmatrix} \boldsymbol{\mathcal{F}}_1'^{-} \\ \boldsymbol{\mathcal{F}}_2'^{+} \end{bmatrix} = a_\mu \begin{bmatrix} \boldsymbol{\mathcal{Q}}^2\mathbf{A}\boldsymbol{\mathcal{F}}_2^{+} \\ \boldsymbol{\mathcal{Q}}^{-2}\mathbf{A}\boldsymbol{\mathcal{F}}_1^{-} \end{bmatrix} = a_\mu \begin{bmatrix} s^{1/2}\mathbf{Q}^2\mathbf{A}\boldsymbol{\mathcal{F}}_2^{+} \\ s^{-1/2}\mathbf{Q}^2\mathbf{A}\boldsymbol{\mathcal{F}}_1^{-} \end{bmatrix}, \tag{5.71}$$

where the matrix $\mathbf{Q}$ is defined identically to $\boldsymbol{\mathcal{Q}}$ [see Eq. (5.57)], except with $\mathbf{Q}_{p,q} = \exp(i\pi p/2)\exp(i\pi q/2)$ used in place of $\boldsymbol{\mathcal{Q}}_{p,q}$, and where we have made use of the fact that $\boldsymbol{\mathcal{Q}}^2 = s^{1/2}\mathbf{Q}^2$ and $\mathbf{Q}^{-2} = \mathbf{Q}^2$. Equations (5.65) and (5.71) determine the relationship

between the upward and downward Bloch vectors:

$$\begin{bmatrix} \boldsymbol{\mathcal{F}}_1'^{-} \\ \boldsymbol{\mathcal{F}}_1'^{+} \end{bmatrix} = a_\mu s^{1/2}\mu \mathbf{C} \begin{bmatrix} \mathbf{Q}^2\boldsymbol{\mathcal{F}}_1^{-} \\ \mathbf{Q}^2\boldsymbol{\mathcal{F}}_1^{+} \end{bmatrix} = \mathbf{C} \begin{bmatrix} \mathbf{Q}^2\boldsymbol{\mathcal{F}}_1^{-} \\ \mathbf{Q}^2\boldsymbol{\mathcal{F}}_1^{+} \end{bmatrix}, \tag{5.72}$$

where the second equality in Eq. (5.72) follows by choosing $a_\mu = s^{-1/2}\mu^{-1}$. The partitions of $\mathbf{F}'$ (the matrix of upward Bloch vectors) are thus related to the partitions of $\mathbf{F}$ (the matrix of downward Bloch vectors), according to

$$\begin{bmatrix} \mathbf{F}'^{-} \\ \mathbf{F}'^{+} \end{bmatrix} = \begin{bmatrix} \mathbf{A}\mathbf{Q}^2\mathbf{F}^{+} \\ \mathbf{A}\mathbf{Q}^2\mathbf{F}^{-} \end{bmatrix}, \tag{5.73}$$

where the order of the columns of $\mathbf{F}^{\pm}$ ($\mathbf{F}'^{\pm}$) is determined by the order of the entries of $\boldsymbol{\Lambda}$ ($\boldsymbol{\Lambda}'$). It follows immediately that

$$\boldsymbol{\mathfrak{R}}^a = \boldsymbol{\mathfrak{R}}^b \tag{5.74}$$

[see Eqs. (5.14)], which is the desired result, and which we have verified numerically. Equation (5.74) relies on our choice of the constants $\{a_\mu\}$; however, in a numerical implementation, $b_\mu \stackrel{\text{def}}{=} a_\mu s^{1/2}\mu$ is unknown initially. The specular channel, *i.e.*, the channel $(p, q) = (0, 0)$, is a fixed point of the permutation $\boldsymbol{\mathcal{A}}$, see Eq. (5.54). Therefore b_μ can be determined using $b_\mu = r f_1'^{-}/f_1^{+}$, where $f_1'^{-}$ and f_1^{+} are the specular components of $\boldsymbol{\mathcal{F}}_1'^{-}$ and $\boldsymbol{\mathcal{F}}_1^{+}$, respectively, and with $r = 1$ if the components are TE polarised, or with $r = -1$ if the components are TM polarised. It is thus possible to locate the surface modes without ever having to evaluate $\mathbf{A}$. A further corollary of Eq. (5.73) is that when $k_x = k_y$, the reflection matrix $\boldsymbol{\mathcal{R}}_\infty'$ for the semi-infinite woodpile that results when the finite woodpile in Fig. 5.1 is extended indefinitely upwards is related to $\boldsymbol{\mathcal{R}}_\infty$ [see Eq. (5.9)] by a similarity transform:

$$\boldsymbol{\mathcal{R}}_\infty' \stackrel{\text{def}}{=} \mathbf{F}'^{-}(\mathbf{F}'^{+})^{-1} = \mathbf{A}\mathbf{Q}^2\boldsymbol{\mathcal{R}}_\infty\mathbf{Q}^2\mathbf{A}.$$

5.C Definitions for the similarity transform in Eq. (5.30).

To effect a shift by an amount of δ_y along the positive y-direction, the following similarity transform is applied to the scattering matrices:

$$\boldsymbol{\mathcal{R}}' = \boldsymbol{\mathcal{Q}}_y\boldsymbol{\mathcal{R}}\boldsymbol{\mathcal{Q}}_y^{-1} \quad \text{and} \quad \boldsymbol{\mathcal{T}}' = \boldsymbol{\mathcal{Q}}_y\boldsymbol{\mathcal{T}}\boldsymbol{\mathcal{Q}}_y^{-1}, \tag{5.75}$$

where the shift operator $\boldsymbol{\mathcal{Q}}_y$ is a block-diagonal matrix of the form

$$\boldsymbol{\mathcal{Q}}_y = \begin{bmatrix} \mathbf{Q}_y^{\mathrm{TE}} & \mathbf{0} \\ \mathbf{0} & \mathbf{Q}_y^{\mathrm{TM}} \end{bmatrix}, \tag{5.76}$$

with

$$\mathbf{Q}_y^{\mathrm{TE}} = \mathbf{Q}_y^{\mathrm{TM}} = \begin{bmatrix} \ddots & & & & \\ & \mathcal{Q}_{-1} & 0 & 0 & \\ & 0 & \mathcal{Q}_0 & 0 & \\ & 0 & 0 & \mathcal{Q}_1 & \\ & & & & \ddots \end{bmatrix}. \tag{5.77}$$

Here,

$$\mathcal{Q}_s = \exp(-i\beta_q \delta_y/2) = \exp(-i\beta_0 \delta_y/2)(-1)^q \tag{5.78}$$

is the phase shift that is appropriate for the diffraction order $s = (p, q)$. The ordering of the elements of $\boldsymbol{\mathcal{F}}^{\pm}_{l,\mathrm{TE}}$ and $\boldsymbol{\mathcal{F}}^{\pm}_{l,\mathrm{TM}}$ must be chosen so that it is consistent with the order of the elements along the diagonal of $\mathbf{Q}_y^{\mathrm{TE}}$ and $\mathbf{Q}_y^{\mathrm{TM}}$. Equation (5.30) follows immediately from Eqs. (5.75)-(5.78) by defining $\mathbf{Q}_y$ as

$$\mathbf{Q}_y = \exp(i\beta_0 \delta_y/2)\, \boldsymbol{\mathcal{Q}}_y, \tag{5.79}$$

and then making use of the fact that $\mathbf{Q}_y = \mathbf{Q}_y^{-1}$.

Conclusion

In this thesis, two new semi-analytical methods for modelling woodpile waveguides were presented. The first method generalises the multipole framework for woodpiles so that defects can be incorporated by way of a super-cell. The super-cell method was used to compute the transmittance of a coupled-resonator optical waveguide (CROW) and a linear waveguide, where each waveguide was embedded inside a woodpile. It was found that, changing the radius of the defect rod was an effective way of increasing the Q-factors of the waveguides, especially the linear waveguide, which had a Q-factor of up to $200,000$. For the CROW, the large stack size did not present a computational challenge for the super-cell method, and the dispersion curves of the defect modes could be obtained. The new method compares favourably with the finite difference time domain method, for which modelling even relatively simple defects is time consuming when the stack size is large [64]. Using the super-cell to compute the dispersion curves of the linear waveguide was difficult because the large size of the super-cell meant that many plane wave orders were required to accurately model the fields. In addition, the high Q-factors of the linear waveguide meant that many realisations were needed in order to resolve the resonances.

To complement the super-cell approach, a two-dimensional fictitious source superposition method was generalised so that woodpile waveguide modes could be computed more efficiently. This method relies on using artificial sources to mimic a defect, and the efficiency was such that an exhaustive study of the parameter space could be performed. For certain values of the defect radius and refractive index, the waveguide modes exhibited slow-light behaviour over a large region of the Brillouin zone ($\sim 15\%$ of the BZ in one instance). Since slow-light waveguides are particularly susceptible to scattering losses [115], an interesting line of inquiry to pursue would be to compare the efficiency of a slow-light woodpile waveguide with that of a 2D PC slow-light geometry.

Scattering matrix and transfer matrix methods were used to obtain new results for the surface modes of woodpiles. When the number of layers is even, direction can be used to discriminate between single- and double-interface modes. When the number of layers

is odd, the coupling strength between the top and bottom surfaces depends strongly on the direction of propagation — for certain directions, decoupling can occur even when there are as few as five layers. This decoupling can either occur for contiguous regions of the Brillouin zone, or just for specific points. In the latter case, the dispersion curves of the double-interface modes are intertwined. This phenomenon also occurs in coupled photonic crystal waveguides [113], and can be explained intuitively by considering how the fields decay in the PC region.

Although the techniques that have been presented here are not as flexible as numerical tools such as FDTD, it was found that the multipole-based scattering matrix approach was accurate and relatively efficient, and, in the case of the surface mode study, the Bloch mode method provided more physical insight than would a purely numerical method.

Future Work

The methods presented in this thesis have a number of potential applications. For example, a natural extension of the surface mode study is to characterise the behaviour of a waveguide that is situated on the surface of a woodpile. Although the waveguide would rely on total internal reflection, the woodpile substrate could be used to control the dispersion and reduce optical losses. This idea has been applied successfully to woodpile surface cavities [17], where the woodpile substrate was shown to be less susceptible to optical losses than 2D PC geometries. In another study, the woodpile parameters were optimsed for use as a substrate in antenna designs [57]. The advantage of the linear waveguide proposed here is that it would be easier to couple into than a waveguide that is completely enclosed by a woodpile cladding. In principle, such a waveguide can be modelled using the FSS method simply by setting $\boldsymbol{F}_I^- = \mathbf{0}$ in Eq. (4.37).

Recently, there has been much interest in materials whose permittivity and permeability are both negative. Such *metamaterials* [102, 103] possess optical properties that are not found in conventional materials like dielectrics. These unique properties can be exploited to create, for example, super-lenses capable of imaging light below the diffraction limit [128], and can also be used to create optical cloaks, whereby the metameterial renders the cloakee invisible to certain wavelengths [129]. The possibility of using photonic woodpiles as three-dimensional metameterials is an open question. Such a material would potentially allow light to be manipulated with greater control than a two-dimensional metamaterial would, and could be modelled using the methods presented in this thesis.

A related area is the study of three-dimensional composite materials that consist of

both dielectric and metamaterial regions. While there is a considerable amount of research into the properties of uniform metamaterials [128–130], the rich physics of composites materials are only starting to be explored [131, 132]. It has already been shown that the optical properties of these composites are radically different from those of the constituent components. However, accurately predicting the optical properties of these new composites is difficult because these materials are strongly dispersive and absorptive. For the methods that we have developed, dispersive materials can be modelled by using a refractive index that is appropriate for the frequency, while absorption can be modelled simply by using a complex refractive index. Hence, our methods are well-suited for studying the properties of composite materials, specifically those that are three dimensional.

Our methods can also be generalised readily to handle coated cylinders. An exterior coating can be modelled by placing smaller cylinders inside the existing ones and then imposing an additional boundary condition of the form given in Eq. (3.16). Alternatively, simply changing the background refractive index results in an inverse woodpile that has an interior coating. Coatings are employed in optical sensing, where, e.g., an optical fibre is coated with a material that increases the sensitivity of the evanescent tails of the fibre modes to the presence of analytes, which are absorbed by the coating [133]. A coated woodpile (or simply the surface) might be more sensitive than a coated fibre sensor because of the larger surface area per unit volume of the woodpile. Dielectric woodpiles with metallic coatings might function as plasmonic 3D optical cloaking materials [134], whereby the parameters of the coated woodpile are chosen so that non-resonant scattering from a dielectric object of interest is suppressed when the object is placed inside the woodpile cloak. Moreover, for certain frequencies, this scattering-cancellation causes the visibility of both the cloak and dielectric object to be reduced profoundly.

One of the advantages of the woodpile geometry is that the complete bandgap can lead to strong suppression of the emission rates of fluorescent sources embedded within the stack [17, 51, 52]. The radiation dynamics of woodpiles containing such sources are determined by the optical local density of states (LDOS), which, in turn, can be computed using the appropriate Green's function. This Green's function represents an idealised point or line source similar to the fictitious sources described in Chapter 4, and can be obtained efficiently by using the techniques outlined in Chapter 2. Once the LDOS is known, radiation lifetimes and coupling strength between an internal source and the PC (for example), as well as the effect that the PC parameters have on these properties, can be determined [135].

Another possibility is the study Anderson localisation in 3D PCs. Few theoretical

studies have been performed in the area of three-dimensional Anderson localisation [136], since the computational barrier usually proves to be insurmountable. The super-cell method presented in this thesis might make such a study feasible, so long as the number of layers is only moderate, and the layer spacing is such that the amount of evanescent coupling is small.

It has been proposed that donor-type woodpile waveguides, whereby a linear waveguide is introduced by adding dielectric, might result in enhanced optical non-linearities inside woodpile waveguides [62]. However, our results for linear waveguides suggest that controlling non-linearities might be more complicated than this because the fields in the vicinity of the waveguide exhibit singular behaviour at points where the radius of curvature vanishes (this situation does not arise in conventional 2D PC waveguides). Near such points, non-linear behaviour would be enhanced due to the large field gradient. These points occur along the entire length of the waveguide, and so their influence on the non-linearity could be substantial, although this has not yet been addressed in the literature.

One last possibility is to model weak defects in woodpiles by applying perturbation methods to the Bloch modes [112]. Weak defects result in defect modes that are highly extended, since the mode lies close to the edge of the bandgap, and are therefore difficult to model using super-cell methds. Though the dispersion of these defect modes can be computed using the ficitious source superposition method presented in Chapter 4, perturbation theory gives more physical insight into the behaviour of the modes, such as the behaviour near mode cutoff [112].

Bibliography

[1] K.O. Hill, Y. Fujii, D. C. Johnson, and B. S. Kawasaki, "Photosensitivity in optical fiber waveguides: application to reflection filter fabrication," Appl. Phys. Lett. **32**, 647 (1978).

[2] Lord Rayleigh, "On the maintenance of vibrations by forces of double frequency, and on the propagation of waves through a medium endowed with a periodic structure," Phil. Mag. **24**, 145 (1887).

[3] J. D. Joannopoulos, S. G. Johnson, J. N. Winn, and R. D. Meade, *Photonic Crystals: Molding the Flow of Light* (Princeton University Press, 2008).

[4] V. P. Bykov, "Spontaneous emission from a medium with a band spectrum," Sov. J. Quantum Electron. **4**, 861 (1975).

[5] K. Ohtaka, "Energy band of photons and low-energy photon diffraction," Phys. Rev. B **19**, 50575067 (1979).

[6] E. Yablonovitch, "Inhibited spontaneous emission in solid-state physics and electronics," Phys. Rev. Lett. **58**, 2059 (1987).

[7] S. John, "Strong localization of photons in certain disordered dielectric superlattices," Phys. Rev. Lett. **58**, 2486 (1987).

[8] P. W. Anderson, "Absence of diffusion in certain random lattices," Phys. Rev. **109**, 1492 (1958).

[9] E. Yablonovitch, and T. J. Gmitter, "Photonic band structure: The face-centered-cubic case employing nonspherical atoms," Phys. Rev. Lett. **67**, 2295 (1991).

[10] K. M. Ho, C. T. Chan, and C. M. Soukoulis, "Existence of a photonic gap in periodic dielectric structures," Phys. Rev. Lett. **65**, 3152 (1990).

[11] B. Song, S. Noda, T. Asano, and Y. Akahane, "Ultra-high-Q photonic double-heterostructure nanocavity," Nat. Mater. **4**, 207 (2005).

[12] T. Baba, "Slow light in photonic crystals," Nat. Photon. **2**, 465 (2008).

[13] P. Strasser, R. Fluckiger, R. Wuest, F. Robin, and H. Jackel, "InP-based compact photonic crystal directional coupler with large operation range," **15**, 8472 (2007).

[14] B. Corcoran, C. Monat, C. Grillet, D. J. Moss, B. J. Eggleton, T. P. White, L. O'Faolain, and T. F. Krauss, "Green light emission in silicon through slow-light enhanced third-harmonic generation in photonic-crystal waveguides," **3**, Nat. Photon. (2009).

[15] E. Özbay, B. Temelkuran, M. Sigalas, G. Tuttle, C. M. Soukoulis, and K. M. Ho, "Defect structures in metallic photonic crystals," Appl. Phys. Lett. **69**, 3797 (1996).

[16] A. Christ, S. G. Tikhodeev, N. A. Gippius, J. Kuhl, and H. Giessen, "Waveguide-plasmon polaritons: strong coupling of photonic and electronic resonances in a metallic photonic crystal slab," Phys. Rev. Lett. **91**, 183901 (2003).

[17] S. Ogawa, M. Imada, S. Yoshimoto, M. Okano, and S. Noda, "Control of Light Emission by 3D Photonic Crystals," Science **305**, 227-229 (2004).

[18] M. Imada, L. H. Lee, M. Okano, S. Kawashima, and S. Noda, "Development of three-dimensional photonic-crystal waveguides at optical-communication wavelengths," Appl. Phys. Lett. **88**, 171107 (2006).

[19] S. Kawashima, K. Ishizaki, and S. Noda, "Light propagation in three-dimensional photonic crystals," Opt. Express **18**, 386-392 (2010).

[20] A. Tandaechanurat, S. Ishida, D. Guimard, M. Nomura, S. Iwamoto, and Y. Arakawa, "Lasing oscillation in a three-dimensional photonic crystal nanocavity with a complete bandgap," Nat. Photon. **5**, 91 (2011).

[21] N. Yamamoto, S. Noda, and A. Chutinan, "Development of one period of a three-dimensional photonic crystal in the 5-10 μm wavelength region by wafer fusion and laser beam diffraction pattern observation techniques," Jpn. J. Appl. Phys. **37**, L1052 (1998).

[22] S. Wu, J. Serbin, and M. Gu, "Two-photon polymerisation for three-dimensional micro-fabrication," J. Photochem. Photobiol. A **181**, 1 (2006).

[23] I. Staude, G. von Freymann, S. Essig, K. Busch, and M. Wegener, "Waveguides in three-dimensional photonic-bandgap materials by direct laser writing and silicon double inversion," Opt. Lett. **36**, 67 (2011).

[24] S. G. Johnson, and J. D. Joannopoulos, " Block-iterative frequency-domain methods for Maxwell's equations in a plane wave basis," Opt. Express **8**, 173 (2001).

[25] G. H. Smith, L. C. Botten, R. C. McPhedran, and N. A. Nicorovici, "Cylinder gratings in conical incidence with applications to modes of air-cored photonic crystal fibers," Phys. Rev. E **66**, 056604 (2002).

[26] G. H. Smith, L. C. Botten, R. C. McPhedran, and N. A. Nicorovici, "Cylinder gratings in conical incidence with applications to woodpile structures," Phys. Rev. E **67**, 056620 (2003).

[27] S. Wilcox, L. C. Botten, R. C. McPhedran, C. G. Poulton, and C. M. de Sterke, "Modeling of defect modes in photonic crystals using the fictitious source superposition method," Phys. Rev. E **71**, 056606 (2005).

[28] K. M. Ho, C. T. Chan, C. M. Soukoulis, R. Biswas and M. Sigalas, "Photonic Band Gaps in Three Dimensions: New Layer-by-Layer Periodic Structures," Solid State Commun. **89**, 413-416 (1994).

[29] H. S. Sözüer, J. P. Dowling, "Photonic Band Calculations for Woodpile Structures," J. Mod. Opt. **41**, 231 (1994).

[30] E. Özbay, A. Abeyta, G. Tutte, M. Tringides, R. Biswas, C. T. Chan, C. M. Soukoulis, and K. M. Ho, "Measurement of a three-dimensional photonic band gap in crystal structure made of dielectric rods", Phys. Rev. B **50**, 1945 (1994).

[31] B. Temelkuran and E. Özbay, "Experimental demonstration of photonic crystal based waveguides", Appl. Phys. Lett. **74**, 486 (1999).

[32] S. Noda, N. Yamamoto, and A. Sasaki, "New realization method for three-dimensional photonic crystal in optical wavelength region", Jpn. J. Appl. Phys. **35**, L909 (1996).

[33] S. Y. Lin, J. G. Fleming, D. L. Hetherington, B. K. Smith, R. Biswas, K. M. Ho, M. M. Sigalas, W. Zubrzycki, S. R. Kurtz, and Jim Bur, "A three-dimensional photonic crystal operating at infrared wavelengths", Nature **394**, 251 (1998).

[34] J. G. Fleming, S. Y. Lin, I. El-Kady, R. Biswas and K. M. Ho, "All-metallic three-dimensional photonic crystals with a large infrared bandgap," Nature **417**, 52-55 (2002).

[35] S. Y. Lin, and J. G. Fleming, "Three-dimensional photonic crystal with a stop band from 1.35 to 1.95 μm", Opt. Lett. **24**, 49 (1999).

[36] S. Noda, K. Tomada, N. Yamamoto, and A. Chutinan, "Full three-dimensional photonic bandgap crystals at near-infrared wavelengths", Science **289**, 604 (2000).

[37] A. Taflove, and S. C. Hagness, *Computational Electrodynamics: The Finite-Difference Time-Domain Method* (Artech House, 2005).

[38] A. Feigel, Z. Kotler, B. Sfez, A. Arsh, M. Klebanov and V. Lyubin, "Interference lithography for 3D photonic band gap crystal layer by layer fabrication," in *Material Research Society Symposium Proceedings, 2001*, edited by, E. D. Jones, O. Manasreh, K. D. Choquette, D. J. Friedman, and D. K. Johnstone, Vol. 692, K2.9.1.

[39] A. Feigel, M. Veinger, B. Sfez, A. Arsh, M. Klebanov and V. Lyubin, "Three-dimensional simple cubic woodpile photonic crystals made from chalcogenide glasses," Appl. Phys. Lett. **83**, 4480-4482 (2003).

[40] S. J. Madden, D. Choi, M. R. Lamont, V. G. Taeed, N. J. Baker, M. D. Pelusi, B. Luther-Davies, and B. J. Eggleton, "Chalcogenide Glass Photonic Chips," Opt. Photon. News **19**, 19-23 (2008).

[41] Y. K. Pang, J. C. W. Lee, C. T. Ho, and W. Y. Tam, "Realization of woodpile structure using optical interference holography," Opt. Express **14**, 9113 (2006).

[42] B. Jin, J. Xu, Y. K. Pang, and W. Y. Tam, "Optical characterization of woodpile structures in gelatin emulsions fabricated by optical interference holography", J. Op. A: Pure Appl. Opt. **10**, 085204 (2008).

[43] Y. Lin, D. Rivera, and K. P. Chen, "Woodpile-type photonic crystals with orthorhombic or tetragonal symmery formed through phase mask techniques," Opt. Express **14**, 887 (2006).

[44] S. Wu, J. Serbin, and M. Gu, "Two-photon polymerisation for three-dimensional micro-fabrication," J. Photochem. Photobiol. A **181**, 1-11 (2006).

[45] G. von Freymann, S. Wong, G. A. Ozin, S. John, F. Pérez-Willard, M. Deubel, and M. Wegener, in *Conference on Lasers and Electro-Optics, 2005*, CTuU5, pp. 1002-1004.

[46] E. Nicoletti, G. Zhou, B. Jia, M. J. Ventura, D. Bulla, B. Luther-Davies, and M. Gu, "Observation of multiple higher-order stopgaps from three-dimensional chalcogenide glass photonic crystals," Opt. Lett. **33**, 2311-2313 (2008).

[47] S. Wong, M. Deubel, F. Pérez-Willard, S. John, G. A. Ozin, M. Wegener, and Georg von Freymann, "Direct laser writing of three-dimensional photonic crystals with a complete photonic bandgap in chalcogenide glasses," Adv. Mater. **18**, 265 (2006).

[48] J. Serbin, A. Ovsianikov, and B. Chichkov, "Fabrication of woodpile structures by two-photon polymerization and investigation of their optical properties," Opt. Express **12**, 5221 (2004).

[49] F. García-Santamaría, M. Xu, V. Lousse, S. Fan, P. V. Braun, and J. A. Lewis, "A germanium inverse woodpile structure with a large photonic band gap," Adv. Mater. **19**, 1567 (2007).

[50] M. Hermatschweiler, M. Wegener, G. A. Ozin, A. Ledermann, and G. von Freymann, "Fabrication of silicon inverse woodpile photonic crystals," in *Conference on Lasers and Electro-Optics, 2001*, CTuY6.

[51] M. J. A. de Dood, A. Polman, and J. G. Fleming, "Modified spontaneous emission from erbium-doped photonic layer-by-layer crystals," Phys. Rev. B **67**, 115106 (2003).

[52] J. Li, B. Jia, G. Zhou, and M. Gu, "Fabrication of three-dimensional woodpile photonic crystals in a PbSe quantum dot composite materal," Opt. Express **14**, 10740 (2006).

[53] K. Ishizaki, and S. Noda, "Manipulation of photons at the surface of three-dimensional photonic crystals," Nature (London) **460**, 367 (2009).

[54] S. N. Tandon, M. Soljacić, G. S. Petrich, J. D. Joannopoulos, and L. A. Kolodziejski, "The superprism effect using large area 2D-periodic photonic crystal slabs," Photon. Nano. Fund. Appl. **3**, 10 (2005).

[55] J. Serbin, and M. Gu, "Superprism phenomena in waveguide-coupled woodpile structures fabricated by two-photon polymerization," Opt. Express **14**, 3563 (2006).

[56] T. Ergin, N. Stenger, P. Brenner, J. B. Pendry, and M. Wegener, "Three-dimensional invisibility cloak at optical wavelengths," Science **328**, 337 (2010).

[57] I. Ederra, J. C. Iriarte, and R. Gonzalo, and P. de Maagt, "Surface waves of finite size electromagnetic band gap woodpile structures," Progress In Electromagnetics Research B **28**, 19 (2011).

[58] A. Chutinan, and S. Noda, "Highly confined waveguides and waveguide bends in three-dimensional photonic crystals," Appl. Phys. Lett. **75**, 3739 (1999).

[59] K. M. Leung, and Y. F. Liu, "Full vector wave calculation of photonic band structures in face-centered-cubic dielectric media," Phys. Rev. Lett. **65**, 2646 (1990).

[60] M. Okano, S. Kako, and S. Noda, "Coupling between a point-defect cavity and a line-defect waveguide in three-dimensional photonic crystal," Phys. Rev. B **68**, 235110 (2003).

[61] S. Kawashima, L. H. Lee, M. Okano, M. Imada, and S. Noda, "Design of donor-type line-defect waveguides in three-dimensional photonic crystals," Opt. Express **13**, 9774 (2005).

[62] S. Kawashima, M. Okano, M. Imada, and S. Noda, "Design of compound-defect waveguides in three-dimensional photonic crystals," Opt. Express **14**, 6303 (2006).

[63] B. Temelkuran, and E. Ozbay, "Experimental demonstration of photonic crystal based waveguides," Appl. Phys. Lett. **74**, 486 (1999).

[64] J. Chen, R. Hong, and J. Yang, "Analysis of planar defect structures in three-dimensional layer-by-layer photonic crystals," J. Appl. Phys. **104**, 063111 (2008).

[65] C. Lpez, "Anderson localization of light: A little disorder is just right," Nat. Phys. **4**, 755 (2008).

[66] A. Chutinan and Noda, "Effects of structural fluctuations on the photonic bandgap during fabrication of a photonic crystal," J. Opt. Soc. Am. B **16**, 240 (1999).

[67] A. Chutinan and Noda, "Effects of structural fluctuations on the photonic bandgap during fabrication of a photonic crystal: a study of a photonic crystal with a finite number of periods," J. Opt. Soc. Am. B **16**, 1398 (1999).

[68] P. Kopperschmidt, "Tetragonal photonic woodpile structures," Appl. Phys. B **76**, 729 (2003).

[69] M. de Dood, B. Gralak, A. Polman, and J. G. Fleming, "Superstructure and finite-size effects in a Si photonic woodpile crystal,", Phys. Rev. **B**, 035322 (2003).

[70] H. Kim, S. Youn, D. E. Shim, and H. T. Hahn, "The optimization of a woodpile photonic crystal and its negative refractive behavior," J. Kor. Phys. Soc. **56**, 747 (2010).

[71] S. Su, L. Tang, and T. Yoshie, "Optical surface Bloch modes of complete photonic bandgap materials as a basis of optical sensing," Opt. Lett. **36**, 2266 (2011).

[72] H. Liu, J. Yao, D. Xu, and P. Wang, "Characteristics of photonic band gaps in woodpile three-dimensional terahertz photonic crystals," Opt. Express **15** (2007).

[73] Z. Zhang and S. Satpathy, "Electromagnetic wave propagation in periodic structures: Bloch wave solution of Maxwells equations," Phys. Rev. Lett. **65**, 2650 (1990).

[74] J. B. Pendry and A. MacKinnon, "Calculation of photon dispersion relations," Phys. Rev. Lett. **69**, 2772 (1992).

[75] J. B. Pendry, "Photonic Band Structures," J. Mod. Opt. **41**, 209 (1994).

[76] P. Bell, J. Pendry, L. Moreno, and A. Ward, "A program for calculating photonic band structures and transmission coefficients of complex structures", Comput. Phys. Commun. **85**, 306 (1995).

[77] B. Gralak, M. de Dood, G. Tayeb, S. Enoch, and D. Maystre, "Theoretical study of photonic band gaps in woodpile crystals," Phys. Rev. E **67**, 066601 (2003).

[78] L. C. Botten, M. S. Craig, R. C. McPhedran, J. L. Adams, and J. R. Andrewartha, "The Dielectric Lamellar Diffraction Grating," Opt. Acta **28**, 413 (1981).

[79] L. Li, "Multilayer modal method for diffraction gratings of arbitrary profile, depth, and permittivity," J. Opt. Soc. Am. A **10**, 2581 (1993).

[80] Y. Wu, and Y. Y. Lu, "Dirichlet-to-Neumann map method for analyzing crossed arrays of circular cylinders," J. Opt. Soc. Am. B **26**, 1984 (2009).

[81] F. J. Lawrence, L. C. Botten, K. B. Dossou, C. Martijn de Sterke, and R. C. McPhedran,"Impedance of square and triangular lattice photonic crystals," Phys. Rev. A **80**, 023826 (2009).

[82] K. Yasumoto, and H. Jia, "Electromagnetic scattering from multilayered crossed-arrays of circular cylinders," SPIE 5445, 200 (2004).

[83] E. Centeno, and D. Felbacq, "Rigorous vector diffraction of electromagnetic waves by bidimensional photonic crystals," J. Opt. Soc. Am. A **17**, 320-327 (2000).

[84] J. L. Adams, L. C. Botten, and R. C. McPhedran, "The crossed lamellar transmission grating," J. Optics (Paris) **9**, 91-100 (1978).

[85] K. Sakoda, *Optical Properties of Photonic Crystals* (Springer, 2001).

[86] R. L. Kronig, and W. G. Penney, "Quantum mechanics of electrons in crystal lattices," Proc. R. Soc. A **130**, 499-513 (1931).

[87] S. Campbell, L. C. Botten, C. M. de Sterke, and R. C. McPhedran, "Fresnel formulation for multi-element lamellar diffraction gratings in conical mountings," Waves Random Complex Media **17**, 455-475 (2007).

[88] L. C. Botten, N. A. Nicorovici, A. A. Asatryan, R. C. McPhedran, C. M. de Sterke, and P. A. Robinson, "Formulation for electromagnetic scattering and propagation through grating stacks of metallic and dielectric cylinders for photonic crystal calculations. Part I. Method," J. Opt. Soc. Am. A **17**, 2165-2177 (2000).

[89] L. C. Botten, R. C. McPhedran, C. M. de Sterke, N. A. Nicorovici, A. A. Asatryan, G. H. Smith, T. N. Langtry, T. P. White, D. P. Fussell, and B. T. Kuhlmey, "From multipole methods to photonic crystal device modelling." In *Electromagnetic Theory and Applications for Photonic Crystals,* K. Yasumoto (CRC Press, Boca Raton, 2005), 47-122.

[90] M. Born, and E. Wolf, *Principles of Optics: Electromagnetic Theory of Propagation, Interference and Diffraction of Light* (Cambridge University Press, Cambridge, 1999). Chap. 1.

[91] L. C. Botten, N. A. Nicorovici, R. C. McPhedran, C. Martijn de Sterke, and A. A. Asatryan, "Photonic band structure calculations using scattering matrices," Phys. Rev. E **64**, 046603 (2001).

[92] Lord Rayleigh, "On the incidence of aerial and electromagnetic waves upon small obstacles in the form of ellipsoids or elliptic cylinders, and the passage of electric waves through a circular aperture in a conducting screen," Phil. Mag. **44**, 28-52 (1897).

[93] Lord Rayleigh, "On the dynamical theory of gratings," Proc. Royal Soc. (London) A **79**, 399-416 (1907).

[94] R. Petit, and M. Cadilhac, Comptes, C. R. Seances Acad. Sci., Ser. B **262**, 468 (1966).

[95] D. Mastyre and M. Cadilhac, "Singularities of the continuation of the fields and validity of Rayleigh's hypothesis," J. Math. Phys. **26**, 2201 (1985).

[96] R. H. T. Bates, "Analytic constraints on electromagnetic field computations," IEEE Trans. Microwave Theory and Tech. **MTT-23**, 605-623 (1975).

[97] A. V. Tishchenko, "Numerical demonstration of the validity of the Rayleigh hypothesis," Opt. Express **17**, 17102 (2009).

[98] P. Yeh, *Optical Waves in Layered Media* (Wiley, New York, 1988). Chap. 4.

[99] L. C. Botten, N. A. Nicorovici, A. A. Asatryan, R. C. McPhedran, C. M. de Sterke, and P. A. Robinson, "Formulation for electromagnetic scattering and propagation through grating stacks of metallic and dielectric cylinders for photonic crystal calculations. Part II. Properties and implementation," J. Opt. Soc. Am. A **17**, 2177-2109 (2000).

[100] B. Gralak, S. Enoch, and G. Tayeb, "From scattering or impedance matrices to Bloch modes of photonic crystals," J. Opt. Soc. Am. A **19**, 1547-1554 (2002).

[101] A. Modinos, N. Stefanou, and V. Yannopapas, "Applications of the layer-KRR method to photonic crystals," Opt. Express **8**, 197-202 (2001).

[102] V. G. Veselago, "The electrodynamics of substances with simulataneousy negative values of ϵ and μ," Sov. Phys. Usp. **10**, 509-514 (1968).

[103] J. B. Pendry, D. Shurig and D. R. Smith, "Controlling electromagnetic fields," Science **312**, 1780-1782 (2006).

[104] A. Moroz, "Exponentially convergent lattice sums," Opt. Lett. **26**, 1119-1121 (2001).

[105] J. Meixner, "The behavior of electromagnetic fields at edges," IEEE Trans. Antennas Propag. **20**, 442-446 (1972).

[106] S. Ha, A. A. Sukhorukov, K. B. Dossou, L. C. Botten, A. V. Lavrinenko, D. N. Chigrin, and Y. S. Kivshar, "Dispersionless tunneling of slow light in antisymmetric photonic crystal couplers," Opt. Express **16**, 1104-1114 (2008).

[107] T. G. Euser, G. Whyte, M. Scharrer, J. S. Y. Chen, A. Abdolvand, J. Nold, C. F. Kaminski, and P. St. J. Russell, "Dynamic control of higher-order modes in hollow-core photonic crystal fibers," Opt. Express **16**, 17972-17981 (2008).

[108] L. C. Botten, K. B. Dossou, S. Wilcox, R. C. McPhedran, C. M. de Sterke, N. A. Nicorovici, and A. A. Asatryan, "Highly accurate modelling of generalized defect modes in photonic crystals using the fictitious source superposition method," International Journal of Microwave and Optical Technology **1**, 133-145 (2006).

[109] F. Zolla, R. Petit, and M. Cadilhac, "Electromagnetic theory of diffraction by a system of parallel rods: the method of fictitious sources," J. Opt. Soc. Am. A **11**, 1087-1096 (1994).

[110] A. Figotin, and V. Goren, "Resolvent method for computations of localized defect modes of H-polarization in two-dimensional photonic crystals," Phys. Rev. E **64**, 056623 (2001).

[111] J. A. C. Weideman, "Numerical integration of periodic functions: A few examples," Am. Math. Monthly **109**, 21-36 (2002).

[112] S. Mahmoodian, C. G. Poulton, K. B. Dossou, R. C. McPhedran, L. C. Botten, and C. M. de Sterke, "Modes of Shallow Photonic Crystal Waveguides: Semi-Analytic Treatment," Opt. Express **17** (2009).

[113] J. S. Brownless, S. Mahmoodian, K. B. Dossou, F. J. Lawrence, L. C. Botten, and C. M. de Sterke, "Coupled waveguide modes in hexagonal photonic crystals," Opt. Express **18**, 25346 (2010).

[114] T. F. Krauss, "Why do we need slow light?," Nature Photonics **2**, 448-450 (2008).

[115] S. Hughes, L. Ramunno, J. F. Young and J. E. Sipe, "Extrinsic Optical Scattering Loss in Photonic Crystal Waveguides: Role of Fabrication Disorder and Photon Group Velocity," Phys. Rev. Lett. **94**, 033903 (2005).

[116] S. Johnson, M. Povinelli, M. Soljačić, A. Kralis, S. Jacobs and J. Joannopoulos, "Roughness losses and volume-current methods in photonic-crystal waveguides," Appl. Phys. B **81**, 283-293 (2005).

[117] I. Tamm, Phys. Z. Sowjetunion **1**, 733 (1932).

[118] V. Heine, "On the general theory of surface states and scattering of electrons in solids," Proc. Phys. Soc. **81**, 300 (1963).

[119] E. Kretschmann, and H. Raether, "Radiative decay of non-radiative surface plasmons excited by light," Z. Naturf. **23**, 2135 (1968).

[120] R. W. Wood, "On a remarkable case of uneven distribution of light in a diffraction grating spectrum," Phil. Mag. **4**, 396-402 (1902).

[121] R. Ulrich, and M. Tacke, "Submillimeter waveguiding on periodic metal structure," Appl. Phys. Lett. **22**, 251-253 (1973).

[122] R. D. Meade, K. D. Brommer, A. M. Rappe, and J. D. Joannopoulos, "Electromagnetic Bloch waves at the surface of a photonic crystal," Phys. Rev. B **44**, 10961 (1991).

[123] M. Galli, M. Belotti, D. Bajoni, M. Patrini, G. Guizzetti, D. Gerace, M. Agio, and L. C. Andreani, "Excitation of radiative and evanescent defect modes in linear photonic crystal waveguides," Phys. Rev. B **70**, 081307(R) (2004).

[124] L. C. Botten, N. A. Nicorovici, R. C. McPhedran, C. M. de Sterke, and A. A. Asatryan, "Photonic band structure calculations using scattering matrices," Phys. Rev. E **64**, 046603 (2001).

[125] F. J. Lawrence, L. C. Botten, K. B. Dossou, R. C. McPhedran, and C. M. de Sterke, "Photonic-crystal surface modes found from impedances," Phys. Rev. A **82**, 053840 (2010).

[126] S. Olivier, H. Benisty, C. J. M. Smith, M. Rattier, C. Weisbuch, and T. F. Krauss, "Transmission properties of two-dimensional photonic crystal channel waveguides", Opt. Quantum Electron. **34**, 171 (2002).

[127] L. C. Botten, R. A. Hansen, and C. M. de Sterke, "Supermodes in multiple coupled photonic crystal waveguides," Opt. Express **14**, 387 (2006).

[128] J. B. Pendry, "Negative refraction makes a perfect lens," Phys. Rev. Lett. **85**, 3966-3969 (2000).

[129] D. Schurig, J. J. Mock, B. Justice, S. A. Cummer, J. B. Pendry, A. F. Starr and D. R. Smith, "Demonstration of a metamaterial electromagnetic cloak at microwave frequencies," Science **314**, 977-980 (2006).

[130] M. G. Silveirinha, C. R. Medeiros, C. A. Fernandes, and J. R. Costa, "Experimental verication of broadband superlensing using a metamaterial with an extreme index of refraction," Phys. Rev. B **81**, 033101 (2010).

[131] J. Li, L.Zhou, C.T. Chan, and P. Sheng, "Photonic band gap from a stack of positive and negative index materials," Phys. Rev. Lett. **90**, 083901 (2003).

[132] A. A. Asatryan, L. C. Botten, M. A. Byrne, V. D. Freilikher, S. A. Gredeskul, I. A. Shadrivov, R. C. McPhedran and Y. S. Kivshar, "Suppression of Anderson localization in disordered metamaterials," Phys. Rev. Lett. **99**, 193902 (2007).

[133] M. Janotta, A. Katzir, and B. Mizaikoff, "Sol-Gel-Coated Mid-Infrared Fiber-Optic Sensors," Appl. Spectros. **57**, 823-828 (2003).

[134] A. Alù, and N. Engheta, "Achieving transparency with plasmonic and metamaterial coatings," Phys. Rev. E **72**, 016623 (2005).

[135] A. A. Asatryan, K. Busch, R. C. McPhedran, L. C. Botten, C. M. de Sterke, and N. A. Nicorovici, "Two-dimensional Green's function and local density of states in photonic crystals consisting of a finite number of cylinders of infinite length," Phys. Rev. E **63**, 046612 (2001).

[136] C. Conti, and A. Fratalocchi, "Dynamic light diffusion, three-dimensional Anderson localization and lasing in inverted opals," Nature Phys. **4**, 794-298 (2008).